Real-time control of oscillating water column wave energy converters

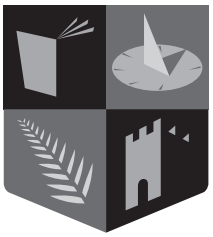

Ollscoil
Mhá Nuad
Ollscoil na hÉireann
Má Nuad

Marco Rosati

A thesis submitted for the degree of
Doctor of Philosophy

Maynooth University

Faculty of Science and Engineering
Electronic Engineering Department
Centre for Ocean Energy Research

June 2024

Head of the department: Prof. Gerard Lacey
Supervisor: **Prof. John V. Ringwood**

Contents

Abstract v

Declaration of authorship vii

Acknowledgements ix

List of Figures xi

Nomenclature xix

List of abbreviations xxxi

I Introduction and preliminaries 1

1 Introduction 3

1.1 Wave energy 6

1.2 Motivation of the thesis 9

1.3 Objectives and contributions 10

1.4 Thesis structure 12

1.5 List of publications 14

2 Oscillating water column systems and linear hydrodynamic modelling 17

2.1 OWC systems 18

2.1.1 Operating principle and main characteristics 18

2.1.2 Origin and development of OWCs 21

2.1.3 OWC PTO mechanism 27

2.2 Linear hydrodynamic modelling 32

2.2.1 Linear wave theory 33

2.2.2 Wave-body interactions 39

2.2.3 Cummins' equation 44

2.2.4 Ocean wave spectra 48

2.3 Summary 49

II OWC WEC modelling 51

3 Oscillating water column modelling from first principles 55
3.1 Hydrodynamic modelling . . . 57
3.1.1 Frequency-domain hydrodynamic model . . . 58
3.1.2 Time-domain hydrodynamic model . . . 59
3.2 Air chamber modelling . . . 59
3.2.1 Time-domain air chamber model . . . 59
3.2.2 Frequency-domain air chamber model . . . 60
3.3 PTO modelling . . . 61
3.3.1 Air turbine model . . . 62
3.3.2 Hydrodynamic/aerodynamic interaction model . . . 64
3.3.3 Electric generator model . . . 65
3.4 Summary . . . 66

4 Data-based hydrodynamic modelling for OWCs 69
4.1 Motivation and background . . . 70
4.1.1 Introduction to system identification . . . 70
4.1.2 Data-based modelling in wave energy . . . 71
4.2 Black-box hydrodynamic modelling for OWCs . . . 73
4.2.1 Experimental campaign . . . 74
4.2.2 Frequency-domain data-based modelling . . . 78
4.2.3 Time-domain data-based modelling . . . 82
4.3 Conclusions . . . 94

III OWC WEC control 97

5 Control problem definition and review of control strategies 99
5.1 OWC wave-to-wire control problem formulation . . . 100
5.1.1 Simplification of the control problem . . . 102
5.1.2 List of constraints . . . 103
5.1.3 Constrained OWC OCP . . . 104
5.1.4 Main control co-design aspects . . . 105
5.2 Review of OWC control strategies . . . 108
5.2.1 Hydrodynamic control . . . 109
5.2.2 Aerodynamic control . . . 114
5.2.3 Wave-to-turbine control . . . 120
5.2.4 Wave-to-wire control . . . 120
5.2.5 Peak-shaving control . . . 120
5.2.6 Grid-side control . . . 122
5.3 Summary . . . 123

6 Static-efficiency-based control for oscillating water columns 129
6.1 Study case definition 131
6.2 Control system design 133
6.2.1 Effect of turbine rotational speed 134
6.2.2 Control system design 135
6.3 Result and discussion 138
6.3.1 Discussion of the results 138
6.3.2 Main control co-design aspects 141
6.4 Conclusions 143

7 Optimal control for oscillating water columns 147
7.1 Pseudospectral control 149
7.1.1 Pseudospectral representation 149
7.1.2 Minimisation of residuals 150
7.2 RHPS control for OWCs 151
7.2.1 OWC OCP formulation 151
7.2.2 Fourier PS approximation 153
7.2.3 OWC OCP simplification 154
7.3 Result and discussion 154
7.3.1 Discussion of the results 155
7.3.2 Main control co-design aspects 158
7.4 Conclusions 161

8 Control co-design of power take-off and bypass valve for oscillating water columns 165
8.1 OWC control co-design 167
8.1.1 Performance function selection 167
8.1.2 PTO and bypass valve specifications 168
8.1.3 Design of the control system 170
8.1.4 Methodology 174
8.2 Results and discussion 174
8.2.1 Results 176
8.2.2 Discussion 176
8.3 Conclusions 181

IV Final remarks 185

9 Conclusions and future perspectives 187
9.1 Main conclusions 187
9.2 Future perspectives 189

Appendices

A Alternative OWC modelling **195**
A.1 Uniform pressure model 195
A.1.1 Hydrodynamic and air chamber modelling 195
A.1.2 Relation between piston and uniform pressure models 196
A.2 Maeda's turbine model 197

Bibliography **199**

Abstract

In order to build a carbon-free society, the production of clean and affordable electric energy is vital. Furthermore, to reduce variability and minimise the need for potentially expensive energy storage systems, the diversification of renewable energy resources is essential. To this end, wave energy is a significant and almost untapped source of renewable energy, which can considerably contribute to the renewable energy mix and, ultimately, to decarbonisation.

Wave energy converters (WECs) harness wave power by exploiting different operating principles. However, due to the relatively high levelised cost of energy (LCoE) associated with wave energy projects, WECs struggle to penetrate in the electric power industry market. A key step to minimise the LCoE, and therefore improve WEC commercialization, is to develop high-performance, real-time, control strategies to maximise the electric energy produced over the WEC lifetime. In particular, this thesis focuses on enhancing the economic viability of a specific type of WEC, known as the oscillating water column (OWC) WEC, by improving state-of-the-art OWC control techniques.

The OWC system is one of the most promising WECs, especially due to its simplicity of operation, the possibility to easily dissipate excessive power, and the fact that all the moving parts are above the water level, meaning that maintenance operations are potentially less complex and expensive. To date, due to the critical importance of turbine performance, OWC control strategies mainly focus on an oversimplified control objective, namely turbine efficiency maximisation, ignoring hydrodynamic and electric generator performance. In this thesis, possible static-efficiency-based and dynamic control strategies to optimise the (overall) wave-to-wire (W2W) energy conversion process of OWC WECs are designed. Furthermore, as an alternative to relatively laborious model determination from first principles, the potential of data-based modelling techniques to provide parsimonious, control-oriented, OWC hydrodynamic models, is investigated. Finally, to maximise OWC WEC profitability, it is important to consider peak-shaving (or rated power) control, to extend the OWC operational range and, consequently, improve the capacity factor. Since peak-shaving control affects the optimal sizing problem for an OWC PTO, a control co-design approach is devised in this thesis to assess the benefit of rated power control. Ultimately, peak-shaving control, used in combination with control co-design techniques, can significantly reduce the LCoE by improving the capacity factor.

Declaration of authorship

I, Marco Rosati, declare that this thesis titled 'Real-time control of oscillating water column wave energy converters' and the work presented in it are my own. I confirm that:

- This work was done wholly or mainly while in candidature for a research degree at this University.
- Where any part of this thesis has previously been submitted for a degree or any other qualification at this University or any other institution, this has been clearly stated.
- Where I have consulted the published work of others, this is always clearly attributed.
- Where I have quoted from the work of others, the source is always given. With the exception of such quotations, this thesis is entirely my own work.
- I have acknowledged all main sources of help.
- Where the thesis is based on work done by myself jointly with others, I have made clear exactly what was done by others and what I have contributed myself.

Date: _____

Signature: _____

Acknowledgements

Personal

In my three years and nine months as a PhD student, I have received vital support from some irreplaceable people, without whom I would have never completed this tortuous, yet truly rewarding, path. Firstly, I would like to thank my supervisor, John Vincent Ringwood, who helped me grow as a researcher and guided me since day one of my PhD. I still do not have the faintest idea of how you manage to supervise all the intern, PhD, and postdoc projects in COER, but keep up with the good work! I also want to express my gratitude to Carrie Anne Barry, my multitasking lab manager and fellow PhD student, for all the hard work you do to make everyone else's lives easier. A special thanks goes to Tom Kelly and João Henriques who have always been there to answer my silly questions. I owe a warm hug to my companions Ahsan, "the bachelor" (not anymore!), Hasana, "the wild", and Edo, "the humongous", for always making my office life big fun. Moreover, to Mahdi, Agustina, Iain, Sandra, Augusto, Thalita, Pedro, Facundo, Matheus, Nahia, Josefredo, Amin, and all other current and past COER members, it was a real pleasure to meet all of you. Wherever I go after PhD, I hope to find a working environment that is half as good as COER lab. Finally, I want to thank all the nice people I met at Maynooth University, particularly Ann Dempsey, Denis Buckley, John Malocco, Séamus McLoone, and Neil Trappe.

On the family side, I owe a huge kiss to my wife, Sara, for the everyday unconditional moral support that you have always given me. It is thanks to you that I managed to keep it together until the end. Last but not least, voglio ringraziare i miei genitori, Livia e Gianluca, mio fratello, Davide, le mie zie, Vilma e Franca, mia nonna, Gemma, i miei suoceri, Antonella e Luca, i miei fratelli acquisiti, Filippo e Sofia, e tutta la mia famiglia allargata. Sappiate che, anche se a distanza, il vostro sostegno è stato fondamentale, non solo in questi ultimi anni, ma durante tutto il mio percorso.

Institutional

Gratitude is expressed to MaREI, the SFI Research Centre for Energy, Climate and Marine, for supporting this work under grant No. 12/RC/2302_P2.

List of Figures

1.1 Primary energy consumption, and the associated energy resources, in the world from 1800 to 2021. On the left side, energy consumption is measured in TeraWatt-hours (TWh), while, on the right side, the corresponding cumulative distribution is shown. Source: [2]. 4
1.2 The figure shows, for different countries/regions of the world: (a) Total electric energy generation in TWh, (b) CO_2 carbon intensity, measured in grams of CO_2 equivalents emitted per kWh of electricity generated, (c) electric energy generated from fossil fuels, and (d) electric energy generated from renewable energy sources. Source: [2]. 5
1.3 Approximation of the average annual wave energy in the world. Figure adapted from [21]. 6
1.4 Plan view of different WEC configurations depending on their dimension and orientation with respect to the incoming waves: (a) is a point absorber, (b) an attenuator, and (c) a terminator. Figure adapted from [35]. 7
1.5 Different types of WECs: (a) is a hinge-barge WEC, (b) a pressure differential point absorber, (c) an overtopping device, (d) a heaving point absorber (HPA), (e) a flap-type WEC, and (f) a fixed oscillating water column. Note that (a), (b), and (c) are offshore WECs, (d) and (e) near-shore devices, and (f) an onshore WEC. The red part of each subfigure represents the PTO system. Source: [46]. 8

2.1 Schematic representation of the essential elements of a fixed OWC WEC. 19
2.2 Schematic representation of the three main types of OWCs: a) Fixed OWC equipped with a Wells turbine, b) Spar-buoy with a biradial turbine installed, and c) Backward Bent Duct Buoy (BBDB) with a Wells turbine fitted. Source: [51]. 20
2.3 Examples of the three main types of OWCs: a) Mutriku wave power plant, Basque Country, b) IDOM Marmok-A5 spar-buoy, and c) OceanEnergy OE35 BBDB. Source: [51]. 21
2.4 This figure shows a) a schematic of Masuda's navigation OWC-buoy and b) a picture of the Kaimei. Source: [66]. 22

2.5 Pictures of the a) Pico power plant and b) OWC device at Toftestallen. Source: [66]. 23
2.6 This figure shows a) the Mighty Whale, b) a schematic of the Seabreath, and c) the 1:3rd scale prototype of the MK3. Source: [66]. 25
2.7 a) A Wells turbine without guide vanes and a single row of rotor blades (i.e., a monoplane turbine). b) A typical aerofoil section of a rotor blade and the inlet velocity triangles for two different flow rates. The variables $V_{1,2}$, $W_{1,2}$, $U_{1,2}$, and $\beta_{1,2}$ are, respectively, the absolute airflow velocity, the relative airflow velocity, the rotor blade velocity (computed as the product of rotational speed and rotor blade radius), and the angle of attack, for two different airflow rates. Source: [51]. . 28
2.8 a) An axial-flow impulse turbine. b) A typical rotor cascade with guide vanes. c) Rotor inlet velocity triangles for two flow rates. The quantities **W**, **U**, and **V** are, respectively, the relative, the transport, and the absolute velocities. In this figure only, R refers to the rotor blade radius. Source: [51]. 29
2.9 a) Biradial turbine with two rows of fixed guide-vanes radially offset from the rotor. b) Cut of the turbine showing the position of the sliding high-speed stop valve (HSSV). c) Picture of a small-scale rotor with a diameter of 0.25 m. Source: [51]. 29
2.10 This figure shows the a) HydroAir and b) Denniss-Auld air turbines. Source: [66]. 31
2.11 Main flow regimes and fluid dynamic models as function of the Knudsen number. Figure adapted from [151]. 33
2.12 Schematic of the wave characteristics. 36
2.13 Schematic of a floating body with the boundary conditions introduced in Sections 2.2.1 and 2.2.2. The term S_{wet} indicates the body wetted surface. 40
2.14 Schematic of the six degrees-of-freedom of a floating body, with their corresponding index numbers. 41
2.15 Hydrodynamic coefficients for the heave mode of a 288 mm wide OWC. A full description of the considered OWC geometry is given in [105]. 45
2.16 Radiation and excitation force kernels for the heave mode of a 288 mm wide OWC. A full description of the considered OWC geometry is given in [105]. 46
2.17 Examples of JONSWAP SDFs with varying parameters (a) T_{p}, (b) H_{s}, and (c) γ_{J}. 48
2.18 Example of a wave elevation time series generated from a JONSWAP SDF with T_{p} =10 s, H_{s} =2 m, and $\gamma_{\text{J}} = 3.3$. 49

3.1 Wave-to-wire power flow in an OWC WEC. The red ovals indicate possible manipulated inputs. All variables are defined in Chapter 3. Figure adapted from [51]. 56
3.2 Schematics of the a) piston and b) uniform pressure models. Source: [66]. 57
3.3 Frequency dependant hydrodynamic parameters for the Mutriku OWC: (a) Added mass, $A_{\mathrm{p}}(\omega)$, and radiation damping, $B_{\mathrm{p}}(\omega)$; (b) magnitude of the excitation force coefficient, $|\hat{F}_{\mathrm{ex}}(\omega)|$, and phase of the excitation force coefficient, $\angle\hat{F}_{\mathrm{ex}}(\omega)$. 59
3.4 Dimensionless models of the (a) Wells turbine and (b) biradial turbine at Mutriku OWC. The figure shows the turbine efficiency, η_{turb}, dimensionless flow rate, Φ, and dimensionless power, Π, as functions of the dimensionless pressure head, Ψ. Figure adapted from [51]. . . . 63
3.5 Turbine efficiency, η_{turb}, as a function of Δp and Ω, for the (a) Wells turbine and (b) biradial turbine at Mutriku OWC. 63
3.6 Turbine damping characteristics for two turbines. Relationship between the pressure difference, Δp, and the air mass flow rate, w_{turb}, as Ω changes, for a Wells turbine, an axial-flow impulse turbine, and a biradial turbine. Figure adapted from [56]. 65

4.1 Schematic representation of the SI loop. Figure adapted from [200]. . 72
4.2 Schematic representation of the input/output model considered in this work. 73
4.3 Picture of the narrow tank at DkIT. Source: [58]. 74
4.4 Schematic representation of the narrow tank and scaled OWC chamber at DkIT. 74
4.5 Bretschneider SDFs used in the irregular wave experiments. 77
4.6 Empirical amplitude response, $|H_i(\jmath\omega)|$. For clarity, the data are divided as follows: (a) $i = 1, \ldots 6$; (b) $i = 1, 3, 5$; (c) $i = 2, 4, 6$. 79
4.7 Schematic of the frequency-domain SI procedure for the regular wave case. 79
4.8 Empirical amplitude response, $|H_i(\jmath\omega)|$, compared to the amplitude response of the models with inconsistent orders, $|H_i^{'}(\jmath\omega)|$. For clarity, the results are divided as follows: (a) $i = 1, 3, 5$; (b) $i = 2, 4, 6$. 83
4.9 Empirical amplitude response, $|H_i(\jmath\omega)|$, compared to the amplitude response of the models with consistent orders, $|H_i^{''}(\jmath\omega)|$. For clarity, the results are divided as follows: (a) $i = 1, 3, 5$; (b) $i = 2, 4, 6$. 83
4.10 Schematic of the linear time-domain SI procedure carried out for the irregular wave case. 84

4.11 Identification and validation NRMSE values for separate ARX models, identified from $D^{\mathrm{B}}_{3_{\mathrm{a}}}$ and validated against $D^{\mathrm{B}}_{3_{\mathrm{b}}}$, using different combinations of n_{a} and n_{b}, with n_{d} = -1. On the right side of the figure, a focus on the case in which $n_{\mathrm{b}} = 2$ is shown. 86
4.12 Validation NRMSE values for separate ARX models, identified from $D^{\mathrm{B}}_{3_{\mathrm{a}}}$ and validated against $D^{\mathrm{B}}_{3_{\mathrm{b}}}$, using different n_{d} values, with $n_{\mathrm{a}} = 6$ and $n_{\mathrm{b}} = 2$. 86
4.13 Schematic of the nonlinear time-domain SI procedure carried out for the irregular wave case. 88
4.14 Identification and validation NRMSE values for separate KGP models, identified from $D^{\mathrm{B}}_{3_{\mathrm{a}}}$ and validated against $D^{\mathrm{B}}_{3_{\mathrm{b}}}$, using different p values, with $n^{'}_{\mathrm{a}} = 6$, $n^{'}_{\mathrm{b}} = 2$, and $n^{'}_{\mathrm{d}} = -1$. 90
4.15 Comparison between the measured output, $y(t)$ (from $D^{\mathrm{B}}_{3_{\mathrm{b}}}$), and the (a) 1-step-ahead, (b) 5-step-ahead, and (c) 10-step-ahead predicted outputs, $y^{\mathrm{arx}}(t)$ and $y^{\mathrm{kgp}}(t)$, respectively related to the validation of the ARX model M^{arx}_{3} and the KGP model M^{kgp}. 91
4.16 Schematic procedure related to the real-time implementation of a multi-linear model. 93
4.17 Chirp signal linearly sweeping the frequency range $0 - 20$ Hz, in the time interval $0 - 2$ s. 95

5.1 Schematic representation of the wave-to-grid power flow of an OWC WEC. Figure adapted from [56]. 101
5.2 Schematic of the OWC control regions as functions of the available wave power. The blue shaded area represents the safe operating area of the OWC WEC. 104
5.3 Schematics of a traditional progressive stepwise design procedure and a CCD procedure, for a generic wave energy project. 106
5.4 a) Typical velocity for an uncontrolled heaving buoy with a natural frequency, ω_{buoy}, higher than the frequency of the excitation force, ω_{wave}. b) Latching control to align the phases of the heave velocity, v_{buoy}, and the excitation force F_{wave}. c) Latching control for a heaving buoy subject to irregular sea waves. The terms $|\bar{v}_{\mathrm{buoy}}|$ and $|\bar{F}_{\mathrm{wave}}|$ are average normalising values for v_{buoy} and F_{wave}, respectively. Figure Source: [223]. 112
5.5 Schematic representation of a twin unidirectional (radial-flow) turbines PTO configuration. Source: [315]. 124

6.1 Radiation convolution approximation with FOAMM. (a) Radiation damping with the interpolation points selected in FOAMM, indicated by the orange crosses; (b) radiation kernel from WAMIT and FOAMM approximation. 132

6.2 Electric generator efficiency, η_{gen}, as a function of the dimensionless rotational speed, $\Omega/\Omega^{\text{max}}$, and the dimensionless control torque, $T_{\text{ctrl}}/T_{\text{ctrl}}^{\text{max}}$. Ω^{max} and $T_{\text{ctrl}}^{\text{max}}$ are, respectively, the maximum allowable rotational speed and the maximum control torque. Adapted from [110].133
6.3 Mutriku wave climate modelling: (a) JONSWAP spectral density functions for the SSs in Table 6.2 and (b) attenuation function, $\varphi_{\text{mtrk}}(\omega)$.134
6.4 Effect of Ω on the OWC system performance, for three sea states: (a) SS1, (b) SS4, and (c) SS8. 135
6.5 (a) The blue curves represent $\bar{P}_{\text{elec}}$, as a function of Ω, for different sea states (SS1 - SS8). Furthermore, the power curves, $P_{\text{ctrl}}^{\text{w2w}}$ from Equation (6.8), and $P_{\text{ctrl}}^{\text{tem}}$ from Equation (6.6), are also shown. (b) Contribution of the linear and exponential terms (6.8) to $P_{\text{ctrl}}^{\text{w2w}}$, with a focus (i.e., the blue shaded area) on the low speed region. 136
6.6 (a) Impact of Ω on w_{turb} (therefore on ζ_{W}), for two different values of Δp, and (b) effect of Ω on w_{turb} and Δp. 138
6.7 Time series of the (a) pneumatic power, P_{pneu}, (b) turbine power, P_{turb}, and (c) electric power, P_{elec}, obtained using TEM and W2W control, for one realisation of SS4. 139
6.8 Time series of the (a) turbine efficiency, η_{turb}, and (b) a focus on η_{turb} (from $t = 620$ s to $t = 680$ s), obtained using TEM and W2W control, for one realisation of SS4. 140
6.9 Time series of the (a) generator control torque, T_{ctrl}, and (b) turbine rotational speed, Ω, obtained using TEM and W2W control, for one realisation of SS4. 141
6.10 ξ_{hydro} and $\bar{\eta}_{\text{turb}}$ for fifteen constant values of Ω, in SS4. For each turbine type, the corresponding shaded area represents the range of possible values of ξ_{hydro}. 142
6.11 Electric energy production over 900 s using TEM and W2W control, for a realization of SS4. 144
6.12 Time series obtained using W2W control, for one realisation of SS4.(a) OWC position, z, and velocity, $\dot{z}$; (b) air chamber density, ρ_{c}, and air chamber volume, V_{c}; (c) pressure difference, Δp, and turbine mass flow rate, w_{turb}; (d) dimensionless pressure head, Ψ, and dimensionless turbine mass flow rate Φ. 145

7.1 Active, and reactive, power region for a generic WEC and an OWC WEC with a self-rectifying air turbine, under optimal control. Figure adapted from: [347]. 152
7.2 Typical time series of the absorbed power for a generic WEC under optimal control. Figure adapted from: [347]. 152

7.3 Graphical representation of efficiencies (and CWRs) obtained with RHPS control (■) and TEM control (♦), for four different sea states (namely SS1, SS4, SS6, and SS8). For each sea state, the values of ξ_{hydro} (top), $\bar{\eta}_{\text{turb}}$ (left), ξ_{aero} (bottom), and $\bar{\eta}_{\text{gen}}$ (right) are reported. The external black circles represent an ideal (i.e., unitary) efficiency/CWR value, while the three dashed circles indicate the isolines for efficiency values equal to 0.25, 0.50, and 0.75. 156
7.4 Time traces, from a realization of SS6, of the chamber pressure difference, Δp, using TEM (Δp^{tem}), RHPS (Δp^{rhps}), and steady-state W2W (Δp^{w2w}) control. 157
7.5 Time traces, from a realization of SS6, of the pneumatic power, P_{pneu}, using TEM ($P^{\text{tem}}_{\text{pneu}}$), RHPS ($P^{\text{rhps}}_{\text{pneu}}$), and steady-state W2W ($P^{\text{w2w}}_{\text{pneu}}$) control. 158
7.6 Graphical representation of efficiencies (and CWRs) obtained with RHPS control (■) and W2W control (●), for four different sea states (namely SS1, SS4, SS6, and SS8). For each sea state, the values of ξ_{hydro} (top), $\bar{\eta}_{\text{turb}}$ (left), ξ_{aero} (bottom), and $\bar{\eta}_{\text{gen}}$ (right) are reported. The external black circles represent an ideal (i.e., unitary) efficiency/CWR value, while the three dashed circles indicate the isolines for efficiency values equal to 0.25, 0.50, and 0.75. 159
7.7 Time traces, from a realization of SS7, of the (a) rotational speed, Ω, and (b) control torque, T_{ctrl}, using TEM (Ω^{tem}, $T^{\text{tem}}_{\text{ctrl}}$), RHPS ($\Omega^{\text{rhps}}$, $T^{\text{rhps}}_{\text{ctrl}}$), and steady-state W2W (Ω^{w2w}, $T^{\text{w2w}}_{\text{ctrl}}$) control. 160
7.8 Time traces, from a realization of SS7, of the turbine efficiency, η_{turb}, using TEM ($\eta^{\text{tem}}_{\text{turb}}$), RHPS ($\eta^{\text{rhps}}_{\text{turb}}$), and steady-state W2W ($\eta^{\text{w2w}}_{\text{turb}}$) control. 161
7.9 Time traces of the control torque, T_{ctrl}, for a realisation of SS4, for each considered control approach. 162
7.10 Percentage of time, compared to the total simulation time, during which reactive power is required, in each SS. Source: [63]. 162
7.11 Rotational speed dynamic range analysis for each control strategy, namely TEM, steady-state W2W, and RHPS control. The figure shows a histogram in the range $\Omega = [100, 400]$ rad/s, with 200 bins. A logarithmic scale is used for the vertical axis. 163

8.1 Wave-to-wire power flow of the OWC system considered in this chapter. 166
8.2 Cost of the moving parts, C_{mov}, as a function of the turbine rotor diameter, d_{r}, and the ratio between bypass valve diameter and turbine rotor diameter, $d_{\text{bypass}}/d_{\text{r}}$. $C^{\text{mtrk}}_{\text{mov}}$ is the cost of the moving parts of Mutriku OWC ($d_{\text{r}} = 0.75$ m, $d_{\text{bypass}}/d_{\text{r}} = 0$). 169
8.3 Maximum rotational speed, Ω^{max}, PTO rated power, P^{rated}, and turbine inertia (top x-axis label), I, as functions of the turbine rotor diameter, d_{r}. If $d_{\text{r}} > 0.7$ m, $\Omega^{\text{max}} = \Omega^{\text{max}}_{\text{turb}}$, whereas if $d_{\text{r}} \leq 0.7$ m, $\Omega^{\text{max}} = \Omega^{\text{max}}_{\text{gen}}$. . . 170

8.4 Wave power threshold, $\bar{P}^{\text{thr}}_{\text{wave}}$, for each considered turbine rotor diameter, d_{r}. 173
8.5 Bypass valve control design. (a) Time-averaged electrical power, $\bar{P}_{\text{elec}}$, as a function of the available wave power, $\bar{P}^{\text{owc}}_{\text{wave}}$. (b) Relative electrical power decrease, $\bar{P}^{\text{decr}}_{\text{elec}}(u_{\text{bypass}})$, as a function of the bypass valve position, u_{bypass}. (c) Bypass valve position controller, u_{bypass}, and its derivative $u'_{\text{bypass}} = \text{d}u_{\text{bypass}}/\text{d}\bar{P}^{\text{owc}}_{\text{wave}}$. 173
8.6 Flow chart of the proposed CCD approach. 174
8.7 Annual wave climate at Mutriku. The four scatter plots show, for each combination of H_{s} and T_{p}, (a) the frequency of occurrence (over a year) of a specific sea state at Mutriku, (b) the mean available wave power, $\bar{P}^{\text{owc}}_{\text{wave}}$, (c) the contribution (specified as a percentage) of each irregular sea state to the total annual wave power available at Mutriku, and (d) the number (from 1 to 58) assigned at each irregular sea state considered in this work. 175
8.8 LCoE^* obtained from all the considered combinations of d_{r} and $d_{\text{bypass}}/d_{\text{r}}$. The green circle (● at Γ^{15}_{55}) highlights the condition for which LCoE^* is minimised, the blue square (■ at Γ^{0}_{60}) indicates the point at which the minimum LCoE^* is achieved without using a bypass valve, and the magenta hexagon (⬢ at Γ^{20}_{50}) shows the condition for which the maximum capacity factor, $\zeta^{\text{max}}_{\text{cf}}$, is found. 177
8.9 Average annual value of the capacity factor, ζ_{cf}, for each combination of turbine rotor diameter, d_{r}, and diameter ratio, $d_{\text{bypass}}/d_{\text{r}}$. The magenta hexagon (⬢ at Γ^{20}_{50}) shows the condition for which the peak value of ζ_{cf}, $\zeta^{\text{max}}_{\text{cf}} = 0.263$, is achieved. 178
8.10 LCoE^* and/or capacity factor, ζ_{cf}, for some significant combinations of d_{r} and/or $d_{\text{bypass}}/d_{\text{r}}$. 178
8.11 Insight into the effect of the bypass valve for Γ^{15}_{55} (and Γ^{0}_{55}). The green shaded areas highlight the sea states for which the bypass valve is closed ($u_{\text{bypass}} = 0$), since $\bar{P}_{\text{wave}} \leq \bar{P}^{\text{thr}}_{\text{wave}}$, meaning that pneumatic power is not dissipated. For each combination of H_{s} and T_{p}, the four scatter plots show: (a) the relative bypassed pneumatic power, P^*_{bypass}, for Γ^{15}_{55}; (b) the capacity factor, ζ_{cf}, for Γ^{15}_{55}; (c) the relative percentage increase in ζ_{cf}, ζ^*_{cf}, obtained for Γ^{15}_{55} in comparison with Γ^{0}_{55}; (d) the LCoE enhancement index, LEI, as defined in Eqs. (8.18) and (8.19). 179
8.12 $E^{\text{life}}_{\text{elec}}$ obtained from all the considered combinations of d_{r} and $d_{\text{bypass}}/d_{\text{r}}$.180
8.13 Schematic of a hybrid WEC combining OWC and overtopping wave energy conversion technologies. Source: [362]. 182

Nomenclature

Roman letters

$A(\omega)$	Matrix with radiation added mass coefficients for the considered DoFs
A_∞	Added mass at infinite frequency
A_{bypass}	Bypass valve area
A_{owc}	Amplitude of the OWC vertical position
$A_{\text{p}}(\omega)$	Added mass of the water piston
A_{p}^{∞}	Added mass of the water piston at infinite frequency
$A_{\text{r}},B_{\text{r}},C_{\text{r}},D_{\text{r}}$ . . .	Matrices of the radiation subsystem SS model
$A_{\text{si}},B_{\text{si}},C_{\text{si}},D_{\text{si}},F_{\text{si}}$	Possible polynomial functions of a linear SI model structure
$A_{\text{ssr}},B_{\text{ssr}},C_{\text{ssr}},D_{\text{ssr}}$	Matrices of the WEC dynamics SSR
A_{turb}	Area of the turbine duct
A_{w}	Wave amplitude
$a_{1,2}$	Parameters of TEM control
$B(\omega)$	Matrix with radiation damping coefficients for the considered DoFs
$B_{\text{p}}(\omega)$	Radiation damping of the water piston
b	Proportional parameter between OpEx and CapEx
$b_{1,2}$	Parameters of the linear term for steady-state W2W control
b_{c}	Turbine rotor blade chord
b_{h}	Turbine rotor blade height
C_{A}	Power coefficient of Maeda's turbine model
C_{bypass}	Cost of the bypass valve
C_{d}	Discharge coefficient of the bypass valve
C_{elec}	Cost of the electric components
C_{h}	Hydrostatic stiffness mass

C_{int} . . . . . Integration constant

C_{mech} . . . . . Cost of the mechanical components

$C_{\text{mech}}^{\text{pico}}$ . . . . . Cost of the mechanical components for Pico OWC

C_{mov} . . . . . Cost of the moving parts

$C_{\text{mov}}^{\text{mtrk}}$ . . . . . Cost of the moving parts for Mutriku OWC

C_{pto} . . . . . Cost of the OWC PTO

C_{safety} . . . . . Cost of the safety valve

C_{steel} . . . . . Cost per unit mass of steel

C_{str} . . . . . Cost of the OWC structure

C_{T} . . . . . Torque coefficient of Maeda's turbine model

$c_{1,2}$ . . . . . Parameters of the exponential term for steady-state W2W control

c_{air} . . . . . Air speed of sound

c_{w} . . . . . Wave celerity

$c_{\text{w}}^{\text{deep}}$ . . . . . Wave celerity in deep water conditions

D^{B} . . . . . Input/output data set generated using a Bretschneider SDF

D^{mer} . . . . . Merged input/output data set

D_{θ} . . . . . Derivative matrix in the Fourier PS approximation

d_{bypass} . . . . . Bypass valve diameter

d_{pp} . . . . . Probe-to-probe distance

d_{r} . . . . . Turbine rotor diameter

d_{mtrk} . . . . . Mutriku OWC turbine rotor diameter

$d_{\text{r}}^{\text{pico}}$ . . . . . Pico OWC turbine rotor diameter

E_{elec} . . . . . Electric energy

$E_{\text{elec}}^{\text{life}}$ . . . . . Produced electrical energy over the OWC WEC lifetime

E_{kin} . . . . . Kinetic energy of a system

E_{pot} . . . . . Potential energy of a system

E_{tot} . . . . . Total energy of a system

$F(\omega)$ . . . . . Fourier transform of the force vector f

$F_{\text{d}}(\omega)$ . . . . . Diffraction force

$F_{\text{ex}}(\omega)$ . . . . . Fourier transform of the excitation force vector f_{ex}

$F_{\text{ext}}(\omega)$ . . . . . Fourier transform of the external force vector f_{ext}

$F_{\mathrm{FK}}(\omega)$ . . . . . Froude-Krylov force

$F_{\mathrm{h}}(\omega)$ . . . . . Fourier transform of the hydrodynamic force vector f_{h}

Fr . . . . . Froude number

$F_{\mathrm{r}}(\omega)$ . . . . . Fourier transform of the radiation force vector f_{r}

$\hat{F}_{\mathrm{ex}}(\omega)$ . . . . . Vector with excitation force frequency domain coefficients for the considered DoFs

f . . . . . Vector of the external forces per unit mass acting of a fluid

f_{bypass} . . . . . Bypass valve control function

$f_{\mathrm{bypass}}^{\mathrm{line}}$ . . . . . Linear bypass valve control function

f_{ex} . . . . . Vector with excitation force values for the considered DoFs

f_{ext} . . . . . Vector with external force values for the considered DoFs

f_{g} . . . . . Gravity force

f_{h} . . . . . Vector with hydrostatic force values for the considered DoFs

f_{i} . . . . . Inertia force

f_{pto} . . . . . Vector with PTO force values for the considered DoFs

f_{r} . . . . . Vector with radiation force values for the considered DoFs

f_{s} . . . . . Sampling frequency

f_{v} . . . . . Viscosity force

f_{w} . . . . . Wave frequency in hertz

$G_{\mathrm{owc}}(\omega)$ . . . . . OWC radiation conductance

$G_{\mathrm{p}}(\omega)$ . . . . . Water piston radiation conductance

G_{θ} . . . . . Block diagonal matrix resulting from the Fourier PS approximation of the radiation convolution integral

g . . . . . Gravitational acceleration constant

$H(\omega)$ . . . . . Empirical transfer function

$H^{'}(\omega)$ . . . . . Model of $H(\omega)$ with inconsistent order

$H^{''}(\omega)$ . . . . . Model of $H(\omega)$ with consistent order

$H_{\mathrm{f2v}}(\omega)$ . . . . . Force-to-velocity frequency response matrix for the considered DoFs

$H^{\mathrm{m}}(\omega)$ . . . . . Model of $H(\omega)$

$H_{\mathrm{owc}}(\omega)$ . . . . . OWC radiation susceptance

$H_{\mathrm{p}}(\omega)$ . . . . . Water piston radiation susceptance

$H^{\mathrm{r}}(\omega)$ . . . . . Rough model of $H(\omega)$

H_{s} . . . . . Significant wave height

H_{w} . . . . . Wave height

h_{sb} . . . . . Water depth

I . . . . . Moment of inertia

I^{mtrk} . . . . . PTO inertia moment at Mutriku

I_{n} . . . . . Identity matrix

$i_{\mathrm{d,q}}$ . . . . . Generator stator currents in the direct/quadrature frame

i_{grid} . . . . . Grid current

J . . . . . Cost functional

K_{d} . . . . . PID derivative gain

K_{i} . . . . . PID integral gain

K_{N} . . . . . Knudsen number

K_{p} . . . . . PID proportional gain

$K_{\mathrm{r}}(\omega)$ . . . . . Fourier transform of the vector k_{r}

k_{e} . . . . . Vector with the excitation force kernel for the considered DoFs

k_{r} . . . . . Vector with the radiation force kernel for the considered DoFs

k_{w} . . . . . Wave number

L_{c} . . . . . Representative physical length scale

$L_{\mathrm{d,q}}$ . . . . . Generator stator inductances in the direct/quadrature frame

M . . . . . Matrix with mass and inertia values for the considered DoFs

M^{arx} . . . . . ARX model

M^{kgp} . . . . . KGP model

Ma . . . . . Mach number

m . . . . . Mass of the system

m_{c} . . . . . Air mass inside the OWC pneumatic chamber

m_{p} . . . . . Mass of the water piston

N_{arx} . . . . . Number of unknown parameters of the ARX model

N_{b} . . . . . Number of turbine rotor blades

N_{c} . . . . . Number of collocation points

N_{lm} . . . . . Number of unknown parameters of the multi-linear model

N_{kgp} . . . . . Number of unknown parameters of the KGP model

N_{p} . . . . . Number of poles of a transfer function

$N_{\mathrm{p}}^{\mathrm{gen}}$ . . . . . Number of poles of an electric generator

N_{z} . . . . . Number of zeros of a transfer function

n_{a},n_{b} . . . . . ARX model orders

$n_{\mathrm{a}}^{'}$,$n_{\mathrm{b}}^{'}$ . . . . . KGP model orders

n_{d},$n_{\mathrm{d}}^{'}$ . . . . . ARX/KGP model input delay

n_{DoF} . . . . . Number of DoF

n_o . . . . . Unit vector normal to a surface

n_{r} . . . . . Number of states of the radiation convolution state space approximation model

n_{ssr} . . . . . Number of states of the WEC dynamics SSR

P^{rated} . . . . . Generator rated power

P_{bypass} . . . . . Pneumatic power dissipated through the bypass valve

P_{bypass}^{*} . . . . . Relative pneumatic power dissipated through the bypass valve

P_{elec} . . . . . Generator (active) electric power

$\bar{P}_{\mathrm{elec}}^{\mathrm{decr}}$ . . . . . Relative electrical power decrease due to the bypass valve

P_{fr} . . . . . Power loss due to bearing friction

P_{pneu} . . . . . Pneumatic power available to the air turbine

$P_{\mathrm{pneu}}^{\mathrm{tem}}$ . . . . . Pneumatic power available to the air turbine with TEM control

$P_{\mathrm{pneu}}^{\mathrm{rhps}}$ . . . . . Pneumatic power available to the air turbine with RHPS control

$P_{\mathrm{pneu}}^{\mathrm{w2w}}$ . . . . . Pneumatic power available to the air turbine with steady-state W2W control

P_{turb} . . . . . Turbine power

$P_{\mathrm{turb}}^{\mathrm{mep}}$ . . . . . Turbine power at the turbine MEP

$\bar{P}_{\mathrm{wave}}$ . . . . . Time-averaged wave power per metre of wave crest

$\bar{P}_{\mathrm{wave}}^{*}$ . . . . . Relative time-averaged wave power per metre of wave crest

$P_{\mathrm{wave}}^{\mathrm{airy}}$ . . . . . Power transported by an Airy wave

$\bar{P}_{\mathrm{wave}}^{\mathrm{max}}$ . . . . . Wave power maximum value for bypass valve control design

$\bar{P}_{\mathrm{wave}}^{\mathrm{owc}}$ . . . . . Time-averaged wave power per metre of wave crest available to the OWC

$\bar{P}_{\mathrm{wave}}^{\mathrm{thr}}$ . . . . . Wave power threshold value for bypass valve control design

p . . . . . Fluid pressure

p_0 . . . . . Air atmospheric pressure

p_c . . . . . Air chamber pressure

q^- . . . . . Backward shift operator

q_bypass . . . . . Bypass valve air volumetric flow rate

q_e . . . . . Excitation air volumetric flow rate

q_h . . . . . Heat flux vector

q_r . . . . . Radiated air volumetric flow rate

q_turb . . . . . Turbine air volumetric flow rate

$R_\mathrm{d,q}$ . . . . . Generator stator resistances in the direct/quadrature frame

Re . . . . . Reynolds number

r_i . . . . . Residual form of the i-th system dynamic equation

r_r . . . . . Mean radius of the turbine rotor blades

S . . . . . Generic power spectral density of η

S^B . . . . . Bretschneider SDF

S_h . . . . . Matrix of hydrostatic stiffness coefficients for the considered DoFs

S_J . . . . . JONSWAP power spectral density

S_mtrk . . . . . JONSWAP power spectral density at Mutriku

S_owc . . . . . Cross-sectional area of the water column

S_wet . . . . . Wetted surface of the device

S_wn . . . . . Power spectral density of a white noise signal

T . . . . . Fluid temperature

T_a . . . . . Axial friction torque

T_ctrl . . . . . Generator control torque

$T_\mathrm{ctrl}^\mathrm{max}$ . . . . . Maximum generator control torque

$T_\mathrm{ctrl}^\mathrm{opt}$ . . . . . Optimal control torque

$T_\mathrm{ctrl}^\mathrm{tem}$ . . . . . Control torque for TEM control

$T_\mathrm{ctrl}^\mathrm{rhps}$ . . . . . Control torque for RHPS control

$T_\mathrm{ctrl}^\mathrm{w2w}$ . . . . . Control torque for steady-state W2W control

T_e . . . . . Energy period

T_{h} . . . . . Receding time window length

T_{p} . . . . . Peak period

T_{r} . . . . . Radial friction torque

T_{w} . . . . . Wave period

t . . . . . Time

t_{h} . . . . . Safety/bypass valve thickness

t_{k} . . . . . Collocation points

$\mathbf{U}$ . . . . . Matrix containing the unknown parameters of the control inputs

U . . . . . Circumferential velocity at the mean radius

$U_{1,2}$ . . . . . Rotor blade velocity

u_{bypass} . . . . . Bypass valve relative position

u_{f} . . . . . Flow velocity vector of a fluid

u_{hsv} . . . . . High-speed valve relative position

$\hat{\mathbf{u}}_{\mathrm{j}}$ . . . . . Vector containing the unknown parameters of the j-th control input

$u_{\mathrm{j}}^{\mathrm{M}}$ . . . . . Pseudospectral approximation of the j-th control input using M basis functions

$\tilde{u}_{\mathrm{j,q}}$ . . . . . Unknown parameter of the j-th control input and q-th basis function

u_{n_o} . . . . . Floating body velocity in the n_o direction

u_{pid} . . . . . PID control input

u_{pitch} . . . . . Pitch angle of the rotor/stator blades

$u_{\mathrm{q}}^{\mathrm{c}}$ . . . . . Unknown parameter of the q-th cosine function in a Fourier PS approximation for the control input

$u_{\mathrm{q}}^{\mathrm{s}}$ . . . . . Unknown parameter of the q-th sine function in a Fourier PS approximation for the control input

u_{throttle} . . . . . Throttle valve relative position

V_0 . . . . . Air chamber volume in still water conditions

$V_{1,2}$ . . . . . Absolute airflow velocity at the rotor inlet

V_{c} . . . . . Air chamber volume

$V_{\mathrm{exit,t}}$ . . . . . Tangential component of the absolute airflow velocity at the turbine exit

v . . . . . OWC vertical velocity

$v_{\mathrm{d,q}}$ . . . . . Generator stator voltages in the direct/quadrature frame

v_{grid} . . . . . Grid voltage

$v_{\mathrm{tip}}^{\mathrm{max}}$ . . . . . Maximum blade tip speed

v_{x} . . . . . Mean axial velocity

$W_{1,2}$ . . . . . Relative airflow velocity at the rotor inlet

w_{bypass} . . . . . Bypass valve air mass flow rate

w_{turb} . . . . . Turbine air mass flow rate

$\mathbf{X}$ . . . . . Matrix containing the unknown parameters of the state variables

$X(\omega)$ . . . . . Fourier transform of the WEC position vector χ

x . . . . . State vector of the WEC dynamics SSR

$\hat{\mathbf{x}}_{\mathrm{i}}$ . . . . . Vector containing the unknown parameters of the i-th state variable

$x_{\mathrm{i}}^{\mathrm{M}}$ . . . . . Pseudospectral approximation of the i-th state variable using M basis functions

$\tilde{x}_{\mathrm{i,q}}$ . . . . . Unknown parameter of the i-th state variable and q-th basis function

$x_{\mathrm{i,q}}^{\mathrm{c}}$ . . . . . Unknown parameter of the q-th cosine function in a Fourier PS approximation for the i-th state variable

$x_{\mathrm{i,q}}^{\mathrm{s}}$ . . . . . Unknown parameter of the q-th sine function in a Fourier PS approximation for the i-th state variable

x_{r} . . . . . State vector of the radiation SSR

Y_{arx} . . . . . ARX model predicted output vector

y . . . . . Output vector of the WEC dynamics SSR

y_{arx} . . . . . ARX model predicted output

y_{kgp} . . . . . KGP model predicted output

y_{r} . . . . . Output vector of the radiation SSR

$Z_{\mathrm{i}}(\omega)$ . . . . . WEC intrinsic impedance

$Z_{\mathrm{pto}}(\omega)$ . . . . . PTO impedance

$Z_{\mathrm{r}}(\omega)$ . . . . . Radiation impedance matrix

z . . . . . OWC vertical position

Greek symbols

α . . . . . Scaling factor

β . . . . . Exponential parameter for computing C_{mech}

$\beta_{1,2}$ . . . . . Angle of attack

Γ_i^j . . . . . Parametric point located at (i,j)

γ . . . . . Specific heat ratio of the specified fluid

γ_{J} . . . . . Peak-shape parameter of the JONSWAP spectrum

$\Delta\bar{P}_{\text{elec}}$ . . . . . Relative increase in electrical power

Δp . . . . . Pressure difference between the air chamber and atmosphere

Δp^{tem} . . . . . Pressure difference between the air chamber and atmosphere with TEM control

Δp^{rhps} . . . . . Pressure difference between the air chamber and atmosphere with RHPS control

Δp^{w2w} . . . . . Pressure difference between the air chamber and atmosphere with steady-state W2W control

ϵ . . . . . Proportional parameter for estimating C_{str} from $C_{\text{mov}}^{\text{mtrk}}$

ζ . . . . . Turbine damping

ζ_{b} . . . . . Biradial turbine damping

ζ_{cf} . . . . . Capacity factor

ζ_{cf}^* . . . . . Relative increase in the capacity factor

ζ_{i} . . . . . Axial-flow impulse turbine damping

ζ_{W} . . . . . Wells turbine damping

η . . . . . Free surface elevation

η_{gen} . . . . . Generator efficiency

η_{turb} . . . . . Turbine efficiency

$\eta_{\text{turb}}^{\text{tem}}$ . . . . . Turbine efficiency with TEM control

$\eta_{\text{turb}}^{\text{rhps}}$ . . . . . Turbine efficiency with RHPS control

$\eta_{\text{turb}}^{\text{w2w}}$ . . . . . Turbine efficiency with steady-state W2W control

θ . . . . . Matrix containing all the basis functions θ_{q}

θ_{arx} . . . . . ARX model parameter vector

$\theta_{\text{arx}}^{\text{opt}}$ . . . . . Optimal (in the LS sense) value of θ_{arx}

θ_{kgp} . . . . . KGP model parameter vector

$\theta_{\text{kgp}}^{\text{opt}}$ . . . . . Optimal (in the LS sense) value of θ_{kgp}

θ_{q} . . . . . The q-th basis function of a basis function expansion

ι . . . . . OWC capture width

κ_{b} . . . . . Biradial turbine geometric constant

$\kappa_{\mathrm{c}}(A)$ . . . . . Condition number of the matrix A

κ_{i} . . . . . Axial-flow impulse turbine geometric constant

κ_{W} . . . . . Wells turbine geometric constant

Λ_{arx} . . . . . Regression matrix of the ARX model

Λ_{kgp} . . . . . Regression matrix of the KGP model

λ_{m} . . . . . Molecular mean free path length

λ_{pm} . . . . . Rotor permanent magnet flux

λ_{w} . . . . . Wavelength

μ . . . . . Manufacturing cost coefficients for the control valves

μ_{f} . . . . . Dynamic viscosity of the fluid

ν_{air} . . . . . Air cinematic viscosity

ξ_{aero} . . . . . Aerodynamic CWR

ξ_{elec} . . . . . Electric CWR

ξ_{hydro} . . . . . Hydrodynamic CWR

Π . . . . . Dimensionless turbine power

π . . . . . Pi Greek

ρ . . . . . Density of a fluid

ρ_0 . . . . . Air atmospheric density

ρ_{air} . . . . . Air density

ρ_{c} . . . . . Air chamber density

ρ_{steel} . . . . . Steel density

ρ_{w} . . . . . Water density

σ . . . . . Cauchy stress tensor

σ_{smc} . . . . . Sliding variable

τ . . . . . Deviatoric stress tensor

Φ . . . . . Dimensionless air mass flow rate

Φ_{d} . . . . . Diffraction velocity potential

Φ_{f} . . . . . Velocity potential of the fluid

Φ_{i} . . . . . Incident wave velocity potential

Φ_r	Radiation velocity potential
Φ_rd	Sum of Φ_r and Φ_d
ϕ	Phase of the wave
ϕ_x	Flow coefficient of Maeda's turbine model
ϕ_r	Unit-amplitude radiation potential
φ_arx	ARX model regression vector
φ_kgp	KGP model regression vector
φ_mtrk	Attenuation function for computing S_mtrk
$\chi, \dot{\chi}, \ddot{\chi}$	Position, velocity, and acceleration vectors of the device for the considered DoFs
Ψ	Dimensionless pressure head
Ψ_mep	Value of Ψ at the maximum efficiency point
Ψ_stall	Value of Ψ at the limit of the Wells turbine stall region
Ω	Turbine/generator rotational speed
Ω^max	Maximum rotational speed
Ω^tem	Rotational speed with TEM control
Ω^thr	Threshold value of the rotational speed
Ω^rhps	Rotational speed with RHPS control
Ω^w2w	Rotational speed with steady-state W2W control
Ω_mep	Value of the rotational speed at the turbine MEP
$\Omega^\mathrm{max}_\mathrm{gen}$	Maximum generator rotational speed
$\Omega^\mathrm{max}_\mathrm{noise}$	Maximum rotational speed to limit noise emissions
$\Omega^\mathrm{max}_\mathrm{turb}$	Maximum turbine rotational speed
Ω_ref	Turbine reference speed value
ω	Wave frequency
ω_e	Generator electric angular frequency

xxx

List of abbreviations

ANN . . . . . Artificial Neural Network

AR . . . . . AutoRegressive

ARMAX . . . . . AutoRegressive Moving-Average with Exogenous Input

ARX . . . . . Autoregressive with Exogenous Input

B2B . . . . . Back-to-Back

BBDB . . . . . Backward Bent Duct Buoy

BC . . . . . Boundary Condition

BEM . . . . . Boundary Element Method

BJ . . . . . Box-Jankins

BS . . . . . Backstepping

BVP . . . . . Boundary Value Problem

CapEx . . . . . Capital Cost

CCD . . . . . Control Co-Design

CFD . . . . . Computational Fluid Dynamics

CoF . . . . . Criterion of Fitting

CR . . . . . Control Region

CTB . . . . . Contribution

CWR . . . . . Capture Width Ratio

DFIG . . . . . Doubly-Fed Induction Generator

DkIT . . . . . Dundalk Institute of Technology

DoF . . . . . Degree-of-Freedom

FGS . . . . . Fuzzy Gain Scheduling

FLC . . . . . Fuzzy Logic Controller

FOAMM . . . . . Finite Order Approximation by Moment-Matching

FPSOM . . . . . Fractional Particle Swarm Optimisation Memetic

FRT . . . . . Fault-Ride-Through

FSE . . . . . Free Surface Elevation

GGW . . . . . Grouped Grey Wolf

HPA . . . . . Heaving Point Absorber

HRCF . . . . . Half-Range Chebyshev-Fourier

HS . . . . . Harmony Search

HSSV . . . . . High-Speed Stop Valve

HSV . . . . . High-Speed Valve

ID . . . . . Identification Data

IFM . . . . . Inverse Fuzzy Model

JONSWAP . . . Joint North Sea Wave Observation Project

KGP . . . . . Kolmogorov-Gabor Polynomial

LCoE . . . . . Levelised Cost of Energy

LEI . . . . . LCoE Enhancement Index

LES . . . . . Large Eddy Simulations

LF . . . . . Lyapunov Function

LPT . . . . . Linear Potential Theory

LS . . . . . Least-Squares

LTI . . . . . Linear Time Invariant

LWT . . . . . Linear Wave Theory

MM . . . . . Moment Matching

MEP . . . . . Maximum Efficiency Point

MPC . . . . . Model Predictive Control

MPPT . . . . . Maximum Power Point Tracking

MWR . . . . . Mean Weighted Residual

NRMSE . . . . . Normalised Root Mean Square Error

NWT . . . . . Numerical Wave Tank

OBJ . . . . . Objective

OpEx . . . . . Operational Cost

OTD . . . . . Overtopping Device

OWC . . . . . Oscillating-Water-Column

P2W . . . . . Pneumatic-to-Wire

PBM . . . . . Physics Based Model

PID . . . . . Proportional-Integral-Derivative

PMG . . . . . Permanent Magnet Generator

PS . . . . . Pseudospectral

PSO . . . . . Particle Swarm Optimisation

PTO . . . . . Power Take-Off

RH . . . . . Receding-Horizon

RHPS . . . . . Receding-Horizon Pseudospectral

RWT . . . . . Real Wave Tank

SCIG . . . . . Squirrel-Cage Induction Generator

SDF . . . . . Spectral Density Function

SI . . . . . System Identification

SMC . . . . . Sliding Mode Control

S/N . . . . . Signal-to-Noise Ratio

SOSMC . . . . . Second Order Sliding Mode Control

SPH . . . . . Smoothed-Particle Hydrodynamics

SS . . . . . Sea State

SSR . . . . . State Space Representation

STA . . . . . Super Twisting Algorithm

SWL . . . . . Still Water Level

TEM . . . . . Turbine Efficiency Maximising

TF . . . . . Transfer Function

THR . . . . . Threshold

TPL . . . . . Technology Performance Level

TRL . . . . . Technology Readiness Level

UN . . . . . United Nations

VD . . . . . Validation Data

VT . . . . . Valve/Turbine

W2T . . . . . Wave-to-Turbine

W2W . . . . . Wave-to-Wire

WEC . . . . . Wave Energy Converter

WEI . . . . . Wind Energy Ireland

ZN . . . . . Ziegler-Nichols

ZPC . . . . . Zero-Pole Cancellation

Part I

Introduction and preliminaries

The formulation of the problem is often more essential than its solution, which may be merely a matter of mathematical or experimental skill.

— Albert Einstein.

1 Introduction

Contents

1.1 Wave energy 6
1.2 Motivation of the thesis 9
1.3 Objectives and contributions 10
1.4 Thesis structure 12
1.5 List of publications 14

The production and distribution of clean, sustainable, and affordable electric energy is one of the most crucial challenges of the XXI century [1]. From an economic perspective, access to affordable energy, at a global level, is key to mitigate poverty and develop welfare around the world [2]. On the other hand, the use of renewable and sustainable energy resources, as an alternative to more historical fossil fuel-based forms of energy, is essential to moderate the global temperature increase [2]. As a matter of fact, global warming [3] is mainly due to carbon dioxide (CO_2), and other greenhouse gases, emissions [4], which are released during the combustion cycle of fossil fuels (such as coal, oil, and natural gas) [5].

Over the last century, due the rapid increase in the world population and industrial sites, global energy consumption has grown exponentially, rising from around 1×10^4 TWh, in 1900, to around 16×10^4 TWh, in 2021. To date, global energy production is still vastly dominated by fossil fuel-based energy sources, as shown in Figure 1.1, while, even considering modern biofuels, only about 10% of the current global primary energy demand is supplied by renewables (i.e., wind, solar,

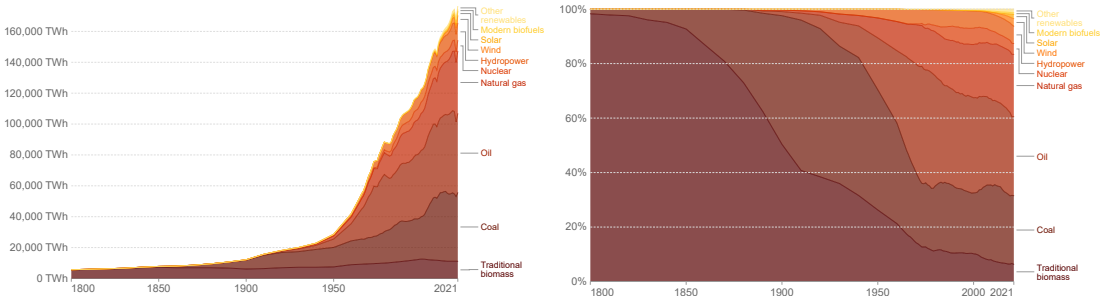

Figure 1.1: Primary energy consumption, and the associated energy resources, in the world from 1800 to 2021. On the left side, energy consumption is measured in TeraWatt-hours (TWh), while, on the right side, the corresponding cumulative distribution is shown. Source: [2].

hydropower, and others). In relatively recent years, a number of countries have adhered to policies which are designed to support and encourage energy transition and, ideally, to set a path towards a low-carbon, renewable-dominated, global energy mix. For instance, following the political commitment to reduce emissions by 55% by 2030, the European Commission is also committed to policies that will contribute to the European Green Deal ambition, namely achieving carbon-neutrality by 2050 [6]. Furthermore, the Global Roadmap for Accelerated SDG7 (Sustainable Development Goal 7) Action [7] was issued by the United Unions (UN), in 2021, to support the 2030 Agenda for Sustainable Development [8] and the Paris Agreement on Climate Change [9]. The SDG7 roadmap essentially sets the milestones to achieve, by 2050, 92% of global energy production from renewable technologies. In addition to eco-aware policy trends, public and private investments in renewable energy technologies have also grown [2], not only driven by ecological/environmental reasons, but also since harvesting the finite amount of easily-available fossil fuels is becoming increasingly difficult and, therefore, expensive [10]. Furthermore, the recent global energy crisis, which has drastically escalated due to a number of factors, such as the fast post-pandemic economic rebound in 2021 and Russia's invasion of Ukraine in 2022, has provoked a record increase in the oil and natural gas prices [11]. However, to counteract the negative impact of the energy crisis, the short-term solution adopted by many countries was to increase subsidies for fossil fuels and burn more coal [12], partially hindering the development of more efficient and sustainable energy services.

In relation to purely electric energy, as opposed to primary energy, production, renewable electricity reached about the 30% of global electric energy generation (~ 29 TWh) in 2022 [12], as shown in Figure 1.2. It is interesting to note that, in 2021, at the end of the COVID pandemic, worldwide electricity generation increased by 6.2% (only 2.3% in 2022), and renewable energy sources contributed to about

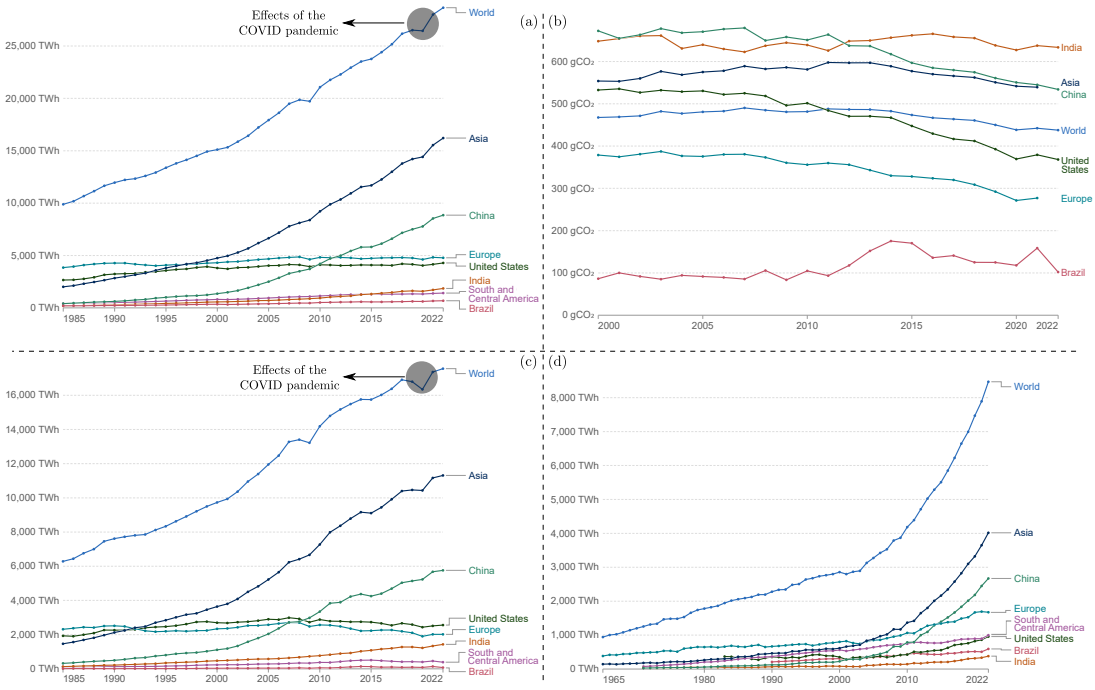

Figure 1.2: The figure shows, for different countries/regions of the world: (a) Total electric energy generation in TWh, (b) CO_2 carbon intensity, measured in grams of CO_2 equivalents emitted per kWh of electricity generated, (c) electric energy generated from fossil fuels, and (d) electric energy generated from renewable energy sources. Source: [2].

92% of the increase [12], showing an encouraging signal. Nowadays, the renewable electric energy market is mainly populated by traditional, well-established, renewable energy sources (i.e., onshore wind, solar, and hydropower), with wind and solar energy responsible for 23.9% of renewable electricity generation. At a national level, with the Climate Action Plan 2024 [13], Ireland envisages installing 9 GW of onshore wind (currently ~ 4.3 GW [14]), at least 5 GW of offshore wind, and 8 GW of solar photovoltaic (currently ~ 0.7 GW [15]) capacities, by 2030. However, to achieve carbon neutrality, *diversification* of renewable energy resources is imperative [16][1], particularly since diversification potentially reduces variability [17, 18], and therefore minimises the need for potentially expensive energy storage systems and non-renewable baseload power. Indeed, one of the main problems of renewable energies, compared to fossil fuels, is that the availability of the energy source is not always guaranteed, with inter- and intra-annual fluctuations that can be significant. For instance, wind energy met 36% of Ireland electricity demand in 2020 (with an average capacity factor of 30%), but dropped to 29.4% in 2021 (with an average capacity factor of 25%) [14]. Variability can be mitigated through optimal combination of different, *poorly correlated* (i.e., *highly complementary*),

[1]The 'amount of diversification' required to achieve carbon neutrality is a site-specific problem, which primarily depends on the types and characteristics of the available renewable resources.

renewable resources. To this end, in addition to traditional renewable technologies, it is essential to incorporate emerging, and still relatively unexploited, renewable energy sources, such as offshore wind, wave, and tidal, into the energy mix. For instance, given the relatively good complementarity between wind and wave resources on the west coast of Ireland [19], optimal combination of wind/wave energy can reduce variability [20].

Since this thesis particularly focuses on wave energy exploitation, the following section highlights the fundamental aspects of wave energy and main wave energy conversion technologies.

1.1 Wave energy

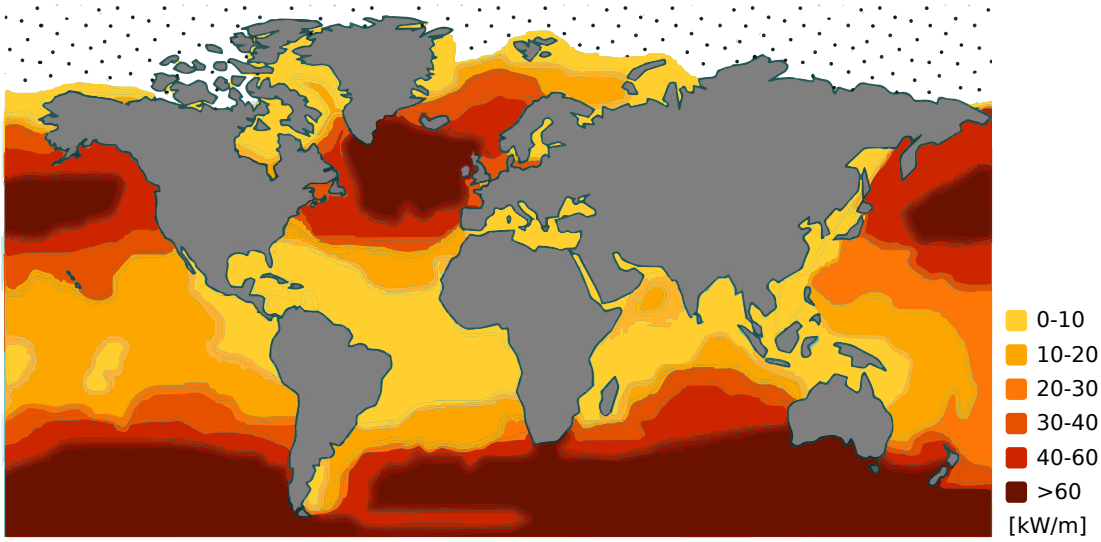

Figure 1.3: Approximation of the average annual wave energy in the world. Figure adapted from [21].

Wave energy, which is harnessed by wave energy converters (WECs), is an almost untapped source of renewable energy, with a higher power density than other renewable energy sources, such as wind and solar [22]. The wave energy average global annual potential has been estimated by a number of different authors, who report values around 32×10^3 TWh/year [23, 24], or $16 - 18.5 \times 10^3$ TWh/year [25], although the energy resource varies temporally (annual and inter-annual variations) and spatially [18]. However, it should be noted that part of the available wave energy resource is located in remote areas (see Figure 1.3), which are typically far from the coast, where the deployment of WECs may be technically difficult and unprofitable. Furthermore, some studies [26, 27] suggest that a

portion of the estimated annual potential may come from extreme events (i.e., storms), during which WECs cannot typically operate to avoid major failures. Finally, as a consequence of ongoing climate change, the global wave energy potential is increasing [28, 29, 30] (particularly at high latitudes [31]), although at a relatively slow variation rate (around 500 TWh/decade on average [18]), and this may potentially cause more frequent, extreme (non-exploitable), meteorological events [32, 33]. Ultimately, although a realistic global potential estimate is yet to be determined, wave energy can significantly contribute to the renewable energy mix and, therefore, to decarbonization [34].

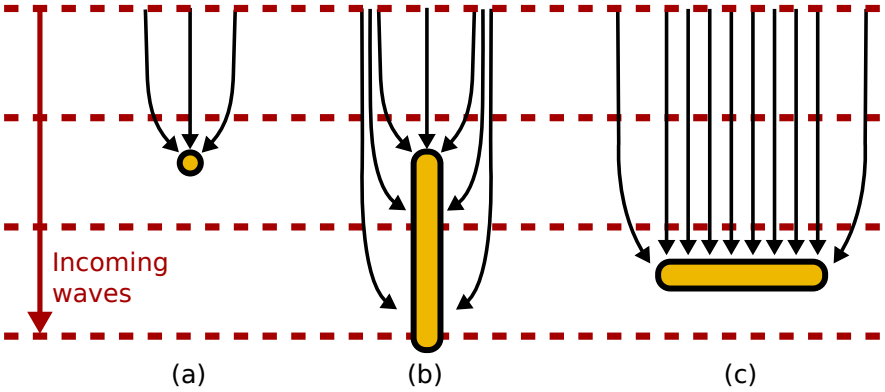

Figure 1.4: Plan view of different WEC configurations depending on their dimension and orientation with respect to the incoming waves: (a) is a point absorber, (b) an attenuator, and (c) a terminator. Figure adapted from [35].

To date, a number of different WEC types have been proposed, with more than one thousand registered patents [36]. Wave energy conversion devices have typically two main subsystems, namely the WEC body (or structure) and power take-off (PTO) mechanism, which converts the wave-induced kinetic power of the WEC body to electricity. In general, WECs can be classified on the basis of three different classification schemes:

- Proximity of the WEC deployment site to the coastline [37]. As such, there exist onshore, near-shore, and offshore (when water depths are about 100 m and loose mooring lines are used) wave energy systems.
- Orientation of the device hull with respect to the incoming wave direction (Figure 1.4) [38]. Within this classification system, it is possible to recognise point absorber, attenuator, and terminator WECs.
- Type of wave energy conversion technology, or working principle [37]. For instance, some popular WECs are shown in Figure 1.5, although many other WEC types can be found in the literature, such as gyroscopic (i.e., the PTO is gyroscopic) [39, 40] and cyclorotor [41] WECs.

Since wave energy harvesting technologies are still relatively immature, the community of researchers and developers has not unanimously converged to a specific WEC concept yet, assuming there will be a single dominant WEC type in the future. It is also possible that, given the different conditions at each specific deployment site (e.g., bathymetry, distance from the shore, annual wave resource characteristic, etc...) and range of possible applications (e.g., electric energy generation for the power grid [42], wave-powered data buoys [43], hydrogen production from wave energy [44], combined wind/wave resource exploitation [45], etc...) in which WECs may be utilised, a number of distinct wave energy conversion technologies may coexist and complement each other.

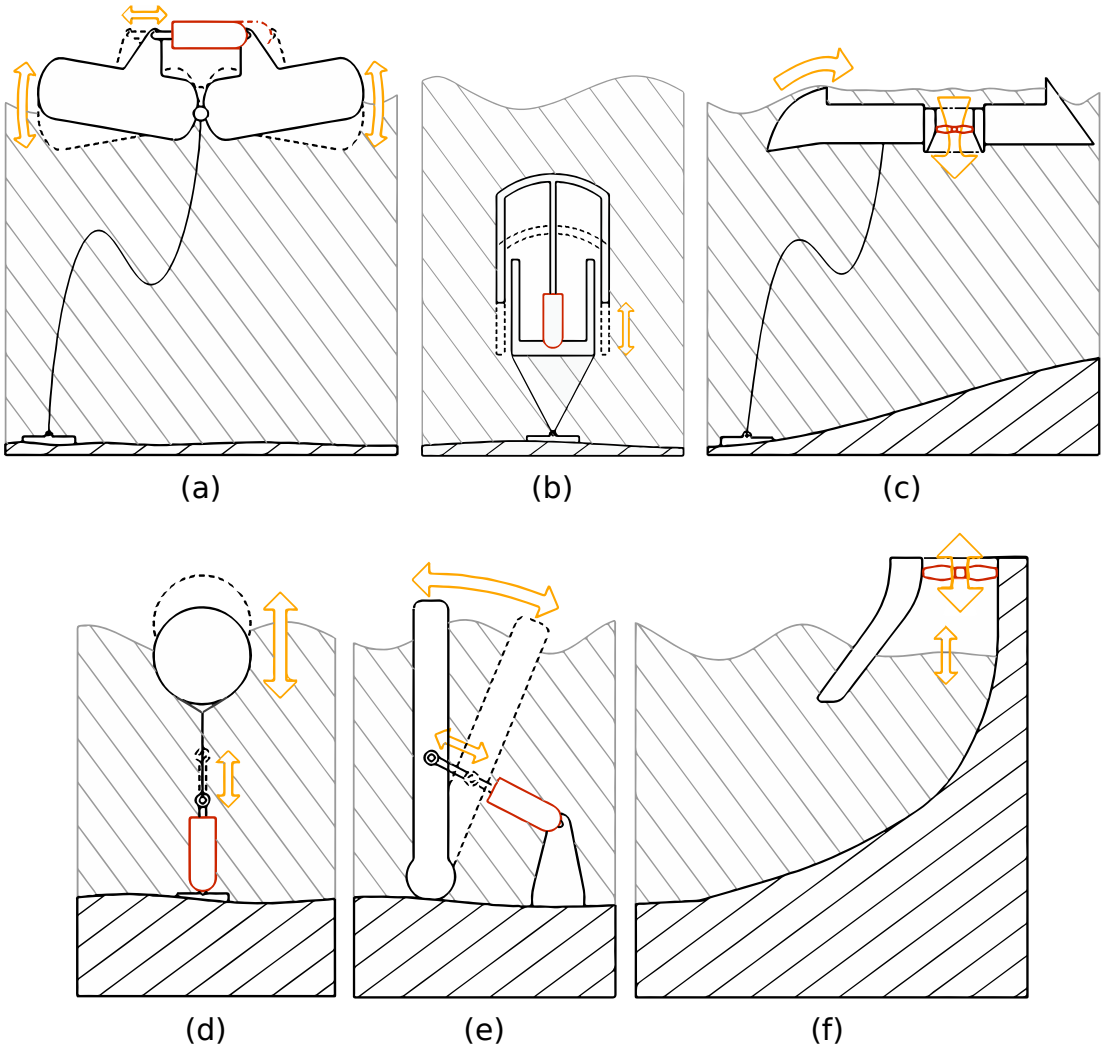

Figure 1.5: Different types of WECs: (a) is a hinge-barge WEC, (b) a pressure differential point absorber, (c) an overtopping device, (d) a heaving point absorber (HPA), (e) a flap-type WEC, and (f) a fixed oscillating water column. Note that (a), (b), and (c) are offshore WECs, (d) and (e) near-shore devices, and (f) an onshore WEC. The red part of each subfigure represents the PTO system. Source: [46].

1.2 Motivation of the thesis

Nowadays, despite the significant potential of wave energy, WECs struggle to penetrate into the electric energy market, particularly since the *levelised cost of energy* (LCoE), defined as

$$\text{LCoE} = \frac{\text{Capital costs (CapEx)} + \text{Operational costs (OpEx)}}{\text{Produced energy over the WEC lifetime}}, \tag{1.1}$$

associated with wave energy projects is relatively high [34], especially if compared to the main alternative renewable energy sources (such as wind and solar) [34, 47]. However, as mentioned previously in this chapter, diversification of renewable energy resources is vital to achieve a sustainable energy mix with moderate variability [16] and, to this end, the contribution of wave energy can be significant. In order to improve WEC profitability, it is therefore essential to minimise the LCoE and, of all possible LCoE-reduction pathways, the development of high-performance energy maximising WEC control strategies is of primary importance [48]. Although energy maximisation is generally desirable, it should not be forgotten that produced energy maximisation is only a *simplified* control objective, which does not necessarily guarantee optimum economic return. Nonetheless, since LCoE minimisation is, as a control objective, difficult to use, especially since reliable and accurate OpEx estimation is challenging, the vast majority of research papers on WEC control focus on energy maximisation [49, 50, 51, 52]. Operational cost estimation is a complex issue in wave energy, especially since there is a dramatic lack of long-term (~ 30 years) data for WECs operating in real sea environments. In any case, produced energy maximisation can be a suitable simplified control objective, providing that one always keeps in mind what the ultimate performance metric is and try to considered costs (at least) in a qualitative way.

In essence, this thesis focuses on enhancing the economic viability of a specific type of WEC, namely the oscillating water column (OWC) WEC (Figure 1.5(f)), exhaustively described in Section 2.1, by broadly improving the state-of-the-art OWC control techniques. The OWC PTO system is typically an air turbine directly coupled with a suitable electric generator. In short, the motion of a water column, subject to ocean wave excitation, generates pneumatic power in an air chamber, which the OWC PTO subsequently converts to electricity. It is interesting to note that the OWC is one of the few wave energy conversion technologies which has achieved technology readiness level (TRL) 8 [53, 54], while other promising WECs (such as HPA and flap-type WECs) are typically at TRL 6-7. For clarity, the TRL metric defines how ready a technology is, where TRL 1 means that the basic physical principles are being studied, while TRL 9 means that an actual system

is successfully proven in real operational environment[2]. Ultimately, to maximise OWC WEC profitability, the work presented in this thesis tackles various OWC control-related issues, which are detailed in Section 1.3, where the objectives and contributions of the thesis are explained.

1.3 Objectives and contributions

A summary of the main objectives (OBJ), and corresponding novel contributions (CTB), of the thesis is presented in the current section.

OBJ.1 One of the objectives of this thesis is to critically examine existing OWC control practices and identify important issues which need to be addressed for improving OWC economic viability. To this end, the contributions of the thesis are:

CTB.1.1 The literature gaps in OWC control are identified and analysed. Furthermore, a novel criterion, based on an objective-focused perspective, is proposed to classify the existing OWC control strategies and an comprehensive formulation of the OWC control problem is presented. Work published in [51, 56].

CTB.1.2 Due to the lack of attention on OWC hydrodynamic control, hydrodynamic control possibilities for OWCs are investigated and discussed. Work published in [56, 57].

OBJ.2 Traditional OWC WEC hydrodynamic modelling from first principles is relatively laborious and complex. On the one hand, linear hydrodynamic models from first principles have a potentially limited range of validity, particularly for WECs under controlled conditions. On the other hand, accurate nonlinear physics-based hydrodynamic modelling can be difficult. In relation to linear and nonlinear OWC hydrodynamic modelling, the contributions of this thesis are summarised as follows:

CTB.2.1 As an alternative to physics-based hydrodynamic models, this thesis investigates the potential of adopting linear, and nonlinear, data-based modelling techniques to obtain some control-oriented (i.e., relatively simple and with a suitable range of validity for control) OWC hydrodynamic models. Work published in [58, 59].

[2]It should be noted that the TRL only indicates the *technical* capability of a technology, while the technology performance level (TPL) defines how well a technology performs from an *economic* perspective [55]. Ultimately, both TRL and TPL are important techno-economical indicators for evaluating the status of a specific technology.

CTB.2.2 Some important real-time implementation aspects of data-based linear and nonlinear models are also analysed. In particular, the advantages of using a (global) nonlinear data-based hydrodynamic model, as opposed to a multi-linear data-based modelling solution, are discussed. Work published in [59].

OBJ.3 The critical review on OWC control has revealed that turbine rotational speed is typically controlled to solely maximise turbine efficiency, ignoring the (generally non-negligible) impact of rotational speed on the OWC hydrodynamic and electric subsystems. Therefore, one of the main objectives of this thesis is to develop more complete turbine rotational speed control strategies, in which rotational speed is modulated to optimise the OWC (overall) wave-to-wire (W2W) energy conversion process. The main contributions of this thesis, in relation to OBJ.3, are summarised as follows:

CTB.3.1 A relatively simple, meaning that no online optimisation is required, static-efficiency-based W2W control approach for OWCs is designed. In comparison to traditional turbine efficiency maximising control (or, simply, turbine control), the proposed W2W efficiency maximising control solution improves electric energy production, specifically since rotational speed is controlled considering the OWC hydrodynamic part and electric generator, without requiring any additional actuator. Work published in [60, 61].

CTB.3.2 A relatively computationally efficient constrained optimal control strategy for energy maximisation of OWCs is devised. In particular, a receding-horizon pseudospectral (RHPS) control approach is designed to tackle the W2W OWC optimal control problem (OCP). Ultimately, RHPS control increases electric energy production, if compared against turbine and steady-state W2W control, especially due to its optimal constraint handling capabilities, which allow the entire rotational speed operational range to be more efficiently exploited. Work published in [62, 63] and further extended in Chapter 7 of this thesis.

OBJ.4 Although the OWC is one of the few WEC types in which power dissipation is relatively simple, peak-shaving (or rated power) control for increasing the capacity factor has received very little attention, particularly for a very common type of OWC air turbine (i.e., the Wells turbine). With Wells turbines, peak-shaving control can be implemented by opening a bypass valve, which essentially dissipates excessive pneumatic power in the air chamber,

potentially extending the OWC operational range. To minimise the LCoE, it is therefore worth considering peak-shaving control possibilities and, to this end, the contributions of this thesis are the following:

CTB.4.1 Since rated power control influences the PTO size optimisation problem, to asses the benefit of peak-shaving control with a bypass valve, control co-design (CCD) techniques have to be adopted. With CCD, it is possible to simultaneously optimise the control system and WEC geometry, although the (offline) computational burden of CCD is usually significant. In this thesis, a computationally simple, and *easily automatable*, parametric CCD approach for the bypass valve and PTO of an OWC is devised, where a LCoE surrogate is selected as a suitable performance function. Ultimately, the LCoE can be considerably reduced, if peak-shaving control is used in combination with CCD. Work published in [64].

CTB.4.2 Given the slow response time of typical bypass valve actuation systems, wave-by-wave peak-shaving control using a bypass valve is challenging. Therefore, a novel sea state based control strategy for the bypass valve is designed in this thesis. Furthermore, a thorough analysis of the impact of peak-shaving control on the LCoE and capacity factor is presented. Work published in [64].

1.4 Thesis structure

This thesis is broadly divided into four parts:

- Part I: Introduction and preliminaries (Chapters 1 and 2).
- Part II: OWC WEC modelling (Chapters 3 and 4).
- Part III: OWC WEC control (Chapters 5, 6, 7, and 8).
- Part IV: Final remarks (Chapter 9).

In addition to the current chapter, the thesis comprises eight additional chapters, which are laid out as follows:

- In the first section of Chapter 2, a thorough description of the OWC-based wave energy conversion system is provided. In particular, the working principle, main PTO configurations, and historical development of OWC WECs are presented. Furthermore, the second section of Chapter 2 introduces linear WEC hydrodynamic modelling. To this end, the modelling assumptions, under which liner wave theory is derived, are explained. Finally, the well-known Cummins' equation, as well as a linear time invariant approximation of the radiation convolution term, are defined for a generic WEC.

- In Chapter 3, a somewhat traditional OWC W2W model from first principles is described and, additionally, the modelling assumptions adopted in this thesis, particularly for OWC model-based control synthesis (part III, Chapters 6, 7, and 8), are motivated.

- Chapter 4 presents some data-based OWC hydrodynamic models, which are proposed in this thesis as an alternative to physics-based OWC hydrodynamic models. Firstly, SI modelling techniques are briefly described and the potential benefit of data-based hydrodynamic models in WEC control is discussed. Furthermore, some suitable linear and nonlinear SI hydrodynamic models for a small-scale OWC chamber are identified and validated, using real wave tank data. Finally, the advantages of a global nonlinear SI hydrodynamic modelling solution, over a multi-linear modelling approach, are examined.

- Chapter 5 provides an overview of OWC WEC control. In particular, the chapter offers an unbiased formulation of the OWC OCP, along with a detailed analysis of the key OWC CCD aspects. Finally, a comprehensive critical review of OWC control strategies is presented and the main literature gaps are identified.

- In Chapter 6, given the importance of considering the complete W2W power train in OWC control, a static-efficiency-based W2W control strategy for OWCs is designed. The proposed W2W control approach is then compared against the traditional turbine efficiency maximising control approach, and a critical discussion of the results is provided.

- Chapter 7 develops a relatively computationally efficient constrained optimal control strategy for OWC WECs. More specifically, a RHPS control approach, using Fourier basis functions, is proposed. To evaluate the optimal control performance, RHPS control is compared against both turbine efficiency maximising, and static-efficiency-based W2W, control. A thorough discussion of the results and main CCD aspects concludes the chapter.

- In Chapter 8, a parametric CCD approach for the PTO and bypass valve of an OWC WEC is devised. To this end, a surrogate of the LCoE is selected as a suitable performance function, where the LCoE minimum indicates the best combination of parameters (i.e., optimal PTO and bypass valve sizes). The proposed CCD approach primarily aims to assess the benefit of peak-shaving control, using a bypass valve, for enhancing the capacity factor.

- In Chapter 9, conclusions are drawn and possible future directions in OWC WEC control are considered.

1.5 List of publications

- **M. Rosati**, T. Kelly, D. Garcia Violini, J. V. Ringwood, *"Data-based hydrodynamic modelling of a fixed OWC wave energy converter"*, Proceedings of the 14th European Wave and Tidal Energy Conference (EWTEC), Plymouth, UK, 2021.
- **M. Rosati**, J. C. C. Henriques, J. V. Ringwood, *"A comprehensive wave-to-wire control formulation for oscillating water column wave energy converters"*, Proceedings of the 5th International Conference on Renewable Energies Offshore (RENEW), Lisbon, Portugal, 2022.
- **M. Rosati**, J. V. Ringwood, *"Towards hydrodynamic control of an oscillating water column wave energy converter"*, Proceedings of the 5th International Conference on Renewable Energies Offshore (RENEW), Lisbon, Portugal, 2022.
- **M. Rosati**, J. V. Ringwood, H. B. Bingham, B. Joensen, K. Nielsen, *"A data-based modelling approach for a vented oscillating water column wave energy converter"*, Proceedings of the 5th International Conference on Renewable Energies Offshore (RENEW), Lisbon, Portugal, 2022.
- I. McLeod, D. Clemente, P. R. Santos, F. T. Pinto, **M. Rosati**, J. V. Ringwood, *"Mathematical modelling of a TENG-powered data buoy"*, Proceedings of the IEEE Oceans Conference, Limerick, Ireland, 2023.
- **M. Rosati**, J. V. Ringwood, *"Wave-to-wire efficiency maximisation for oscillating water column systems"*, Proceedings of the 22nd IFAC World Congress, Yokohama, Japan, 2023.
- **M. Rosati**, A. H. Said, J. V. Ringwood, *"Wave-to-wire control of an oscillating water column wave energy system equipped with a Wells turbine"*, Proceedings of the 15th European Wave and Tidal Energy Conference (EWTEC), Bilbao, Spain, 2023.

- **M. Rosati**, J. V. Ringwood, *"Receding-horizon pseudospectral control for energy maximization of oscillating-water-column wave energy systems"*, Accepted for Publication into the Proceedings of the 22nd European Control Conference (ECC), Stockholm, Sweden, 2024.

- **M. Rosati**, T. Kelly, J. V. Ringwood, *"Nonlinear data-based hydrodynamic modeling of a fixed oscillating water column wave energy device"*, IEEE Access, vol. 9, 2021.
- **M. Rosati**, J. C. C. Henriques, J. V. Ringwood, *"Oscillating-water-column wave energy converters: A critical review of numerical modelling and control"*, Energy Conversion and Management: X, vol. 16, 2022.
- **M. Rosati**, J. V. Ringwood, *"Control co-design of power take-off and bypass valve for OWC-based wave energy conversion systems"*, Renewable Energy, vol. 219, 2023.
- **M. Rosati**, J. V. Ringwood, *"Electric energy maximization for oscillating water column wave energy systems using a receding-horizon pseudospectral control approach"*, Submitted to IEEE Transaction on Sustainable Energy, 2024.

2

Oscillating water column systems and linear hydrodynamic modelling

Contents

2.1 OWC systems 18
2.1.1 Operating principle and main characteristics 18
2.1.2 Origin and development of OWCs 21
2.1.3 OWC PTO mechanism 27
2.2 Linear hydrodynamic modelling 32
2.2.1 Linear wave theory 33
2.2.2 Wave-body interactions 39
2.2.3 Cummins' equation 44
2.2.4 Ocean wave spectra 48
2.3 Summary 49

The first section of this chapter provides a general description of OWC-based wave energy conversion systems. In particular, the operating principle, main characteristics, and historical development of OWCs are presented and, furthermore, consideration is given to the advantages/disadvantages of the OWC concept, as compared to other types of WECs. Finally, various possible PTO arrangements for OWCs are discussed and briefly compared.

Subsequently, Section 2.2 focuses on linear WEC hydrodynamic modelling, which is based on the linear wave theory (LWT). To this end, starting from the fully nonlinear Navier-Stokes equations, and introducing the typical LWT assump-

tions, the mathematical theory modelling linear wave-body interactions (i.e., the interactions between the ocean waves and a floating body) is outlined.

2.1 OWC systems

2.1.1 Operating principle and main characteristics

The OWC WEC, which is schematically represented in Figure 2.1, is a relatively old and well-known system to harness wave power [42, 65]. The essential principle of operation is common to all OWC systems, although several different OWC typologies exist [66]. Due to the excitation force of the incoming ocean waves, a water column is displaced, mainly vertically. The relative displacement of the water column (with respect to the device structure/hull) alternatively compresses and decompresses a volume of air in a pneumatic chamber. The air compression/decompression process typically generates a bidirectional airflow, which can be exploited in various ways, depending on the specific type of PTO mechanism. Among all possible OWC PTOs [66], the most popular PTO is a self-rectifying air turbine [67], directly coupled with a suitable rotary electric generator [68]. Self-rectifying air turbines are particularly suitable for operating with a bidirectional airflow [69], since the turbine rotor always spins in the same direction, regardless of the airflow incoming direction. It should be noted that unidirectional air turbines can also be used but, unless the airflow is rectified through a set of control valves [66], unidirectional turbines can only function during either the air inhalation, or exhalation, process. With a self-rectifying turbine, the bidirectional airflow is directly used to drive the turbine, eliminating the need for an air rectifying mechanism. Subsequently, the rotary electric generator converts the turbine mechanical power into electrical power. Finally, the 'raw' generator electrical power is converted, using power electronics, to a form which is suitable[1] for a specific power grid [71].

In comparison to other WECs, besides the relatively simple operating principle, OWC systems present several advantages:

1. The minimal number of moving parts, all located above the water level, simplifies maintenance operation and improves device reliability.

2. The OWC is arguably the WEC with the highest PTO speed, meaning that, in comparison to other WECs with similar rated powers, torques and stresses are lower [51].

[1] National grid codes dictate, for each country, the standard requirements in terms of power quality. A review of such requirements, for wind farms, can be found in [70].

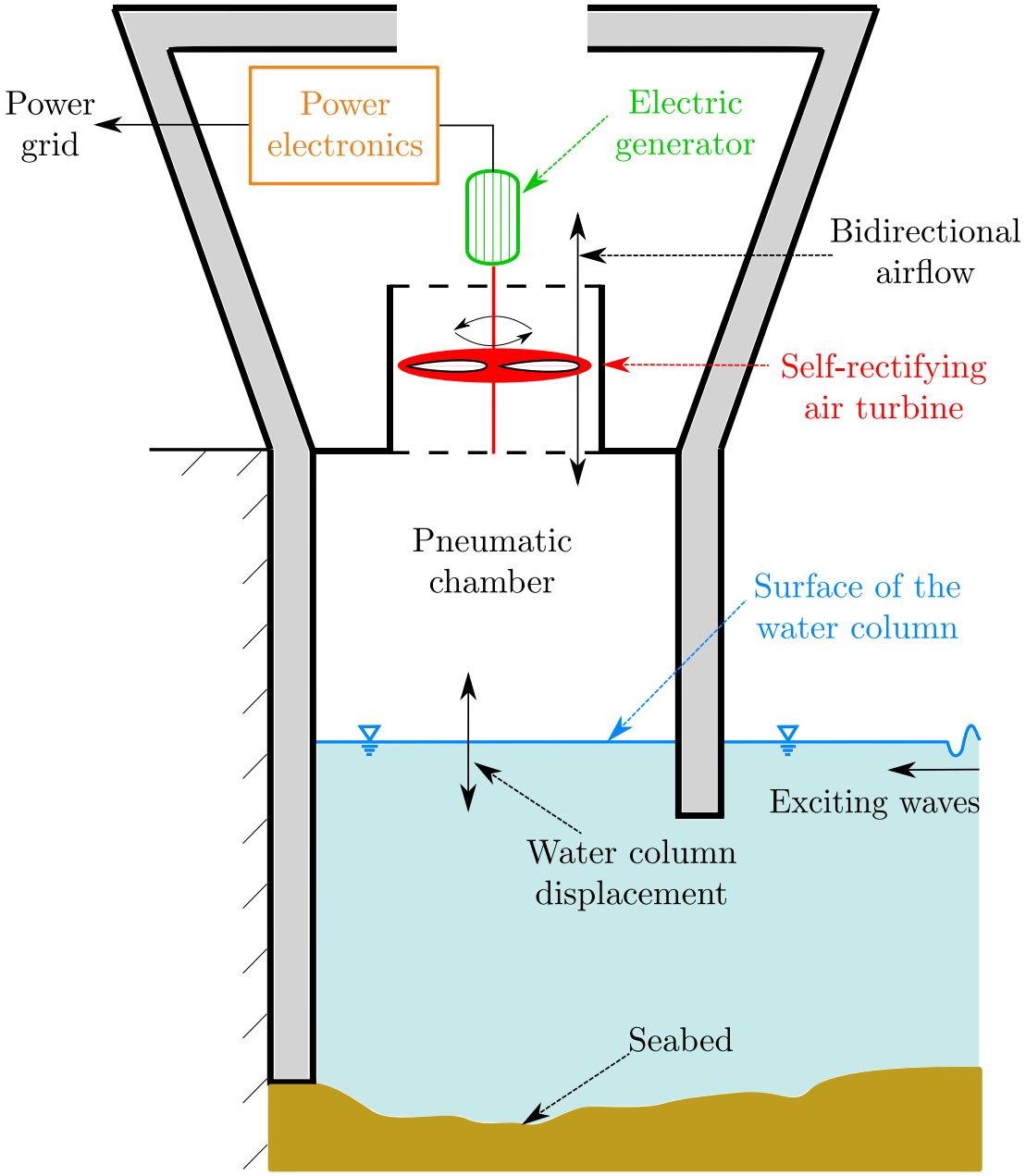

Figure 2.1: Schematic representation of the essential elements of a fixed OWC WEC.

3. The high turbine rotational speed also allows the generator to operate at high efficiency, without the need for a complex, and potentially expensive, gearbox.

4. In addition to the lower PTO stresses, the spring-like effect of air compressibility in the air chamber reduces structural stresses and fatigue problems [72], consequently decreasing OpEx and improving device reliability.

5. From a control perspective, a significant advantage of OWCs is the possibility to implement *peak-shaving*, or rated power, control for improving the device capacity factor [64]. Without peak-shaving control, a WEC may be often

required to prematurely go into safety mode and, consequently, suspend power production.

6. Finally, OWCs work with rotary, as opposed to linear, electric generators. To this end, rotary generators are generally less expensive and more efficient than their linear counterparts [73].

On the other hand, the biggest disadvantage of OWC systems is arguably the relatively high structural cost due to high volume of material [64, 74, 75], which increases the LCoE. Additionally, air compressibility modifies the phase response of the OWC and may significantly impact the control design, especially in phase matching control strategies (discussed in Section 5.2.1). Finally, traditional WEC hydrodynamic control, which requires power to be injected into the system, is difficult to implement on OWCs due to the absence of suitable actuators (further explained in Chapter 5).

From a structural perspective, OWC systems fall into two main categories: Fixed and floating OWCs. Fixed OWCs may be single structures, as shown in Figure 2.2 a) or, to reduce cost, another possibility is to incorporate multiple OWCs into breakwaters, as for the case of the Mutriku wave power plant [76] (Figure 2.3 a)). Additionally, other traditional fixed OWC configurations include, but are not limited to, U-OWCs [77] and vented-OWCs. In vented-OWCs, the device, which is equipped with a unidirectional turbine and a stop valve, only harnesses wave power during half of the wave energy cycle [78]. Similarly to the fixed OWC case, diverse technical solutions also exist for floating OWCs. In particular, the spar-buoy OWC [79] and the Backward Bent Duct Buoy (BBDB) [80], which are shown, respectively, in Figures 2.2 b) and c), have reached the prototype stage.

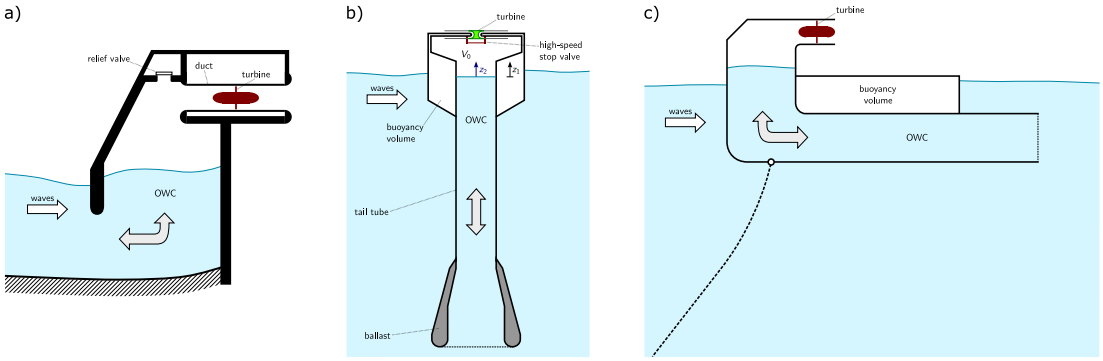

Figure 2.2: Schematic representation of the three main types of OWCs: a) Fixed OWC equipped with a Wells turbine, b) Spar-buoy with a biradial turbine installed, and c) Backward Bent Duct Buoy (BBDB) with a Wells turbine fitted. Source: [51].

From a control-oriented point of view, OWC WECs can be divided depending on the type of PTO. Indeed, each PTO intrinsically offers (or limits) some control possibilities, meaning that the control problem (and solution) is a function of the PTO typology. For instance, in the case of self-rectifying air turbines, the number of available actuators, and the effect of the PTO on the OWC hydrodynamic part, depend on the turbine type [56] (further explained in Section 5.1).

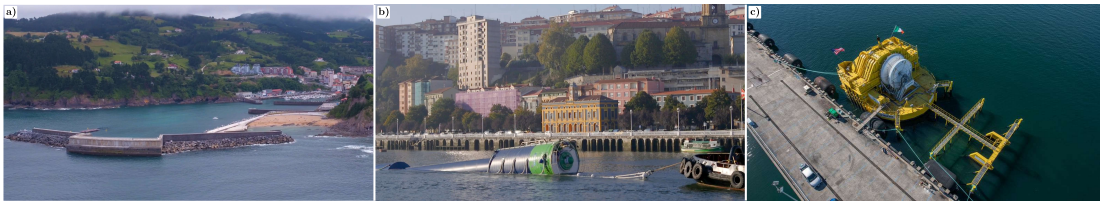

Figure 2.3: Examples of the three main types of OWCs: a) Mutriku wave power plant, Basque Country, b) IDOM Marmok-A5 spar-buoy, and c) OceanEnergy OE35 BBDB. Source: [51].

2.1.2 Origin and development of OWCs

The terminology 'oscillating water column' was first formally introduced by Evans, in 1978, in a paper in which the hydrodynamic parameters of a water column were derived, in a closed form solution, for a simple geometry (a thin-walled vertical pipe) [81]. However, the origin of the water column concept has its root in 1799, when an early patent was filed by Girard and sons [82]. Furthermore, long before they were systematically studied for electricity production, OWCs were already employed as navigation buoys. In the 1880s, several navigation buoys, equipped with air-driven whistles, were deployed in the USA to assist the sailors in night time navigation [83]. Furthermore, in 1910, more than a century after Girard, M. Bochaux-Praceique installed an OWC near Bordeaux to generate electric power for his house [84]. M. Bochaux-Praceique had the brilliant idea to use a 1 kW turbine to exploit a natural airflow coming from a hole in a cliff.

2.1.2.1 Early development of OWCs

The systematic development of OWC systems began, in 1964, at the Japan Research and Development Corporation (JRDC) with Yoshio Masuda [85, 86]. At that time, Masuda was developing wave-powered navigation buoys considering two different concepts: One buoy was based on a pendulum mechanism, while the second buoy was an OWC-based buoy, shown in Figure 2.4 a). The OWC-based buoy, which used an air rectifying mechanism and an impulse turbine, proved to

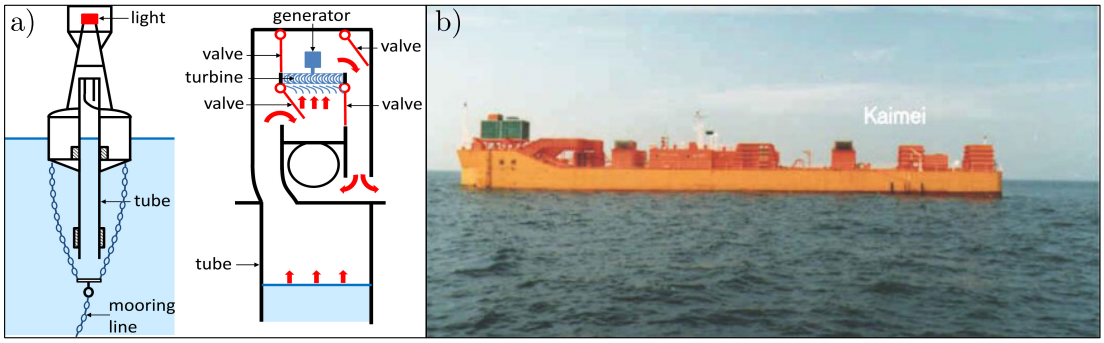

Figure 2.4: This figure shows a) a schematic of Masuda's navigation OWC-buoy and b) a picture of the Kaimei. Source: [66].

be the most successful concept and was extensively deployed, with some buoys even operating for more than 30 years [87].

The oil crisis in the 1970s, the immediate success of Masuda's buoys, and the invention of the self-rectifying Wells [88] (in 1976) and axial-flow impulse [89] (in 1978) turbines, encouraged further research into OWCs. Between 1978 and 1980, under Masuda's supervision, the Japan Agency for Marine-Earth Science and Technology (JAMSTEC), in collaboration with the International Energy Agency, deployed the Kaimei, shown in Figure 2.4 b). In the Kaimei, an 820 t floating device containing several OWC chambers[2], eight unidirectional turbines of different designs were initially installed, in combination with various air rectification systems. After some maintenance and modification, the Kaimei was then redeployed in 1985. In its second deployment [90, 66], the Kaimei was equipped with two self-rectifying turbines, specifically a Wells turbine and a McCormick turbine [92, 93] (which is a contra-rotating impulse turbine), and three unidirectional air turbines.

In concert with the first Kaimei deployment, a multi-chamber onshore OWC was under consideration at the University of Stellenbosch, in South Africa [94]. In the Stellenbosch OWC, the idea was to obtain a single unidirectional airflow using an air rectifying system connected with multiple OWC chambers. In 1974, a similar idea to manifold the airflow from multiple OWC chambers was patented, in the USA, by Bolding [95].

In the early 80s, the UK government funded investigations into a number of wave energy conversion technologies, including the shoreline multi-OWC device of the National Engineering Laboratory (NEL) [96]. However, the NEL OWC, which was also supposed to work as a breakwater, was never completed since the project funding ceased as the effects of the oil crisis became less intense.

[2]In the literature, the reported number of OWC chambers varies: 8 in [90], 11 in [86, 91], or 13 in [66].

The enthusiasm due to the Kaimei deployment rapidly faded out since the device output power was significantly below expectations [86]. Such a disappointing performance was partially due to the poor motion of the water column and partially to the dissipative motion of the device hull [97]. With the intention to improve wave power absorption, and use OWCs in shallow water, the BBDB was devised by Masuda and his team in 1986 [80]. During an experimental campaign, it was accidentally discovered that the BBDB performance improved if the back of buoy faced the incident waves [80], as shown in Figure 2.2 c).

2.1.2.2 Onshore and nearshore OWCs

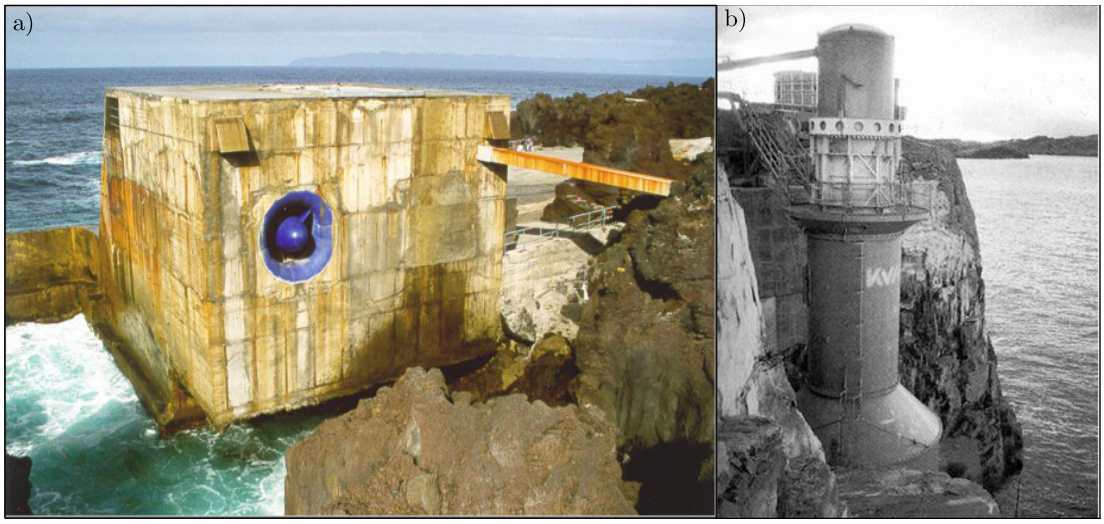

Figure 2.5: Pictures of the a) Pico power plant and b) OWC device at Toftestallen. Source: [66].

In tandem with the Kaimei and BBDB, the 80s (and the early 90s) were also a productive period for onshore OWCs. In 1984, a team from the JRDC, including Masuda, installed a 40 kW onshore OWC at Sanze, Japan [86]. Furthermore, at Toftestallen, in Norway, a shoreline OWC was deployed in 1985 [66]. Unfortunately, the Norwegian device, shown in Figure 2.5 b), was destroyed by a storm in 1988. In 1991, an OWC device with a rating of 75 kW was also constructed on the island of Islay, Scotland [98]. In Asia, a 60 kW OWC with five chambers integrated into a breakwater [99, 100] and a 125 kW bottom-standing OWC [101] were deployed, respectively, in 1989 at Sakata Port, Japan, and in 1990 at Trivandrum, India.

In Europe, the construction of onshore OWCs rapidly accelerated in the 90s thanks to the funding allocated into the JOULE 2 programme by the European Commission [102]. The JOULE 2 programme culminated with the construction of two demonstration OWC power plants, specifically a 400 kW OWC on the island of

Pico (Azores, Portugal) and the so-called Land Installed Marine Pneumatic Energy Transformer (LIMPET) OWC device on the island of Islay (close to the earlier 75 kW OWC [98]). The Pico power plant, commissioned in 1999, was equipped with a Wells turbine. During its turbulent lifetime, the Pico OWC operated intermittently, until the power plant was decommissioned due to insufficient continuation funding. Furthermore, all connections to the Pico OWC were removed in 2017, following a partial collapse of the structure [103]. The 500 kW LIMPET OWC, whose construction begun in 1998, was equipped with two contra-rotating Wells turbines, although the rating power was later reduced to 250 kW [104]. The LIMPET remained active from 1990 to 2013.

In more recent years, a 500 kW, bottom-mounted, nearshore OWC device, was successfully deployed in 2015 at Jeju, South Korea [66].

2.1.2.3 OWCs incorporated into a breakwater

Since the Sakata OWC (1989), the integration of OWC chambers into breakwaters became an increasingly popular configuration, especially due to the possibility to share the cost of infrastructure. In Japan, a 30 kW OWC, a 40 kW OWC, and a 130 kW OWC were constructed, respectively, in Kujukuri in 1987 [105], into the Niigata breakwater between 1986 and 1988 [106], and into a breakwater in Fukushima in 1996 [107]. Furthermore, in China, a 100 kW OWC integrated into a breakwater was commissioned in 2001 [108].

Some years later than the Japan and China initiatives, OWCs integrated into breakwaters were also considered in Europe. For instance, the OWC chambers in the Mutriku breakwater, in the Basque Country, Spain, were commissioned in 2011 and, despite some operational issues, this grid-connected power plant continues to function [76]. However, only 14 of the 16 OWC chambers are currently operational, with a total installed capacity of 296 kW. The primary purpose of the Mutriku OWC is to serve as a test site for turbine and control design [109]. In the years immediately after its commission, the Mutriku plant was solely equipped with Wells turbines but, in 2017, a 30 kW radial-flow impulse turbine was mounted for experimental testing within the H2020 OPERA project [110]. Furthermore, the Resonant Wave Energy Converter 3 (REWEC3) is an OWC device integrated into the breakwater of Civitavecchia, Italy [111, 112]. In particular, REWEC3 is a so-called U-OWC, since the cross-sectional profiles of the OWC chambers in this installation are U-shaped.

For the interested readers, a review of breakwaters incorporating WECs may be found in [113].

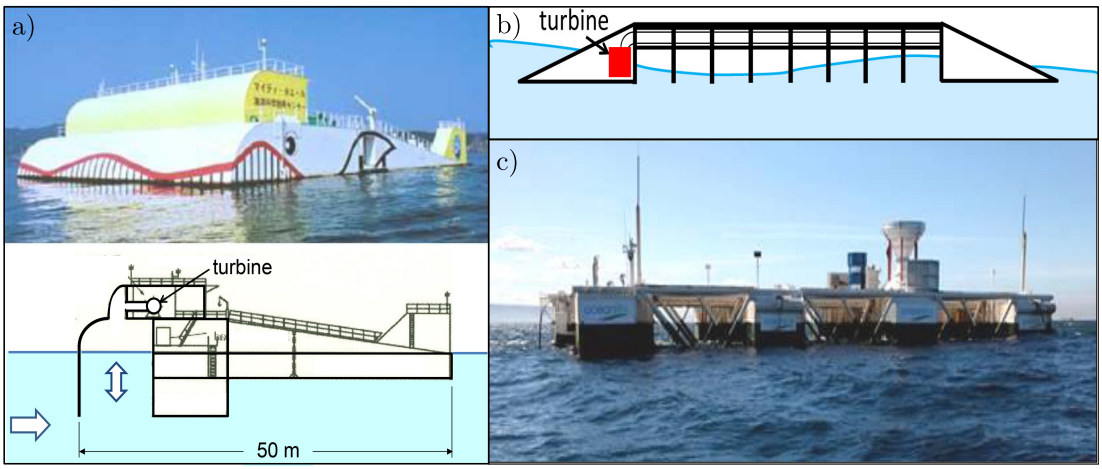

Figure 2.6: This figure shows a) the Mighty Whale, b) a schematic of the Seabreath, and c) the 1:3rd scale prototype of the MK3. Source: [66].

2.1.2.4 Floating OWCs after Kaimei and BBDB

After the Kaimei, another large ship-like, floating device, known as the Mighty Whale was deployed in Japan in 1998 [114]. This 4400 t device, which resembled the shape of a whale (as shown in Figure 2.6 a)), comprised three OWC chambers, all equipped with Wells turbines, and had a total rating of 110 kW [66].

In 2010, the Australian company Oceanlinx successfully deployed a 1:3rd scale grid-connected model of the 2.5 MW full-scale OWC device, known as the Mk3 [66]. The MK3 was a eight-chamber OWC equipped with two types of turbines: The Denniss-Auld turbine [67], which is a variable pitch turbine developed by Oceanlinx, and the HydroAir turbine, a self-rectifying axial-flow impulse turbine designed by Dresser-Rand [66].

In 2008, the so-called Seabreath OWC [115], whose schematic is shown in Figure 2.6 b), was patented. The device, currently under development at Padova University, Italy, is a floating attenuator, meaning that the structure is aligned with the propagation direction of the ocean waves. Similarly to the idea of the Stellenbosch OWC, the airflow generated by each OWC chamber of the Seabreath is rectified and used to drive a single unidirectional air turbine. Furthermore, the LEANCON device is also a multiple-chamber floating OWC equipped with a single unidirectional turbine and air rectifying valves. A 1:40th scale model of the LEANCON, with 120 OWC chambers, was tested in the deep wave tank of Aalborg University, in Denmark [116].

Aside from large multiple-chamber OWCs such as the Kaimei, Mighty Whale, and MK3, other researchers have focused their attention on smaller scale floating OWCs. For instance, the so-called ‘spar-buoy’ concept, which is essentially a long axi-symmetric floating OWC suitable for deep water locations, has been extensively

investigated numerically [117], experimentally [118], and in some hardware-in-the-loop testing [119].

Finally, the Irish company OceanEnergy has recently tested a 500 kW prototype of the full-scale 1.25 MW OE35 OWC in Hawaii [120]. The same company is also planning to build another large-scale device, the OE50 OWC, with a rated power of 2.5 MW.

2.1.2.5 Some tragic events in the OWC history

Like the OWC device at Toftestallen, some other OWCs had also a quite dramatic epilogue. For instance, the Osprey device, supported by the Irish and UK governments, was a 2 MW, nearshore, bottom-mounted OWC which was destroyed by storm in 1995, before its final deployment could be completed [106]. In 2014, similarly to the tragic experience of the Osprey device, Oceanlinx attempted to deploy a 1 MW bottom-mounted, offshore OWC. Unfortunately, the Australian device, called the greenWAVE, was lost during deployment [66].

2.1.2.6 OWC-based technology: Other applications and unconventional design solutions

Apart as WECs and navigation buoys, OWC-based devices have been also considered for reducing the hydrostatic response of very large floating platforms which include, but are not limited to, offshore wind farms, floating bridges, and floating houses. For a review, the reader is referred to [121].

In contrast with other types of WECs, since the pneumatic power available in the air chamber depends on the relative motion of the water column and the device hull, the OWC is potentially able to harness wave power, while also reducing the hull motion. For this reason, OWCs have been also considered for combined wind-wave resource exploitation on offshore wind platforms [122, 45, 105], where the control objectives are typically energy maximisation and platform motion minimisation. For instance, the Wind Energy Ireland (WEI) floating platform, conceived in 2008, is a V-shaped floating platform equipped with 32 OWC chambers and two undidirectional air turbines [105].

Another potentially moderate-cost application for OWCs is that of self-powered data-buoys equipped with data acquisition sensors [87, 123]. Such buoys measure the water column height variations to infer the water free surface variations, namely the undisturbed (by the OWC WEC) ocean wave elevation. A review of wave energy powered data-buoys is found in [43].

Finally, a number of unconventional PTO arrangements have also been devised. For instance, in the Aquabuoy 2.0 device [124], the motion of the water column is used to drive a piston which pumps water to drive a Pelton (water) turbine. Another notable example is the PolyWEC device [125], in which the pressure in the air chamber is used to deform a dielectric elastomer. The material deformation creates a potential difference across the elastomer and, consequently, electricity is generated.

2.1.3 OWC PTO mechanism

Except for some unconventional PTOs, such as those used in the Aquabuoy 2.0 and PolyWEC devices, the traditional OWC PTO is typically an air turbine coupled with an electric generator. Due to the reciprocating motion of the ocean waves, wave energy has an inherent oscillatory nature and, therefore, the airflow between the OWC chamber and atmosphere is bidirectional. To exploit such a bidirectional airflow, different solutions have been devised. Arguably, the most popular solution is that of using a self-rectifying air turbine, although unidirectional air turbines are still considered for vented-OWCs. Furthermore, if an air rectifying mechanism (typically a set of pressure-driven non-return valves) is utilised, unidirectional turbines can harness wave power for the complete wave cycle (and not only for half cycle)

Some reviews on air turbines for OWCs can be found in [66, 67, 69].

2.1.3.1 Self-rectifying air turbines

Self-rectifying air turbines can be divided into two main groups, namely the (i) Wells and (ii) impulse-like turbines. This section primarily aims to outline the aerodynamic and geometric characteristics of self-rectifying air turbines, without extensively focusing on control-related aspects. The role of the turbine typology in the control system design is thoroughly discussed in Section 5.1.

Wells turbines The Wells turbine, invented by Prof. Alan Arthur Wells [126], is traditionally an axial-flow self-rectifying air turbine. In its simplest configuration, the Wells turbine rotor is a set of airfoil-shaped blades, which are symmetrically positioned about a plane normal to the rotational axis [88], as shown in Figure 2.7 a) and b). However, the Wells turbine of Figure 2.7 suffers from significant kinetic energy losses due to swirling flow at the exit of the rotor[3]. The swirl kinetic energy loss can be reduced introducing two rows of guide vanes, one on each side of the

[3]The swirl kinetic energy per unit mass lost at the turbine exit is computed as $(1/2)V_{\text{exit,t}}^2$, where $V_{\text{exit,t}}$ is the tangential component of the absolute flow velocity at the turbine exit.

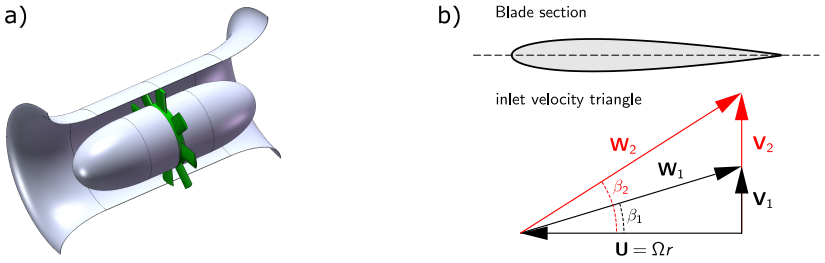

Figure 2.7: a) A Wells turbine without guide vanes and a single row of rotor blades (i.e., a monoplane turbine). b) A typical aerofoil section of a rotor blade and the inlet velocity triangles for two different flow rates. The variables $V_{1,2}$, $W_{1,2}$, $U_{1,2}$, and $\beta_{1,2}$ are, respectively, the absolute airflow velocity, the relative airflow velocity, the rotor blade velocity (computed as the product of rotational speed and rotor blade radius), and the angle of attack, for two different airflow rates. Source: [51].

rotor. A less straightforward solution to mitigate the energy loss due to swirl is to use a contra-rotating Wells turbine without guide vanes. In the contra-rotating Wells turbine, two rows of rotor blades rotate, at the same speed, in opposite directions and, therefore, the rotor work per unit mass of air is doubled [66]. However, with the contra-rotating configuration, the complexity (and cost) of the Wells turbine increases and, furthermore, the duplication of the electric components (i.e., the electric generator and power electronics) is required. Another solution for increasing the rotor work (per unit mass of air) is to use two axially-offset rows of rotor blades mounted on a single rotor (i.e., a biplane rotor) [127]. The biplane Wells turbine, also installed at the Mutriku site [76], may (or may not) have a row of guide vanes on each side of the rotor to reduce the swirl kinetic losses [67]. Furthermore, a novel configuration of the biplane Wells turbine, in which a row of guide vanes is placed in between the two rows of rotor blades, is considered in [128]. Finally, a quite unique *radial-flow* Wells turbine was first proposed in [129], although recent investigations have revealed that its efficiency characteristics are comparable to those of the classic axial-flow Wells turbine [130, 131].

Axial-flow impulse turbines To operate effectively with a bidirectional airflow, axial-flow impulse turbines, patented by Ivan A. Babinstev [89], must have two rows of guide vanes, the first one before (upstream) and the second one after (downstream) of the turbine rotor [132], as shown in Figure 2.8. The role of the upstream guide vanes is to increase the airflow kinetic energy by reducing the air pressure, therefore increasing velocity. However, the downstream row of guide vanes, which is needed due to flow symmetry, behaves as a partial flow blockage, significantly reducing turbine efficiency. More precisely, the blockage effect is caused by the excessive incidence flow angle at the entry to the second row of

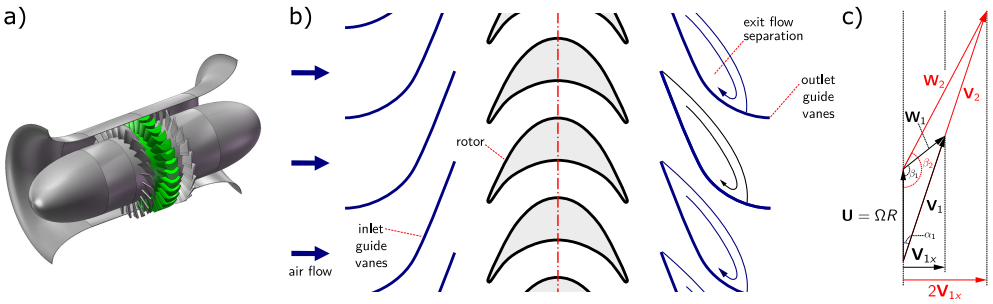

Figure 2.8: a) An axial-flow impulse turbine. b) A typical rotor cascade with guide vanes. c) Rotor inlet velocity triangles for two flow rates. The quantities **W**, **U**, and **V** are, respectively, the relative, the transport, and the absolute velocities. In this figure only, R refers to the rotor blade radius. Source: [51].

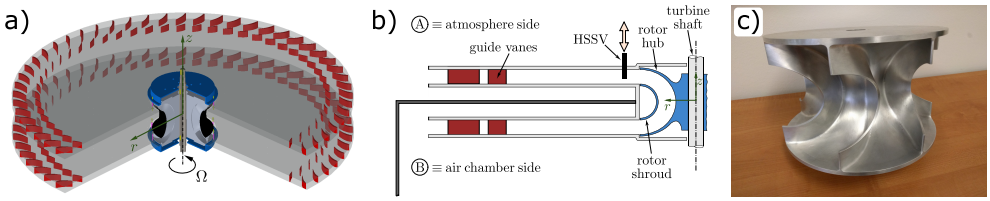

Figure 2.9: a) Biradial turbine with two rows of fixed guide-vanes radially offset from the rotor. b) Cut of the turbine showing the position of the sliding high-speed stop valve (HSSV). c) Picture of a small-scale rotor with a diameter of 0.25 m. Source: [51].

guide vanes. This issue cannot be avoided since, due to the required symmetric geometry, one cannot simultaneously obtain the desired flow incidence at the rotor blades and at the second row of guide vanes (for more details see, for instance, [66]). To reduce the excessive incidence problem, and improve turbine efficiency, a possible solution is to have guide vanes with a variable pitch angle [133, 132]. Furthermore, the complexity of an active control system for the variable pitch guide vanes may be avoided, since the position of the blades can be (passively) controlled using the aerodynamic moments acting on them [66]. Finally, contra-rotating axial-flow impulse turbines have also been proposed by McCormik [93, 92], but the excessive incidence issue remains.

Radial-flow impulse turbines Radial-flow impulse turbines with fixed guide vanes [134], variable-pitch guide vanes [135], and axially sliding guide vanes [136] have been considered for OWCs. However, the peak efficiency values remain significantly lower (between 45% and 57% [134, 135, 136]) than the typical peak efficiency of a Wells turbine (which can reach 75% [137]). Arguably, the first high-efficiency radial-flow impulse turbine, also known as the biradial turbine [138], was patented in 2012 by the IDMEC research group [139]. A possible configuration of the biradial turbine, shown in Figure 2.9, features two rows of fixed radially

offset guide vanes to reduce aerodynamic losses. With the configuration shown in Figure 2.9, the biradial turbine has a peak efficiency of around 68% [51], but, if controllable guide vanes are used, the peak efficiency of the biradial turbine can increase up to 78% [140].

A comparison between Wells and impulse turbines When compared to an axial-flow impulse turbine, a Wells turbine generally has a larger rotor diameter, a lower moment of inertia, a lower cost, and a higher peak efficiency (except for the biradial turbine). However, the Wells turbine efficiency curve is quite peaky and narrow, meaning that Wells turbines have a relatively small operational range. Furthermore, Wells turbines are characterized by a hard stall condition. Under stall conditions, the Wells turbine efficiency dramatically drops. To delay stall and improve Wells turbine performance under stall conditions, a passive flow control technique based on multiple suction slots on the rotor blades is investigated in [141, 142]. On the other hand, impulse-like turbines do not present such a hard stall issue and their operational range is relatively wide. Furthermore, Wells turbines typically operate at higher rotational speed values and, consequently, are also noisier [143]. It should be noted that, in contrast with impulse-like turbines, Wells turbines ideally operate in OWCs characterised by relatively low pressure oscillations [67]. To this end, multi-stage Wells turbines (namely Wells turbines with more than two rows of rotor blades) have been investigated, as an alternative to impulse-like turbines, for OWCs having large pressure oscillations in the air chamber [66]. From a control perspective, the main difference between Wells and impulse-like turbines concerns the impact of the turbine rotational speed on the OWC hydrodynamic performance and the presence/absence of some types of actuators (further discussed in Section 5.1).

Other self-rectifying air turbines In the literature, some alternative self-rectifying air turbines, typically inspired by the more traditional Wells and axial-flow impulse turbines, have emerged. For instance, the HydroAir turbine [144], shown in Figure 2.10 a), is a variation of a classic axial-flow impulse turbine. In the HydroAir turbine, to reduce the airflow blockage problem, the upstream and downstream rows of guide vanes are installed in a conical duct at a larger radius. The idea is essentially to reduce the axial and tangential velocity components, as a consequence of the duct area increase and the conservation of angular momentum [66]. Another peculiar self-rectifying air turbine is the Denniss-Auld turbine, shown in Figure 2.10 b). Since the position of the rotor blades of the Denniss-Auld turbine is controllable, this turbine shares some similarities with variable pitch turbines, although the range of available blade positions varies [66]. Furthermore, the Denniss-Auld rotor blade

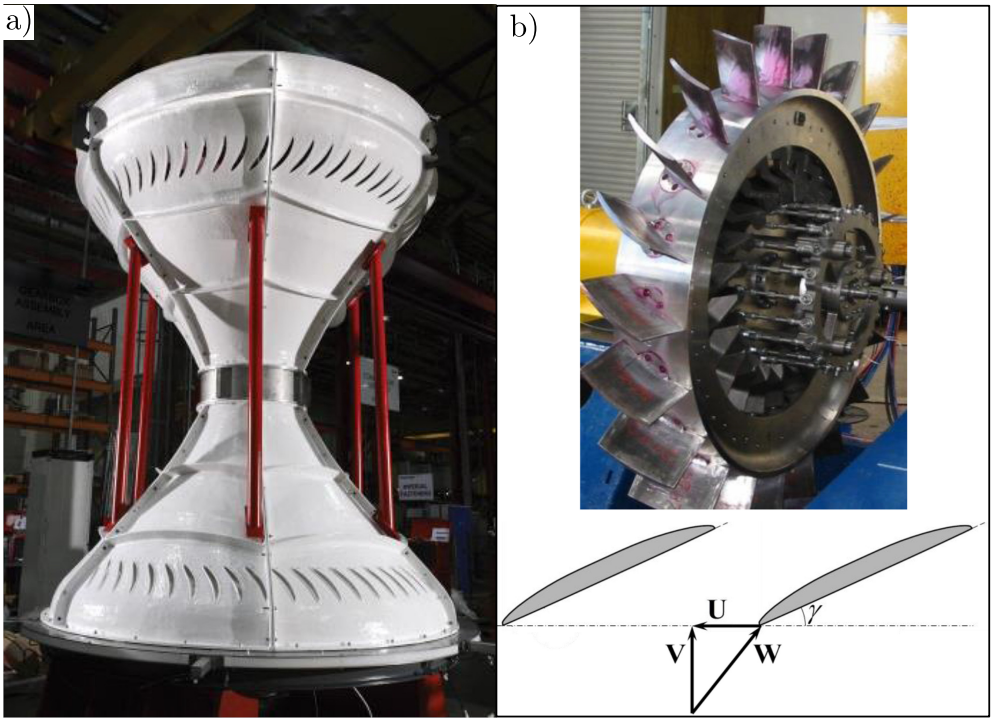

Figure 2.10: This figure shows the a) HydroAir and b) Denniss-Auld air turbines. Source: [66].

edges are identical, since they alternatively work as trailing/leading edges, while variable pitch turbines typically have airfoil-shaped rotor blades, as in Wells turbines.

2.1.3.2 Other types of turbines for OWCs

Unidirectional air turbines are more efficient than self-rectifying air turbines, specifically since the design of the angle of attack can be optimised for a single airflow direction. In general, the use of unidirectional turbines is not convenient for a single-chamber OWC, since the improved efficiency is not worth the cost of the air rectifying mechanism. Furthermore, thanks to increasingly effective design solutions, the efficiency of self-rectifying air turbines is improving [145]. However, as briefly outlined in Section 2.1.2, single unidirectional turbines are often considered in large floating platforms with multiple OWC chambers, where the air rectifying system can be also used to minimize the platform motion.

Finally, variable pitch turbines have also been considered for OWCs. Variable pitch turbines are sometimes called variable pitch Wells turbines since, when the rotor blades are at their neutral positions, the turbine becomes essentially a Wells turbine. However, variable pitch turbines are arguably more similar to unidirectional turbines than to self-rectifying turbines, since the leading edge of the rotor blades is controlled to face the incoming airflow. Furthermore, in contrast with self-rectifying

air turbines, which do not work efficiently as compressors, variable pitch turbines can be potentially employed to compress air and, therefore, inject power into the OWC system (further discussed in Chapter 5).

2.1.3.3 Electric generators

Different types of rotary electric generators have been considered to work with OWC systems [68], particularly induction generators, such as doubly-fed induction generators (DFIGs), squirrel cage induction generators (SCIGs), and permanent magnet generators (PMG). In general, suitable electric generators for OWCs should resist corrosion caused by water salinity and, moreover, should efficiently operate at different rotational speed values. In [68], the problem of generator selection is discussed, primarily comparing capital costs, performance, and suitability for the marine environment of different electric generators. However, generator selection is also a control-related issue, since the generator efficiency characteristics may, to some extent, influence OWC control design [56] (further explained in Section 5.1).

2.2 Linear hydrodynamic modelling

As mentioned in the introduction, one of the objectives of this thesis is to develop complete model-based control strategies for OWC WECs. To date, since wave energy conversion technologies are still relatively immature, and since accurate modelling of the associated nonlinear hydrodynamic effects is difficult, linear WEC hydrodynamic models are typically used in WEC model-based control design [146, 49]. A significant advantage of linear WEC models is their relative computational simplicity, meaning that it is potentially easier to achieve *real-time* control performance, if optimisation-based control strategies are used.

For certain types of WECs, although linear models provide, to some extent, an accurate representation of the wave-body interactions under uncontrolled conditions, linear models may not be representative under WEC hydrodynamic control conditions [147]. Indeed, traditional WEC hydrodynamic control for maximum energy extraction tends to exaggerate the motion of the device, consequently violating the assumptions under which linear WEC models are valid. However, such a problem, also known as the WEC *modelling paradox*, is not especially related to OWC WECs, since traditional hydrodynamic control is typically not feasible on OWCs [56] (further explained in Section 5.2).

For brevity of notation, the dependence on the independent variables (for instance, the time t) is omitted if already clear from the context.

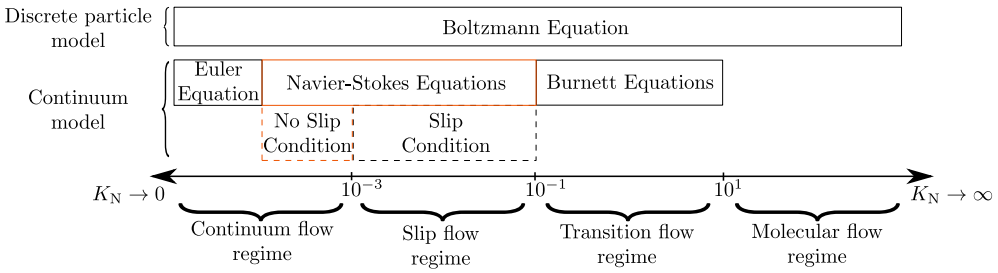

Figure 2.11: Main flow regimes and fluid dynamic models as function of the Knudsen number. Figure adapted from [151].

2.2.1 Linear wave theory

Linear hydrodynamic modelling is based on LWT, or Airy's wave theory [148], which is often used to model the propagation of waves on the ocean free-surface. In essence, the fully nonlinear fluid dynamic model described by the Navier-Stokes equations is simplified, using the linear potential theory (LPT) assumptions and considering only small amplitude waves. It should be noted that this thesis focuses on the investigation of OWC systems in power production mode, therefore operating modes under which energy maximising control strategies are required. In this regard, the wave resource characterising typical operational conditions can be described, in most cases, by LWT [149].

2.2.1.1 Preliminaries: Introduction to fluid dynamics

In fluid dynamics [150], the different flow regimes are classified using the Knudsen number, K_N, defined as

$$K_N = \frac{\lambda_m}{L_c}, \tag{2.1}$$

where λ_m and L_c are, respectively, the molecular mean free path length and a representative physical length scale. The main flow regimes (namely, the continuum, slip, transition, and free-molecule flow regimes), and different possible fluid dynamic models, as functions of K_N are shown in Figure 2.11.

In the wave modelling case, since $K_N << 10^{-3}$ (i.e., water is a continuum), the (no-slip) Navier-Stokes system of equations can be used as a suitable fluid dynamic model. For a continuum volume of fluid[4], the mass conservation, momentum conservation, and energy conservation equations in differential form are specified,

[4] If the volume of fluid is not continuum, integral Navier-Stokes equations must be used.

respectively, [152] as

$$\frac{\delta\rho}{\delta t} + \nabla \cdot (\rho\, u_\mathrm{f}) = 0 \tag{2.2a}$$

$$\frac{\delta(\rho\, u_\mathrm{f})}{\delta t} + \nabla \cdot (\rho\, u_\mathrm{f} \otimes u_\mathrm{f}) = \nabla \cdot \sigma + \rho f \tag{2.2b}$$

$$\frac{\delta E_\mathrm{tot}}{\delta t} + \nabla \cdot (E_\mathrm{tot} u_\mathrm{f}) = \nabla \cdot (\sigma \cdot u_\mathrm{f}) - \nabla \cdot q_\mathrm{h}, \tag{2.2c}$$

where $\rho \in \mathbb{R}$ is the fluid density, $u_\mathrm{f} \in \mathbb{R}^3$ is the flow velocity vector, $f \in \mathbb{R}^3$ is the external force vector per unit mass, $q_\mathrm{h} \in \mathbb{R}^3$ is the heat flux vector, $E_\mathrm{tot} \in \mathbb{R}$ is the total energy of the system (i.e., the sum of kinetic and internal energies), and $\sigma \in \mathbb{R}^{3\times3}$ is the Cauchy stress tensor, defined as the sum of a viscous stress term (known as the deviatoric stress tensor), $\tau \in \mathbb{R}^{3\times3}$, and a pressure term (volumetric stress), $-pI_\mathrm{n} \in \mathbb{R}^{3\times3}$, as

$$\sigma = \tau - pI_\mathrm{n}, \tag{2.3}$$

where I_n is the identity matrix. The operators ∇, $\nabla\cdot$, and $\otimes$ are, respectively, the gradient, divergence, and tensor product operators. For a Newtonian fluid, in which the viscous stress is a linear function of the strain rate, $\nabla \cdot \tau$ can be written as

$$\nabla \cdot \tau = \mu_\mathrm{f}(\nabla^2 u_\mathrm{f} + \frac{1}{3}\nabla(\nabla \cdot u_\mathrm{f})), \tag{2.4}$$

where μ_f is the dynamic viscosity of the fluid and $\nabla^2 = \nabla(\nabla\cdot)$ indicates the Laplacian operator. Finally, to complete the Navier-Stokes system of equations (2.2), suitable initial conditions, boundary conditions, and an equation of state relating the thermodynamic variables (i.e., density, pressure, and temperature), have to be defined.

It should be noted that, in linear WEC hydrodynamic modelling, only the mass and momentum conservation equations are needed. Therefore, the energy conservation equation is typically omitted and, using Equation (2.3) and the following identity,

$$\nabla \cdot (\rho\, u_\mathrm{f} \otimes u_\mathrm{f}) = u_\mathrm{f} \nabla \cdot (\rho\, u_\mathrm{f}) + \rho\, u_\mathrm{f} \cdot \nabla u_\mathrm{f}, \tag{2.5}$$

the Navier-Stokes system of equations (2.2) simplifies to:

$$\frac{\delta\rho}{\delta t} + \nabla \cdot (\rho\, u_\mathrm{f}) = 0 \tag{2.6a}$$

$$\frac{\delta(\rho\, u_\mathrm{f})}{\delta t} + u_\mathrm{f} \nabla \cdot (\rho\, u_\mathrm{f}) + \rho\, u_\mathrm{f} \cdot \nabla u_\mathrm{f} = \nabla \cdot \tau - \nabla p + \rho f. \tag{2.6b}$$

In contrast to linear WEC models, high-fidelity hydrodynamic WEC models, based on the Navier-Stokes equations (2.6), may be used to obtain a fully nonlinear characterisation of the wave-body interactions. Such nonlinear WEC models can

be built using different numerical fluid dynamic tools, such as computational fluid dynamic (CFD) [153], smoothed-particle hydrodynamics (SPH) [154], and large-eddy simulations (LES) [155]. However, due to the high computational cost, fully nonlinear WEC models are not compatible with the typical real-time WEC control requirements [156] and, therefore, they are not considered in this thesis. For the interested reader, a review of CFD models for OWCs is found in [157].

2.2.1.2 The linear potential theory equations

To derive the equations which model a linear potential flow, two assumptions are introduced:

AS.1 The flow is incompressible ($\nabla \cdot u_\mathrm{f} = 0$),
AS.2 The flow is irrotational ($\nabla \times u_\mathrm{f} = 0$).

It should be noted that, for incompressible flow (which is different from assuming a constant density, i.e., $\rho = \mathrm{constant}$), the pressure does not change the volume of a fluid element, resulting in a solenoidal velocity field, namely $\nabla \cdot u_\mathrm{f} = 0$. Furthermore, for irrotational flow, vorticity ($\nabla \times u_\mathrm{f}$), defined as twice the angular speed of a fluid particle, is zero, meaning that fluid particles do not rotate. If the assumptions **AS.1** and **AS.2** hold, from the identity,

$$\nabla \times (\nabla \times u_\mathrm{f}) = \nabla(\nabla \cdot u_\mathrm{f}) - \nabla^2 u_\mathrm{f}, \tag{2.7}$$

it follows that the considered flow is also inviscid ($\nabla^2 u_\mathrm{f} = 0$). If the flow is irrotational and inviscid, there exists a *scalar* function, Φ_f, commonly known as the velocity potential [150], such that

$$u_\mathrm{f} = \nabla \Phi_\mathrm{f}. \tag{2.8}$$

The existence of a velocity potential implies that, in linear potential flow, a fluid particle that moves along a certain streamline will always remain on that streamline.

Using Equation (2.8) and the assumptions **AS.1** and **AS.2**, the mass conservation equation (2.6a) can be replaced by the Laplace equation:

$$\nabla^2 \Phi_\mathrm{f} = 0. \tag{2.9}$$

Similarly, if the external force is defined as the gravitational force $f = [0, 0, -\rho g]$, after integrating the momentum conservation equation (2.6b), the unsteady (i.e., $\frac{\delta}{\delta t} \neq 0$) Bernoulli equation is obtained as

$$\frac{p}{\rho} + \frac{\delta \Phi_\mathrm{f}}{\delta t} + \frac{1}{2}(\nabla \Phi_\mathrm{f})^2 + gz = C_\mathrm{int}, \tag{2.10}$$

where C_int is an integration constant. Equations (2.9) and (2.10) model, together with a set of suitable boundary conditions, linear potential flow. The velocity potential (therefore also the velocity field) is found by solving the Laplace equation (2.9) and, once Φ_f is known, the pressure field is computed from the Bernoulli equation (2.10).

2.2.1.3 Boundary conditions

The Laplace and Bernoulli equations are solved as a boundary value problem (BVP). For the case of the propagation of ocean waves, three boundary conditions need to be used, namely the seabed impermeability condition, the free surface kinematic condition, and the free surface dynamic condition. For simplicity, it is assumed that ocean waves propagate only towards the x-axis positive direction (i.e., the problem becomes two-dimensional) and that the z-axis is the vertical coordinate, which is positive for values that are above the still water level (SWL), as shown in Figure 2.12. In Figure 2.12, η is the free surface elevation (FSE) at a given point on the x-axis, λ_w is the wavelength, h_{sb} is the seabed depth with respect to the SWL, assumed flat in the present analysis, H_w is the wave height, and $A_w = H_w/2$ is the wave amplitude.

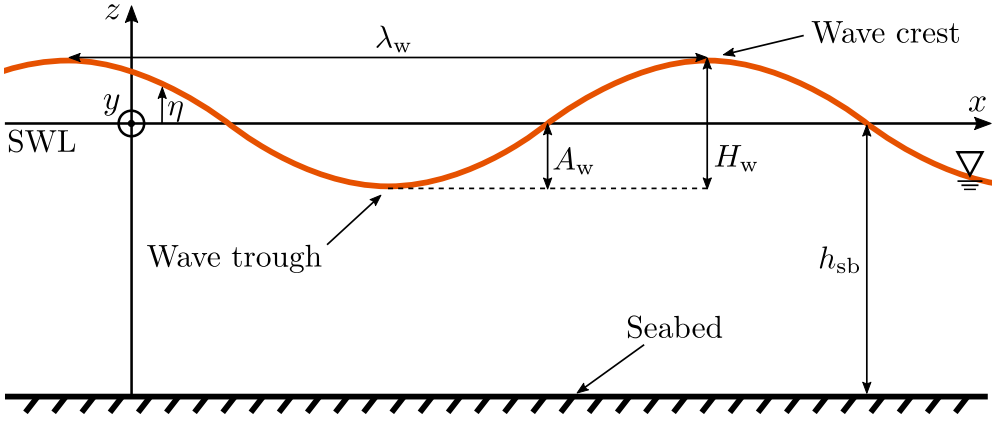

Figure 2.12: Schematic of the wave characteristics.

The boundary conditions characterising the ocean wave propagation phenomenon are specified as follows:

BC.1 The seabed is assumed to be impermeable, i.e. no fluid penetrates (or leaves) the seabed, which means that the vertical component of the fluid velocity will be zero at the seabed,

$$\frac{\delta \Phi_f}{\delta z} = 0 \qquad \text{on } z = -h_{sb}. \tag{2.11}$$

BC.2 The free surface kinematic condition implies that a water particle on the ocean free surface remains on the free surface,

$$\frac{\delta \Phi_f}{\delta z} = \frac{\delta \eta}{\delta t} + \frac{\delta \Phi_f}{\delta x}\frac{\delta \eta}{\delta x} + \frac{\delta \Phi_f}{\delta y}\frac{\delta \eta}{\delta y} \qquad \text{on } z = \eta. \tag{2.12}$$

BC.3 The free surface dynamic condition expresses the conservation of the momentum at the free surface. Therefore, the condition is obtained by specifying the Bernoulli equation at the free surface

$$\rho \frac{\delta \Phi_f}{\delta t} + \frac{1}{2}\rho(\nabla \Phi_f)^2 + \rho g \eta = C_{int} \quad \text{on } z = \eta. \tag{2.13}$$

2.2.1.4 Small amplitude waves

The most commonly used, and simplest, ocean wave theory was first introduced by George Airy at the end of the 19th century [148]. Airy's theory was developed for long-crested regular (i.e., sinusoidal) waves in two dimensions (i.e., $\delta\Phi_\mathrm{f}/\delta y = 0$), which are periodic in time and in space. In addition to assumptions **AS.1** and **AS.2**, Airy's theory also assumes that:

AS.3 Ocean waves propagate in deep water depths ($h_\mathrm{sb} > 0.5\lambda_\mathrm{w}$).
AS.4 The wave height, H_w, is small compared to the wavelength, λ_w.

The instantaneous FSE for a regular wave, therefore a wave characterised by single (constant) amplitude and frequency values, propagating in deep water, is expressed [148] as

$$\eta = \frac{H_\mathrm{w}}{2}\cos(k_\mathrm{w}x - \omega t), \tag{2.14}$$

where $\omega = 2\pi/T_\mathrm{w}$ is the wave frequency, T_w is the wave period, and $k_\mathrm{w} = 2\pi/\lambda_\mathrm{w}$ is the wave number, or spatial wave frequency. As a consequence of **AS.4**, the free surface kinematic (**BC.2**) and dynamic (**BC.3**) boundary conditions can be applied to $z = 0$, as opposed to $z = \eta$, meaning that **BC.2** and **BC.3** are linearised. Therefore, for small amplitude waves, the linearised free surface kinematic (2.12) and dynamic (2.13) boundary conditions can be written, respectively, as

$$\frac{\delta\Phi_\mathrm{f}}{\delta z} - \frac{\delta\eta}{\delta t} = 0 \qquad \text{on } z = 0, \tag{2.15}$$

and

$$\frac{\delta\Phi_\mathrm{f}}{\delta t} + g\eta = 0 \qquad \text{on } z = 0. \tag{2.16}$$

By using Equation (2.14) and the boundary conditions (2.11), (2.15), and (2.16)), the Laplace equation can be solved, using the separation of variables technique, for Φ_f, as

$$\Phi_\mathrm{f} = \frac{gH_\mathrm{w}}{2\omega}\frac{\cosh(k_\mathrm{w}z + k_\mathrm{w}h_\mathrm{sb})}{\cosh(k_\mathrm{w}h_\mathrm{sb})}\sin(k_\mathrm{w}x - \omega t). \tag{2.17}$$

Furthermore, the water particle velocity components in the x and z directions can be computed from (2.17), respectively, as

$$\frac{\delta\Phi_\mathrm{f}}{\delta x} = \frac{gH_\mathrm{w}k_\mathrm{w}}{2\omega}\frac{\cosh(k_\mathrm{w}z + k_\mathrm{w}h_\mathrm{sb})}{\cosh(k_\mathrm{w}h_\mathrm{sb})}\cos(k_\mathrm{w}x - \omega t), \tag{2.18}$$

and

$$\frac{\delta\Phi_\mathrm{f}}{\delta z} = \frac{gH_\mathrm{w}k_\mathrm{w}}{2\omega}\frac{\sinh(k_\mathrm{w}z + k_\mathrm{w}h_\mathrm{sb})}{\cosh(k_\mathrm{w}h_\mathrm{sb})}\sin(k_\mathrm{w}x - \omega t). \tag{2.19}$$

By substituting Φ_{f} (2.17) into the Bernoulli equation (2.10), the pressure due to ocean waves is computed as

$$p = \frac{\rho g H_{\mathrm{w}}}{2} \frac{\cosh(k_{\mathrm{w}} z + k_{\mathrm{w}} h_{\mathrm{sb}})}{\cosh(k_{\mathrm{w}} h_{\mathrm{sb}})} \cos(k_{\mathrm{w}} x - \omega t) - \rho g z. \tag{2.20}$$

In Equation (2.20), the first term on the right side is the dynamic pressure variation due to ocean waves, while the second term (i.e., $-\rho g z$) represents the hydrostatic pressure.

If the expression for Φ_{f} (2.17) is combined with the linearised free surface conditions (2.15) and (2.16), a relationship between ω and k_{w} can be found:

$$\omega^2 = g k_{\mathrm{w}} \tanh(k_{\mathrm{w}} h_{\mathrm{sb}}) = g \frac{2\pi}{\lambda_{\mathrm{w}}} \tanh(k_{\mathrm{w}} h_{\mathrm{sb}}). \tag{2.21}$$

The relationship in (2.21) is known as the dispersion relationship. Furthermore, the wave celerity, defined as

$$c_{\mathrm{w}} = \frac{\lambda_{\mathrm{w}}}{T_{\mathrm{w}}} = \frac{\omega \lambda_{\mathrm{w}}}{2\pi}, \tag{2.22}$$

can be expressed, using Equations (2.21) and (2.22), as a function of ω, h_{sb}, and k_{w}:

$$c_{\mathrm{w}} = \frac{g}{\omega} \tanh(k_{\mathrm{w}} h_{\mathrm{sb}}). \tag{2.23}$$

In deep water conditions, since $\tanh(k_{\mathrm{w}} h_{\mathrm{sb}}) \approx 1$, the dispersion relationship (2.21) and wave celerity (2.23) become, respectively,

$$\omega^2 = g k_{\mathrm{w}} = g \frac{2\pi}{\lambda_{\mathrm{w}}} \tag{2.24}$$

and

$$c_{\mathrm{w}}^{\mathrm{deep}} = \frac{g}{\omega} = g \frac{T_{\mathrm{w}}}{2\pi} = \left(\frac{g \lambda_{\mathrm{w}}}{2\pi} \right)^{1/2}. \tag{2.25}$$

Therefore, in deep water, c_{w} and λ_{w} are solely functions of ω. On the other hand, in shallow-water conditions, since $\tanh(k_{\mathrm{w}} h_{\mathrm{sb}}) \approx 2\pi h_{\mathrm{sb}} / \lambda_{\mathrm{w}}$, the wave celerity is only a function of h_{sb}, meaning that shallow water waves are not frequency dispersive, while deep water waves are.

The total energy per metre in the wave, E_{tot}, can be computed as the sum of the potential, E_{pot}, and kinetic, E_{kin}, energies. The kinetic energy per unit area is found by integrating the term, $(1/2)\rho((\delta\Phi_{\mathrm{w}}/\delta x)^2 + (\delta\Phi_{\mathrm{w}}/\delta z)^2)$, from the free water surface to the seabed [158]. Using the expressions of the velocity components, $\delta\Phi_{\mathrm{w}}/\delta x$ (2.18) and $\delta\Phi_{\mathrm{w}}/\delta z$ (2.19), the integration of the aforementioned term yields [158]:

$$E_{\mathrm{kin}} = \frac{\rho g H_{\mathrm{w}}^2}{16}. \tag{2.26}$$

The time-averaged potential energy, per unit area, is computed [158], as

$$E_{\text{pot}} = \overline{\int_0^{\eta} \rho g z \, \mathrm{d}z} = \frac{1}{2}\rho g \overline{\eta^2} = \frac{\rho g H_{\text{w}}^2}{16}, \tag{2.27}$$

where the overbar indicates the time-average operator. The total energy per unit area is calculated as

$$E_{\text{tot}} = E_{\text{kin}} + E_{\text{pot}} = \frac{\rho g H_{\text{w}}^2}{8}, \tag{2.28}$$

meaning that, in Airy's theory, $E_{\text{tot}}/2 = E_{\text{kin}} = E_{\text{pot}}$. Finally, the time-averaged wave power per metre of wave crest, transported by an Airy wave, is computed as

$$P_{\text{wave}}^{\text{airy}} = E_{\text{tot}} c_{\text{g}}^{\text{deep}} = \frac{\rho g^2}{32\pi} H_{\text{w}}^2 T_{\text{w}}, \tag{2.29}$$

where $c_{\text{g}}^{\text{deep}} = c_{\text{w}}^{\text{deep}}/2$ is the wave group velocity in deep water.

A full treatment of the derivation of the velocity potential, using Airy's theory, is found, for instance, in [159]. Furthermore, a more comprehensive treatment of the computation of energy and power for a sinusoidal wave can be found in [158]. It should be noted that other wave theories, such as Stokes' finite amplitude and Cnoidal wave theories, exist. For the interested reader, a review of the historical development of wave theories can be found in [160].

2.2.2 Wave-body interactions

For the case of a floating body, such as a WEC, excited by ocean waves, the velocity potential, which exists under the LPT assumptions introduced in Section 2.2.1, can be decomposed as

$$\Phi_{\text{f}} = \Phi_{\text{i}} + \Phi_{\text{d}} + \Phi_{\text{r}}, \tag{2.30}$$

where Φ_{i}, Φ_{d}, and Φ_{r} are, respectively, the incident, diffracted, and radiated velocity potentials. In essence, Φ_{i} is the velocity potential associated with the undisturbed incident waves (Equation (2.17)), Φ_{d} is the velocity potential due to the waves which are diffracted around the floating body, and Φ_{r} is the velocity potential of radiated waves, which are waves generated by the motion of the floating body (if subject to an external force).

In linear WEC modelling, it is assumed that the amplitudes of the incoming wave, and floating body motion, are small. Furthermore, to obtain Φ_{i}, Φ_{d}, and Φ_{r}, a set of five boundary conditions, which are schematically represented in Figure 2.13, are required. In addition to the seabed impermeability condition (2.11) and the linearised free surface kinematic (2.15), and dynamic (2.16), boundary conditions, the remaining two boundary conditions are the following:

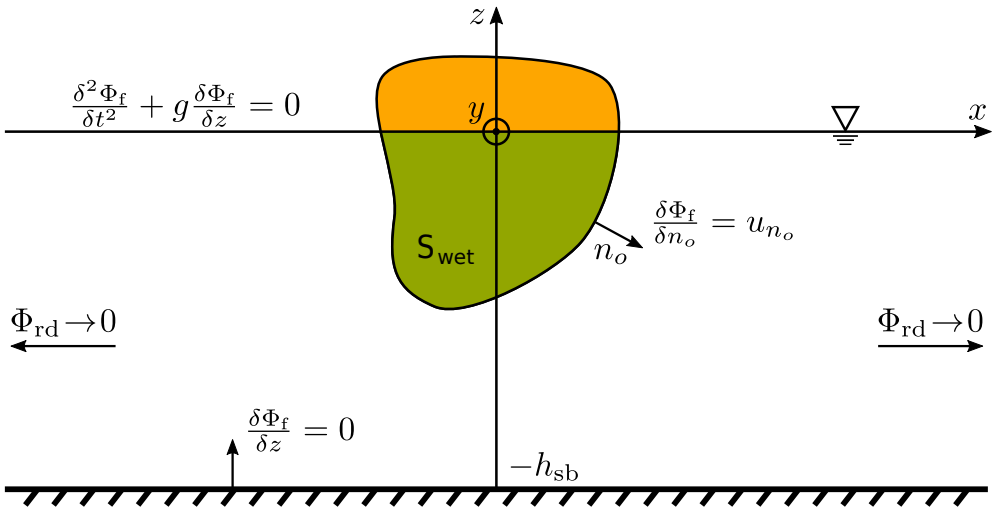

Figure 2.13: Schematic of a floating body with the boundary conditions introduced in Sections 2.2.1 and 2.2.2. The term S_wet indicates the body wetted surface.

BC.4 Similarly to the seabed (2.11), the floating body is also impermeable, meaning that, at the body surface, the normal component of the fluid velocity with respect to the body wetted surface ($\delta\Phi_\mathrm{f}/\delta n_o$) must be equal to the velocity of the body in the same direction (u_{n_o})

$$\frac{\delta\Phi_\mathrm{f}}{\delta n_o} = u_{n_o} \qquad \text{on } S_\mathrm{wet}, \tag{2.31}$$

where n_o is a unity vector normal to the wetted surface.

BC.5 The fifth, and last, boundary condition states that, far away from the floating body, the wave field is identical to the incoming wave field (i.e., the wave field is undisturbed by the floating body). Therefore, radiation and diffraction waves fade out as the distance to the floating body increases:

$$\Phi_\mathrm{rd} \approx 0 \qquad \text{as } d_\mathrm{fb} \to \infty, \tag{2.32}$$

where $\Phi_\mathrm{rd} = \Phi_\mathrm{r} + \Phi_\mathrm{d}$ and d_fb is the radial distance from the floating body.

In general, as shown in Figure 2.14, a floating body can move in any degree-of-freedom (DoF), namely surge, sway, heave, roll, pitch, or yaw. According to Newton's second law, the equation of motion of a floating body, in the time-domain, can be written as

$$M\ddot{\chi}(t) = \sum f_k(t), \tag{2.33}$$

where $\chi(t) \in \mathbb{R}^{n_\mathrm{DoF}}$ is the position of the floating body, $f_k(t) \in \mathbb{R}^{n_\mathrm{DoF}}$ are the vectors of all the forces, and moments, acting on the body, and $M \in \mathbb{R}^{n_\mathrm{DoF}\times n_\mathrm{DoF}}$ is the mass

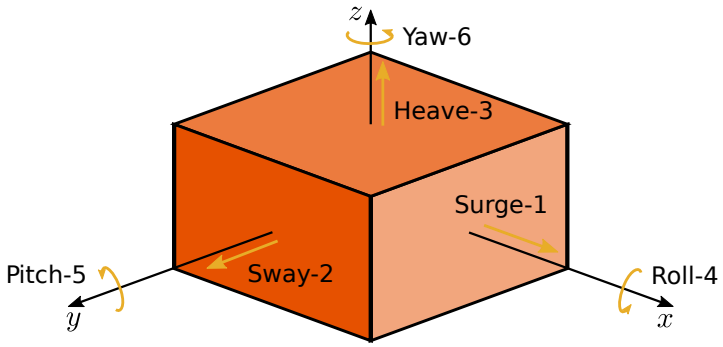

Figure 2.14: Schematic of the six degrees-of-freedom of a floating body, with their corresponding index numbers.

(and inertia) matrix of the floating body, defined as:

$$M = \begin{bmatrix} m & 0 & 0 & 0 & mz_{\mathrm{g}} & -my_{\mathrm{g}} \\ 0 & m & 0 & -mz_{\mathrm{g}} & 0 & mx_{\mathrm{g}} \\ 0 & 0 & m & my_{\mathrm{g}} & -mx_{\mathrm{g}} & 0 \\ 0 & -mz_{\mathrm{g}} & my_{\mathrm{g}} & I_{11} & I_{12} & I_{13} \\ mz_{\mathrm{g}} & 0 & -mx_{\mathrm{g}} & I_{21} & I_{22} & I_{23} \\ -my_{\mathrm{g}} & mx_{\mathrm{g}} & 0 & I_{31} & -I_{32} & I_{33} \end{bmatrix}. \tag{2.34}$$

In Equation (2.34), m is the mass of the body, I_{ij} are the inertia moments (if $i = j$) and products (if $i \neq j$) of the body, and $(x_{\mathrm{g}}, y_{\mathrm{g}}, z_{\mathrm{g}})$ are the coordinates of the body gravity centre. Due to the fact that the considered system is linear, the superposition principle holds and, therefore, the total force acting on the floating body can be expressed as a sum of different hydrodynamic forces:

$$M\ddot{\chi}(t) = f_{\mathrm{ex}}(t) + f_{\mathrm{r}}(t) + f_{\mathrm{h}}(t) + f_{\mathrm{ext}}(t), \tag{2.35}$$

where $f_{\mathrm{ex}}(t)$ is the excitation force due to the incoming waves, $f_{\mathrm{r}}(t)$ is the radiation force (resulting from radiated waves), $f_{\mathrm{h}}(t)$ is the hydrostatic restoring force (which results from the balance between the gravity and buoyancy forces), and $f_{\mathrm{ext}}(t)$ represents the sum of all possible external forces. In WEC hydrodynamic modelling, typical external forces may be the PTO system force (or control force) and, in the case of a floating WEC, the mooring force.

Alternatively, since the motion of the floating body and ocean waves can be considered (since the system is linear) harmonic, Equation (2.35) can be also expressed in the frequency-domain. For a harmonic motion, the position, velocity, and acceleration of the body can be expressed, respectively, as

$$\chi(t) = \Re(\hat{\chi} e^{\jmath\omega t}), \tag{2.36a}$$

$$\dot{\chi}(t) = \Re(\jmath\omega\hat{\chi} e^{\jmath\omega t}), \tag{2.36b}$$

$$\ddot{\chi}(t) = \Re(-\omega^2\hat{\chi} e^{\jmath\omega t}), \tag{2.36c}$$

and, furthermore, the velocity potential is also a harmonic function:

$$\Phi_{\mathrm{f}}(x, y, z, \omega, t) = \Re(\hat{\Phi}_{\mathrm{f}}(x, y, z, \omega)e^{\jmath\omega t}). \tag{2.37}$$

In Equations (2.36) and (2.37), $\jmath$ indicates the imaginary unit, $\Re$ refers to the real part of the argument, e is Euler's number, and the hat (^) indicates the complex amplitude of the corresponding variable. Finally, Equation (2.35) is written, in the frequency-domain, as

$$M\ddot{X}(\omega) = F_{\mathrm{ex}}(\omega) + F_{\mathrm{r}}(\omega) + F_{\mathrm{h}}(\omega) + F_{\mathrm{ext}}(\omega). \tag{2.38}$$

2.2.2.1 Excitation force

In diffraction theory, the excitation force (and excitation moment) acting on the floating body is a frequency-dependant parameter that depends on the incident and diffraction potentials. In particular, $F_{\mathrm{ex}}(\omega)$ is the sum of the (dynamic) Froude-Krylov force [161], $F_{\mathrm{FK}}(\omega)$, and diffraction force, $F_{\mathrm{d}}(\omega)$, expressed [158] as

$$\begin{aligned} F_{\mathrm{ex}}(\omega) = F_{\mathrm{FK}}(\omega) + F_{\mathrm{d}}(\omega) = &\jmath\omega\rho \int_{S_{\mathrm{wet}}} \hat{\Phi}_{\mathrm{i}} n_o \mathrm{d}S_{\mathrm{wet}} + \jmath\omega\rho \int_{S_{\mathrm{wet}}} \hat{\Phi}_{\mathrm{d}} n_o \mathrm{d}S_{\mathrm{wet}} = \\ &= \jmath\omega\rho \int_{S_{\mathrm{wet}}} (\hat{\Phi}_{\mathrm{i}} + \hat{\Phi}_{\mathrm{d}}) n_o \mathrm{d}S_{\mathrm{wet}}, \end{aligned} \tag{2.39}$$

where the diffraction potential is obtained by solving a BVP, known as the diffraction problem. The diffraction problem is formulated, for a fixed body (i.e., a body for which $\hat{\Phi}_{\mathrm{r}} = 0$), by applying the impermeability condition on S_{wet} (2.31), such as

$$-\frac{\delta\hat{\Phi}_{\mathrm{d}}}{\delta n_o} = \frac{\delta\hat{\Phi}_{\mathrm{i}}}{\delta n_o} \quad \text{on } S_{\mathrm{wet}}. \tag{2.40}$$

Additionally, $F_{\mathrm{ex}}(\omega)$ can be also expressed as a function of the incident waves, as

$$F_{\mathrm{ex}}(\omega) = A_{\mathrm{w}}(\omega)\hat{F}_{\mathrm{ex}}(\omega), \tag{2.41}$$

where $\hat{F}_{\mathrm{ex}}(\omega)$ is the vector of the complex amplitudes of $F_{\mathrm{ex}}(\omega)$.

It should be noted that, in addition to diffraction theory, other theories for computing F_{ex} exist. For instance, in Froude-Krylov theory, the effect of the diffraction potential in Equation (2.39) is neglected, meaning that no diffraction takes place or, alternatively, that the floating body does not interfere with the wave field.

2.2.2.2 Radiation force

Similarly to the case of the diffraction problem, another BVP, known as the radiation problem, has to be solved to find $\hat{\Phi}_{\mathrm{r}}$ and, hence, F_{r}. Since the problem is assumed to be linear and, therefore, the superposition principle holds, the radiation problem can be formulated in the absence of incident waves. The radiation potential must satisfy the boundary condition (2.31) while the body oscillates in any DoF. Therefore, $\hat{\Phi}_{\mathrm{r}}(\omega)$ can be written [158], as

$$\hat{\Phi}_{\mathrm{r}}(\omega) = \jmath\omega \sum_{i=1}^{n_{\mathrm{DoF}}} \hat{\chi}_i \phi_{\mathrm{r}_i}, \tag{2.42}$$

where ϕ_{r_i}, which is the solution of radiation problem, is the unit-amplitude radiation potential due to the i-th mode of motion. In general, each mode of motion of the floating body may generate radiated waves and, hence, a radiation force is defined for each mode. The radiation force for the i-th mode of motion is expressed [158], as

$$F_{\mathrm{r}_i}(\omega) = -\omega^2 \rho \int_{S_{\mathrm{wet}}} \sum_{j=1}^{n_{\mathrm{DoF}}} (X_j(\omega)\phi_{\mathrm{r}_j})\, n_{o_i} \mathrm{d}S_{\mathrm{wet}}. \tag{2.43}$$

Alternatively, using an electrical/mechanical analogy, $F_{\mathrm{r}_i}(\omega)$ can be also specified as

$$F_{\mathrm{r}_i}(\omega) = -\jmath\omega \sum_{j=1}^{n_{\mathrm{DoF}}} Z_{\mathrm{r}_{ij}}(\omega) X_j(\omega), \tag{2.44}$$

where $Z_{\mathrm{r}_{ij}}(\omega)$ is an element of the radiation impedance matrix, $Z_{\mathrm{r}}(\omega) \in \mathbb{R}^{n_{\mathrm{DoF}} \times n_{\mathrm{DoF}}}$, defined as

$$Z_{\mathrm{r}}(\omega) = B(\omega) + \jmath\omega A(\omega). \tag{2.45}$$

In Equation (2.45), the frequency-dependant matrices $B(\omega) \in \mathbb{R}^{n_{\mathrm{DoF}} \times n_{\mathrm{DoF}}}$ and $A(\omega) \in \mathbb{R}^{n_{\mathrm{DoF}} \times n_{\mathrm{DoF}}}$ are known, respectively, as the radiation damping (the real part of Z_{r}) and the added mass (the imaginary part of Z_{r}). Finally, F_{r} can be written [158], as

$$F_{\mathrm{r}}(\omega) = -Z_{\mathrm{r}}(\omega)\dot{X}(\omega) = -(B(\omega) + \jmath\omega A(\omega))\dot{X}(\omega). \tag{2.46}$$

2.2.2.3 Hydrostatic force

The hydrostatic (restoring) force, or static Froude-Krylov force [161], which is due to the variation in the mass of water displaced by the floating body, is obtained by integrating the hydrostatic pressure over the instantaneous wetted surface. However, due to the assumption of small body motion, S_{wet} does not vary and, therefore, F_{h} is linear and proportional to the body displacement as

$$F_{\mathrm{h}} = -C_{\mathrm{h}}\, X(\omega), \tag{2.47}$$

where $C_{\mathrm{h}} \in \mathbb{R}^{n_{\mathrm{DoF}} \times n_{\mathrm{DoF}}}$ is the hydrostatic stiffness matrix.

2.2.2.4 Force-to-velocity frequency response

If Equations (2.41), (2.46), and (2.47) are replaced in Equation (2.38), the frequency-domain model for a multiple-DoF floating body can be specified as

$$\dot{X}(\omega) = (F_{\mathrm{ex}} + F_{\mathrm{ext}})\, H_{\mathrm{f2v}}(\omega), \tag{2.48}$$

where $H_{\mathrm{f2v}}(\omega) \in \mathbb{R}^{n_{\mathrm{DoF}} \times n_{\mathrm{DoF}}}$ is the force-to-velocity frequency response, defined as

$$H_{\mathrm{f2v}}(\omega) = \left[\frac{C_{\mathrm{h}}}{\jmath\omega} + \jmath\omega(M + A(\omega)) + B(\omega) \right]^{-1}. \tag{2.49}$$

The diagonal terms of $H_{\mathrm{f2v}}(\omega)$ model the force-to-velocity response of each DoF, while the off-diagonal terms describe the interactions between different DoFs. Typically, WECs significantly move in a limited number of DoFs and, therefore, $H_{\mathrm{f2v}}(\omega)$ can be simplified according to the specific case.

The frequency-dependant parameters (i.e., $\hat{F}_{\mathrm{ex}}(\omega)$, $A(\omega)$, and $B(\omega)$), for a desired frequency range, and C_{h}, can be numerically computed using a boundary element method (BEM) solver. For instance, Figure 2.15 shows the frequency-dependant parameters for the heave mode of a 288 mm wide OWC [105], computed with the WAMIT software. The atypical trend of $A(\omega)$ in Figure 2.15(c) is explained in Section 2.2.3. BEM solvers are based on the so-called 'panel method'[5] (see, for instance, [162]), initially developed in the 60s as a low order method for solving incompressible and subsonic flows [163]. Traditional BEM solvers for linear WEC modelling include frequency-domain solvers, for instance WAMIT (commercial) [164], Aqwa (commercial) [165], and NEMOH (open source) [166], as well as time-domain solvers, such as ACHIL3D (commercial) [167].

2.2.3 Cummins' equation

The time-domain equivalent of Equation (2.48), first introduced by Cummins in 1962 [168], can be expressed as

$$(M + A_\infty)\ddot{\chi}(t) = -C_{\mathrm{h}}\chi(t) - \int_{-\infty}^{t} k_{\mathrm{r}}(t-\tau)\dot{\chi}(\tau)d\tau + f_{\mathrm{ext}}(t) + f_{\mathrm{ex}}(t), \tag{2.50}$$

where $A_\infty = A(\omega)|_{\omega\to\infty}$ is the (constant) value of the added mass at infinite frequency, $k_{\mathrm{r}} \in \mathbb{R}^{n_{\mathrm{DoF}} \times n_{\mathrm{DoF}}}$ is the radiation force kernel, and f_{ex} is written as

$$f_{\mathrm{ex}}(t) = \int_{-\infty}^{\infty} k_{\mathrm{ex}}(t-\tau)\eta(\tau)\mathrm{d}t, \tag{2.51}$$

[5] Panel methods use Green's third theorem, or identity, to transform the flow problem into a problem of doublet (i.e., source-sink) distribution on the body surface [162].

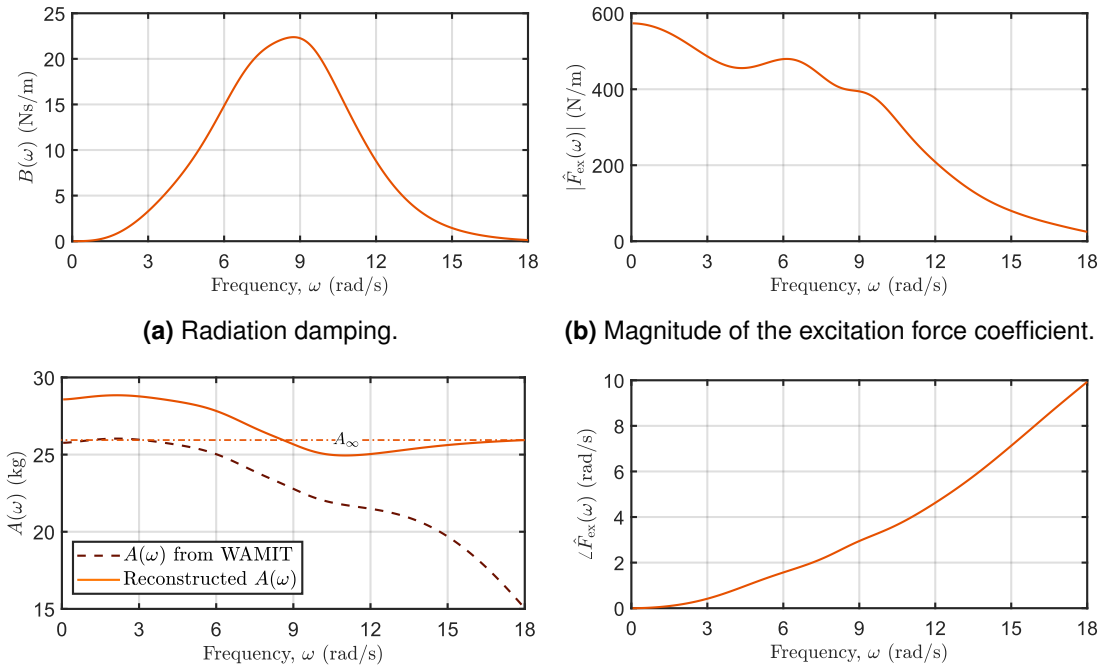

(a) Radiation damping.

(b) Magnitude of the excitation force coefficient.

(c) Added mass before and after reconstruction.

(d) Angle of the excitation force coefficient.

Figure 2.15: Hydrodynamic coefficients for the heave mode of a 288 mm wide OWC. A full description of the considered OWC geometry is given in [105].

where $k_{ex} \in \mathbb{R}^{n_{DoF} \times n_{DoF}}$ is the excitation force kernel, computed as the inverse Fourier transform of $\hat{F}_{ex}(\omega)$. The excitation and radiation force kernels of the heave mode for a 288 mm wide OWC are shown in Figure 2.16. Furthermore, $A(\omega)$, $B(\omega)$, and $k_r(t)$ are related to each other through the Ogilvie's relations [169], from the frequency to the time-domain, as

$$k_r(t) = \frac{2}{\pi} \int_0^\infty B(\omega)\cos(\omega t)\mathrm{d}\omega, \tag{2.52}$$

and, from the time to the frequency-domain, as

$$B(\omega) = \omega \int_0^\infty k_r(t)\cos(\omega t)\mathrm{d}t \tag{2.53a}$$

$$A(\omega) = A_\infty - \frac{1}{\omega} \int_0^\infty k_r(t)\sin(\omega t)\mathrm{d}t. \tag{2.53b}$$

As shown in Figure 2.15(c), BEM solvers typically fail in reproducing the expected behaviour of the OWC added mass. Indeed, although the value of A_∞ returned by WAMIT, for the OWC considered in Figure 2.15, is 26.4 kg, the asymptotic trend is not correctly represented. However, since the OWC radiation damping can be proved to be trustworthy[6], one can 'reconstruct' the added mass, through the Ogilvie's relations (2.55), using $B(\omega)$ [105].

[6]The value of $B(\omega)$ from WAMIT is compared to the analytical solution for the $B(\omega)$ of a water column presented in [81].

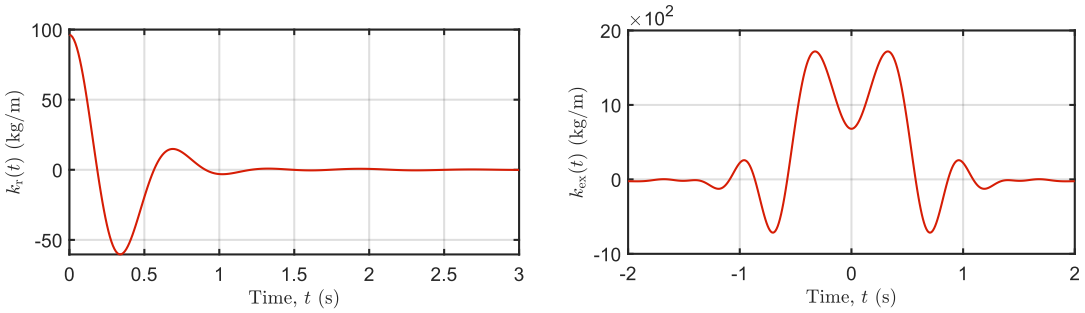

(a) Kernel of the radiation force.

(b) Kernel of the excitation force.

Figure 2.16: Radiation and excitation force kernels for the heave mode of a 288 mm wide OWC. A full description of the considered OWC geometry is given in [105].

It should be noted that, as suggested by the upper integration limit (i.e., ∞) in Equation (2.51), f_{ex} is *noncausal*, meaning that the wave excitation force acting on a floating body depends on both past, and future, values of the FSE [170]. The noncausality of f_{ex} is due to the fact that, when an ocean wave is propagating towards a floating body, the pressure field around the body starts varying before the wave hits the body. Therefore, the body can somewhat perceive the presence of the incoming excitation wave in advance [171].

2.2.3.1 Radiation convolution approximation

The radiation convolution term, or memory term, in Equation (2.50) models the fluid memory effect associated with the wave radiation phenomenon [158]. Since the direct computation of the radiation convolution term requires an excessively high computational burden, the convolution term is typically approximated, using a model reduction technique, with a suitable linear time invariant (LTI) system [172, 173]. The LTI system that approximates the convolution term can be defined, using a state space representation (SSR), as

$$\dot{x}_{\text{r}}(t) = A_{\text{r}} x_{\text{r}}(t) + B_{\text{r}} \dot{\chi}(t) \tag{2.54a}$$

$$y_{\text{r}}(t) = C_{\text{r}} x_{\text{r}}(t) \approx \int_{-\infty}^{t} k_{\text{r}}(t-\tau)\dot{\chi}(\tau)d\tau, \tag{2.54b}$$

where $x_{\text{r}} \in \mathbb{R}^{n_{\text{r}}}$ is the state vector of the radiation convolution SSR, $y_{\text{r}}(t) \in \mathbb{R}^{n_{\text{DoF}}}$ is the approximated convolution integral term (which is also the output of the LTI system), and the matrices (or parameters) $A_{\text{r}} \in \mathbb{R}^{n_{\text{r}} \times n_{\text{r}}}$, $B_{\text{r}} \in \mathbb{R}^{n_{\text{r}} \times n_{\text{DoF}}}$, and $C_{\text{r}} \in \mathbb{R}^{n_{\text{DoF}} \times n_{\text{r}}}$ can be obtained with a number of methods available in the literature. Such methods use either frequency-domain [174], or time-domain (such as BEMIO[7] [176] and

[7] BEMIO (Boundary Element Method Input/Output) is a utility used within the WEC motion simulator WEC-*Sim* [175].

Prony's method [177]), identification techniques to obtain A_r, B_r, and C_r. In the time-domain and frequency-domain identification methods, the matrices in Equation (2.54) are identified using, respectively, $k_\mathrm{r}(t)$ and $Z_\mathrm{r}(\omega)$ (therefore, $A(\omega)$ and $B(\omega)$). Finally, in more recent years, an identification technique based on model order reduction by moment-matching (MM) has also emerged [178]. Similarly to the frequency-domain identification approach, the MM-based identification method also uses frequency domain-data (i.e., $A(\omega)$ and $B(\omega)$).

2.2.3.2 WEC state-space representation

The radiation convolution approximation (2.54) allows to model the WEC dynamic (2.50), for any number of DoFs, using a SSR as

$$\dot{x}(t) = A_\mathrm{ssr}x(t) + B_\mathrm{ssr}f(t) \tag{2.55a}$$

$$y(t) = C_\mathrm{ssr}x(t) + D_\mathrm{ssr}f(t), \tag{2.55b}$$

where $x(t) = \begin{bmatrix}\chi(t) & \dot{\chi}(t) & x_\mathrm{r}(t)\end{bmatrix}^\mathsf{T} \in \mathbb{R}^{n_\mathrm{ssr}}$, $f(t) = \begin{bmatrix}f_\mathrm{ex}(t) & f_\mathrm{ext}(t)\end{bmatrix}^\mathsf{T} \in \mathbb{R}^{p_\mathrm{ssr}}$, $y(t) = \begin{bmatrix}\chi(t) & \dot{\chi}(t) & \ddot{\chi}(t)\end{bmatrix}^\mathsf{T} \in \mathbb{R}^{q_\mathrm{ssr}}$, and the matrices $A_\mathrm{ssr} \in \mathbb{R}^{n_\mathrm{ssr}\times n_\mathrm{ssr}}$, $B_\mathrm{ssr} \in \mathbb{R}^{n_\mathrm{ssr}\times p_\mathrm{ssr}}$, $C_\mathrm{ssr} \in \mathbb{R}^{q_\mathrm{ssr}\times n_\mathrm{ssr}}$, and $D_\mathrm{ssr} \in \mathbb{R}^{q_\mathrm{ssr}\times p_\mathrm{ssr}}$ are given by

$$\begin{aligned} A_\mathrm{ssr} &= \begin{bmatrix} 0 & \mathbb{I}_{n_\mathrm{DoF}} & 0 \\ -M^*S_\mathrm{h} & 0 & -M^*C_\mathrm{r} \\ 0 & B_\mathrm{r} & A_\mathrm{r} \end{bmatrix}, B_\mathrm{ssr} = \begin{bmatrix} 0 & 0 \\ M^* & M^* \\ 0 & 0 \end{bmatrix}, \\ C_\mathrm{ssr} &= \begin{bmatrix} \mathbb{I}_{n_\mathrm{DoF}} & 0 & 0 \\ 0 & \mathbb{I}_{n_\mathrm{DoF}} & 0 \\ -M^*S_\mathrm{h} & 0 & -M^*C_\mathrm{r} \end{bmatrix} \text{and } D_\mathrm{ssr} = \begin{bmatrix} 0 & 0 \\ 0 & 0 \\ M^* & M^* \end{bmatrix}, \end{aligned} \tag{2.56}$$

where $M^* = (M + A_\infty)^{-1}$, $n_\mathrm{ssr} = 2n_\mathrm{DoF} + n_\mathrm{r}$, $p_\mathrm{ssr} = 2n_\mathrm{DoF}$, and $q_\mathrm{ssr} = 3n_\mathrm{DoF}$. Furthermore, the term $\mathbb{I}_{n_\mathrm{DoF}}$ indicates an identity matrix of size n_DoF, and the symbol 0 denotes any zero element dimensioned according to the context.

It should be noted that the general formulation in Equation (2.55) can be adapted depending on the specific case (i.e., number of modelled DoFs, dimension of the parametric SSR for approximating the radiation convolution (2.54), and different external forces acting on the system). Furthermore, although the formulation in Equation (2.55) considers, as outputs, position, velocity, and acceleration of the WEC, it is also possible to consider only some of them (e.g., velocity only).

2.2.4 Ocean wave spectra

The (deterministic) regular waves presented in Equation (2.14) do not provide a realistic description of the real ocean waves. Real ocean waves, which have a stochastic nature, are better approximated by irregular waves. Irregular waves are typically generated considering a wave spectral density function (SDF), which represents a sea state (SS) in terms of wave energy distribution as a function of frequency. In the literature, several wave spectral models, derived from empirical measurements and physical considerations, have been proposed. Among such wave spectra, the most widely adopted SDFs are the Bretschneider spectrum, for developing seas [179], the JONSWAP[8] spectrum, for wind-generated seas with fetch limitations [180], and the Pierson-Moskowitz spectrum, for fully-developed seas [181]. For instance, Figure 2.17 shows how the JONSWAP spectrum varies when changing (a) the peak period, T_p, (b) the significant wave height, H_s, and (c) the peak-shape parameter, γ_J, which are the three parameters that characterise the JONSWAP spectrum, written [180] as:

$$S_\mathrm{J}(\omega) = \frac{\alpha_s g^2}{\omega^5} e^{-\frac{5}{4}\left(\frac{\omega_\mathrm{p}}{\omega}\right)^4} \gamma_\mathrm{J}^{r_s(\omega)} \tag{2.57}$$

where $r_s(\omega) = e^{-\frac{(\omega-\omega_\mathrm{p})^2}{2\sigma_s^2\omega_\mathrm{p}^2}}$, $\omega_\mathrm{p} = \frac{2\pi}{T_\mathrm{p}}$, α_s, and σ_s are constant values determined using data collected during the JONSWAP experiment [180]. The statistical parameter

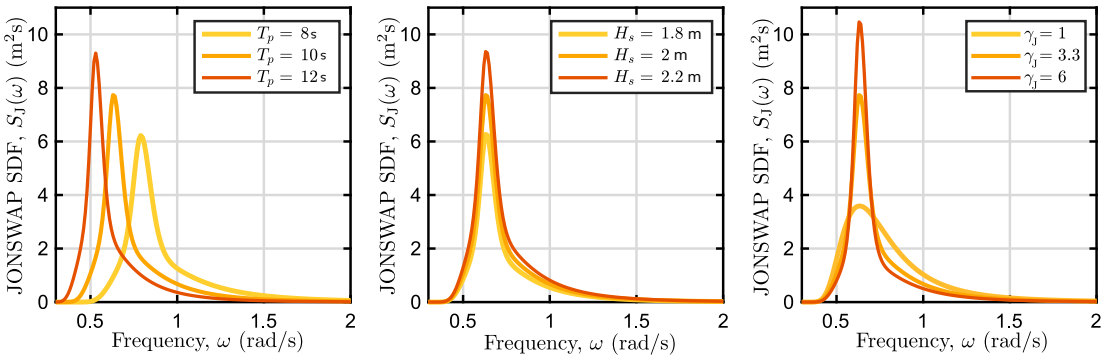

(a) H_s =2 m and $\gamma_\mathrm{J} = 3.3$. **(b)** T_p =10 s and $\gamma_\mathrm{J} = 3.3$. **(c)** T_p =10 s and H_s =2 m.

Figure 2.17: Examples of JONSWAP SDFs with varying parameters (a) T_p, (b) H_s, and (c) γ_J.

H_s is defined as the average of the one-third highest waves in a wave train record, while T_p is the period in a spectrum with the maximum energy. Similarly to Airy's

[8]JONSWAP (Joint North Sea Wave Observation Project).

waves, for a given wave spectrum, the time-averaged wave power per metre of wave crest is computed [158], as

$$\bar{P}_{\text{wave}} = \frac{\rho g^2}{64\pi} H_{\text{s}}^2 T_{\text{e}}, \tag{2.58}$$

where T_{e} is the energy period, defined as the wave period corresponding to the weighted average of the wave energy in a spectrum.

To generate a wave time series realization, with the statistical properties of a target SDF, different methods can be employed. A well-known method, also used in this thesis, for generating an irregular wave time series is that of approximating irregular waves with a linear superposition of harmonic waves of different random frequencies, amplitudes, and phases [182]. Another popular approach, is to calculate the inverse Fourier transform, $\mathscr{F}^{-1}$, of $S_{wn}(\omega)S(\omega)$, as

$$\eta(t) = \mathscr{F}^{-1}\{S_{wn}(\omega)S(\omega)\}, \tag{2.59}$$

where $S_{wn}(\omega)$ and $S(\omega)$ are, respectively, the power spectral densities of a white noise input signal and the wave (e.g., a JONSWAP SDF).

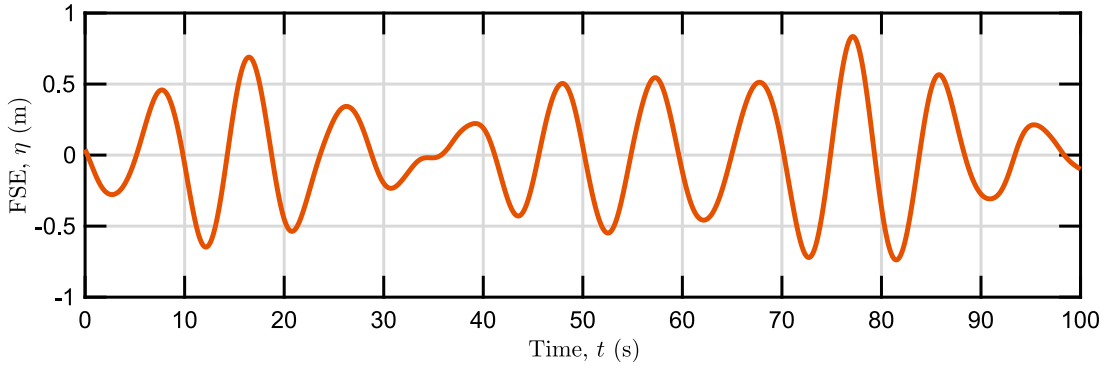

Figure 2.18: Example of a wave elevation time series generated from a JONSWAP SDF with T_{p} =10 s, H_{s} =2 m, and $\gamma_{\text{J}} = 3.3$.

By way of example, Figure 2.18 shows an irregular wave elevation η time series, which is generated using the linear superposition method [182] from a JONSWAP SDF with T_{p} =10 s, H_{s} =2 m, and $\gamma = 3.3$.

2.3 Summary

In this chapter, an overview on OWC systems (Section 2.1) and an introduction to linear hydrodynamic modelling (Section 2.2) have been provided. In particular, the operating principle, main advantages/disadvantages, historical development, and PTO components of OWC WECs have been presented. Furthermore, under LWT

assumptions, the linear Cummins' equation modelling the wave-body interactions in 6 DoFs has been derived. In Section 3.1, the linear Cummins' equation will be specified for the particular case of an OWC WEC.

Apart from the linear Cummins' equation and high-fidelity nonlinear models based on the Navier-Stokes equations, WEC hydrodynamic models with different shades of nonlinearity have also emerged. A review on nonlinear WEC hydrodynamic modelling can be found in [156].

Part II

OWC WEC modelling

What you do makes a difference, and you have to decide what kind of difference you want to make.

— Jane Goodall.

3

Oscillating water column modelling from first principles

Contents

3.1 Hydrodynamic modelling 57
3.1.1 Frequency-domain hydrodynamic model 58
3.1.2 Time-domain hydrodynamic model 59
3.2 Air chamber modelling 59
3.2.1 Time-domain air chamber model 59
3.2.2 Frequency-domain air chamber model 60
3.3 PTO modelling 61
3.3.1 Air turbine model 62
3.3.2 Hydrodynamic/aerodynamic interaction model 64
3.3.3 Electric generator model 65
3.4 Summary 66

This chapter presents a unbiased W2W model from first principles, or physics-based model (PBM), for a generic fixed OWC WEC. In PBMs, the OWC subsystems, namely the hydrodynamic part, air chamber, and PTO, are modelled utilising physical principles. Arguably, the main advantage of PBMs is that the mathematical model retains, to some extent, knowledge of the real physical process. Additionally, from an OWC control perspective, PBMs are attractive since it is relatively easy to assess the impact of a control action on the performance of each OWC subsystem. In contrast with PBMs, physical knowledge of the system is totally, or marginally,

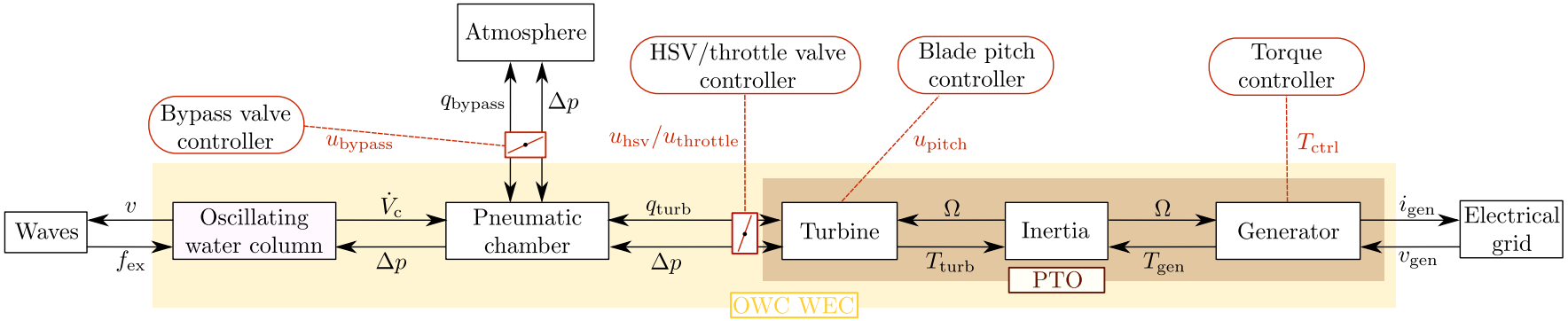

Figure 3.1: Wave-to-wire power flow in an OWC WEC. The red ovals indicate possible manipulated inputs. All variables are defined in Chapter 3. Figure adapted from [51].

lost if using data-based models, although the modelling process is potentially less laborious (further discussed in Section 4).

Figure 3.1 shows the schematic of the W2W power flow for an OWC WEC. In particular, the typical components of an OWC device, and the physical variables involved at each step of the energy conversion chain, are specified. Furthermore, the red ovals indicate possible manipulated inputs that may be used in a control strategy.

3.1 Hydrodynamic modelling

As already mentioned in Section 2.2, WEC hydrodynamic modelling is based on LWT. In particular, the OWC hydrodynamic part can be modelled using two related physics-based modelling approaches (schematically shown in Figure 3.2), namely a) the piston model, which is presented in this section, and b) the uniform pressure model. In this thesis, the piston model is used when designing OWC control strategies (Chapters 6, 7, and 8), since it provides a relatively accurate and computationally efficient mathematical model for the considered OWC device (i.e., the Mutriku OWC) [183].

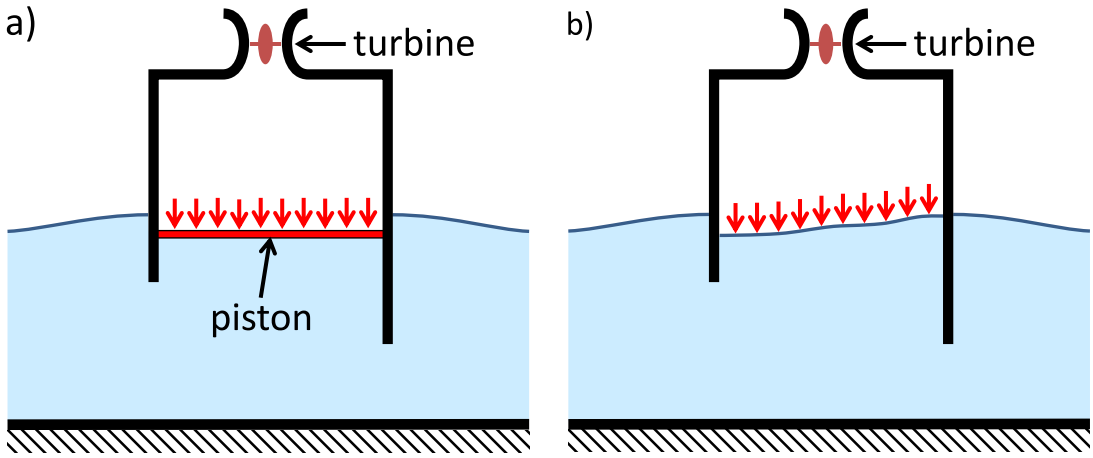

Figure 3.2: Schematics of the a) piston and b) uniform pressure models. Source: [66].

Due to its close relationship with the piston model, and for the sake of completeness, the uniform pressure model is briefly presented in Appendix A. A full treatment of the uniform pressure model, also known as the admittance approach, can be found in [158].

3.1.1 Frequency-domain hydrodynamic model

In the piston model, first proposed by Evans [81], the surface of the water column is treated as a neutrally buoyant massless piston which solely displaces in the vertical direction (i.e., heave mode only). The buoyant piston is characterised by frequency dependant hydrodynamic parameters, namely added mass, $A_{\mathrm{p}}(\omega)$, radiation damping, $B_{\mathrm{p}}(\omega)$, and excitation force, $F_{\mathrm{ex}}(\omega)$, which are computed either experimentally [184] or numerically [105] using a BEM solver (which solves the BVP detailed in Section 2.2). For instance, Figure 3.3 shows the frequency dependant hydrodynamic parameters characterising the buoyant piston for one of the OWC chambers at Mutriku facility. The piston model is a suitable modelling approach if the OWC chamber dimensions are small compared to the typical wavelengths of the incoming ocean waves [66], which is not an unrealistic scenario for many OWCs under normal energy harvesting conditions. For smaller wavelengths, the water column stops behaving like a buoyant piston and other modes of motion [185], such as sloshing [186], may appear. However, OWC wave power capture is primarily affected by the heave mode of the water column [184] and, therefore, other modes of motions are often neglected to avoid needless modelling complexity.

Ultimately, the OWC piston model, in the frequency domain, is derived by specifying the generic hydrodynamic model in Equation (2.48) for a heaving water column (i.e., a water column moving in heave mode only). Therefore, the equation of motion of the water column, subject to harmonic excitation at a frequency ω, may be written [184], as

$$\left[\jmath\left(\omega(m_{\mathrm{p}} + A_{\mathrm{p}}(\omega)) - \frac{C_{\mathrm{h}}}{\omega}\right) + B_{\mathrm{p}}(\omega)\right]\hat{v} = -\Delta\hat{p}\, S_{\mathrm{owc}} + F_{\mathrm{ex}}(\omega), \tag{3.1}$$

where m_{p} is the water piston mass, $C_{\mathrm{h}} = \rho_{\mathrm{w}} g S_{\mathrm{owc}}$ denotes the hydrostatic stiffness, S_{owc} is the cross-sectional area of the water column, and ρ_{w} is the water density. Furthermore, A_{p} and B_{p} are the added mass and radiation damping associated with the heave mode of the water piston, respectively. Finally, $\hat{v}$ and $\Delta\hat{p}$ are the complex amplitudes of the OWC vertical velocity and the pressure difference between the air chamber and the atmosphere, respectively, such that $v(t) = \Re(\hat{v}\, e^{\jmath\omega t})$ and $\Delta p(t) = \Re(\Delta\hat{p}\, e^{\jmath\omega t})$. In Equation (3.1), the term $\Delta\hat{p} S_{\mathrm{owc}}$ represents the external force acting on the water column, namely the force resulting from the chamber pressure difference.

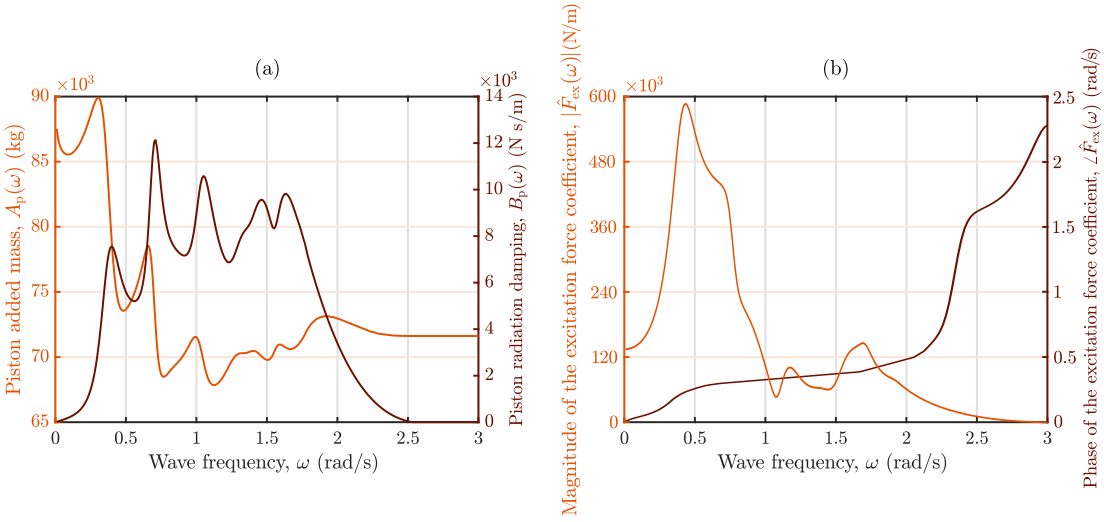

Figure 3.3: Frequency dependant hydrodynamic parameters for the Mutriku OWC: (a) Added mass, $A_{\mathrm{p}}(\omega)$, and radiation damping, $B_{\mathrm{p}}(\omega)$; (b) magnitude of the excitation force coefficient, $|\hat{F}_{\mathrm{ex}}(\omega)|$, and phase of the excitation force coefficient, $\angle\hat{F}_{\mathrm{ex}}(\omega)$.

3.1.2 Time-domain hydrodynamic model

The time-domain equivalent of Equation (3.1) is essentially the classic Cummins' equation (2.50), specified for a heaving water column [81]:

$$\begin{aligned} m_{\mathrm{p}}\dot{v} &= -\rho_{\mathrm{w}} g S_{\mathrm{owc}} z - S_{\mathrm{owc}}\Delta p + f_{\mathrm{ex}} - f_{\mathrm{r}} \\ \dot{z} &= v, \end{aligned} \tag{3.2}$$

where z is the OWC vertical position (positive upward), $\Delta p = p_{\mathrm{c}} - p_0$, p_{c} is the air chamber pressure, and p_0 is standard atmospheric pressure. Finally, the radiation force is defined [168] as

$$f_{\mathrm{r}} = A_p^{\infty}\dot{v} + \int_{-\infty}^{t} k_{\mathrm{r}}(t-\tau)\, v(\tau)\, \mathrm{d}\tau, \tag{3.3}$$

where A_p^{∞} is the value of A_p at infinite frequency and the kernel, k_{r}, is the piston impulse response function computed from the OWC radiation damping, $B_{\mathrm{p}}(\omega)$, using the Ogilvie's relations (2.52).

3.2 Air chamber modelling

3.2.1 Time-domain air chamber model

For a fixed OWC with an air turbine and a bypass valve (which is a control valve in parallel with the turbine), the mass balance in the pneumatic chamber is expressed [51] as

$$\frac{\mathrm{d}\left(\rho_{\mathrm{c}} V_{\mathrm{c}}\right)}{\mathrm{d}t} = -w_{\mathrm{turb}} - w_{\mathrm{bypass}}, \tag{3.4}$$

where ρ_c is the air density in the chamber, $V_c = V_0 - S_{owc}z$ is the air chamber volume, and V_0 is the chamber volume in still water conditions. On the right side of Equation (3.4), w_{turb} and w_{bypass} are the turbine and bypass valve mass flow rates (both positive for outward airflow), respectively. Furthermore, w_{bypass} is a function of the bypass valve relative position, $0 \leq u_{bypass} \leq 1$, and Δp, such that

$$w_{bypass}\left(\Delta p, u_{bypass}\right) = \mathrm{sgn}(\Delta p)\, C_d\left(u_{bypass}\right) A_{bypass} \sqrt{2\rho_{air}|\Delta p|}, \tag{3.5}$$

where $C_d\left(u_{bypass}\right)$ is the discharge coefficient, A_{bypass} is the bypass valve area and the operator 'sgn' indicates the signum function. The air density (at the bypass valve inlet) is computed as

$$\rho_{air} = \max(\rho_c, \rho_0), \tag{3.6}$$

where ρ_0 is the air atmospheric density. Assuming that the air behaves as an ideal gas, the air compression/expansion process is modelled as an isentropic process [72] and, therefore, ρ_c is computed as

$$\rho_c = \rho_0 \left(\frac{p_c}{p_0}\right)^{1/\gamma}, \tag{3.7}$$

where γ is the air specific heat ratio. By substituting Equation (3.7) in Equation (3.4), and after some straightforward manipulation, the air mass balance in the pneumatic chamber becomes

$$\frac{\dot{p}_c}{p_c} = -\gamma \left(\frac{\dot{V}_c}{V_c} + \frac{w_{turb} + w_{bypass}}{m_c}\right), \tag{3.8}$$

where $m_c = \rho_c V_c$ is the instantaneous air mass inside the chamber.

Finally, the pneumatic power available to the turbine is computed as $P_{pneu} = q_{turb}\, \Delta p$, while the pneumatic power dissipated through the bypass valve is calculated as $P_{bypass} = q_{bypass}\, \Delta p$. The variables $q_{turb} = w_{turb}/\rho_{air}$ and $q_{bypass} = w_{bypass}/\rho_{air}$ are the turbine and bypass valve volumetric flow rates, respectively.

3.2.2 Frequency-domain air chamber model

To derive the frequency-domain air chamber model, Equation (3.8) is linearized, considering the following three assumptions: (i) If compared to the atmospheric pressure, the magnitude of the pressure oscillations inside the air chamber is negligible, then $p_c + p_0 \approx p_0$; (ii) since w_{bypass} is a nonlinear function of Δp and u_{bypass}, the bypass valve cannot be included in a frequency-domain formulation and, consequently, $w_{bypass} := 0$; and (iii) w_{turb} is linearly related to Δp, as:

$$\Delta p = \zeta w_{turb}, \tag{3.9}$$

where ζ is the turbine damping, further discussed in Section 3.3. As a consequence of assumption (i), $\rho_c \approx \rho_0$ (i.e., the air compressibility effect in the pneumatic chamber is negligible) and, furthermore, $V_c \approx V_0$. Using the aforementioned assumptions, the linearisation of Equation (3.4) yields:

$$\frac{V_0}{\gamma p_0}\dot{p}_c + \frac{\Delta p}{\rho_0 \zeta} = -\dot{V}_c. \tag{3.10}$$

The rate of change of air volume, $\dot{V}_c$, is computed from the frequency-domain hydrodynamic model (3.1), as

$$-\dot{V}_c = S_{owc}\Re(\hat{v}e^{j\omega t}). \tag{3.11}$$

It should be noted that, due to assumption (iii), the linearised chamber equation (3.10) is only valid for an air turbine having $\zeta = \text{constant}$. Such turbine damping is relevant only for a specific type of turbine, namely a Wells turbine, operating at constant speed. However, due to the reciprocating nature of the ocean waves, variable speed control strategies are required to efficiently operate the air turbine for different chamber pressure levels [51]. In this thesis, only variable speed control strategies are considered and, therefore, the time-domain description in Equations (3.2) and (3.8) is used.

3.3 PTO modelling

The PTO system dynamics are modelled [56] as

$$\frac{\mathrm{d}}{\mathrm{d}t}\left(\frac{1}{2}I\Omega^2\right) = P_{turb} - T_{ctrl}\,\Omega - P_{fr}, \tag{3.12}$$

where

$$P_{fr} = (T_a + T_r)\,\Omega. \tag{3.13}$$

In Equations (3.12) and (3.13), Ω is the turbine rotational speed, I is the inertial moment of the rotating parts, T_{ctrl} is the generator control torque, P_{turb} is the turbine mechanical power, and P_{fr} indicates the bearing viscous friction loss due to radial and axial loads. The radial load, T_r ($\sim$ constant), which is due to the weight of the rotating parts, can be experimentally computed from a rotational speed decay test with $T_{ctrl} = w_{turb} = 0$ [187]. For a given turbine geometry, the axial load, T_a, which is produced by the aerodynamic forces on the turbine rotor, is a function of w_{turb}. Assuming incompressible and irrotational airflow, T_a can be estimated using the 'two-dimensional cascade of blades' approach (a well-known aerodynamic design tool for turbomachines [188]) as shown, for example, in [187].

In the OWC PTO, the bearing friction losses are typically negligible compared to the aerodynamic losses in the air turbine [187], which are about two orders of magnitude larger than P_{fr}. Therefore, in this thesis, only aerodynamic losses are considered (in the turbine model), while bearing friction losses are neglected.

3.3.1 Air turbine model

Under design operating conditions, i.e., large Reynolds ($\text{Re} = \Omega d_{\text{r}}^2/\nu_{\text{air}} > 10^6$) and low Mach ($\text{Ma} = \Omega d_{\text{r}} 0.5/c_{\text{air}} < 0.3$) numbers at the turbine blade tips, a dimensionless air turbine model can be derived using the Buckingham Pi Theorem[1] [188], as:

$$\Phi = f_{\Phi}(\Psi, u_{\text{hsv/throttle}}, u_{\text{pitch}}),\ \Pi = f_{\Pi}(\Psi, u_{\text{hsv/throttle}}, u_{\text{pitch}}), \tag{3.14}$$

where

$$\Phi = \frac{w_{\text{turb}}}{\rho_{\text{air}}\,\Omega\,d_{\text{r}}^3},\ \Pi = \frac{P_{\text{turb}}}{\rho_{\text{air}}\,\Omega^3\,d_{\text{r}}^5},\ \Psi = \frac{\Delta p}{\rho_{\text{air}}\,\Omega^2\,d_{\text{r}}^2}. \tag{3.15}$$

In Equations (3.14) and (3.15), Φ is the dimensionless air mass flow rate, Π is the dimensionless turbine power, Ψ is the dimensionless pressure head, d_{r} is the turbine rotor diameter, and $\rho_{\text{air}} = \min(\rho_{\text{c}}, \rho_0)$ is the air density at the turbine inlet. The manipulated inputs u_{pitch} and $0 \leq u_{\text{hsv/throttle}} \leq 1$ are, respectively, the pitch angle of rotor/stator blades and the relative position of a valve in series with the turbine. Such a valve is either a standard (i.e., butterfly) throttle valve or, for the biradial turbine only, a high-speed valve (HSV). Furthermore, ν_{air} is the air dynamic viscosity and c_{air} is the air speed of sound at the turbine inlet. Finally, the turbine efficiency is defined as

$$\eta_{\text{turb}}(\Psi, u_{\text{hsv/throttle}}, u_{\text{pitch}}) = \frac{P_{\text{turb}}}{P_{\text{pneu}}} = \frac{f_{\Pi}(\Psi, u_{\text{hsv/throttle}}, u_{\text{pitch}})}{\Psi\, f_{\Phi}(\Psi, u_{\text{hsv/throttle}}, u_{\text{pitch}})}. \tag{3.16}$$

By way of example, the dimensionless functions f_{Φ}, f_{Π}, and η_{turb}, for the Wells turbine and biradial turbine installed at the Mutriku facility, are shown in Figure 3.4. Figure 3.4 also shows Ψ_{mep} and Ψ_{stall} which are, respectively, Ψ at the turbine maximum efficiency point (MEP), and Ψ at the limit of the Wells turbine stall region. Furthermore, for each turbine, Figure 3.5 shows η_{turb} as a function of Δp and Ω. Figures 3.4 and 3.5 highlight two important turbine-related issues, already mentioned in Section 2.1.3. Firstly, the operational range of the Wells turbine in terms of Ψ (Figure 3.4), or, equivalently, in terms of Δp and Ω (Figure 3.5), is narrow compared to the biradial turbine operational range. Secondly, in contrast to the biradial turbine, the Wells turbine has a hard stall condition for $\Psi \geq \Psi_{\text{stall}}$.

[1] The Buckingham Pi Theorem states that for any physical process described by n variables, if $k < n$ is the minimum number of independent variables required to fully characterize the process, then the physical process can be described using $n - k$ dimensionless functions.

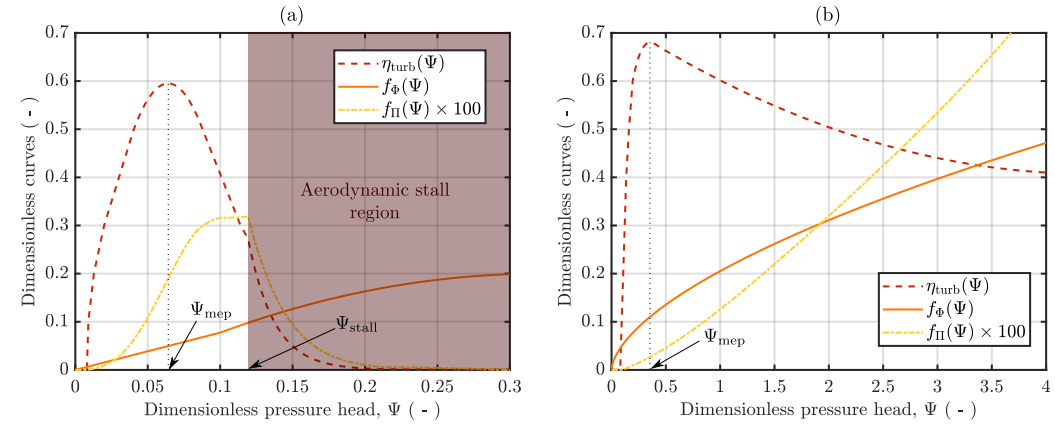

Figure 3.4: Dimensionless models of the (a) Wells turbine and (b) biradial turbine at Mutriku OWC. The figure shows the turbine efficiency, η_{turb}, dimensionless flow rate, Φ, and dimensionless power, Π, as functions of the dimensionless pressure head, Ψ. Figure adapted from [51].

The dimensionless approach, which is a standard modelling method used in turbomachinery, is particularly convenient for a number of reasons. In the first place, the dimensionless model is solely a function of the turbine geometry (e.g., solidity, type of turbine, number of rotor blades,. . .), meaning that, for a given turbine geometry, the dimensionless turbine model remains unchanged for any value of d_{r}. Secondly, the dimensionless approach provides a suitable turbine description, while avoiding modelling the aerodynamic forces on the turbine blades. Accurate modelling of the aerodynamic forces is difficult and does not provide any additional useful information from a control perspective [66]. Finally, in the dimensionless description, the turbine power and turbine efficiency are expressed as functions of a single variable (Ψ) rather than two variables (Ω and Δp).

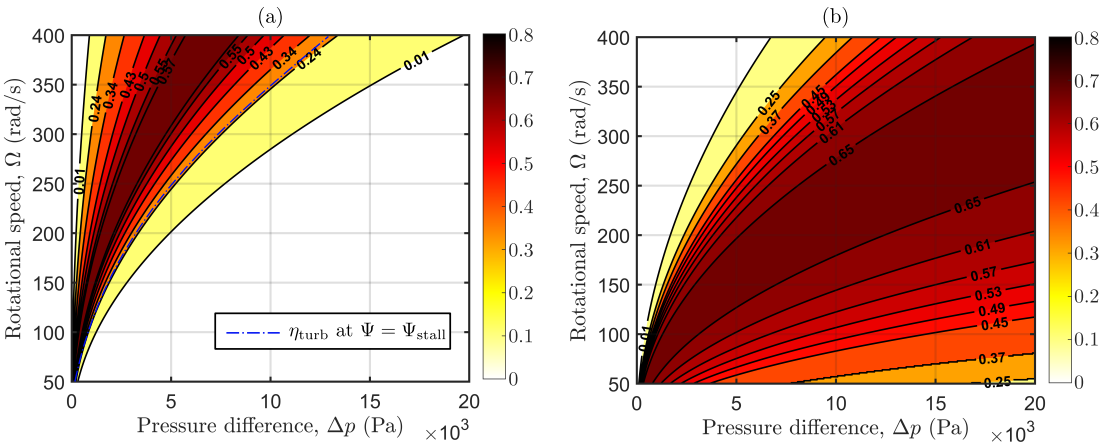

Figure 3.5: Turbine efficiency, η_{turb}, as a function of Δp and Ω, for the (a) Wells turbine and (b) biradial turbine at Mutriku OWC.

It should be noted that the model in Equations (3.14) and (3.15), which is used in this thesis, is not the only possible turbine dimensionless description. In Appendix A, an alternative dimensionless turbine model, first proposed by Maeda [189], is reported. However, Maeda's formulation requires knowledge of the axial airflow velocity, which is difficult to measure without intrusive probes.

3.3.2 Hydrodynamic/aerodynamic interaction model

Hydrodynamic/aerodynamic interaction, namely the effect of the turbine on the hydrodynamic part, depends on the turbine damping characteristics. Turbine damping, defined as the ratio $\zeta = \Delta p / w_{\text{turb}}$, is generally not constant and is usually a function of Ω.

3.3.2.1 Wells turbines

For a Wells turbine, the relationship between Ψ and Φ is linear [66]:

$$\Psi = \kappa_{\text{w}} \Phi, \tag{3.17}$$

where κ_{w} is a constant that depends on the Wells turbine geometry, but not on its size (i.e., d_{r}). By substituting the definitions of Φ and Ψ (Equation (3.15)) into Equation (3.17), the following relationship is obtained

$$w_{\text{turb}} = \frac{d_{\text{r}}}{\kappa_{\text{w}} \Omega} \Delta p = \zeta_{\text{w}} \Delta p, \tag{3.18}$$

where ζ_{w} is the Wells turbine damping. It should be noted that ζ_{w} is a function of Ω, meaning that the OWC hydrodynamic performance is influenced by the turbine rotational speed.

3.3.2.2 Impulse-like turbines

In axial-flow impulse [66] and biradial turbines [110], the relationships between Ψ and Φ are, respectively,

$$\Psi = \kappa_{\text{i}} \Phi^2, \tag{3.19}$$

and

$$\Psi = \kappa_{\text{b}} \Phi^{5/3}, \tag{3.20}$$

where κ_{i} and κ_{b} are turbine geometric constants. Similarly to the Wells turbine case, the turbine damping of the axial-flow impulse and biradial turbines are written, respectively, as

$$\zeta_{\text{i}} = \frac{d_{\text{r}}^4 \rho_{\text{air}}}{\kappa_{\text{i}}}, \tag{3.21}$$

and

$$\zeta_{\mathrm{b}} = \frac{1}{\kappa_{\mathrm{b}}^{3/5}} \left(\frac{d_{\mathrm{r}}^{9/5}}{\Omega^{1/5}} \right) \left(\frac{\rho_{\mathrm{air}}}{\Delta p} \right)^{2/5} . \tag{3.22}$$

Therefore, for a biradial turbine, ζ_{b} only marginally depends on Ω, meaning that the wave-to-pneumatic energy conversion process is not significantly affected by Ω. Furthermore, since ζ_{i} is not a function of Ω, the axial-flow impulse turbine rotational speed does not influence the OWC hydrodynamic behaviour.

Figure 3.6 shows the relationship between Δp and w_{turb}, as Ω varies within a typical range of values, for different turbines. The larger shaded area of the Wells turbine, if compared to the other air turbines, indicates the greater impact of Ω on the hydrodynamic efficiency.

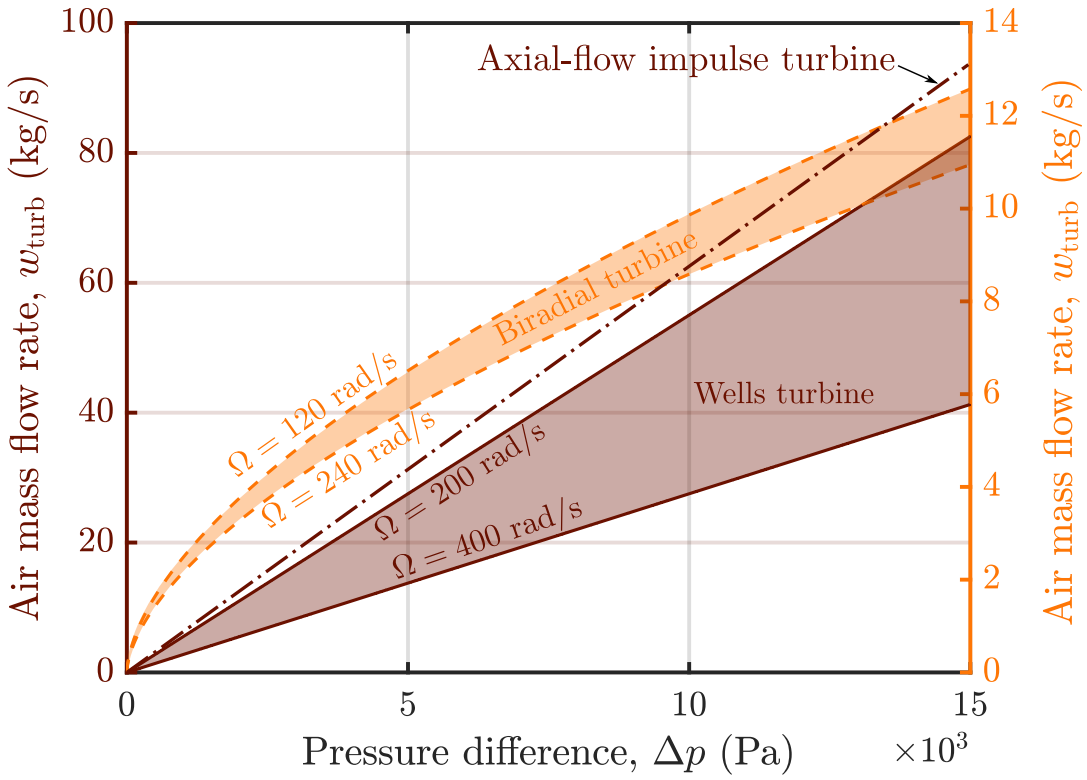

Figure 3.6: Turbine damping characteristics for two turbines. Relationship between the pressure difference, Δp, and the air mass flow rate, w_{turb}, as Ω changes, for a Wells turbine, an axial-flow impulse turbine, and a biradial turbine. Figure adapted from [56].

3.3.3 Electric generator model

As already mentioned in Section 2.1.3, suitable electric generators for OWC WECs are typically the DFIGs, SCIGs, and PMGs [68]. For instance, the PMG model in

the direct-quadrature (d-q) frame is specified [190], as

$$\begin{aligned}\frac{\mathrm{d}i_\mathrm{d}}{\mathrm{d}t} &= -\frac{R_\mathrm{d}}{L_\mathrm{d}}i_\mathrm{d} + \omega_\mathrm{e} i_\mathrm{q} + \frac{1}{L_\mathrm{d}}v_\mathrm{d} \\ \frac{\mathrm{d}i_\mathrm{q}}{\mathrm{d}t} &= -\frac{R_\mathrm{q}}{L_\mathrm{q}}i_\mathrm{q} - \omega_\mathrm{e} i_\mathrm{d} - \frac{\lambda_\mathrm{pm}\omega_\mathrm{e}}{L_\mathrm{q}} + \frac{1}{L_\mathrm{q}}v_\mathrm{q}\end{aligned} \tag{3.23}$$

and

$$T_\mathrm{ctrl} = \frac{3}{4}N_\mathrm{p}^\mathrm{gen}(i_\mathrm{q}\lambda - i_\mathrm{q}i_\mathrm{d}(L_\mathrm{d} - L_\mathrm{q})), \tag{3.24}$$

where i_d (i_q), v_d (v_q), L_d (L_q), and R_d (R_q) are, respectively, the stator current, stator voltage, stator inductance, and stator resistance in the d-q frame. Furthermore, $\omega_\mathrm{e} = (\Omega N_\mathrm{p}^\mathrm{gen})/2$, $N_\mathrm{p}^\mathrm{gen}$, and λ_pm are, respectively, the generator electric angular frequency, the number of poles, and the rotor permanent magnet flux. Finally, the generator active (real) power is written as

$$P_\mathrm{elec} = \frac{3}{2}(v_\mathrm{d}i_\mathrm{d} + v_\mathrm{q}i_\mathrm{q}) - \underbrace{(R_\mathrm{q}i_\mathrm{q}^2 + R_\mathrm{d}i_\mathrm{d}^2)}_{\text{copper losses}}. \tag{3.25}$$

The mathematical models for DFIGs and SCIGs can be found in [191].

3.4 Summary

In this chapter, a W2W model of a fixed OWC WEC, which is potentially suitable for model-based control applications, being relatively computationally simple and valid under typical controlled operating conditions, is presented. Furthermore, the assumptions under which the W2W model is valid, and the main simplifications considered in this thesis, are explained. Ultimately, in this thesis, since the system model is primarily used for designing control strategies (Chapters 6 and 7), the selected OWC W2W model should be as suitable as possible for control synthesis.

In addition to the linear hydrodynamic modelling assumptions presented in Section 2.2, the main modelling assumptions introduced in this chapter are: (i) The water column is modelled (Equation (3.2)) as a massless buoyant piston of infinitesimal thickness; (ii) the air compression/expansion process, described in Equation (3.7), is an isentropic process; (iii) the turbine dimensionless model presented in Equations (3.14) and (3.15), is valid for high Reynolds and low Mach numbers.

It should be noted that the mathematical model presented in this chapter can be also easily extended to floating OWCs since, apart from the hydrodynamic part, the model equations do not change. For the hydrodynamic model of a floating OWC, two coupled Cummins' equations are used to describe the dynamics of

two distinct floating bodies, namely the water column and the device hull. The hydrodynamic model of a floating OWC is found, for example, in [87]. Experimental validation of of the hydrodynamic and air chamber models are found, for instance, in [105, 184, 192] , while the turbine model and generator model validations may be found, respectively, in [193, 194] and [195].

4

Data-based hydrodynamic modelling for OWCs

Contents

4.1 Motivation and background 70
4.1.1 Introduction to system identification 70
4.1.2 Data-based modelling in wave energy 71
4.2 Black-box hydrodynamic modelling for OWCs 73
4.2.1 Experimental campaign 74
4.2.2 Frequency-domain data-based modelling 78
4.2.3 Time-domain data-based modelling 82
4.3 Conclusions 94

This chapter focuses on data-based, or system identification (SI), hydrodynamic modelling for OWC WECs. Data-based modelling techniques represent an alternative strategy to provide the OWC hydrodynamic model, compared to the physics-based modelling approach detailed in Section 3.1. In the current study, some experimental data gathered at the narrow tank, or wave flume, of Dundalk Institute of Technology (DkIT) are used to provide some frequency-domain, linear time-domain, and nonlinear time-domain SI hydrodynamic models for a scaled OWC chamber. In the literature, OWC hydrodynamic modelling has already been the subject of a number of studies [192, 184, 196, 197], which typically adopt either linear BEM models or a CFD-based approach. However, linear BEM models may be not ideal for OWC hydrodynamic modelling [198], while CFD may be too complicated

for many practical purposes, such as real-time control. The SI models presented in this chapter, which are naturally validated against data gathered from the real system, offer the possibility of obtaining linear hydrodynamic models without making the assumption of small motion around the equilibrium point (Section 4.2.3.1) and, additionally, capturing nonlinear effects with fast computation (Section 4.2.3.2).

The reminder of this chapter is organised as follows. In Section 4.1, the motivation for considering SI hydrodynamic modelling for OWCs is further explained and an introduction to data-based modelling, with a focus on WEC SI modelling, is provided. Section 4.2 details the SI hydrodynamic modelling approach devised for the DkIT OWC. More specifically, frequency-domain and time-domain SI modelling are discussed in Sections 4.2.2 and 4.2.3, respectively. Finally, some concluding remarks are given in Section 4.3.

4.1 Motivation and background

As already mentioned in Chapter 1, in addition to high CapEx and OpEx, the commercial viability of OWCs is also currently hindered by the lack of efficient control strategies. To this end, it is imperative to note that the control problem is intrinsically characterized by modelling-related assumptions and requirements [199]. In addition to model determination from first principles, SI techniques [200] represent an alternative strategy to provide linear, and nonlinear, WEC models [201]. On one side, the relative simplicity of linear SI models including, but not limited to, their suitability as a platform for model-based control, is appealing. On the other side, nonlinear SI models can be more accurate and have, depending on the data space on which the model is determined, broader validity. Another key advantage of linear data-based WEC models is that, if suitable input data are employed to identify the model, they are potentially more representative of a wider operational range [202] than those derived from first principles using LWT, which assumes small displacements around an equilibrium point (typically the SWL).

4.1.1 Introduction to system identification

The term ‘system identification’ was arguably coined by Lotfi A. Zadeh, in 1956, in a paper in which the identification problem for a type of nonlinear transducer, used in signal transmission and communication engineering, was addressed [203].

System identification is a data-based modelling procedure in which the parameters of the model are identified from input/output data by minimizing a cost function, usually related to the model fidelity. Depending on the specific parameterisation, SI

models can be linear or nonlinear [204]. Furthermore, SI parametric models can be exclusively based on data (black-box SI models), or else can incorporate, up to a customisable extent, some physics-based information (grey-box SI models) [205]. In either case, a suitable model structure, and a criterion of fitting (CoF), which is required in order to evaluate the performance of the model, have to be selected [200]. The model parameters are then identified by feeding a numerical optimisation algorithm with training, or identification, data. Finally, the identified model is validated against a separate set of validation data, meaning that the capacity of the model to predict the behaviour of the system, while working with a different data set, is assessed. It should be noted that the identification/validation data sets can be either time-domain data sets, used for time-domain identification techniques, or frequency-domain data sets, employed in frequency-domain SI approaches. A generic SI modelling procedure is schematically summarized by the loop shown in Figure 4.1.

It is important to keep in mind that the validation data must be different from those used for the identification, but must also belong to the same operational space of the identification data. Additionally, the choice of a suitable input signal is essential for the parametric model to be representative over the desired range of operating conditions. More specifically, the range of amplitudes, and frequencies, of the input signals employed in the identification phase should correspond to the range of (equivalent) amplitudes, and frequencies, over which model validity is required [201].

4.1.2 Data-based modelling in wave energy

Although the use of SI in wave energy is relatively recent [206], a significant number of papers concerning WEC data-based modelling, primarily for HPA WECs [206], has rapidly emerged over the last ten years [202, 201, 204, 207, 208, 209, 210, 211].

In two joint publications [201, 204], a wave-to-position model and a force-to-position model (with the force being the PTO force) for a HPA WEC are identified using three discrete time parametric structures. The identification/validation data are generated from numerical wave tank (NWT) experiments, which are built with open source CFD software. Two of the three model structures, namely the autoregressive (AR) with exogenous input (ARX) and the nonlinear Kolmogorov-Gabor polynomial (KGP) models, are linear in the parameters, while the multi-layer perceptron artificial neural network (ANN), is nonlinear in the parameters, meaning that the identification of the optimal parameters is more challenging. In [208], the hydrodynamic model of a HPA WEC is identified using a linear black-box model and a nonlinear Hammerstein-Wiener model. In contrast with [201, 204], the input/output data used in [208] are gathered from real wave tank (RWT) experiments. In a relatively recent paper [210],

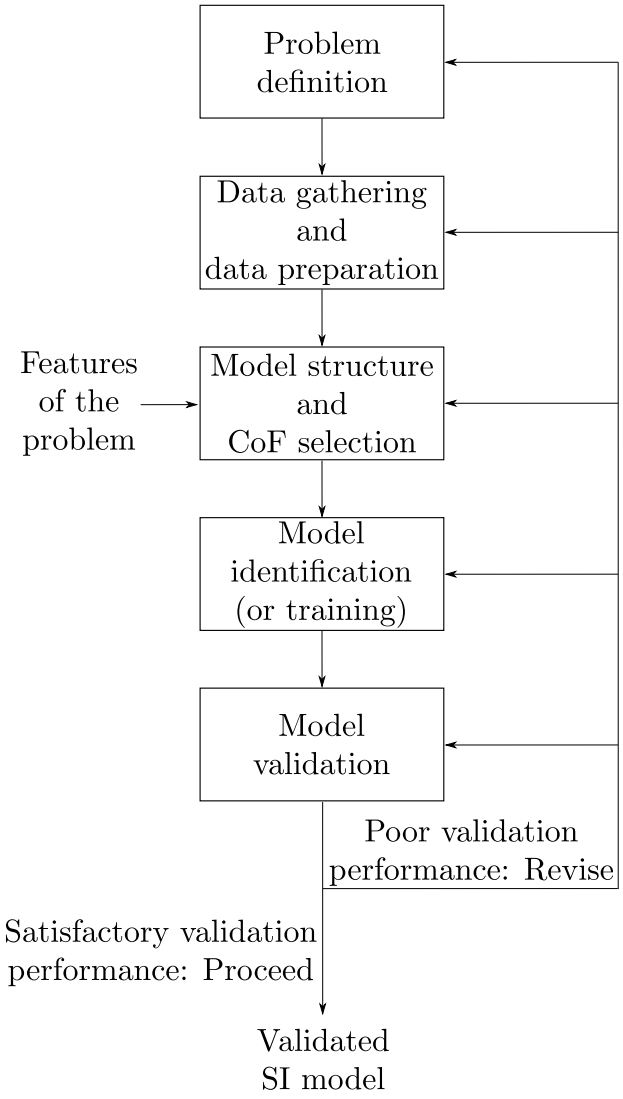

Figure 4.1: Schematic representation of the SI loop. Figure adapted from [200].

a linear force-to-position model, where force is the PTO force, for a three-body hinged-barge WEC is identified using real wave tank (RWT) data. Parametric model identification is carried out using frequency-domain and time-domain SI techniques.

In [58, 59] (which is the work presented in Section 4.2), some linear and nonlinear, black-box, wave-to-position models of a scaled OWC device, experimentally tested in regular and irregular waves, are identified. Furthermore, a wave-to-pressure grey-box SI model for a vented OWC is identified in [212]. The identification procedure developed in [212] combines a linear black-box ARX model with a simple physics-inspired function, the objective of which is to incorporate the nonlinear behaviour of the air venting system (i.e., a one-way bypass valve).

Finally, in [213], a thermodynamic SI model of an OWC chamber is identified. However, the identification procedure proposed in [213] has two issues. First, since the model input (i.e., the position of the water column) depends on the control action,

such a thermodynamic model is difficult to use for control. Secondly, the input/output data used in the identification/validation phases are not generated through high fidelity numerical simulation, nor through some physical experiments, but from a relatively low-fidelity air chamber model derived from first principles. To this end, one should note that a SI model is, at most, only as good as the data used in the model training phase and, therefore, low-fidelity models should be never used to generate input/output signals for data-based modelling.

A comprehensive review on WEC data-based modelling and data-driven control is found in [206].

4.2 Black-box hydrodynamic modelling for OWCs

In this section, linear and nonlinear black-box hydrodynamic models for a scaled fixed OWC device are identified, using frequency-domain and time-domain SI techniques. The identified models, schematically depicted in Figure 4.2, are both wave-to-position models. In particular, the model input, $u(t)$, is the free surface elevation, namely the water elevation associated with an undisturbed (by the presence of a device) wave, while the output of the model, $y(t)$, is the vertical position of the water column measured at its centroid. Ultimately, the wave-to-position model of Figure 4.2 is a mapping between FSE and the displacement of the water column. To derive the SI models, the time traces of the FSE, $u(t) = \eta(t)$, and the water column displacement, $y(t) = z(t)$, are gathered during some RWT experiments, in which the scaled fixed OWC model is tested in regular and irregular waves. The data sets obtained with regular waves are employed to derived frequency-domain models (further detailed in Section 4.2.2), while the input/output time traces recorded during the irregular wave experiments are used to identify separate linear, and nonlinear, time-domain models (further explained in Section 4.2.3).

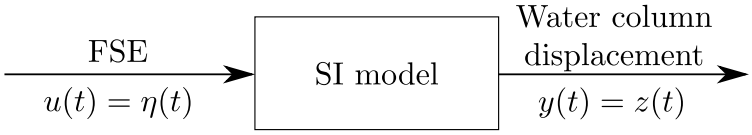

Figure 4.2: Schematic representation of the input/output model considered in this work.

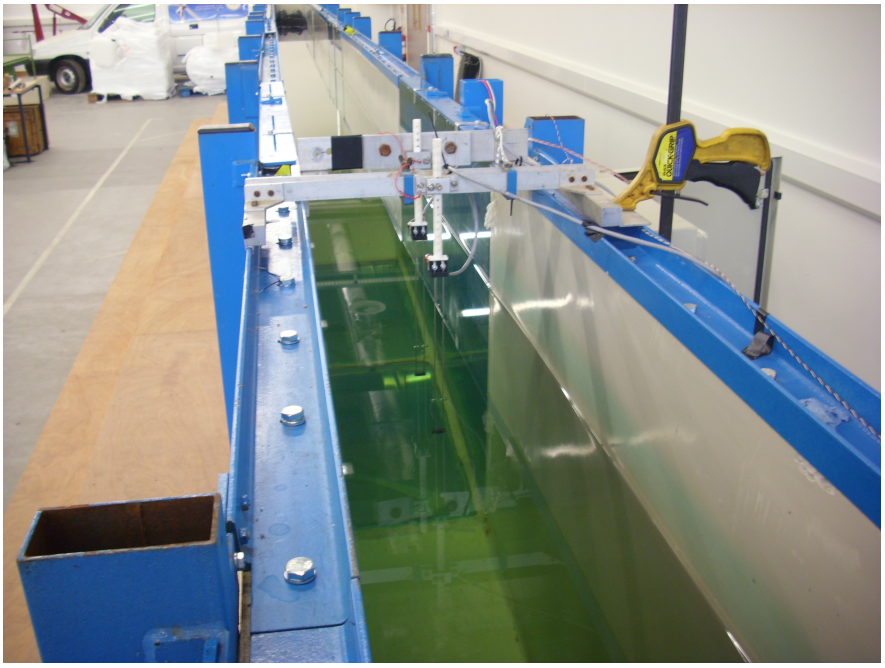

Figure 4.3: Picture of the narrow tank at DkIT. Source: [58].

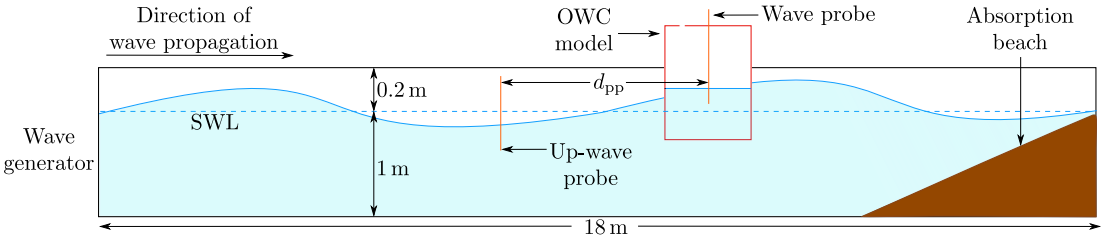

Figure 4.4: Schematic representation of the narrow tank and scaled OWC chamber at DkIT.

4.2.1 Experimental campaign

4.2.1.1 Experimental setup

Figure 4.3 shows the (two-dimensional) narrow wave tank, or wave flume, at DkIT, which is used to gather the RWT experimental data. The wave flume, schematically shown in Figure 4.4, is equipped, on one side, with a flap-type wave generator and, on the other side, with an absorption beach for minimising wave reflections from the beach towards the OWC model. The DkIT tank is 18 m long, 350 mm wide, 1 m deep, and has a freeboard of 0.2 m. The probe-to-probe distance, d_{pp} in Figure 4.4, is approximately 3 m, though the spacing is was not precisely recorded. During an experimental run, the displacement of the water column, $y(t)$, is recorded using a wave probe, positioned at the water column centroid. To record $\eta(t)$, at the same location where $y(t)$ is measured, the experiment has to be identically repeated in the absence of the OWC chamber in the wave flume. Particular care has been taken to ensure that $\eta(t)$ and $y(t)$ are measured at the same location.

The 1:5 scaled fixed OWC chamber is made from marine plywood and scaled in accordance with Froude scaling [105], to preserve the main hydrodynamic effects. The OWC chamber is 288 mm wide and is equipped with an iris valve, which simulates the damping effect of a turbine on the water column. The iris-type valve is mounted at the top of the pneumatic chamber, and the diameter of its pupil is set at 30 mm. A more detailed description of the DkIT narrow tank and the scaled OWC model can be found in [105].

It should be noted that the air spring effect due to air compressibility [72] does not scale correctly if the air volume is scaled by the cube of the scaling factor. Indeed, if the pneumatic chamber is small, the air compressibility effects are essentially negligible. It can be shown that it is not an easy task to correctly scale both hydrodynamic effects and aerodynamic effects simultaneously. To this end, the Froude number and the Reynolds number are introduced, respectively, [105] as[1]

$$\mathrm{Fr} = \sqrt{\frac{f_\mathrm{i}}{f_\mathrm{g}}} = \omega\sqrt{\frac{L}{g}}, \tag{4.1}$$

and

$$\mathrm{Re} = \frac{f_\mathrm{i}}{f_\mathrm{v}} = \frac{\rho\omega L^2}{\mu}, \tag{4.2}$$

where f_i indicates the inertia forces, f_g are the gravity forces, f_v represents the viscosity forces, L is a characteristic length of the system, ω is the characteristic frequency of the flow, while ρ and μ are, respectively, the density and dynamic viscosity of the considered fluid. If a system is geometrically scaled with respect to a second system by a factor α, such that $L_1 = \alpha L_2$, to preserve the Froude number between the two systems, the following relation must hold

$$\omega_1\sqrt{\frac{L_1}{g_1}} = \omega_1\sqrt{\frac{\alpha L_2}{g_1}} = \omega_2\sqrt{\frac{L_2}{g_2}}, \tag{4.3}$$

hence

$$\frac{\omega_1}{\omega_2} = \sqrt{\alpha\frac{g_1}{g_2}}. \tag{4.4}$$

Similarly, to preserve the Reynolds number:

$$\alpha^2 = \frac{\rho_1\omega_1\mu_2}{\rho_2\omega_2\mu_1}. \tag{4.5}$$

To preserve both Fr and Re, Equations (4.4) and (4.5) must be true, therefore:

$$\alpha^{1.5} = \frac{\rho_1\mu_2}{\rho_2\mu_1}\sqrt{\frac{g_1}{g_2}} = \frac{\rho_1\mu_2}{\rho_2\mu_1}. \tag{4.6}$$

[1] Note that $f_\mathrm{i} \propto \rho u^2L^2 \propto \rho\omega^2L^4$, $f_\mathrm{g} \propto \rho g L^3$, and $f_\mathrm{v} \propto \mu u L \propto \mu\omega L^2$.

From Equation (4.6), it is clear that the only way to preserve both Fr and Re (assuming that $g_1 = g_2$), if $\alpha \neq 1$, is to use a different fluid in the two systems. Since the full-scale system (i.e., the OWC WEC) works in water, the second fluid should be designed to satisfy Equation (4.6).

4.2.1.2 Data gathering

For the experimental campaign, the National Instruments LabVIEW software [214] is used to sample and record $y(t)$ and $\eta(t)$.

Regular waves The experiments in regular waves were conducted as part of previous work [105], in which the OWC chamber has been tested under different regular wave trains of the form:

$$\eta(t) = A_{\mathrm{w}} \cos(2\pi f_{\mathrm{w}} t + \phi), \tag{4.7}$$

where A_{w} is the wave amplitude, ϕ is the (random) phase of the wave, and f_{w} the wave frequency in Hertz. During the experimental campaign, sixty different regular wave sequences, obtain by combining six amplitudes and ten frequencies, are tested. The frequencies range from 0.4 to 1.3 Hz, with increments of 0.1 Hz, while the range of amplitudes spans from 5 to 30 mm, with increments of 5 mm. Each experiment runs until steady-state conditions are reached, then $y(k)$ is recorded for ninety seconds with a sampling frequency, f_{s}, of 32 Hz. It should be noted that, in the regular wave case, the time traces of the FSE were not recorded. Although knowledge of the empirical input data is incomplete, since A_{w} and f_{w} of the tested regular waves are known, a data-based modelling procedure for the regular wave case can be established.

Irregular waves The input/output data gathered during the irregular wave experiments comprise three data sets [215]. In particular, the OWC model is tested under three SSs, generated from different Bretschneider SDFs, $S_i^{\mathrm{B}}(f)$, shown in Figure 4.5. The wave maker utilises an inbuilt function to generate a wave time series, whose spectrum matches the target Bretschneider spectrum, expressed as

$$S_i^{\mathrm{B}}(f) = \frac{5}{16} H_{\mathrm{s}}^2 \frac{f_{\mathrm{w}}^{-5}}{T_{\mathrm{e}}^4} e^{-\frac{5}{4}(T_{\mathrm{e}} f_{\mathrm{w}})^{-4}}, \quad i = 1, 2, 3. \tag{4.8}$$

Table 4.1 reports T_{e} and H_{s} for the three Bretschneider SDFs considered in this thesis. For each irregular wave spectrum, $y(k)$ is recorded for thirty minutes with $f_{\mathrm{s}} = 128$ Hz. In relation to the frequency bands of the three Bretschneider SDFs,

f_s considerably exceeds the minimum sampling frequency required by the Nyquist-Shannon sampling theorem [216]. To record $\eta(k)$ at the OWC chamber location, the chamber is removed from the wave tank and the experiments are identically repeated. For clarity, the input/output data sets gathered during the experiments with $S_1^B(f)$, $S_2^B(f)$, and $S_3^B(f)$ are called D_1^B, D_2^B, and D_3^B, respectively. It should be noted that each spectrum covers a different range of frequencies, and amplitudes, over which the OWC chamber is tested. To this end, $S_3^B(f)$ is the most significant SDF, since the frequencies of the incident waves lie within the resonant band of the OWC heaving mode, that is the frequency band in which the uncontrolled device is designed to optimally capture wave energy [217, 158]. However, it is also worth considering the OWC behaviour over the frequency bands covered by $S_2^B(f)$ and $S_3^B(f)$, since a control strategy may increase the range of frequencies at which the device can operate [218]. For instance, rotational speed control strategies may affect the wave-to-pneumatic energy absorption process of the OWC [56].

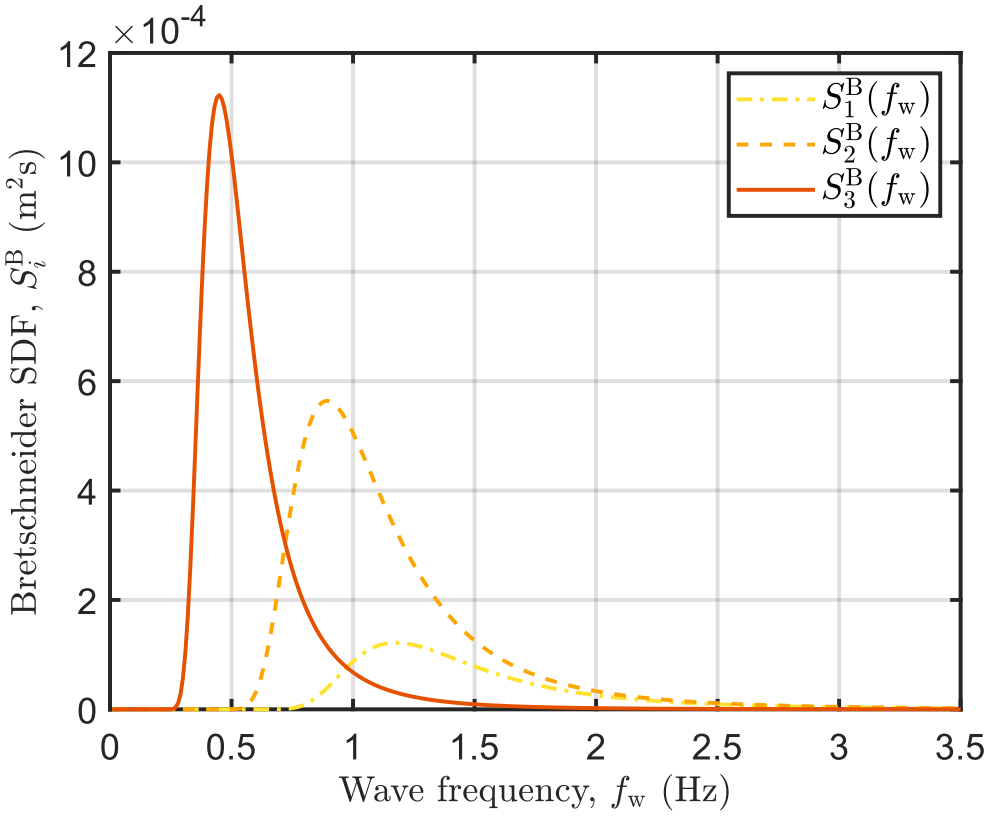

Figure 4.5: Bretschneider SDFs used in the irregular wave experiments.

4.2.1.3 Data preparation for SI

The 'raw' experimental data must be prepared before they can be employed in SI. Such a preprocessing procedure may involve several different steps, depending

Table 4.1: Bretschneider spectra.

S_i^{B}	T_{e} (s)	H_{s} (mm)
S_1^{B}	0.85	40
S_2^{B}	1.12	75
S_3^{B}	2.23	75

on the nature of the data (numerical or experimental), the type of SI techniques (frequency-domain or time-domain), and other factors (e.g., quality of the probes, data acquisition systems, etc). For this work, four preprocessing steps are needed: (i) The probe offsets are removed; (ii) the experimental data are filtered to reduce noise introduced by the acquisition sensors. ; (iii) input and output time traces are temporally aligned; (iv) since only a portion of the signal time traces can be employed for SI, suitable record lengths are extracted from each data set.

To characterise the filter, the noise frequency content is computed by applying a fast Fourier transform to the available noise data from the probes, collected during the experimental campaign. In relation to step (iii), the acquisition system and the wave maker are entirely isolated from each other, therefore the generation of incident waves and the wave data acquisition do not begin at the same moment. As such, the time traces of the output, $z(t)$, needs to be temporarily aligned with those of the input, $\eta(t)$. To this end, during the two experiments, the FSE measurements gathered from the up-wave probe, shown in Figure 4.4, are cross-correlated to estimate the time delay. Furthermore, the tank repeatability, i.e., the capability of the tank to reproduce a pseudo-random wave elevation time series, has already been assessed in previous work [184].

Regarding step (iv), the usable interval of each time trace starts from the moment in which steady state conditions are achieved to the moment when reflected waves (from the absorption beach) hit the OWC chamber.

4.2.2 Frequency-domain data-based modelling

For the regular wave case, a frequency-domain identification method is developed to derive some parametric models of the transfer function (TF) of the OWC chamber. Parametric SI generally offers a variety of modelling approaches in the frequency-domain [200], which typically requires full knowledge of the empirical frequency response function (FRF), namely the amplitude and phase responses of the empirical transfer function, $H(j\omega)$. In essence, once a suitable parametric TF model structure and CoF are chosen, the model parameters are optimized on the basis of the CoF.

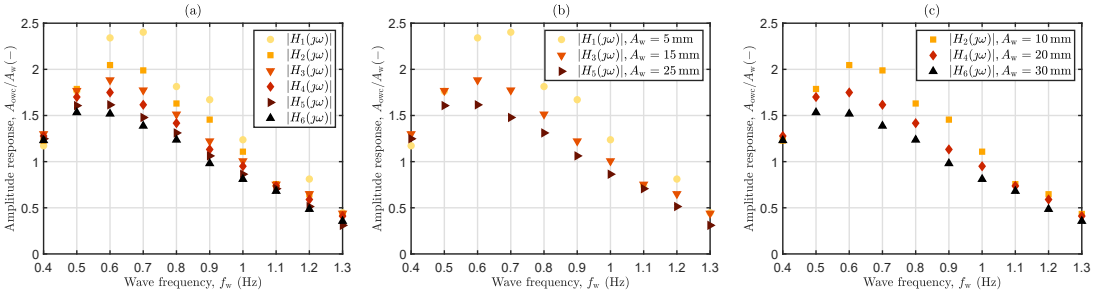

Figure 4.6: Empirical amplitude response, $|H_i(j\omega)|$. For clarity, the data are divided as follows: (a) $i = 1, \ldots 6$; (b) i = 1, 3, 5; (c) i = 2, 4, 6.

However, since the FSE time traces are missing, and the empirical FRF is consequently partially unknown, the SI procedure adopted in this work is somewhat unusual. Due to the fact that the identification is carried out for regular waves (whose A_w and f_w values are known), although the knowledge of the input signals is incomplete, it is still possible to compute the empirical amplitude response, i.e., $|H(j\omega)|$. To this end, it should be noted that $y(t)$, namely the displacement of the water column recorded during the experiments, is a sinusoid, whose frequency is equal to the frequency of $\eta(t)$. Therefore, in the regular wave case, and for the specific model sought here, the input/output signals are sinusoids with the same frequency but possibly different amplitude and phase. As such, $|H(j\omega)|$ is simply computed as the ratio $A_\mathrm{owc}/A_\mathrm{w}$, where A_owc is the amplitude of the (sinusoidal) output signal. Figure 4.6 shows the empirical amplitude responses of the sixty input/output couples. As clarified by Figure 4.6, the sixty amplitude responses are equally spilt, according to the input amplitude, into six distinct sets of ten data points each, $|H_i(j\omega)|$ with $i = 1, \ldots 6$. It should be noted that, in comparison to the other cases, $|H_1(j\omega)|$ has a more irregular trend. Such an unrealistic behaviour of the system dynamics is arguably due to the poor signal-to-noise ratio (S/N) characterizing the input/output data when A_w = 5 mm. As a consequence, when the input amplitude is relatively small, the empirical measurements are noisy and not fully trustworthy.

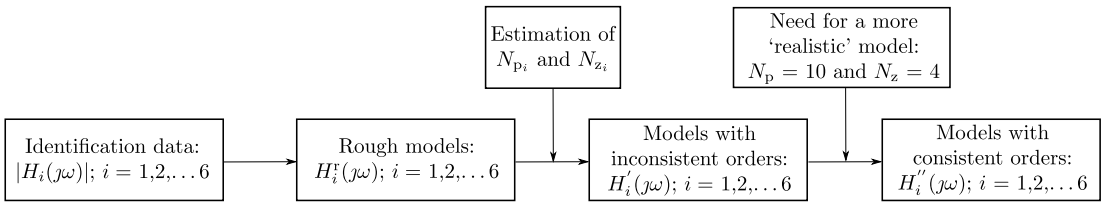

Figure 4.7: Schematic of the frequency-domain SI procedure for the regular wave case.

In the remainder of Section 4.2.2, the frequency-domain SI modelling procedure described schematically in Figure 4.7 is applied. Such a SI approach aims to identify

a family of TF models with consistent orders, by relying solely on $|H_i(j\omega)|$ as the identification data. To asses the performance of the models, the normalized root mean squared error (NRMSE), specified, for the regular wave case, as

$$\mathrm{NRMSE}_i = \sqrt{\sum_k \frac{||H_i(j\omega_k)| - |H_i^{\mathrm{m}}(j\omega_k)||^2}{\sum_k |H_i(j\omega_k) - \bar{H}|^2}}, \tag{4.9}$$

where $\bar{H}$ is the mean value of the identification data, is chosen as the error metric. In contrast with other possible metrics, the NRMSE is normalised with respect to the magnitude of the empirical data (unlike the mean squared error) and, moreover, does not provide a distorted picture of the error for values close to zero (which is important for the irregular wave case). In Equation (4.9), $|H^{\mathrm{m}}(j\omega_k)|$ is the amplitude response of a TF parametric model, calculated for the k-th tested regular wave frequency.

4.2.2.1 Initial (rough) models

For the initial step of the identification strategy, a family of TF (initial) models, expressed as

$$H_i^{\mathrm{r}}(j\omega) = g_i \frac{(z_i + j\omega)^{N_{\mathrm{z}_i}}}{(p_i + j\omega)^{N_{\mathrm{p}_i}}}, \tag{4.10}$$

is chosen. In Equation (4.10), g_i, p_i, z_i, N_{p_i}, and N_{z_i} are, respectively, the gains, poles, zeros, number of poles, and number of zeros of the parametric TF model. It should be noted that g_i, p_i, z_i, N_{p_i}, and N_{z_i} are all free parameters which are optimized by solving six separate data-fitting problems (one for each set of identification data, i.e., $|H_i(j\omega)|$), in the least-squares (LS) sense. The sole purpose of the TF models in Equation (4.10) is to roughly estimate the optimal values of N_{p_i} and N_{z_i}, which are reported in Table 4.2.

Table 4.2: Estimation of N_{z_i} and N_{p_i}.

$H_i^{\mathrm{r}}(j\omega)$	A_{w} (mm)	N_{z_i}	N_{p_i}
H_1^{r}	5	7	14
H_2^{r}	10	5	12
H_3^{r}	15	5	10
H_4^{r}	20	4	9
H_5^{r}	25	3	10
H_6^{r}	30	3	9

4.2.2.2 Models with inconsistent orders

In the second step of the identification procedure, the optimal values of N_{z_i} and N_{p_i} are used to define a second family of TF models, $H_i^{'}(\jmath\omega)$, of the form:

$$H_i^{'}(\jmath\omega) = g_i \frac{\prod_{n=1}^{N_{z_i}} (z_{i,n} + b_{i,n}\,\jmath\omega)}{\prod_{m=1}^{N_{p_i}} (p_{i,m} + d_{i,m}\,\jmath\omega)}. \tag{4.11}$$

In Equation (4.11), $z_{i,n}$ and $p_{i,m}$ are respectively the n-th zero and m-th pole of the i-th TF model. Furthermore, $b_{i,n}$ and $d_{i,m}$ are additional free parameters of $H_i^{'}(\jmath\omega)$. To optimize the free parameters of $H_i^{'}(\jmath\omega)$, six separate LS optimization problems are solved and, therefore, six distinct TF models are identified. The solution of a linear least square optimisation problem is presented in Section 4.2.3.1.

4.2.2.3 Models with consistent orders

Since the training data are collected from the same OWC chamber, there is no specific *a-priori* reason why the TF model orders should vary. As such, the final step of the SI procedure aims to find a family of TF models with consistent orders. To equalize the TF orders, the numbers of poles and zeros must be fixed. To this end, suitable values for N_z and N_p are chosen as follows:

$$N_z = \frac{\sum_{i=2}^{5} N_{z_i}}{5} = 4, \quad N_p = \frac{\sum_{i=2}^{5} N_{p_i}}{5} = 10. \tag{4.12}$$

From Table VI, one can note that the values of N_{z_i} and N_{p_i} do not significantly vary, with the only exceptions being N_{z_1} = 7 and N_{p_1} = 14. Such an anomalous result is arguably due to the poor S/N of the empirical measurements, rather than to the real behaviour of the system. Therefore, since N_{z_1} and N_{p_1} are not entirely trustworthy, they are not considered in Equation (4.12). Ultimately, the family of TF models with consistent orders, $H_i^{''}(\jmath\omega)$, is trivially obtained by rearranging Equation (4.11), as

$$H_i^{''}(\jmath\omega) = g_i \frac{\prod_{n=1}^{N_z} (z_{i,n} + b_{i,n}\,\jmath\omega)}{\prod_{m=1}^{N_p} (p_{i,m} + d_{i,m}\,\jmath\omega)}, \tag{4.13}$$

where $N_z = 4$ and $N_p = 10$. As for $H_i^r(\jmath\omega)$ and $H_i^{'}(\jmath\omega)$, the unknown parameters of $H_i^{''}(\jmath\omega)$ are identified by solving six LS optimization problems.

4.2.2.4 Result and discussion

To assess the performance of the TF models, the amplitude response of the models with consistent ($|H_i''(\jmath\omega)|$), and inconsistent ($|H_i'(\jmath\omega)|$), orders are compared against the empirical data ($|H_i(\jmath\omega)|$). Table VII reports the model fidelity, computed as

$$\text{Fidelity} = 100(1 - \text{NRMSE}), \tag{4.14}$$

for $|H_i''(\jmath\omega)|$ and $|H_i'(\jmath\omega)|$ with respect to the identification data (ID). Although, as expected, $H_i'(\jmath\omega)$ performs lightly better than the corresponding $H_i''(\jmath\omega)$, the fidelity of the two families of TF models is comparable, for all the relevant cases. Unsurprisingly, since N_{z_1} and N_{p_1} are not taken into account in Equation (4.12), the fidelity of $\hat{H}_1''(\jmath\omega)$ is significantly lower than that of $\hat{H}_1'(\jmath\omega)$. However, for the reasons already explained in Section 4.2.2.3, the empirical data $|H_1(\jmath\omega)|$ and the corresponding models are not trustworthy.

Table 4.3: Fidelity of $\hat{H}_i'(\jmath\omega)$ and $\hat{H}_i''(\jmath\omega)$.

ID	A_w (mm)	$H_i'(\jmath\omega)$	$H_i''(\jmath\omega)$
$\|H_1(\jmath\omega)\|$	5	96.38	87.39
$\|H_2(\jmath\omega)\|$	10	99.35	97.95
$\|H_3(\jmath\omega)\|$	15	99.84	99.74
$\|H_4(\jmath\omega)\|$	20	99.82	99.80
$\|H_5(\jmath\omega)\|$	25	99.47	99.46
$\|H_6(\jmath\omega)\|$	30	99.68	99.68

Figures 4.8 and 4.9 compares the empirical amplitude responses to the parametric amplitude responses of $H_i'(\jmath\omega)$ and $H_i''(\jmath\omega)$, respectively. As anticipated by the results in Table 4.3, it is difficult to appreciate any difference between $|H_i'(\jmath\omega)|$ and $|\hat{H}_i''(\jmath\omega)|$ (except for $i = 1$).

4.2.3 Time-domain data-based modelling

In this Section, some linear and nonlinear time-domain SI models, of the type in Figure 4.2, are derived using irregular wave experimental data. The identification procedures followed in the linear SI and nonlinear SI cases are schematically shown in Figures 4.10 and 4.13, respectively.

The work of this section particularly focuses on assessing the value of a global nonlinear SI modelling approach over a multi-linear SI modelling solution for OWCs. Despite the fact that linear models might sound more attractive than nonlinear models, the multi-linear modelling strategy designed here has some significant caveats,

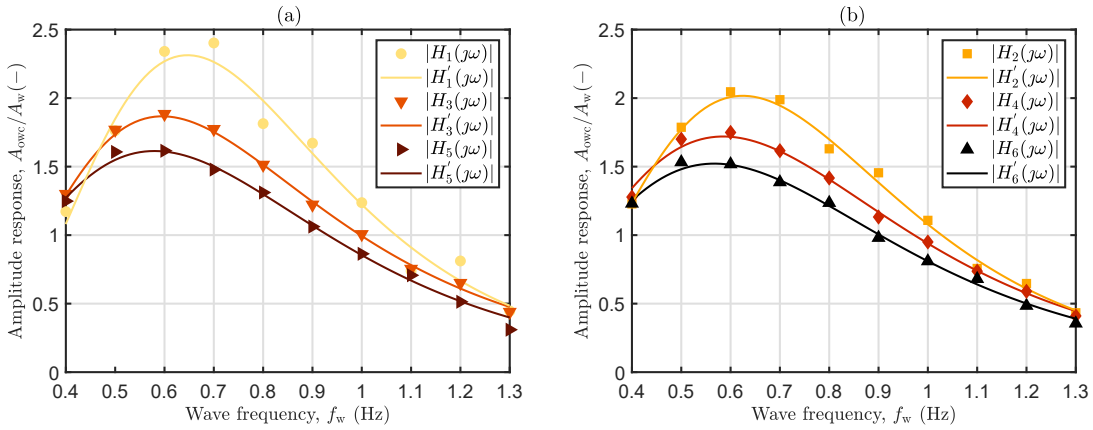

Figure 4.8: Empirical amplitude response, $|H_i(j\omega)|$, compared to the amplitude response of the models with inconsistent orders, $|H_i^{'}(j\omega)|$. For clarity, the results are divided as follows: (a) i = 1, 3, 5; (b) i = 2, 4, 6.

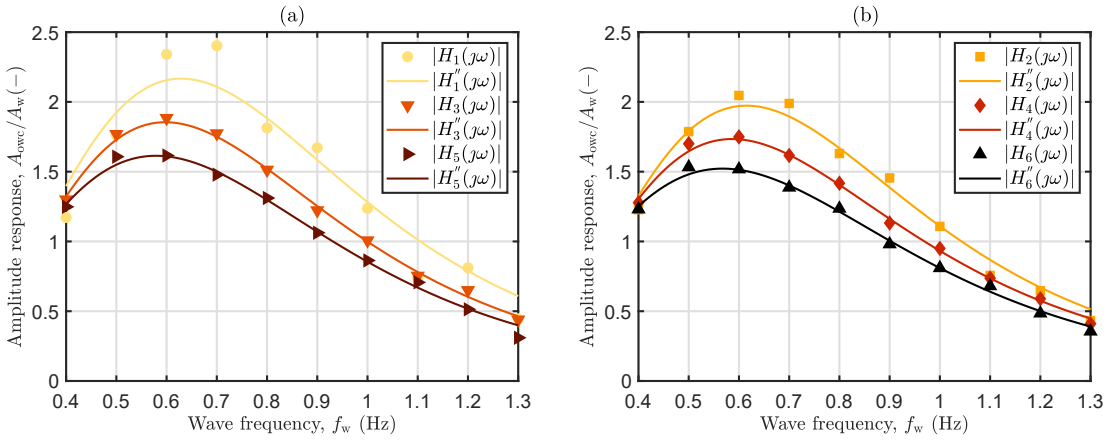

Figure 4.9: Empirical amplitude response, $|H_i(j\omega)|$, compared to the amplitude response of the models with consistent orders, $|H_i^{''}(j\omega)|$. For clarity, the results are divided as follows: (a) i = 1, 3, 5; (b) i = 2, 4, 6.

which are specifically related to real-time implementation aspects. Therefore, to provide a more complete and fair comparison, some practical issues concerning real-time implementation of multi-linear and nonlinear SI models are discussed in Section 4.2.3.3.

4.2.3.1 Linear SI model

All linear SI model structures found in the literature can be derived from the following general form [200]

$$A_{si}(q^-)y_{si}(t) = \frac{B_{si}(q^-)}{F_{si}(q^-)}u_{si}(t) + \frac{C_{si}(q^-)}{D_{si}(q^-)}e_{si}(t), \tag{4.15}$$

where A_{si}, B_{si}, C_{si} , D_{si}, and F_{si} are five polynomial functions containing the unknown parameters that need to be identified, y_{si} is the output signal, u_{si} is the input signal,

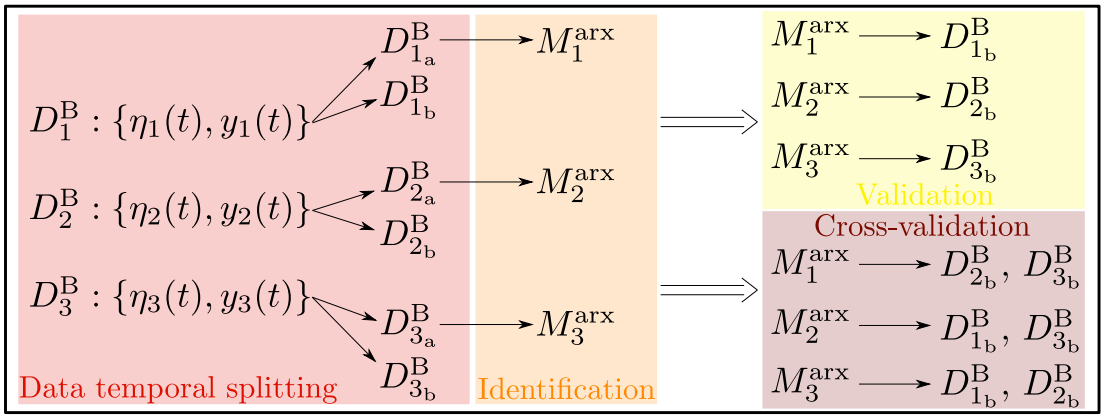

Figure 4.10: Schematic of the linear time-domain SI procedure carried out for the irregular wave case.

e_{si} is a disturbance term, and q^- is the backward shift operator[2]. Depending on which of the five polynomials are used, thirty-two different model structures can be defined. For instance, four of the most common structures are reported in Table 4.4. Since this work focuses on modelling the input/output dynamics, rather than describing the properties of the disturbance term, a linear polynomial ARX model is chosen. In comparison with more sophisticated models, such as the autoregressive moving-average with exogenous input (ARMAX) and Box-Jankins (BJ) models, the main drawback of the ARX model is the lack of flexibility in modelling the disturbance term, which is, however, not of interest to this specific work, since the disturbance is essentially the white noise signal from the probes.

Table 4.4: Possible linear SI model structures.

Model structure	Used polynomials
AR	A_{si}
ARX	A_{si}, B_{si}
ARMAX	A_{si}, B_{si}, C_{si}
BJ	B_{si}, C_{si}, D_{si}, F_{si}

ARX model definition The polynomial $A_{\mathrm{si}}(q^-)$ and $B_{\mathrm{si}}(q^-)$ are specified [200] as

$$A_{\mathrm{si}}(q^-) = 1 + a_1 q^{-1} + a_2 q^{-2} + \ldots a_{n_\mathrm{a}} q^{-n_\mathrm{a}}, \tag{4.16a}$$

$$B_{\mathrm{si}}(q^-) = b_1 q^{-1} + b_2 q^{-2} + \ldots b_{n_\mathrm{b}} q^{-n_\mathrm{b}}. \tag{4.16b}$$

[2]For instance: $q^{-1}y(t) = y(t-1)$ and, similarly, $q^{-4}u(t) = u(t-4)$.

Using Equation (4.16), the ARX model, whose unknown parameters are a_i and b_i, can be expressed in the so-called predictor form [200], as

$$y_{\mathrm{arx}}(k) = \underbrace{-\sum_{i=1}^{n_{\mathrm{a}}} a_i y(k-i)}_{\text{Autoregressive term}} + \underbrace{\sum_{i=0}^{n_{\mathrm{b}}} b_i u(k-n_{\mathrm{d}}-i)}_{\text{Exogenous input term}}. \tag{4.17}$$

In Equation (4.17), $y_{\mathrm{arx}}(k)$ is the k-th predicted model output, $y(k)$ and $u(k)$ are, respectively, the k-th samples of the output and input, while n_{a} and n_{b} are the orders of the ARX model, with n_{d} the input delay. The number of unknown parameters in the ARX model of Equation (4.17) is computed as, $N_{\mathrm{arx}} = n_{\mathrm{a}} + n_{\mathrm{b}} + 1$. Similarly to the regular wave case, to identify and validate the ARX models, the NRMSE, defined as [219]

$$\mathrm{NRMSE} = \sqrt{\frac{\sum_k |y(k) - y_{\mathrm{arx}}(k)|^2}{\sum_k |y(k) - \bar{y}|^2}}, \tag{4.18}$$

is chosen as the error metric. It should be noted that, if the NRMSE is greater than 1, it means that the identified model is no better at fitting the empirical data than a straight line equal to the mean of the data [219]. In order to determine n_{a}, n_{b}, and n_{d}, a sequence of systematic model identification trials, with incremental changes in n_{a}, n_{b}, and n_{d}, has been implemented. After each trial, the NRMSE is used to evaluate the performance of the model. Since the identification NRMSE cannot be considered as a reliable estimator of the model performance, n_{a}, n_{b}, and n_{d} should be always chosen on the basis of the validation NRMSE [200]. As an illustrative case, Figure 4.11 shows the training/validation NRMSE computed for different combinations of n_{a} and n_{b} (at fixed n_{d}) and, moreover, a focus on the case in which $n_{\mathrm{b}} = 2$. Ultimately, the leading model order is n_{a}, while, in this application, only minor variations in the NRMSE are appreciated by varying n_{b} and n_{d}. As already mentioned, N_{arx} depends on the model orders and, generally, the model performance improves as N_{arx} increases. Therefore, a trade-off between model complexity and model accuracy is required. To this end, the principle of *parsimony*, in the spirit of [220], can help to set n_{a} and n_{b} such that a 'parsimonious model', which is a model whose complexity ideally matches the problem complexity, is found. For this work, $n_{\mathrm{a}} = 6$ (from Figure 4.11, only minimal improvements are obtained for $n_{\mathrm{a}} > 6$) and $n_{\mathrm{b}} = 2$ are chosen. Furthermore, as shown in Figure 4.12, the input delay is -1 since the validation NRMSE has a minimum for $n_{\mathrm{d}} = -1$. It should be noted that a negative value of n_{d} means that the ARX model is noncausal, therefore both past and future values of $u(k)$ are used to compute $y_{\mathrm{arx}}(k)$. If $n_{\mathrm{d}} > 0$, a causal ARX model is found, meaning that $y_{\mathrm{arx}}(k)$ solely depends on past values of $u(k)$. As already explained in Section 2.2.2, the negative value for n_{d} is arguably due to the noncausality of the wave excitation force (Equation (2.51)).

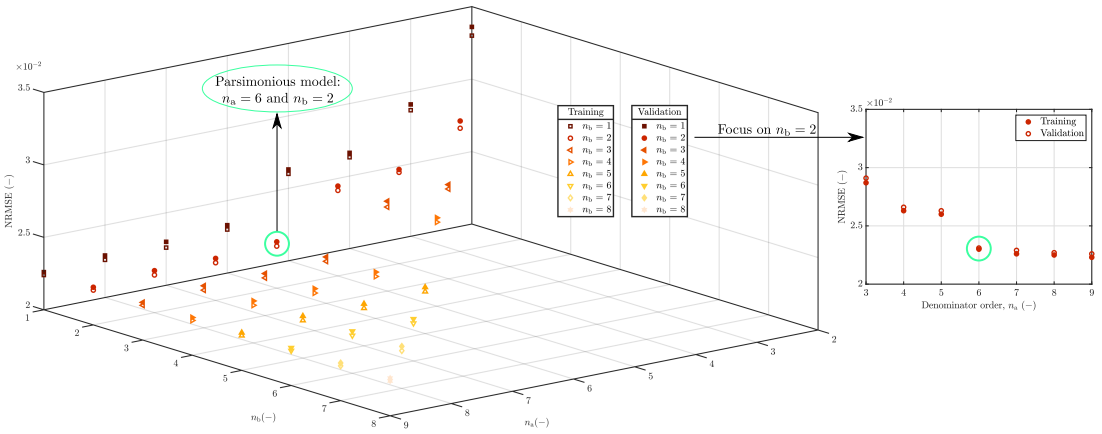

Figure 4.11: Identification and validation NRMSE values for separate ARX models, identified from $D_{3_a}^{B}$ and validated against $D_{3_b}^{B}$, using different combinations of n_a and n_b, with n_d = -1. On the right side of the figure, a focus on the case in which $n_b = 2$ is shown.

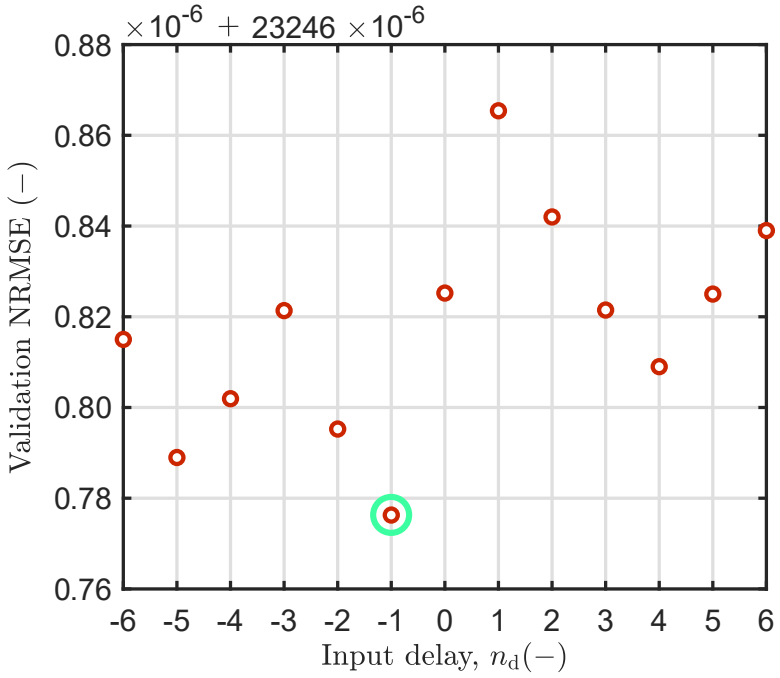

Figure 4.12: Validation NRMSE values for separate ARX models, identified from $D_{3_a}^{B}$ and validated against $D_{3_b}^{B}$, using different n_d values, with $n_a = 6$ and $n_b = 2$.

Optimisation problem formulation The unknown parameters, a_i and b_i, are found by solving a relatively simple LS optimisation problem. To this end, Equation (4.17) is rewritten in a more compact form by introducing two vectors, namely the regression vector, $\varphi_{arx}(k) \in \mathbb{R}^{N_{arx}}$:

$$\varphi_{arx}(k) = [-y(k-1) \ldots -y(k-n_a)\ u(k-n_d-1) \ldots u(k-n_d-n_b)]^{\intercal}, \tag{4.19}$$

and the parameter vector, $\theta_{arx} \in \mathbb{R}^{N_{arx}}$:

$$\theta_{arx} = [a_1\ a_2 \ldots a_{n_a-1}\ a_{n_a}\ b_0\ b_1 \ldots b_{n_b-1}\ b_{n_b}]^{\intercal}. \tag{4.20}$$

Using Equations (4.17), (4.19), and (4.20), the predicted output becomes

$$y_{\mathrm{arx}}(k) = \theta_{\mathrm{arx}}^{\intercal}\varphi_{\mathrm{arx}}(k) = \varphi_{\mathrm{arx}}(k)^{\intercal}\theta_{\mathrm{arx}}. \tag{4.21}$$

The linear regression in Equation (4.21) can be easily extended for all samples, $k = 1, 2, \ldots N_k$, as:

$$Y_{\mathrm{arx}} = \Lambda_{\mathrm{arx}}\theta_{\mathrm{arx}}, \tag{4.22}$$

where $\Lambda_{\mathrm{arx}} \in \mathbb{R}^{N_{\mathrm{k}} \times N_{\mathrm{arx}}}$ is the regression matrix and $Y_{\mathrm{arx}} = [y_{\mathrm{arx}}(1)\ y_{\mathrm{arx}}(2) \ldots y_{\mathrm{arx}}(N_k)]^{\intercal}$ $\in \mathbb{R}^{N_{\mathrm{k}}}$ is the model output vector. Finally, by introducing the empirical output vector, $Y = [y(1)\ y(2) \ldots y(N_k)]^{\intercal} \in \mathbb{R}^{N_{\mathrm{k}}}$, the prediction error vector can be defined as

$$\epsilon = Y - Y_{\mathrm{arx}} = Y - \Lambda_{\mathrm{arx}}\theta_{\mathrm{arx}}, \tag{4.23}$$

while the LS optimization problem is written as

$$\theta_{\mathrm{arx}}^{\mathrm{opt}} = \underset{\theta_{\mathrm{arx}}}{\mathrm{argmin}}(\epsilon^{\intercal}\epsilon), \tag{4.24}$$

with the well-known solution [200]:

$$\theta_{\mathrm{arx}}^{\mathrm{opt}} = (\Lambda_{\mathrm{arx}}^{\intercal}\Lambda_{\mathrm{arx}})^{-1}\Lambda_{\mathrm{arx}}^{\intercal}Y. \tag{4.25}$$

The LS problem in Equation (4.25) is not solved directly, since the relatively high condition number[3] of $\Lambda_{\mathrm{arx}}^{\intercal}\Lambda_{\mathrm{arx}}$, which is approximately the square of the condition number of Λ_{arx}, potentially makes the matrix inversion problem, $(\Lambda_{\mathrm{arx}}^{\intercal}\Lambda_{\mathrm{arx}})^{-1}$, an ill-conditioned problem. To solve Equation (4.25), a QR factorization method is used to compute the LS solution directly from Λ_{arx}, without using $\Lambda_{\mathrm{arx}}^{\intercal}\Lambda_{\mathrm{arx}}$ [200].

Identification and validation phases The identification and validation phases are carried out as schematically shown in Figure 4.10. Firstly, the input/output time traces in D_1^{B}, indicated as $\eta_1(k)$ and $y_1(k)$, are temporally split into two parts, $D_{1_{\mathrm{a}}}^{\mathrm{B}}$ and $D_{1_{\mathrm{b}}}^{\mathrm{B}}$. Similarly to D_1^{B}, the data 'splitting' procedure is also applied to D_2^{B} and D_3^{B}. Ultimately, three ARX models, named M_1^{arx}, M_2^{arx}, and M_3^{arx} are identified using the data sets $D_{1_{\mathrm{a}}}^{\mathrm{B}}$, $D_{2_{\mathrm{a}}}^{\mathrm{B}}$, and $D_{3_{\mathrm{a}}}^{\mathrm{B}}$, respectively. Subsequently, M_1^{arx}, M_2^{arx}, and M_3^{arx} are validated against their respective validation data set, namely $D_{1_{\mathrm{b}}}^{\mathrm{B}}$, $D_{2_{\mathrm{b}}}^{\mathrm{B}}$, and $D_{3_{\mathrm{b}}}^{\mathrm{B}}$. Finally, to assess the cross-validation capability of the linear SI models, M_1^{arx} is also cross-validated against $D_{2_{\mathrm{b}}}^{\mathrm{B}}$ and $D_{3_{\mathrm{b}}}^{\mathrm{B}}$. Like M_1^{arx}, the cross-validation procedure is also equivalently repeated for M_2^{arx} and M_3^{arx}.

[3]The condition number of a square matrix, A, is $\kappa_{\mathrm{c}}(A) = \|A\|\,\|A^{-1}\| \geq 1$. Considering a generic linear equation $Ax = b$, $\kappa_{\mathrm{c}}(A)$ relates the variations in the solution vector, b, to the variations in the matrix A, as $(\|\delta b\|/\|b\|) \leq \kappa_{\mathrm{c}}(A)(\|\delta A\|/\|A\|)$.

The fidelity values (Equation (4.14)) of the M_1^{arx}, M_2^{arx}, M_3^{arx}, with respect to their corresponding identification data (namely $D_{1_a}^{\text{B}}$, $D_{2_a}^{\text{B}}$, and $D_{3_a}^{\text{B}}$), are 94.09%, 96.18%, and 97.37%, respectively. It should be noted that the identification fidelity of the models broadly reflects the S/N of the identification data. As such, the experimental data D_3^{B}, which have a relatively high S/N (as suggested by the high peak of S_3^{B} in Figure 4.5), produces the ARX model with the highest fidelity value, namely M_3^{arx}. The validation and cross-validation fidelities of each ARX model are reported, respectively, in Tables 4.5 and 4.6. The model validation results are discussed in Section 4.2.3.3.

4.2.3.2 Nonlinear SI model

Typically, nonlinear models are significantly more complex than their linear counterparts [156]. However, in this work, the proposed nonlinear modelling procedure is a somewhat natural, and relatively straightforward, extension of the linear modelling approach, at least for the considered SI model structures (i.e., linear ARX and nonlinear KGP models).

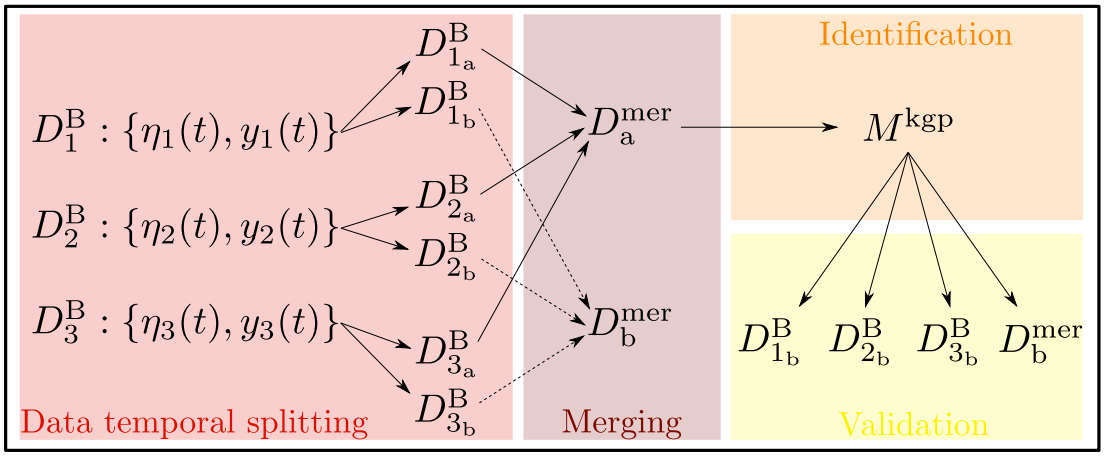

Figure 4.13: Schematic of the nonlinear time-domain SI procedure carried out for the irregular wave case.

KGP model description In general, a nonlinear KGP model, whose unknown parameters are $a_{i,j}$, $b_{i,j}$, $c_{i,j}$, $d_{i,j}$, and $e_{i,j}$, is written, in the predictor form [221], as

$$\begin{aligned} y^{\mathrm{kgp}}(k) = &\sum_{j=1}^{p}\Bigg[- \sum_{i=1}^{n_{\mathrm{a}}^{'}} a_{i,j} y^{j}(k-i) + \sum_{i=0}^{n_{\mathrm{b}}^{'}} b_{i,j} u^{j}(k-n_{\mathrm{d}}^{'}-i)\Bigg] + \\ &\sum_{\substack{i,j=1 \\ i\neq j}}^{n_{\mathrm{a}}^{'}} c_{i,j} y(k-i)y(k-j) + \sum_{\substack{i,j=0 \\ i\neq j}}^{n_{\mathrm{b}}^{'}} d_{i,j} u(k-n_{\mathrm{d}}^{'}-i)u(k-n_{\mathrm{d}}^{'}-j) + \\ &\sum_{i=1}^{n_{\mathrm{a}}^{'}}\sum_{j=0}^{n_{\mathrm{b}}^{'}} e_{i,j} y(k-i)u(k-n_{\mathrm{d}'}-j), \end{aligned} \tag{4.26}$$

where $n_{\mathrm{a}}^{'}$, $n_{\mathrm{b}}^{'}$, and the polynomial order, p, are the KGP model orders, while $n_{\mathrm{d}}^{'}$ is the input delay of the KGP model. It should be noted that the cross-product terms (or cross-product regressors) in Equation (4.26) potentially lead to stability problems [221]. More specifically, due to the presence of the cross-product regressors, some input-dependent terms appear inside the model Jacobian and, consequently, the stability properties depend on the specific input signal [204]. To avoid such a problem, the cross-product terms are typically discarded and Equation (4.26) simplifies to

$$y^{\mathrm{kgp}}(k) = \sum_{j=1}^{p}\Bigg[- \sum_{i=1}^{n_{\mathrm{a}}^{'}} a_{i,j} y^{j}(k-i) + \sum_{i=0}^{n_{\mathrm{b}}^{'}} b_{i,j} u^{j}(k-n_{\mathrm{d}}^{'}-i)\Bigg]. \tag{4.27}$$

Although the model structure in Equation (4.27) is evidently nonlinear, the KGP polynomial model is, just as the ARX model, linear in the unknown parameters, namely $a_{i,j}$ and $b_{i,j}$. In other words, it is possible to express Equation (4.27) as a linear regression and, therefore, $a_{i,j}$ and $b_{i,j}$ are optimised by solving a LS problem. The number of unknown parameters for the KGP model (without cross-product terms) is computed as $N_{\mathrm{kgp}} = p(n_{\mathrm{a}}^{'}+n_{\mathrm{b}}^{'}+1)$. Similarly to the procedure followed for the ARX model, the KGP model orders ($n_{\mathrm{a}}^{'}$, $n_{\mathrm{b}}^{'}$, and p) are determined by implementing a sequence of systematic trials, and considering the validation NRMSE. Ultimately, as shown in Figure 4.14, a parsimonious choice for the polynomial order is $p = 2$, while $n_{\mathrm{a}}^{'} = 6$, $n_{\mathrm{b}}^{'} = 2$ and $n_{\mathrm{d}}^{'} = -1$.

Optimisation problem formulation The regressor, φ_{kgp}, and parameter, θ_{kgp}, vectors for the KGP model (4.27) are written, respectively, as

$$\begin{aligned} \varphi_{\mathrm{kgp}}(k) = &[-y(k-1)\ldots -y(k-n_{\mathrm{a}})\ u(k-n_{\mathrm{d}}-1)\ldots u(k-n_{\mathrm{d}}-n_{\mathrm{b}})\ldots \\ &-y^{p}(k-1)\ldots -y^{p}(k-n_{\mathrm{a}})\ u^{p}(k-n_{\mathrm{d}}-1)\ldots u^{p}(k-n_{\mathrm{d}}-n_{\mathrm{b}})]^{\intercal}, \end{aligned} \tag{4.28}$$

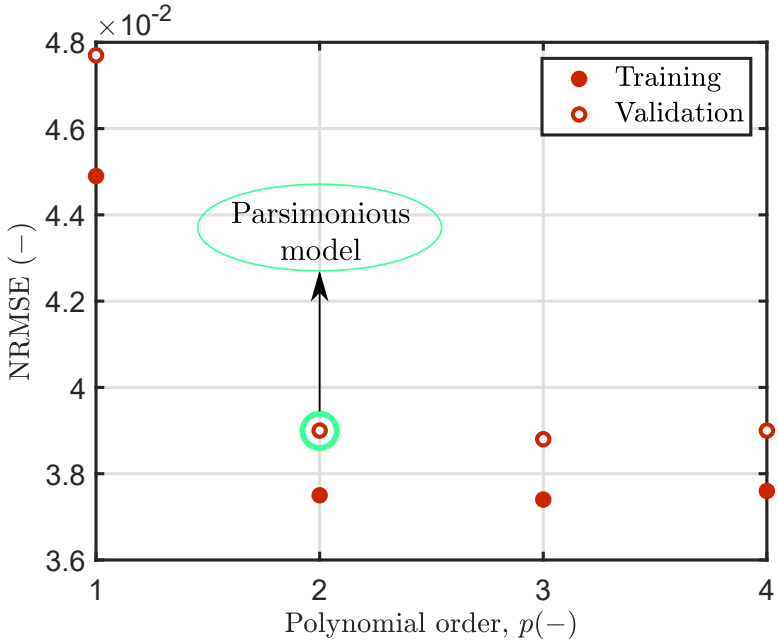

Figure 4.14: Identification and validation NRMSE values for separate KGP models, identified from $D^{\mathrm{B}}_{3_{\mathrm{a}}}$ and validated against $D^{\mathrm{B}}_{3_{\mathrm{b}}}$, using different p values, with $n'_{\mathrm{a}} = 6$, $n'_{\mathrm{b}} = 2$, and $n'_{\mathrm{d}} = -1$.

and

$$\theta_{\mathrm{kgp}} = [a_{1,1} \dots a_{n'_{\mathrm{a}},1}\ b_{0,1} \dots b_{n'_{\mathrm{b}},1} \dots a_{1,p} \dots a_{n'_{\mathrm{a}},p}\ b_{0,p} \dots b_{n'_{\mathrm{b}},p}]^{\intercal}. \tag{4.29}$$

To find the N_{kgp} unknown parameters (4.29), an LS optimisation problem, written as

$$\theta^{\mathrm{opt}}_{\mathrm{kgp}} = \underset{\theta_{\mathrm{kgp}}}{\mathrm{argmin}}(\epsilon^{\intercal}\epsilon) = (\Lambda^{\intercal}_{\mathrm{kgp}}\Lambda_{\mathrm{kgp}})^{-1}\Lambda^{\intercal}_{\mathrm{kgp}}Y, \tag{4.30}$$

where Λ_{kgp} is the regression matrix of the KGP model, is solved using a QR factorization method.

Identification and validation phases The identification and validation phases are carried out as schematically shown in Figure 4.13. Firstly, the input/output time traces of the data sets D^{B}_1, D^{B}_2, and D^{B}_3 are split into two parts. Subsequently, $D^{\mathrm{B}}_{1_{\mathrm{a}}}$, $D^{\mathrm{B}}_{2_{\mathrm{a}}}$, and $D^{\mathrm{B}}_{3_{\mathrm{a}}}$ are merged together and a new data set, $D^{\mathrm{mer}}_{\mathrm{a}}$, is derived. Similarly, another data set, $D^{\mathrm{mer}}_{\mathrm{b}}$, is obtained by merging $D^{\mathrm{B}}_{1_{\mathrm{b}}}$, $D^{\mathrm{B}}_{2_{\mathrm{b}}}$, and $D^{\mathrm{B}}_{3_{\mathrm{b}}}$. Finally, a KGP model, M^{kgp}, is identified from $D^{\mathrm{mer}}_{\mathrm{a}}$ and validated against data $D^{\mathrm{mer}}_{\mathrm{b}}$, $D^{\mathrm{B}}_{1_{\mathrm{b}}}$, $D^{\mathrm{B}}_{2_{\mathrm{b}}}$, and $D^{\mathrm{B}}_{3_{\mathrm{b}}}$. The model fidelity (4.14) for M^{kgp} with respect to the identification data is about $96.25\,\%$. It should be noted that, likely due to the linear nature of the ARX model (further discussed in Section 4.2.3.3), $D^{\mathrm{mer}}_{\mathrm{a}}$ cannot be effectively used to identify a linear ARX model with identification and validation fidelities comparable to those of M^{kgp}.

Table 4.5: Fidelity percentage values for the ARX model validation.

Model	VD	1-step-ahead	5-step-ahead	10-step-ahead
M_1^{arx}	$D_{1_b}^{\text{B}}$	94.24	82.03	60.22
M_2^{arx}	$D_{2_b}^{\text{B}}$	96.25	85.09	67.97
M_3^{arx}	$D_{3_b}^{\text{B}}$	97.89	93.57	88.49

Table 4.6: Fidelity percentage values for the ARX model cross-validation.

Model	VD	1-step-ahead	5-step-ahead	10-step-ahead
M_1^{arx}	$D_{2_b}^{\text{B}}$	87.44	64.21	31.53
M_1^{arx}	$D_{3_b}^{\text{B}}$	91.71	76.39	42.21
M_2^{arx}	$D_{1_b}^{\text{B}}$	84.01	61.58	30.08
M_2^{arx}	$D_{3_b}^{\text{B}}$	92.74	77.57	44.63
M_3^{arx}	$D_{1_b}^{\text{B}}$	83.82	61.12	29.92
M_3^{arx}	$D_{2_b}^{\text{B}}$	87.14	64.10	31.48

4.2.3.3 Result and discussion

Validation performance Tables 4.5 and 4.7 show the validation performance, with respect to each set of validation data, of the three linear ARX models and the nonlinear KGP model, respectively. Each SI model is validated considering three different output predictions, namely 1-step-ahead, 5-step-ahead, and 10-step-ahead predictions. For clarity, in a k-step-ahead prediction, the i-th predicted output is calculated using previously measured outputs up to time instant $i-k$ and all relevant input values until time instant i. By way of example, Figure 4.15 compares the predicted outputs of M_3^{arx} and M^{kgp}, to the empirical output, $y(t)$, for the validation data set $D_{3_b}^{\text{B}}$.

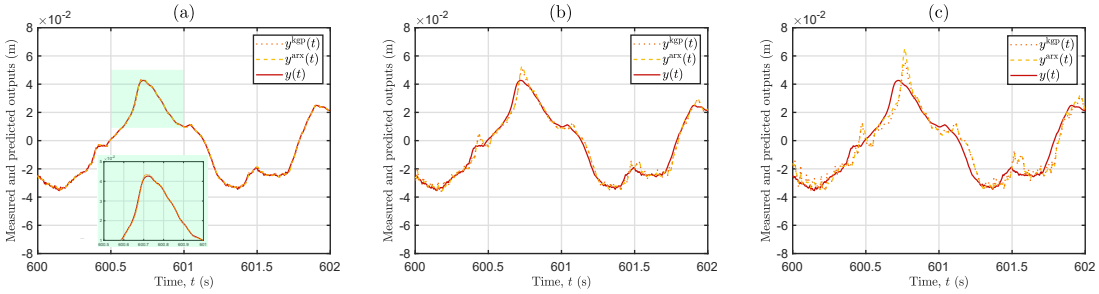

Figure 4.15: Comparison between the measured output, $y(t)$ (from $D_{3_b}^{\text{B}}$), and the (a) 1-step-ahead, (b) 5-step-ahead, and (c) 10-step-ahead predicted outputs, $y^{\text{arx}}(t)$ and $y^{\text{kgp}}(t)$, respectively related to the validation of the ARX model M_3^{arx} and the KGP model M^{kgp}.

As shown in Table 4.5, the validation performance of the ARX models remain consistent throughout the validation phase. Firstly, the model fidelity unsurprisingly

Table 4.7: Fidelity percentage values for the KGP model validation.

Model	VD	1-step-ahead	5-step-ahead	10-step-ahead
M^{kgp}	$D^{\text{B}}_{1_{\text{b}}}$	94.25	81.61	57.43
M^{kgp}	$D^{\text{B}}_{2_{\text{b}}}$	96.33	85.05	66.69
M^{kgp}	$D^{\text{B}}_{3_{\text{b}}}$	97.71	92.95	84.58
M^{kgp}	$D^{\text{mer}}_{\text{b}}$	96.10	86.54	69.57

decreases as the number of prediction steps ahead increases. Secondly, the model fidelity of M^{arx}_1 is always the lowest, while, due to superior S/N of $D^{\text{B}}_{3_{\text{a}}}$, the fidelity of M^{arx}_3 is the highest in all cases. Like the ARX models, M^{kgp} also shows strong consistency during the validation process in relation to the number of prediction steps (Table 4.7). Furthermore, the highest validation fidelity of M^{kgp} is found for $D^{\text{B}}_{3_{\text{b}}}$, which is the validation data set with the best S/N. Finally, the validation of M^{kgp} against $D^{\text{mer}}_{\text{b}}$ provides a 'mean fidelity'. For instance, in the 1-step-ahead predictions of M^{kgp} against $D^{\text{B}}_{1_{\text{b}}}$, $D^{\text{B}}_{2_{\text{b}}}$, $D^{\text{B}}_{3_{\text{b}}}$, and $D^{\text{mer}}_{\text{b}}$, the model fidelities are, respectively, 94.25%, 96.33%, 97.71% and 96.10%, with: $(94.25\% + 96.33\% + 97.71\%)/3 \approx 96.10\%$.

The cross-validation performance of the ARX models are reported in Table 4.6. In contrast to a traditional SI procedure, the range of frequencies, and amplitudes, of the input signals employed in the cross-validation procedure is different from the range of frequencies, and amplitudes, over which the model is trained. Therefore, the cross-validation exercise essentially represents a case where unsuitable training data are deliberately chosen and, consequently, poor validation performance (particularly for the 5-step-ahead and 10-step-ahead predictions) is obtained.

From Tables 4.5 and 4.7, it should be clear that when the same validation data are considered across ARX and KGP models, the ARX model performs consistently better than the KGP model. For instance, for $D^{\text{B}}_{3_{\text{b}}}$, the validation fidelity of M^{arx}_3 for the 1-step-ahead, 5-step-ahead, and 10-step-ahead predictions is 97.89%, 93.57%, and 88.49%, respectively. On the other hand, M^{kgp} has a validation fidelity of 97.71%, 92.95%, and 84.58% for the 1-step-ahead, 5-step-ahead, and 10-step-ahead predictions, respectively. Furthermore, as the number of prediction steps increases, the difference between the ARX and KGP models becomes more and more pronounced. However, it is essential to highlight that, in the nonlinear modelling case, a *single* KGP model (M^{kgp}) provides satisfactory validation performance across different data sets, namely $D^{\text{B}}_{1_{\text{b}}}$, $D^{\text{B}}_{2_{\text{b}}}$, and $D^{\text{B}}_{3_{\text{b}}}$. On the contrary, since the cross-validation performance of the ARX models is relatively poor, the ARX model (e.g., M^{arx}_1) provides good validation results only with a single validation data set (e.g., $D^{\text{B}}_{1_{\text{b}}}$).

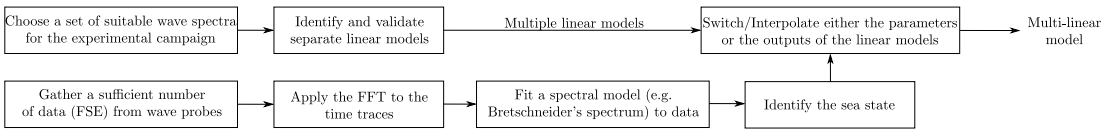

Figure 4.16: Schematic procedure related to the real-time implementation of a multi-linear model.

Real-time implementation issues Despite the fact that a linear SI modelling approach may appear appealing, due to its relative simplicity, and convenient, for the superior validation performance compared to those of the nonlinear KGP model (at least when the same validation data are considered), there are some practical aspects which must be considered. Such aspects concern the necessary steps required to implement a multi-linear model to cover the complete frequency/amplitude operational range in real-time (Figure 4.16).

To employ the linear ARX models in real-time, it is necessary to derive a (single) multi-linear model which can represent the system behaviour across all relevant sea states. To this end, a switching/interpolating mechanism for either the parameters, or the predicted outputs, of the different linear ARX models is essential. Additionally, since the switching/interpolating process relies on knowledge of the sea state, the sea state must be estimated, in real-time, by fitting a wave spectral model to Fourier-transformed FSE data gathered from wave probes. In the case of a switching mechanism, one of the available linear models is chosen to operate with the corresponding estimated sea state. Alternatively, if an interpolating mechanism is devised, either the interpolated model outputs or the interpolated model parameters are computed, using a set (at least two) of outputs/parameters corresponding to the relevant set of linear models. To this end, since the wave spectral models are typically defined by two parameters (i.e., H_{s} and T_{e}), the interpolation is actually a two dimensional interpolation.

Ultimately, the procedure illustrated in Figure 4.16 has two critical interrelated issues: (i) Sea state estimation and (ii) (explicit) switching/interpolating mechanism. Regarding issue (i), sea state estimation can be a difficult task to perform in real-time and in a real sea environment. Firstly, a spectral model for the sea state needs to be selected and suitable locations (undisturbed by the presence of the device) for the wave probes have to be identified. Secondly, to guarantee an adequate statistical description, a sufficient number of FSE data must be collected from the wave probes; otherwise, the accuracy of the spectral model may be excessively poor and, therefore, the selected linear model could be far from being the optimum model associated with the true sea state. Finally, aside from the spectral model accuracy, the sea state estimation procedure clearly requires some

time and, to this end, delays in deducting the multi-linear model might severely affect the overall accuracy, and efficacy, of the multi-linear SI modelling approach. In relation to issue (ii), the efficacy of the switching/interpolating process is strictly connected to the correct identification of the sea state. Furthermore, in either model selection mechanism (switching or interpolation), the multi-linear model is expected to optimally perform only when the estimated sea state matches *exactly* one of the sea states originally utilized during the experimental campaign (i.e., in the SI model training phase). In such an ideal condition, the multi-linear model fidelity should be roughly comparable to the values shown in Table 4.5, regardless of the model selection rationale. On the other hand, when the estimated sea state is not one of those employed in the identification phase, a multi-linear model operating with a suitable interpolating mechanism is expected to perform better than one equipped with a switching mechanism.

In comparison to the laborious multi-linear SI modelling technique, the main advantage of the nonlinear model is its capability to *implicitly* interpolate the predicted output, meaning that the nonlinear SI modelling approach does not require either an explicit switching/interpolating mechanism, nor the estimation of the sea state. Additionally, the number of unknown parameters of the KGP model, namely $p(n_\mathrm{a} + n_\mathrm{b} + 1)$, is likely smaller than the parameters of the multi-linear modelling solution, $N_\mathrm{lm}(n_\mathrm{a} + n_\mathrm{b} + 1)$, where N_lm is the number of multiple linear ARX models.

4.3 Conclusions

In this chapter, frequency-domain, linear time-domain, and nonlinear time-domain SI modelling techniques are utilized to identify some hydrodynamic models, of the type in Figure 4.2, for a scaled OWC chamber.

In general, frequency-domain SI models can provide some preliminary useful information about the system, such as the TF model order and the system resonant bandwidth, which should then ideally inform the time-domain identification procedure [200]. Indeed, knowledge of the frequency-domain SI models may help the SI user in making some key design choices concerning time-domain data-based modelling, such as the selection of suitable training data and the choice of a SI model structure. In data-based hydrodynamic modelling of WECs, a chirp signal, shown in Figure 4.17, may be particularly suitable for SI since the input signal linearly sweeps a desired frequency range during its evolution and, consequently, the signal frequency content is fairly evenly distributed across that range [201]. In any case, the main objective of this work was to investigate the possibility to obtain

SI hydrodynamic models for OWCs which are potentially suitable for control. To this end, the multisine signals used in the irregular wave experiments (Section 4.2.1) are suitable for such an objective, since they excite the device in both resonant (where the uncontrolled device optimally works), and off-resonant (where a hypothetical controlled device may efficiently works), frequency bandwidths.

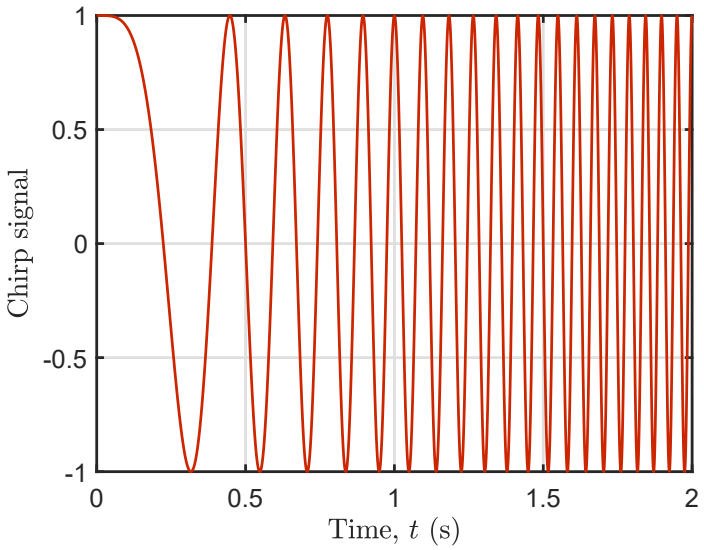

Figure 4.17: Chirp signal linearly sweeping the frequency range $0 - 20$ Hz, in the time interval $0 - 2$ s.

In light of the discussion in Section 4.2.3.3, for the specific case considered here, a nonlinear SI strategy has some significant advantages over a multi-linear data-based modelling solution, especially when considering some aspects of the real-time implementation procedure. Indeed, although the ARX model performance metrics (Table 4.5) are mildly superior to those of the KGP model (Table 4.7) in the validation on their corresponding data sets, the real-time implementation of a multi-linear ARX model, to cover the full operational range, is relatively time-consuming and complex. On the other hand, the nonlinear SI modelling approach considered in this chapter is significantly less laborious than the multi-linear alternative, particularly since the KGP model is a somewhat simple and natural evolution of the ARX model. It should be noted that, apart from the KGP model, there may be other nonlinear SI models, such as simple ANNs, which are suitable (in terms of model accuracy/complexity) for OWC hydrodynamic modelling. In this chapter, the efficacy of a simple nonlinear model structure and the validity of a nonlinear approach are shown. Ultimately, the KGP model is ideal for model-based control applications, being both computationally and parametrically simple, and also captures the essential hydrodynamic nonlinearity in the system.

Part III

OWC WEC control

Science is not only a disciple of reason but, also, one of romance and passion.

— Stephen Hawking

5

Control problem definition and review of control strategies

Contents

5.1 OWC wave-to-wire control problem formulation 100
5.1.1 Simplification of the control problem 102
5.1.2 List of constraints 103
5.1.3 Constrained OWC OCP 104
5.1.4 Main control co-design aspects 105
5.2 Review of OWC control strategies 108
5.2.1 Hydrodynamic control 109
5.2.2 Aerodynamic control 114
5.2.3 Wave-to-turbine control 120
5.2.4 Wave-to-wire control 120
5.2.5 Peak-shaving control 120
5.2.6 Grid-side control 122
5.3 Summary 123

As already mentioned in Section 1.2, to improve the economic viability of OWCs, it is essential to minimise the LCoE. However, since LCoE minimisation is, as a performance objective, difficult to handle, especially due to the problem of accurate and reliable OpEx estimation, many researchers typically focus on a simplified control objective, namely produced energy maximisation. Furthermore, due to the critical issue of turbine performance, the OWC control problem is often further simplified to a rotational speed tracking problem for maximising turbine efficiency.

It should be noted that turbine efficiency maximisation may be, to some extent, a fairly reasonable control objective for OWCs, providing that turbine rotational speed does not significantly affect the OWC hydrodynamic subsystem. Such a condition is, however, not generally satisfied, especially for Wells turbines, where the impact of turbine speed on the hydrodynamic performance cannot be ignored. Ultimately, since the OWC control problem strictly depends on design choices (e.g., type of turbine), there exist different suitable low-level control objectives (e.g., energy maximisation, turbine efficiency maximisation,...) that a control engineer may consider. Nevertheless, the high-level performance objective, namely LCoE minimisation, remains unchanged and should never be disregarded.

This chapter discusses the main OWC control-related aspects and offers an overview of the state-of-the-art control strategies. In particular, an unbiased formulation of the (overall) W2W control problem for OWC WECs is presented in Section 5.1, while a review of control strategies is provided in Section 5.2.

5.1 OWC wave-to-wire control problem formulation

In this Section, to provide a platform for devising a comprehensive model-based control strategy, an unbiased formulation of the OWC control problem is presented, while considering all the control effectors in Figure 5.1. To this end, in Section 5.1.1, some possible simplifications of the OWC control problem are discussed and a suitable objective function, for an optimal control problem formulation, is selected. Subsequently, the constraints of the control problem are listed (Section 5.1.2) and the constrained OWC optimal control problem is formulated (Section 5.1.3). Finally, the main CCD aspects are highlighted in Section 5.1.4.

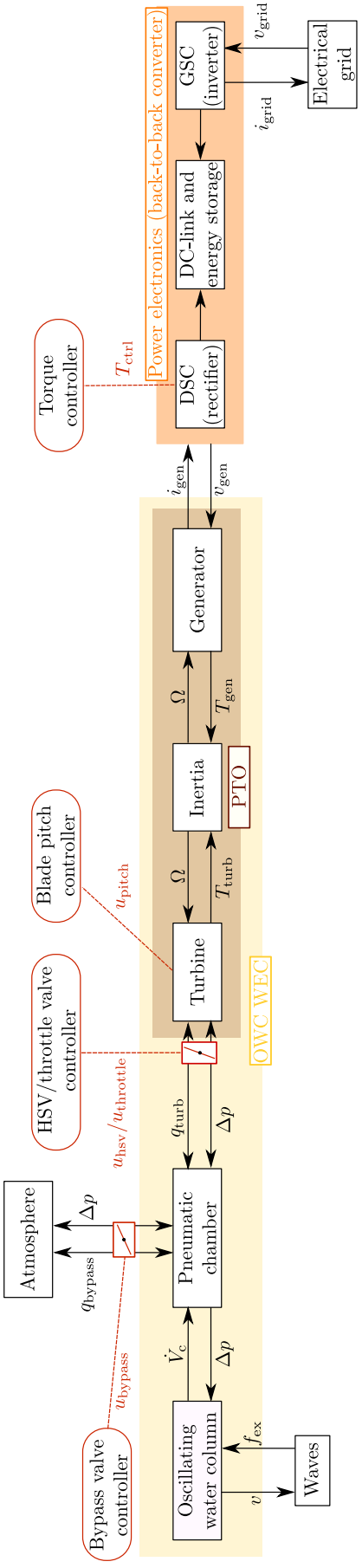

Figure 5.1: Schematic representation of the wave-to-grid power flow of an OWC WEC. Figure adapted from [56].

5.1.1 Simplification of the control problem

As already mentioned, the high-level performance function in OWC WEC control is LCoE minimisation but, since estimating OpEx is difficult, the control objective typically simplifies to electric energy maximisation. In this thesis, such a simplification is generally accepted when designing OWC control strategies (Chapters 6 and 7). The only exception is the work presented in Chapter 8, where a parametric CCD approach for the PTO and bypass valve of an OWC is devised. As further detailed in Chapter 8, such a CCD strategy is specifically conceived to minimise (a surrogate of) the LCoE.

In principle, to maximise energy production, a control strategy should consider the overall wave-to-grid power flow, as shown in Figure 5.1. In this way, a suitable control strategy could potentially take into account all the relevant aspects of hydrodynamic, aerodynamic, electrical, and grid-side control. However, it should be noted that a natural simplification of the control problem is possible. Indeed, fully-rated back-to-back (B2B) power converters offer the possibility to naturally decouple the control problem by separating grid-side and device-side at the level of the DC-link [222]. Therefore, device-side control (which is the focus of this thesis) aims to maximise the electric energy produced by the generator, while grid-side control deals with grid requirements [71], which mainly concern power quality and fault-ride-through (FRT) capabilities, by regulating the DC-link voltage and managing electrical energy storage.

Apart from electric energy maximisation, mechanical energy maximisation, namely the optimisation of the wave-to-turbine energy conversion process, has been sometimes considered as an alternative control objective in the literature. For OWC WECs equipped with a Wells turbine, mechanical energy maximisation through turbine rotational speed modulation may be an appropriate control objective, if a suitable electric generator (in terms of its operational range) is selected. Indeed, if correctly chosen, electric generators may efficiently convert mechanical power into electrical power over most of the expected torque/rotational speed operating conditions. With an impulse-like air turbine, the efficacy of mechanical energy maximisation through speed control is limited, since rotational speed only marginally affects hydrodynamic performance. However, mechanical energy maximisation for biradial turbines may still be considered, since the HSV of the biradial turbine can be potentially used to improve the OWC hydrodynamic performance (with latching control [223]). As further discussed in Section 5.2.1, except for the HSV of the biradial turbine, dedicated actuators for hydrodynamic control are typically not available on OWCs.

Since the air turbine is the most important element of the OWC, the vast majority of OWC control strategies focus on turbine efficiency maximising (TEM) control [51]. In TEM control the hydrodynamic/aerodynamic interaction is ignored and, consequently, the broad energy maximising control problem simplifies to a maximum power point tracking (MPPT) problem for the turbine rotational speed [187]. Ultimately, TEM control may be relatively effective for impulse-like turbines but, due to the significant effect of rotational speed on hydrodynamic efficiency, is not ideal for Wells turbines [60, 61, 62, 63].

Finally, the modelling assumptions considered in this section are the same assumptions introduced in Section 2.2 (i.e., the LWT assumptions) and Chapter 3 (e.g., high Reynolds and low Mach numbers at the turbine rotor blade tips).

5.1.2 List of constraints

The safe operating region of an OWC, shown in Figure 5.2, is delimited by three main physical constraints concerning the PTO system, namely the constraints on the maximum allowable speed, $\Omega \leq \Omega^{\max}$, maximum control torque, $T_{\text{ctrl}} \leq T_{\text{ctrl}}^{\max}$, and generator rated power, $T_{\text{ctrl}}\Omega \leq P^{\text{rated}}$. The maximum speed value is written [56] as

$$\Omega^{\max} = \min(\Omega_{\text{turb}}^{\max}, \Omega_{\text{gen}}^{\max}, \Omega_{\text{noise}}^{\max}), \tag{5.1}$$

where $\Omega_{\text{noise}}^{\max}$ is the maximum speed to prevent excessively high turbine noise emissions [143, 224, 225], $\Omega_{\text{gen}}^{\max}$ is the maximum generator speed to limit centrifugal stresses, and $\Omega_{\text{turb}}^{\max} = v_{\text{tip}}^{\max}(2/d_{\text{r}})$ is the turbine maximum speed to avoid air compressibility effects (such as shock waves) at the rotor blade tips [183], with $v_{\text{tip}}^{\max}$ being the maximum blade tip speed.

From a control perspectives, four control regions (CR_1, CR_2, CR_3, and CR_4) can be identified as functions of the available wave power (Figure 5.2). In CR_1, the available wave power is below the minimum threshold required to start wave power extraction. On the right side of Figure 5.2, CR_4 represents the case in which excessive wave power is available and, consequently, one cannot simultaneously satisfy the following conditions: $\Omega \leq \Omega^{\max}$ and $T_{\text{ctrl}}\Omega \leq P^{\text{rated}}$. Therefore, in region CR_4, the OWC WEC must enter a safety mode by closing a safety valve (i.e., a valve in series with the turbine), which interrupts pneumatic excitation of the turbine to avoid major failures. In region CR_2, due to the limited available wave power, the OWC device cannot achieve P^{rated}. In such an operating condition, a control strategy should maximise wave power extraction, while keeping $T_{\text{ctrl}} \leq T_{\text{ctrl}}^{\max}$. Finally, since the available wave power in CR_3 is sufficiently high, it is potentially possible to achieve P^{rated}, providing that a suitable control approach is used. In essence, to

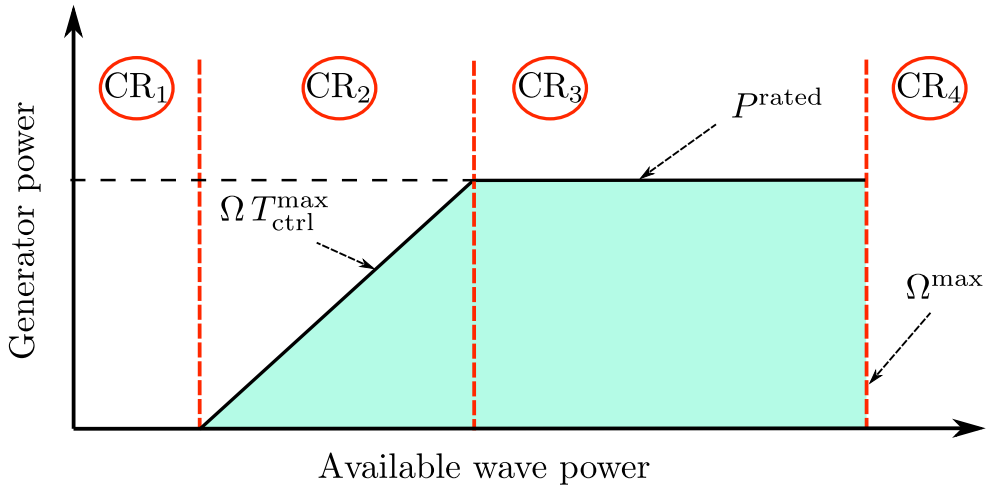

Figure 5.2: Schematic of the OWC control regions as functions of the available wave power. The blue shaded area represents the safe operating area of the OWC WEC.

maximise energy production in CR_3, a suitable control strategy should keep the OWC device working at its rated power and, to this end, peak-shaving control is used (Section 5.2.5). As already mentioned in Chapter 1, peak-shaving control is relatively simple on OWCs, especially due to the presence of suitable actuators which can limit the pneumatic power available to the turbine (e.g., a bypass valve).

5.1.3 Constrained OWC OCP

The constrained OWC OCP is to find the control input, $u_{\text{ctrl}}(t)$, to maximise electric energy production, expressed as

$$J = \int_0^T P_{\text{elec}}(\Omega(t))\mathrm{d}t, \;\; t \in [0 \; T], \tag{5.2}$$

subject to the OWC system dynamics (in (3.2), (3.8), (3.12), and (3.23)) and the state/input constraints presented in Section 5.1.2. In general, $u_{\text{ctrl}}(t)$ may include all, or some, of the four manipulated inputs shown in Figure 5.1 (namely, T_{ctrl}, u_{bypass}, $u_{\text{throttle/hsv}}$, and u_{pitch}). If only a limited set of manipulated variables are available, some control actions may be more difficult (or impossible) to implement.

The impact of the manipulated inputs on Ω is better clarified by substituting P_{turb} (3.15) into the PTO dynamics (3.12), as

$$\dot{\Omega} = \frac{\rho_{\text{air}}\Omega^2 d_{\text{r}}^5 f_{\Pi}(\Psi(\Omega, \Delta p), u_{\text{hsv/throttle}}, u_{\text{pitch}}) - T_{\text{ctrl}}}{I}. \tag{5.3}$$

Additionally, the control input u_{bypass} appears in the air chamber equation (3.8), where $\Delta p = \Delta p(z, w_{\text{bypass}}, w_{\text{turb}})$, with $w_{\text{bypass}} = w_{\text{bypass}}(\Delta p, u_{\text{bypass}})$ (3.5) and $w_{\text{turb}} = \Delta p\, \zeta_*$, where ζ_* denotes the damping of a generic turbine. It should be noted that a bypass valve can only be used to dissipate pneumatic power [226], therefore it is always kept closed (i.e., $u_{\text{bypass}} = 0$) in CR_2.

5.1.4 Main control co-design aspects

Despite the control objective specified in Section 5.1.3 being electric energy maximisation, since the final objective in OWC WEC control is the LCoE minimisation, it is worth highlighting some of the main CCD aspects. Indeed, since the WEC geometry optimisation problem is typically coupled with the WEC control problem [227, 228], CCD techniques [229, 230] are vital to achieve the optimum control-informed WEC design [228, 231, 232, 233]. Traditionally, design is a sequential procedure where control aspects are not taken into account until a relatively late stage, as shown in Figure 5.3. Additionally, in a traditional design approach, the design choices made at each step limit the design possibilities of the next step [234]. In other words, each step reduces the design flexibility of the next step, therefore making a design adjustment increasingly expensive and difficult. In CCD, control aspects are considered from an initial design phase, at an early TRL, potentially improving flexibility and control-awareness in overall design optimisation [234].

5.1.4.1 Air chamber design

The air chamber is typically designed considering the frequency content of the most frequent SSs at the desired deployment site. Therefore, unless a variable chamber geometry [235] or other form of hydrodynamic control is utilised to extend the hydrodynamic operating range of the OWC, as the actual sea state varies from the design condition, a degradation of the hydrodynamic performance is expected. Furthermore, the geometry of the chamber front wall may be optimised to reduce hydrodynamic viscous losses, which are primarily due to vortex shedding phenomena in fixed OWCs [236]. Finally, to avoid a catastrophic system failure, the OWC chamber volume should be sufficiently large to prevent green water from reaching the turbine blades.

5.1.4.2 Air turbine

Turbine selection Due to the critical importance of the pneumatic-to-mechanical energy conversion process, the selection of a suitable turbine type is a key issue in the PTO system design. The leading parameter for choosing a suitable turbine is the root-mean-square of the pressure oscillations in the pneumatic chamber [67], since Wells and impulse-like turbines most efficiently operate at different pressure levels. In particular, Wells turbines generally have a superior time-averaged efficiency when working with relatively large air flow rates and low pressure ranges. In contrast to Wells turbines, impulse-like turbines typically operate at high efficiency under larger

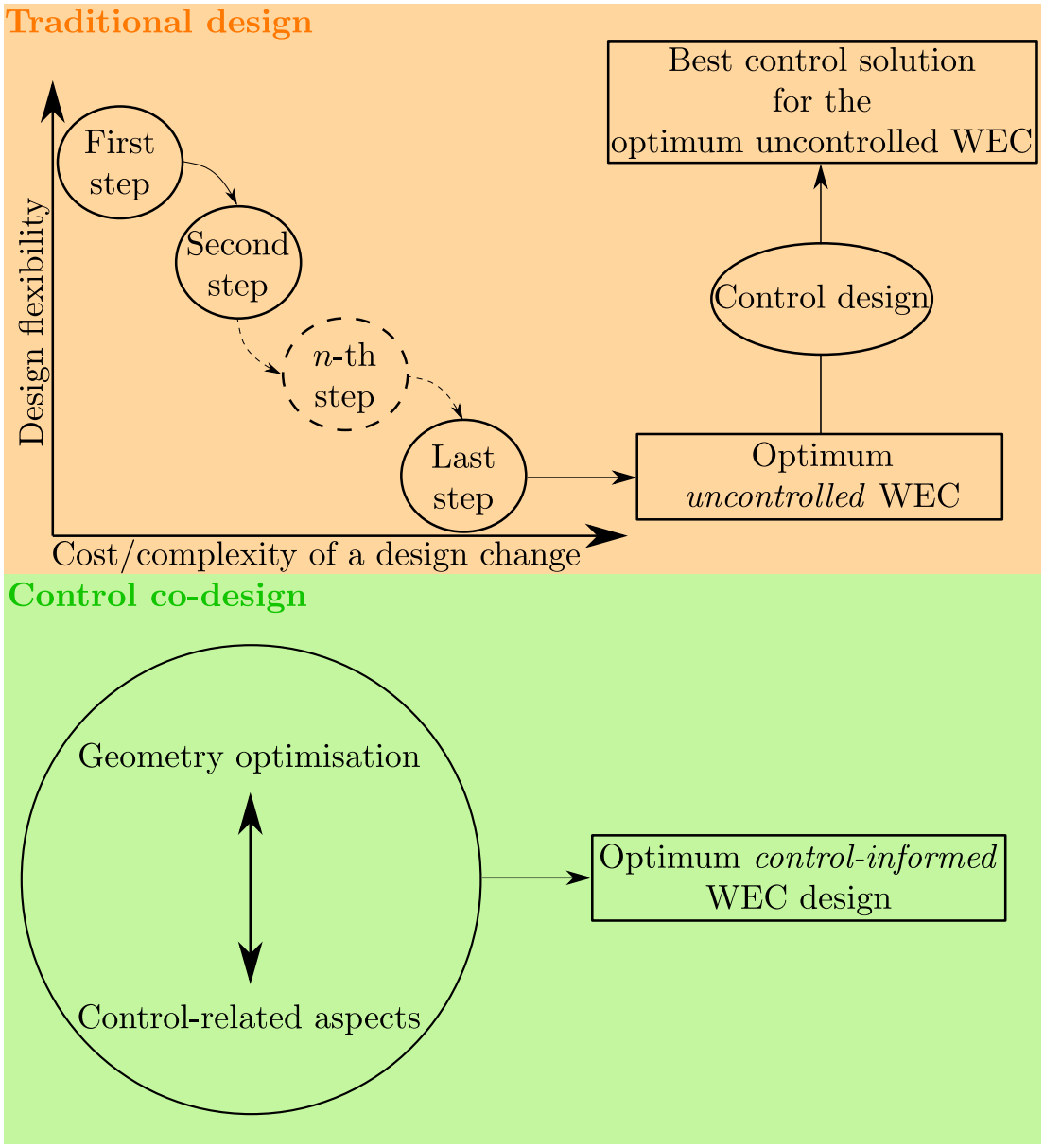

Figure 5.3: Schematics of a traditional progressive stepwise design procedure and a CCD procedure, for a generic wave energy project.

pressure fluctuations and at lower flow rates. Although not a popular solution due to high costs and additional complexity, multi-stage Wells turbines are able to work with larger pressure fluctuations, but require properly designed inter-stage guide vanes [66]. A complete comparison between different turbine types is found in [67].

From a rotational speed control perspective, each type of turbine has some specific efficiency characteristics (see, for instance, Figure 3.4) which influence the control problem. For instance, Wells turbines have a narrow high-efficiency operating region and a hard stall characteristic, which make rotational speed control more difficult. On the other hand, in light of their broader high-efficiency range

and soft stall characteristics, impulse turbines require a smaller speed control effort to provide satisfactory performance. In addition to the turbine efficiency characteristics, the inertia of the PTO system, which is mainly a function of the turbine diameter and rotor material, also affects rotational speed control [51, 183]. In general, speed control is simpler (i.e., it is easier to track the reference speed), and mean turbine efficiency is higher, if the inertia is smaller [66, 183]. To this end, Wells turbine inertia is typically lower than impulse turbine inertia, for equivalent rotor diameters [66]. However, although the biradial turbine has a relatively large inertia, it can operate efficiently if $\Psi > \Psi_{\text{mep}}$ (Figure 3.4) and, therefore, the negative impact of inertia on control is limited.

As already mentioned in Section 5.1.1, turbine damping characteristics significantly influence the control problem. On the one hand, Wells turbine damping (3.18) is a function of rotational speed, meaning that speed control impacts hydrodynamic performance. On the other hand, impulse turbine rotational speed only marginally affects the OWC hydrodynamic process (Equations (3.21) and (3.22)).

In the case of shoreline fixed OWCs, especially if located near populated areas, noise levels are an important issue. Under normal operating conditions, Wells turbines are generally noisier than impulse turbines since they operate at higher rotational speed values [66, 143]. Therefore, although operating at high speed may positively influence electric performance, since generators generally work more efficiently at high speed, Ω may be limited to decrease noise emissions (i.e., $\Omega \leq \Omega_{\text{noise}}^{\max}$). Furthermore, Wells turbines generate high noise levels in the case of (i) aerodynamic stall and (ii) shock waves at the rotor blade tips for Mach numbers [237]. However, such extreme events may be avoided if turbine rotational speed is effectively controlled. Finally, in impulse turbines, the main noise source is aerodynamic stall at the exit stator blades, although noise emissions (and aerodynamic losses) can be reduced by increasing the axial offset of the stator blades [66].

Turbine type and available actuators The available actuators are strictly related to the type of air turbine installed on the OWC. To date, although some attempts have been made to devise a HSV for a Wells turbine using a pneumatic actuation system [238], HSVs are only simple (and cheap) to install on biradial turbines [110], due to the relatively narrow ducts connecting the turbine with the air chamber and the atmosphere (Figure 2.9). In terms of control possibilities, HSVs can potentially be employed for latching and wave-by-wave peak-shaving control by throttling the HSV (further explained in Section 5.2). In light of the significantly different control-related possibilities, a clear distinction between HSVs (u_{hsv}) and standard

(butterfly) throttle valves (u_{throttle}) is now made. In this thesis, although HSVs can be also throttled, a HSV specifically refers to a valve in series with a biradial turbine, while throttle valve refers to a butterfly valve in series with any other turbine type (e.g., Wells and axial-flow impulse turbines). Ultimately, standard throttle valves cannot be typically employed for latching or wave-by-wave peak-shaving control, due to their limited actuation speed.

To independently control Ω, Δp, and w_{turb}, turbines with a variable-pitch rotor are required [239]. Furthermore, variable-pitch turbines may be also potentially used as air compressors to provide reactive power [239] for reactive hydrodynamic control strategies (Section 5.2.1.1). However, variable pitch air turbines have a relatively low efficiency when used as compressors, thus limiting their efficacy in this context.

5.1.4.3 Electric generator selection

Due to the corrosive working environment and the broad range of operating conditions, variable-speed electric generators with salinity resistance are required on OWC WECs [68]. Furthermore, since the typical turbine speed range is compatible with standard off-the-shelf generators, potentially expensive and mechanically complicated gearboxes are unnecessary.

On the control side, it is important to note that some (or even all) of the control constraints (i.e., $\Omega^{\max}$, $T_{\text{ctrl}}^{\max}$, and P^{rated}) depend on the electric generator. In particular, the generator size (i.e., P^{rated}) should be chosen considering the expected wave power at the deployment site, the possibility (or impossibility) to use peak-shaving control, and the cost of the electrical equipment. To this end, the cost of the electrical equipment, such as the generator itself and the power converter, increases as the generator size increases. On one side, an over-sized generator is relatively expensive, but it may virtually operate in high-energy SSs without the need for peak-shaving control, therefore simplifying the OWC control problem. On the other side, under-sized generators are undesirable since they cannot exploit the available wave power at its full potential, although they are cheaper and have a higher capacity factor than over-sized generators.

5.2 Review of OWC control strategies

As show in Figure 5.1, controllers for OWC systems typically use some of the following manipulated inputs:

- Generator electromagnetic torque, T_{ctrl},

- blade pitch position, u_{pitch},
- bypass valve position, u_{bypass}, and
- HSV/throttle valve position, $u_{\text{hsv/throttle}}$.

Since the control possibilities strictly depend on the device components (both system and available actuators), a broad classification of OWC control strategies based on an *objective-focused* perspective is proposed. On the device-side, it may be possible to identify four main possible control objectives, namely hydrodynamic control (Section 5.2.1), aerodynamic (or turbine) control (Section 5.2.2), wave-to-turbine control 5.2.3, and wave-to-wire control (Section 5.2.4). Additionally, peak-shaving, or rated power, control (Section 5.2.5) may be considered to operate an OWC WEC at its rated power in CR_3 of Figure 5.2, if suitable actuators are installed. Finally, although the focus of the thesis is on device-side control, grid-side control aspects are briefly discussed in Section 5.2.6.

5.2.1 Hydrodynamic control

Hydrodynamic control for OWCs aims to optimise the wave-to-pneumatic energy conversion process, using two main approaches: Reactive (hydrodynamic) control (Section 5.2.1.1) and phase control (Section 5.2.1.2). Furthermore, some authors have also investigated the possibility to improve the hydrodynamic response of fixed OWCs by using (i) an air chamber with a moving frontal wall [240] or (ii) harbour walls at different opening angles [241]. However, solutions based on a variable chamber geometry have several critical issues and, ultimately, may not positively affect the LCoE. Firstly, the approaches proposed in [240, 241] solely focus on improving the wave-to-pneumatic energy conversion process, while ignoring the PTO, therefore their overall efficacy remains questionable. To this end, since the air turbine is designed to optimally operate at specific pressure levels (Section 5.1.4.2), a change in the chamber geometry [235] is expected to significantly impact on aerodynamic performance. Secondly, the study in [235] only considers regular waves, while disregarding a more realistic multi-frequency excitation scenario. Finally, although it is relatively cheap to build a moving frontal wall, or harbour walls, for small-scale model testing, developing such structures for a full-scale OWC is likely complex and expensive.

5.2.1.1 Reactive control

The conditions for optimal wave energy absorption can be expressed, in the frequency-domain, as an impedance matching problem [217]. If the external force, $F_{\mathrm{ex}}(\omega)$, of Equation (2.48) is equal to the PTO force, $F_{\mathrm{pto}}(\omega)$, then the intrinsic impedance of the considered WEC, $Z_{\mathrm{i}}(\omega)$, and the PTO impedance, $Z_{\mathrm{pto}}(\omega)$, can be defined (5.5), respectively, as

$$Z_{\mathrm{i}}(\omega) = H_{\mathrm{f2v}}(\omega)^{-1} = B(\omega) + \jmath\omega\left[M + A(\omega) - \frac{C_{\mathrm{h}}}{\omega^2}\right], \tag{5.4}$$

and

$$Z_{\mathrm{pto}}(\omega) = \frac{F_{\mathrm{pto}}(\omega)}{\dot{X}(\omega)}. \tag{5.5}$$

The optimum PTO impedance, which maximises the maximum power transfer from the WEC to the PTO, can be written [170], as

$$Z_{\mathrm{pto}}(\omega) = Z_{\mathrm{i}}^{*}(\omega), \tag{5.6}$$

where $()^*$ denotes the complex conjugate. From the control formulation in Equation (5.6), a corresponding control structure, known as approximate complex conjugate, which provides the exact conjugate at a single key frequency, can be derived [146].

For OWC WECs, the control formulation in Equation (5.6) can be alternatively expressed in terms of an optimal chamber pressure profile [158], as

$$\Delta\hat{p}(\omega) = \frac{\hat{q}_{\mathrm{e}}(\omega)}{2G_{\mathrm{owc}}(\omega)}, \tag{5.7}$$

where $G_{\mathrm{owc}}(\omega)$ is the OWC radiation conductance, while $\hat{q}_{\mathrm{e}}$ and $\Delta\hat{p}$ are the complex amplitudes of the excitation flow rate and pressure difference, respectively (further explained in Appendix A).

The control formulations in Equations (5.6) and (5.7) have some significant implications [146]:

- Such formulations are only valid at a *single frequency*, ω, although some attempts to generalise Equation (5.6) to multi-frequency case are reported, for instance, in [242].

- Since $G(\omega) \geq 0$, but $\Delta\hat{p}(\omega)$ and $\hat{q}_{\mathrm{e}}(\omega)$ (as well as $F_{\mathrm{pto}}(\omega)$ and $\dot{X}(\omega)$) can have opposite signs, to achieve impedance matching conditions, *reactive power* (i.e., power from the PTO to the system) is required. In other words, the PTO should be able to *supply* power for some parts of the wave energy conversion cycle.

- The control formulations of (5.6) and (5.7) do not take into account any physical constraint of the OWC/PTO.

- For the formulation in Equation (5.6), since $k_{\mathrm{r}}(t)$ (i.e., the radiation kernel) is causal, the dynamical system associated with Z_{i}^{*} is anticausal, meaning that future knowledge of the excitation force is required to compute the optimal control force (i.e., $k_{\mathrm{pto}}(t) = \mathcal{F}^{-1}(Z_{\mathrm{pto}}(\omega))$ is anticausal).

In OWC WECs, it is typically difficult to effectively supply reactive power (which differs from the definition of electrical reactive power in electric generators [222]), especially given the poor ability to provide hydrodynamic reactive power. As a matter of fact, due to their symmetric nature, self-rectifying air turbines do not operate efficiently as air compressors [243]. Furthermore, even if a variable-pitch turbine is used for compressing air, the peak reactive power can be significant and losses are not expected to be negligible for a bi-directional power transfer process [244].

In spite of the significant difficulties, a few papers on reactive hydrodynamic control for OWCs can be found. For instance, OWC hydrodynamic reactive control with a variable-pitch turbine, which is alternatively used to expand and compress air, is investigated in [244, 245]. Although wave power capture increases using a variable-pitch turbine, the required compression energy is significant [244]. Finally, an alternative method to provide reactive power for OWCs is considered in [246], where a lightweight piston is controlled to apply force to the OWC and improve the hydrodynamic response.

5.2.1.2 Phase control

Latching control A relatively simpler, passive (i.e., with no need for reactive power), alternative to reactive control was proposed by Budal and Falnes [247] in 1982. In this (suboptimal) control method, known as latching, the WEC is kept at a fixed position (or latched) during a part of the wave cycle, and subsequently released (unlatched), so that the WEC velocity is in phase with the wave excitation force. Figure 5.4 schematically shows how latching control works for an oscillating buoy subject to b) regular waves and c) irregular waves. Latching is a suboptimal control strategy, since it exclusively aims to satisfy the phase matching, and not also the amplitude matching, condition of Equations (5.6) and (5.7).

In OWC latching control, first studied in the 80s for fixed OWCs [248, 249], a valve in series with the turbine (or latching valve) is alternatively closed and opened to, respectively, latch and unlatch the water column. Closing the latching valve notably reduces OWC displacement, but does not completely eliminate water

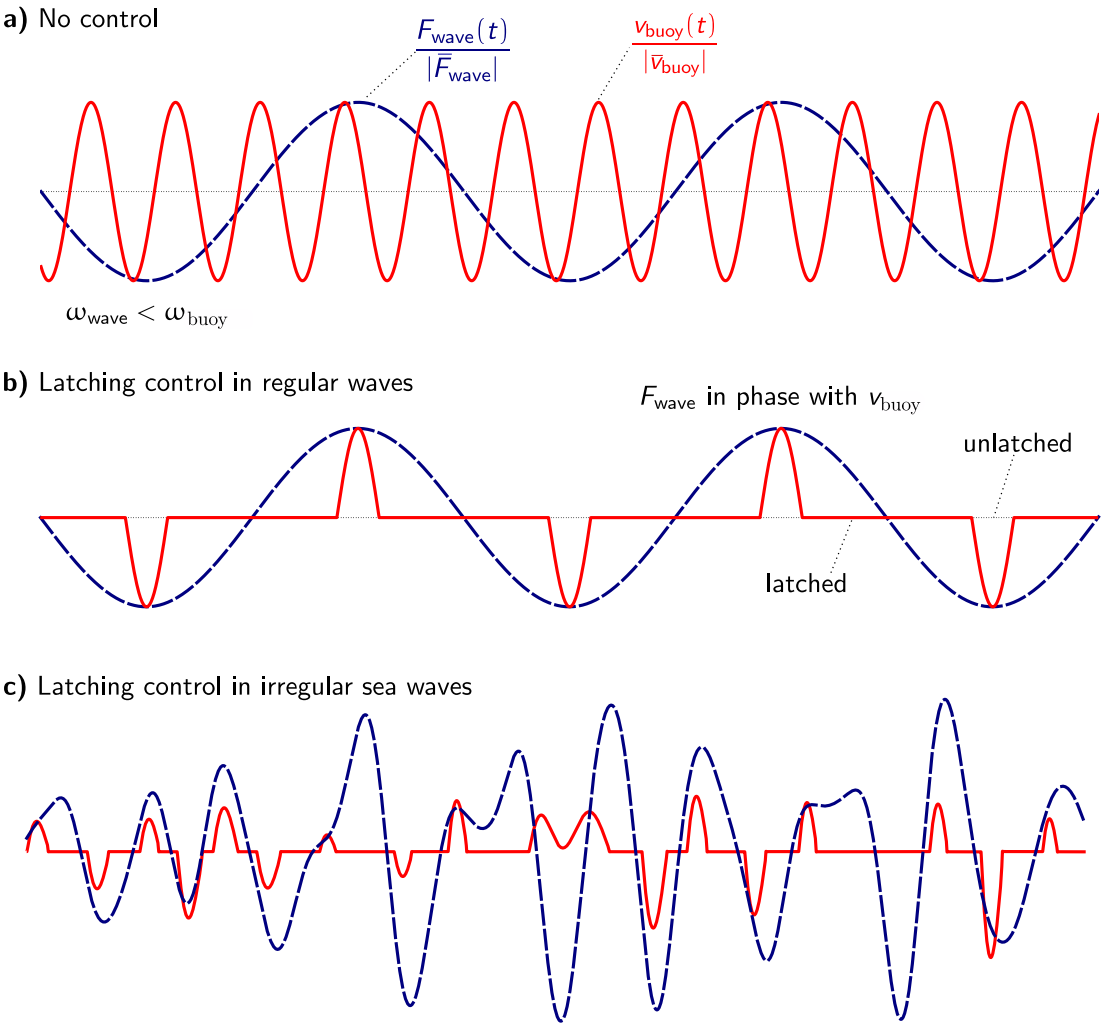

Figure 5.4: a) Typical velocity for an uncontrolled heaving buoy with a natural frequency, ω_{buoy}, higher than the frequency of the excitation force, ω_{wave}. b) Latching control to align the phases of the heave velocity, v_{buoy}, and the excitation force F_{wave}. c) Latching control for a heaving buoy subject to irregular sea waves. The terms $|\bar{v}_{\text{buoy}}|$ and $|\bar{F}_{\text{wave}}|$ are average normalising values for v_{buoy} and F_{wave}, respectively. Figure Source: [223].

column motion, due to the spring-like air compressibility effect. However, although air compressibility virtually eliminates the possibility of achieving perfect phase matching conditions, OWC latching can still significantly improve wave energy absorption, particularly when the incident wave period is higher than the OWC resonant period. In other words, latching can slow down the WEC motion to achieve resonance conditions.

It should be noted that the design and operation of a latching valve, which is essentially a high-speed stop valve (HSSV), for axial-flow air turbines is difficult, especially due to the large turbine duct diameter [238]. Salter [238] proposed a complex HSSV for the Wells turbine of the Pico power plant, but the valve was never installed. On the other hand, due to the small ducts connecting chamber, turbine,

and atmosphere, the biradial turbine can be equipped with a relatively simple and effective HSSV, which can be used for OWC latching.

An important issue in OWC latching is the high sensitivity of latching control performance to a delay between the control decision and the actual (mechanical) valve closure/opening [250]. Furthermore, as shown in [223], latching in irregular waves generally requires future knowledge of the excitation force to be effective. Wave forecasting over a sliding time window utilising, for instance, AR models or recurrent ANN algorithms, can potentially improve latching control [251]. Up-wave and AR methods for short-term wave forecasting for an OWC WEC are investigated in [252], while a review of wave forecasting techniques can be found in [253].

In [254, 255], some latching control strategies, for a spar-buoy OWC equipped with a biradial turbine, are devised. In [254], OWC latching control in regular waves is numerically tested. Unsurprisingly, latching in regular waves is much simpler than in irregular waves, since, in regular waves, the latching time can be optimised off-line and, subsequently, latching control is identically iterated at each wave cycle. Latching control is significantly more challenging in irregular waves, as shown, for instance, in [255], where two different latching strategies are designed. The first control approach in [255] provides superior performance in terms of converted wave power, but requires future knowledge of the excitation force, while the second latching control approach only requires easily measurable variables, such as rotational speed and air pressure. However, the first strategy in [255] does not take into account possible prediction errors in the excitation force, which may have a significant impact on control performance.

Latching control for an OWC spar-buoy is also considered in [223], where an unconstrained model predictive control (MPC) approach is tested in numerical simulation. The optimal control problem (i.e., find the optimal HSSV position to maximise wave power extraction) is solved over a receding-horizon (RH), where the excitation force is assumed to be known. Ultimately, wave power absorption only improves when the RH time window is sufficiently larger than the considered T_{e}. Finally, the unconstrained optimal control approach developed in [223] is extended in [256], to take into account the system constraints.

Declutching (or unlatching) control In declutching control, the PTO mechanism is disconnected from the WEC floater, therefore allowing free movement of the WEC during part of the wave cycle to accelerate the device motion. Subsequently, the PTO mechanism is engaged at the desired velocity [257]. Declutching is essentially the counterpart of latching and typically achieves resonant conditions when the incident wave period is shorter than the WEC resonant period.

In OWC declutching, the idea is to open a bypass valve to decouple the OWC/PTO and then close the valve at a later stage of the wave cycle [258]. However, to the best of the author's knowledge, declutching has not been considered for OWCs yet. The lack of attention on declutching control may be due to the fact that OWC declutching potentially leads to large water column excursions, which must be avoided to prevent green water from reaching the turbine blades. Arguably, another reason behind this literature gap is that bypass valves are typically slow, meaning that they are difficult to use in wave-by-wave control strategies, such as declutching control [64].

5.2.2 Aerodynamic control

Aerodynamic, or turbine, control aims to keep the turbine around its maximum efficiency point (i.e., Ψ_{mep} in Figure 3.4), or, equivalently, to optimise the pneumatic-to-mechanical energy conversion process, while neglecting the impact of Ω on hydrodynamic and electric performance. In essence, turbine control is a relatively simple setpoint following control problem for turbine rotational speed, as a function of Ψ [187]. The setpoint following problem for turbine rotational speed can be divided into (i) a setpoint determination problem (Section 5.2.2.1) and (ii) a setpoint tracking problem (Section 5.2.2.2).

In general, turbine rotational speed can be controlled by either the generator control torque alone, or, alternatively, T_{ctrl} used in combination with valves in series ($u_{\text{throttle/hsv}}$), and/or in parallel (u_{bypass}), with the turbine. In the literature, alternative names to turbine rotational speed control are sometimes utilised, such as torque control, or flow control (when control valves are used). However, it should be noted that control valves are used in CR_3 (Figure 5.2), but cannot be typically employed in CR_2 (except for latching control with the HSV of the biradial turbine). The reason behind this limitation is due to the dissipative nature of such valves: Opening a bypass valve, and/or partially closing a valve in series with the turbine, reduces the pneumatic power available in the air chamber. Therefore, in parallel, and in series, valves can be generally used only for peak-shaving control and to avoid turbine overspeeding. Nevertheless, some studies which consider throttle valves for controlling Ω in CR_2 can be found [259, 260], but the large aerodynamic losses induced by the valve partial closure are always ignored and, therefore, the value of such control strategies remains questionable.

5.2.2.1 Setpoint determination

To maximise turbine efficiency, one can generally use either a dynamic control approach or a steady-state control solution.

Dynamic TEM control The turbine MEP is an operating point at a fixed Ψ, denoted as Ψ_{mep} in Figure 3.4. Since Ψ_{mep} is unique, for a given Δp, the instantaneous rotational speed that maximises turbine efficiency is computed, from Equation (3.15), as

$$\Omega_{\text{mep}} = \sqrt{\frac{|\Delta p|}{\rho_{\text{air}} d_{\text{r}}^2 \Psi_{\text{mep}}}}. \tag{5.8}$$

One of the main issues in tracking Ω_{mep} (5.8) is the relatively large torque variation typically required by most controllers [261], especially due to significant inertia of the rotating parts [262], and the large fluctuations of Δp within each pseudo half-wave cycle. Additionally, when Δp tends to zero, Ω_{mep} also drops to zero (5.8), but such an intermittent behaviour is highly undesirable in terms of power supply quality and overall system efficiency. From an electrical power quality perspective, the control strategy should ideally take advantage of the kinetic rotational energy stored in the PTO, meaning that the PTO does not necessarily have to move in concert with the water column [61]. Since the available pneumatic power grows from zero to a peak value during each pseudo half-wave cycle, to improve the pneumatic-to-mechanical energy conversion process, it is essential to operate the turbine at Ψ_{mep} when the pneumatic power is maximal, while a less important issue concerns turbine operation at low efficiency, when pneumatic power is relatively small [60]. It should be also noted that, when Ω is driven to zero, the assumption of high Reynolds numbers, under which the dimensionless turbine model is derived, is violated. Therefore, tracking Ω_{mep} (5.8) generates a sort of *turbine modelling paradox*, since the control action cyclically drives the system to a condition where the model used for control is not valid!

In addition to the formulation in Equation (5.8), the value of Ω_{mep} can be also calculated, using Maeda's turbine model (Appendix A), from the mean axial airflow velocity, v_{x}. However, since it is difficult to directly measure v_{x} in real-time and without intrusive probes, v_{x} needs to be estimated from the mean flow rate, $q_{\text{turb}} = v_{\text{x}} A_{\text{turb}}$, computed using Δp. At the maximum efficiency point, the flow rate coefficient is $\Phi_{\text{mep}} = q_{\text{turb}}/(\Omega d_{\text{r}}^3)$, giving

$$\Omega_{\text{mep}} = \underbrace{\frac{A_{\text{turb}}}{\Phi_{\text{mep}} d_{\text{r}}^3}}_{\text{constant}} v_{\text{x}}. \tag{5.9}$$

Steady-state TEM control A possible TEM control algorithm, introduced in [263], can be derived considering the PTO dynamics at steady-state:

$$T_{\text{ctrl}}\Omega \approx P_{\text{turb}}. \tag{5.10}$$

When $\Psi = \Psi_{\text{mep}}$, the turbine power output is given by

$$P_{\text{turb}}^{\text{mep}} = \rho_{\text{air}}\Omega^3 d_{\text{r}}^5 \Pi\left(\Psi_{\text{mep}}\right). \tag{5.11}$$

Since $\rho_{\text{air}} \approx \rho_0$, $P_{\text{turb}}^{\text{mep}} \propto \Omega^3$ and, therefore, using Equations (5.10) and (5.11), the control torque which maximises turbine efficiency is

$$T_{\text{ctrl}}^{\text{tem}} = a_1\Omega^{a_2}, \tag{5.12}$$

where $a_1 = \rho_{\text{air}} d_{\text{r}}^5 \Pi\left(\Psi_{\text{bep}}\right)$ and $a_2 = 2$.

The unconstrained TEM control formulation in Equation (5.12) can be easily extended [183], as

$$T_{\text{ctrl}} = \min\left(a_1\Omega^{a_2}, \frac{P^{\text{rated}}}{\Omega}, T_{\text{ctrl}}^{\text{max}}\right), \tag{5.13}$$

to avoid exceeding P^{rated} (by detuning the controller) and $T_{\text{ctrl}}^{\text{max}}$. Furthermore, a supervisory safety valve controller is always required to avoid exceeding Ω^{max} [183]. In essence, when Ω^{max} is reached, a safety valve in series with the turbine is closed and, subsequently, reopened when Ω reduces below a customisable threshold value, Ω^{thr}. It should be noted that, for OWCs, torque detuning can be only applied by reducing T_{ctrl} (i.e., $T_{\text{ctrl}} < T_{\text{ctrl}}^{\text{tem}}$), meaning that Ω increases. Indeed, increasing the torque beyond $T_{\text{ctrl}}^{\text{tem}}$ is not a viable torque detuning solution, as Ω decreases and the turbine may stall (accompanied by a risk of damaging the turbine [264, 265] and high noise emission [143, 225]). Another possible option to reduce turbine speed may be to open a bypass valve to limit the pneumatic power in the air chamber [266].

Constant reference speed In addition to Ω_{mep} (5.8), another possible TEM control solution is to keep Ω fixed at a suitable constant reference value, $\Omega_{\text{ref}} = \text{constant}$, depending on the sea state. For instance, in [267], two different TEM control strategies are considered for the Wells turbine equipped on one of the U-shaped OWC chambers of the breakwater at Civitavecchia (Italy). In the first approach, the rotational speed reference value is a function of the sea state only, meaning that, for each sea state, Ω_{ref} is constant, while the second strategy considers $\Omega_{\text{ref}} = \Omega_{\text{mep}}$ (5.8).

Ultimately, although TEM control using a constant SS-based Ω_{ref} may provide, especially for high-inertia turbines, satisfactory performance in relatively low-energy

SSs [261], where pressure oscillations are small, such an approach cannot be effectively utilised in medium-to-high energy SSs (i.e., the most relevant operating conditions). Indeed, with large pressure oscillations, a turbine working at a constant reference speed operates, for most of the time, far from Ψ_{mep} (and, for a Wells turbine, Ψ may also often exceed Ψ_{stall}). Furthermore, to infer the SS-based Ω_{ref}, the sea state needs to be estimated using, typically, data collected from wave probes. Therefore, besides the increase in CapEx and OpEx due to the wave probes, if the sea state estimate is not accurate, Ω_{ref} is incorrect and the benefit of turbine control is potentially compromised.

5.2.2.2 Setpoint tracking

To track the reference speed, many possible controllers can be employed. For OWCs, the two most popular solutions are Proportional-Integral-Derivative (PID) control and sliding mode control (SMC), which have quite different characteristics, with the broad distinction of linear/nonlinear, respectively.

Aside from the type of controller, tracking of the instantaneous rotational speed is also influenced by the PTO inertia. Low-inertia turbines require small torque variations to operate close to Ψ_{mep} [262] although, even with a relatively high-inertia turbine, if enough T_{ctrl} is applied, it may be feasible to track relatively rapid variations in the speed reference. However, larger torque variations require a more powerful (and expensive) electric generator, which may consequently have a low capacity factor (i.e., the generator may be oversized). To this end, since the high-level control objective is LCoE minimisation, increasing the generator size may not be an ideal solution.

PID controllers PID control is a well-known intuitive control technique for setpoint-following feedback loops [268]. As such, PID control has been considered for some OWC subsystems, including the primary function of rotational speed control and, at a lower level, servo control for valve positioning. Defining $e(t)$ as the difference between the actual value of the variable to be tracked (e.g., rotational speed) and the desired reference value of that variable, the control input provided by a PID is given by

$$u_{\text{pid}} = K_{\text{p}} e(t) + K_{\text{i}} \int_0^t e(\tau)\,\mathrm{d}\tau + K_{\text{d}} \frac{\mathrm{d}e(t)}{\mathrm{d}t}, \tag{5.14}$$

where K_{p}, K_{i}, and K_{d} are, respectively, the proportional, integral, and derivative gains of the PID controller.

Although satisfactory performance may be achieved using PID control, and PID tuning is relatively straightforward, linear controllers may not be the best solution for rotational speed control on OWCs, especially since the OWC W2W system dynamics are, in general, nonlinear. Additionally, WECs operate in different irregular SSs, for which the relatively limited envelop characterising typical linear operation/control may not suffice [269]. To better deal with multiple irregular SSs, some solutions which utilise linear controllers with adaptive gains have emerged [270, 271]. However, such adaptive linear controllers typically require the solution, in real-time, of an optimisation problem to obtain the optimal control gains, with an associated increase in the computational burden.

In the literature, many studies on TEM control with PID controllers can be found, where the main difference is generally in the tuning method of the PID controller and/or, sometimes, in the type of considered actuators. For instance, in [259, 260], the rotational speed of a Wells turbine is controlled, initially using T_{ctrl} alone and then $T_{\text{ctrl}}/u_{\text{throttle}}$, with PID-like controllers tuned with the closed-loop Ziegler–Nichols (ZN) method. Apart from the closed-loop ZN method, a variety of PID tuning algorithms/methods can be found in the literature [272], such as the grouped grey wolf (GGW) optimisation [271], ANNs [273, 274, 275], zero-pole cancellation (ZPC) [262, 276], harmony search (HS) [277], self-adaptive global-best harmony search (SGHS) [278], particle swarm optimisation (PSO) [279], fractional PSO memetic (FPSOM) [279], and fuzzy gain scheduling (FGS) [277]. Typically, PID controllers with adaptive tuning methods, such as FGS [277], provide better tracking performance, although the complexity of the tuning method increases significantly. Ultimately, the use of sophisticated tuning methods only marginally improves the performance of PID controllers, while simpler tuning techniques, such as the closed-loop ZN [259, 260], can still provide satisfactory performance, at least for the sea state in which the controller is tuned.

Sliding mode controllers A possible attractive nonlinear control approach for tracking the turbine rotational speed is SMC [280, 281], especially due to its ability to deal with system uncertainties, unmodelled dynamics, nonlinear system dynamics, and external disturbances. In SMC, a sliding variable, σ_{smc}, is defined, as a function of the system states, so that the control objectives are satisfied when $\sigma_{\text{smc}} = 0$. The condition $\sigma_{\text{smc}} = 0$ defines a sliding surface in the state space [281]. For OWC aerodynamic control, the sliding variable may be defined as

$$\sigma_{\text{smc}} = \Omega - \Omega_{\text{ref}}. \tag{5.15}$$

To obtain the control law, σ_{smc} is differentiated until the manipulated variables (e.g., quadrature voltage or quadrature current of the generator [282, 283]) explicitly appear. The order of the derivative of σ_{smc} determines the order of the SMC approach. With first-order SMC, $\dot{\sigma}_{\text{smc}}$ is computed and, subsequently, the SMC gains are tuned (using any of the available tuning methods in the literature) to make the system converge, robustly and in a finite time, to the condition $\sigma = 0$ [281]. In general, in a SMC scheme of n-*th* order, $\mathrm{d}^n\sigma_{\text{smc}}/\mathrm{d}t^n$ is calculated and, then, the control action makes the system converge to the condition $\sigma_{\text{smc}} = \dot{\sigma}_{\text{smc}} = \ldots = \mathrm{d}^{n-1}\sigma_{\text{smc}}/\mathrm{d}t^{n-1} = 0$.

Unsurprisingly, the tracking performance with SMC [284] is significantly superior to that of PID controllers [279]. In general, depending on how the SMC is tuned, as well as on torque limits with respect to the inertia of the rotating parts, SMC may present high peaks in T_{ctrl} [261]. To this end, higher control torque peaks typically lead to higher peak-to-average power ratios and, therefore, to inferior power quality.

In the literature, SMC has been successfully implemented for OWC aerodynamic control with biradial turbines [285] and Wells turbines [282, 283], coupled with different electric generators, such as DFIGs [285, 282] and PMGs [283]. It should be noted that first-order SMC schemes suffer from chattering [285], a phenomenon that causes high-frequency oscillations of the manipulated variable. To ameliorate chattering, therefore reducing the high-frequency oscillations, second-order SMC (SOSMC) using, for example, a super twisting algorithm (STA) has been considered for OWCs [282]. Finally, similarly to the case of PID controllers, adaptive tuning methods, such as FGS [286], have been considered for SMC as well, primarily to improve tracking performance and reduce chattering.

Other possibilities for rotational speed tracking Model predictive control, relatively popular for other WEC types [50], has also been considered for OWC TEM control [287, 288]. In general, MPC-based strategies can provide good tracking performance for a constant rotational speed reference [287], as well as for a time-varying reference speed value [288]. The main advantage of MPC, compared to the most popular alternatives in TEM control (i.e., PID control and SMC), is the possibility to naturally incorporate physical constraints, which can be easily taken into account in the optimisation problem [52]. Arguably, the main disadvantage of MPC is the relatively high computational cost [289], specifically since MPC requires prediction, at each time step, of some future states of the system over a receding-horizon (RH). Therefore, real-time control using MPC may be challenging due to the significant computational burden, especially when long prediction horizons are employed.

In addition to SMC, alternative nonlinear controllers, which are suitable for OWC TEM control, include, but are not limited to, backstepping (BS) [290, 291] and fuzzy logic controllers (FLC) [292].

5.2.3 Wave-to-turbine control

Wave-to-turbine (W2T) control aims to optimise the OWC wave-to-mechanical energy conversion process. In the literature, OWC W2T control is carried out using either optimisation-based control techniques (or optimal control, e.g., [293, 62]), or a simple steady-state control solution based on a generalization of Equation (5.12), where the parameters a_1 and a_2 are adjusted to consider the hydrodynamic/aerodynamic interaction [294, 295].

As already mentioned, W2T control is particularly important for Wells turbines, given the possibility to improve (or deteriorate) hydrodynamic performance through turbine rotational speed modulation. For instance, W2T control using a RH pseudospectral (PS) optimal control strategy, for a Wells turbine, is developed in [62] (further discussed in Chapter 7). Despite the relative ineffectiveness of W2T control on impulse turbines, some papers on W2T optimal control for biradial turbines using MPC [293, 296], and inverse fuzzy model (IFM) [297], can be found.

5.2.4 Wave-to-wire control

Similarly to W2T control, the objective of W2W control is to optimise the overall (wave-to-wire) energy conversion process of the OWC. For Wells turbines, simple W2W steady-state [60, 61], and more sophisticated W2W receding-horizon pseudospectral (RHPS) [63], control solutions have emerged (further discussed in Chapters 6 and 7, respectively).

5.2.5 Peak-shaving control

In CR_3, the available pneumatic power in the air chamber can be large and, if a suitable peak-shaving control approach is utilised, the OWC can operate close to its rated power; otherwise, the device must be shut down to avoid major failure. In essence, peak-shaving control aims to extend the OWC operational range, consequently increasing its capacity factor.

There are typically two methods to apply peak-shaving control on OWCs, namely (i) methods based on control valves (Section 5.2.5.1) or (ii) methods based on speed control detuning (Section 5.2.5.2). In the methods based on control valves, the available pneumatic power to the turbine is limited by opening a bypass valve, or by partially closing a valve in series with the turbine. With speed control detuning methods, the rotational speed controller, whose aim is to maximise wave power extraction in CR_2, is detuned so that the OWC system operates away from the maximum power point in CR_3.

5.2.5.1 Methods based on control valves

Methods based on bypass valves A bypass, or relief, valve can be partially, or fully, opened to limit the available pneumatic power in the air chamber. In [298], a possible control law for the bypass valve of the Pico power plant is proposed. Such a control law regulates the bypass valve position depending on the instantaneous pressure values, Δp, in relation to a prescribed threshold value, Δp^{thr}. The numerical simulation shows that, if the bypass valve has a sufficient dimension, pneumatic power can be effectively dissipated [298]. However, to date, due to the slow actuation system of real bypass valves, the wave-by-wave peak-shaving control approach proposed in [298] is difficult to use in practice. To counteract possible issues due to the finite time-response of the bypass valve, wave prediction can be considered [252], although it does not completely solve the problem. Alternatively, the bypass valve position can be controlled depending on the sea state, or, equivalently, on the available wave energy [64]. Such a SS-based control approach for peak-shaving control with a bypass valve is described in Chapter 8.

Methods based on throttle valves and HSVs Throttle valves are installed in series with the turbine to reduce q_{turb} and, consequently, limit the available pneumatic power to the turbine [260, 277, 279]. Similarly to the bypass valve, throttle valves cannot be effectively employed for wave-by-wave peak-shaving control, due to the relatively slow actuation speed. Furthermore, an undesirable side effect of throttle valves is the non-axisymmetric air flow downstream of these types of valves, which significantly reduces turbine performance for one of the airflow directions. In other words, throttle valves induce large aerodynamic losses in either inhalation, or exhalation, making accurate peak-shaving control significantly more difficult. On the other side, bypass valves reduce pneumatic power without directly disturbing the turbine air flow, meaning that the dissipative action is equivalent during the air inhalation and exhalation.

As already mentioned, the small HSV of the biradial turbine can be effectively used for wave-by-wave peak-shaving control [256, 299, 300], particularly due to its relatively fast actuation speed. Additionally, the HSV introduces only a local disturbance, which has a negligible effect on the airflow at the turbine rotor level. A possible peak-shaving control algorithm, based on the instantaneous rotational speed value, for the HSV of a biradial turbine, was validated in sea trials at the Mutriku OWC during the H2020 OPERA project [299].

5.2.5.2 Methods based on speed control detuning

A possible alternative to peak-shaving through control valves is to consider rotor blade pitch control, widespread in wind energy [301]. Pitch control reduces the turbine power by decreasing the angle of attack of the rotor blades. However, since pitch control requires a turbine with a relatively complex variable-pitch rotor, likely increasing CapEx and OpEx, it has never been applied on OWCs.

In addition to pitch control, torque detuning can be used to avoid exceeding P^{rated} (see, for instance, [183]). However, torque detuning alone does not typically provide enough control flexibility to keep the device working at its rated power, while also avoiding exceeding $\Omega^{\max}$ [64].

5.2.6 Grid-side control

Although this thesis mainly focuses on device-side control strategies for OWC WECs, some studies concerning OWC grid-side control are briefly discussed. Grid-side, and energy storage, control cope with grid requirements, which primarily cover power quality aspects, FRT capabilities, and, more broadly, the overall stability of the power grid. For an overview of grid integration aspects for wave energy conversion systems, the interested reader is referred to [71].

In [302, 303], some control strategies to improve the FRT capability during balanced voltage drops in the transmission system, for an OWC system equipped with a DFIG coupled with a Wells turbine, are developed. During a balanced fault, which may be due to natural causes, faulty components, or cyber attacks, an equal (symmetric) voltage drop on all three phases of the grid appears [304]. To counteract such a fault, the grid-side converter is controlled, using, for instance, PID [302] or ANN-based [303] controllers, to supply electric reactive power to the grid.

In [305], a MPC scheme is developed to cope with open-switch faults in a B2B power converter. In open-switch faults, which may be due to electromagnetic interference or material ageing, some of the converter switches, which are used to modulate the electric signals, are unavailable. Furthermore, some MPC strategies have been also considered to improve power quality for grid-side converters of OWC devices [287, 306, 307, 288].

Finally, some studies on electrical energy storage systems for power smoothing, using ultracapacitors [276], supercapacitors [308, 309], and Li-ion batteries [287], are also found in the literature. In opposition to other WEC types, power smoothing on OWCs may be less difficult, especially due to the possibility of smoothing large power peaks on the device-side through, for instance, bypass valves [226].

5.3 Summary

For each device-side control objective presented in Section 5.2, the corresponding OWC control strategies found in the literature are summarised in five distinct tables, namely Tables 5.1 (hydrodynamic control), 5.2 (aerodynamic control), 5.3 (W2T control), 5.4 (W2W control), and 5.5 (peak-shaving control). Reading from the left to the right, each table shows:

- The control approach used to achieve the considered control objective.
- The type of turbine, namely Wells (W), biradial (B), axial-flow impulse (I), and unidirectional (U).
- The corresponding reference.
- The type of test: Numerical simulation (Num) and/or experimental test (Exp).
- The year of publication.
- The type of controller, if specified.
- The manipulated input used by the control strategy.

It should be noted that each publication may consider multiple types of turbines, types of tests, controllers, and/or manipulated inputs.

As clarified by the evident different lengths of the five summary tables, the focus is predominantly on TEM control, especially due to the importance of turbine efficiency and also to the relative simplicity of the TEM control problem. In more recent years, the attention towards more complete control objectives has increased and, consequently, some W2T (Table 5.3) and W2W (Table 5.4) control strategies have emerged. Furthermore, more consideration has been recently given also to other OWC control-related issues, such as peak-shaving control (Table 5.5), turbine noise emissions [143, 225], and, to some extent, power quality [287, 306, 307, 288]. In relation to impulse turbine rotational speed control, rather than focusing on W2T and W2W control, it is arguably more important to optimise the pneumatic-to-wire (P2W) energy conversion process. For instance, in [310], the rotational speed of a biradial turbine is modulated to optimise the P2W performance (i.e., air turbine and generator), using an improved version of Equation (5.13), where a_1 and a_2 are functions of Ω.

Some OWC control aspects which remain, to date, relatively unexplored are device-side FTC [311], as well as data-based and data-driven control [312]. On the one hand, FTC allows the system to operate in the presence of some faults,

specifically faults which the system is tolerant to. Therefore, although the system may not necessarily work at its full potential under fault conditions, FTC can improve maintenance operation flexibility and, consequently, limit any increase in LCoE due to power production interruptions. To this end, it may be also interesting to consider some more exotic OWC PTO configurations, such as a twin unidirectional turbine configuration (see, for instance, [313, 314, 315]), which provides natural redundancy in the PTO system. With twin unidirectional turbines, which can be either axial-flow [313, 314] or radial-flow [315] turbines, one turbine works during inhalation, while the second turbine operates in the exhalation phase (see, for instance, Figure 5.5). Therefore, if one of the turbines fails, the OWC can still harvest energy during half of the wave pseudo-cycle. On the other hand, data-based and data-driven control techniques offer the possibility to exploit, at different levels of the WEC control synthesis procedure, static and dynamic datasets, respectively [206].

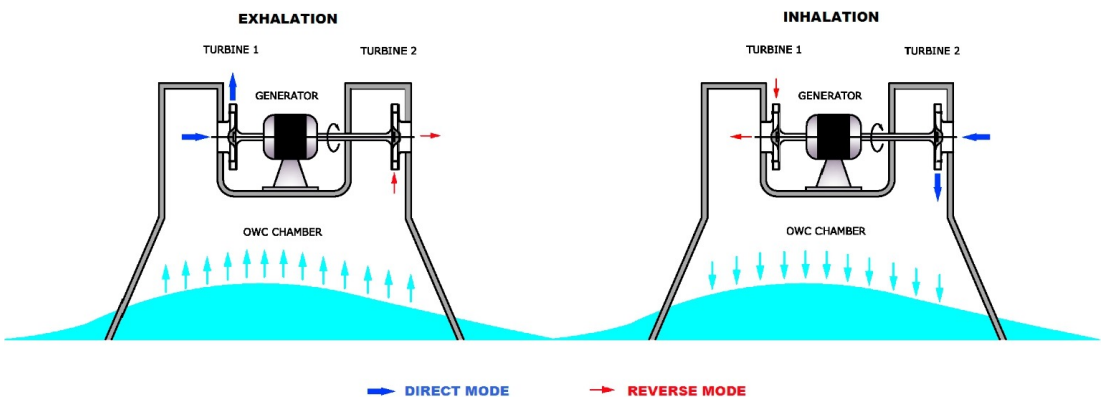

Figure 5.5: Schematic representation of a twin unidirectional (radial-flow) turbines PTO configuration. Source: [315].

In relation to high-level control objectives, as already stated in Section 5.1.4, CCD techniques are vital to minimise the LCoE and, to this end, a possible CCD approach for OWCs is devised in Chapter 8 of this thesis. However, some complex issues related to WEC control, such as the evaluation of the impact of the control action on OpEx [316] and on the WEC lifetime, still need substantial investigation.

Table 5.1: Summary table on OWC control strategies, part 1 of 5: Hydrodynamic control.

Control approach	Turbine type	Ref.	Test type	Year	Controller	Manipulated input
Reactive control						
	-	[246, 317]	Exp	1991	-	-
	W	[245, 244]	Num	2003	-	u_{pitch}
Latching control						
	B	[254, 255]	Num	2013-14	-	u_{hsv}
	B	[223, 256]	Num/Exp	2016	MPC	u_{hsv}
	W	[318]	Num	2016	-	u_{hsv}
	B	[319]	Num	2017	-	u_{hsv}

Table 5.2: Summary table on OWC control strategies, part 2 of 5: Aerodynamic, or TEM, control. The dashed-horizontal lines divide PID, SMC, and other controllers.

Control approach	Turbine type	Ref.	Test type	Year	Controller	Manipulated input
Steady state						
	W	[263]	Num	1999	-	T_{ctrl}
	W	[187, 74]	Num	2002-04	-	T_{ctrl}
	B/W	[294]	Num	2016	-	T_{ctrl}
	B	[119]	Num/Exp	2016		
					-	$T_{\text{ctrl}}/u_{\text{bypass}}$
					-	$T_{\text{ctrl}}/u_{\text{hsv}}$
	B/W	[183]	Num/Exp	2019	-	$T_{\text{ctrl}}/u_{\text{hsv}}$
	U	[320, 321]	Exp	2020-21	-	T_{ctrl}
	W	[322]	Num	2022	-	$T_{\text{ctrl}}/u_{\text{hsv}}$
Dynamic control						
	W	[259]	Num	2011		
					PI	T_{ctrl}
					ZN–PID	u_{throttle}
	W	[273]	Num	2011	ANN–PI	T_{ctrl}
	W	[260, 323]	Num/Exp	2011–13	PI/PID	$T_{\text{ctrl}}/u_{\text{throttle}}$
	W	[262, 276]	Num/Exp	2013–15	ZPC–PI	T_{ctrl}
	W	[267]	Num	2016	P	T_{ctrl}
	W	[279]	Num	2017		
					PSO–PID	u_{throttle}
					FPSOM–PID	u_{throttle}
	W	[277]	Num	2019		
					HS–PID	u_{throttle}
					FGS–PID	u_{throttle}
	I	[271]	Num	2019	GGW–PID	T_{ctrl}
	W	[274]	Num	2020	ANN–PI	T_{ctrl}
	W	[278]	Num	2020	SGHS–PID	u_{throttle}
	W	[324]	Num	2020	PSO–PID	u_{throttle}
	W	[275]	Num	2020	ANN–PI	u_{throttle}
	W	[269]	Num	2012	SMC	T_{ctrl}
	W	[325]	Num	2018	SMC	T_{ctrl}
	W	[284]	Num	2018	SMC	T_{ctrl}
	W	[326]	Num	2018	SMC	T_{ctrl}
	B	[285]	Num	2019	SMC	$T_{\text{ctrl}}/u_{\text{hsv}}$
	I	[327]	Num	2019	GGW–SOSMC	T_{ctrl}
	W	[286]	Num	2020	FGS–SMC	T_{ctrl}
	W	[282]	Num	2020	SOSMC	T_{ctrl}
	B	[328]	Num	2020	SOSMC	T_{ctrl}
	B	[261]	Num	2021	SOSMC	$T_{\text{ctrl}}/u_{\text{hsv}}$
	W	[329]	Num	1999	-	$u_{\text{bypass}}/u_{\text{throttle}}$
	I	[330, 331]	Num	2015–16	-	T_{ctrl}
	U	[287]	Num	2017	MPC	T_{ctrl}
	W	[326]	Num	2018	BS	T_{ctrl}
	W	[291]	Num	2020	BS	T_{ctrl}
	W	[292]	Num	2021	FLC	T_{ctrl}
	W	[288]	Num/Exp	2021	MPC	T_{ctrl}
	W	[332]	Num	2023	FLC	T_{ctrl}
	W	[333]	Num	2023	MPC	T_{ctrl}

Table 5.3: Summary table on OWC control strategies, part 3 of 5: W2T control.

Control approach	Turbine type	Ref.	Test type	Year	Controller	Manipulated input
Steady state						
	W/B	[294]	Num	2016	-	T_{ctrl}
	B	[295]	Num	2017	-	T_{ctrl}
Dynamic control						
	B	[293]	Num	2022	MPC	T_{ctrl}
	B	[297]	Num	2023	IFM	T_{ctrl}
	B	[296]	Num	2023	MPC	T_{ctrl}
	W	[62]	Num	2024	PS	T_{ctrl}

Table 5.4: Summary table on OWC control strategies, part 4 of 5: W2W control.

Control approach	Turbine type	Ref.	Test type	Year	Controller	Manipulated input
Steady state						
	W	[60]	Num	2023	-	T_{ctrl}
	W	[61]	Num	2023	LC	T_{ctrl}
Dynamic control						
	W	[63]	Num	2024	PS	T_{ctrl}

Table 5.5: Summary table on OWC control strategies, part 5 of 5: Peak-shaving control.

Control approach	Turbine type	Ref.	Test type	Year	Controller	Manipulated input
Methods based on bypass valves						
	W	[263]	Num	1999	-	u_{bypass}
	W	[298]	Num	2003	-	u_{bypass}
	W	[64]	Num	2023	-	u_{bypass}
Methods based on HSVs						
	B	[256, 299]	Num	2016–17	-	u_{hsv}
	B	[261]	Num	2021	-	u_{hsv}
	B	[300]	Num/Exp	2023	-	u_{hsv}

6

Static-efficiency-based control for oscillating water columns

Contents

6.1 Study case definition 131
6.2 Control system design 133
6.2.1 Effect of turbine rotational speed 134
6.2.2 Control system design 135
6.3 Result and discussion 138
6.3.1 Discussion of the results 138
6.3.2 Main control co-design aspects 141
6.4 Conclusions 143

As stated in Section 5.3, the vast majority of OWC control strategies in the literature focus on a simplified control objective, namely turbine efficiency maximisation. The significant attention on TEM control is due to three main reasons:

1. The lack of suitable actuators makes traditional WEC hydrodynamic control [146] (which, for OWC WECs, corresponds to the optimisation of the wave-to-pneumatic energy conversion process) more difficult for OWCs [57].

2. To obtain satisfactory levels of energy production, it is essential to to keep the turbine operating around its MEP [183].

3. The simplicity of TEM control, being a standard setpoint following control problem for the turbine rotational speed, is attractive.

These motivations have steered researches to optimise the pneumatic-to-mechanical energy conversion process, while ignoring the effect of turbine rotational speed on hydrodynamic and electrical performance [51]. Although TEM control may effectively work with impulse turbines, for which the hydrodynamic/aerodynamic interaction is negligible, impulse turbines do not efficiently operate on OWCs where the pressure oscillations are relatively small [67] and, in this case, a Wells turbine should be utilised. Hypothetically, a device developer may design an OWC chamber that, for a specific deployment site, works efficiently with an impulse turbine. However, such a design solution does not necessarily guarantee the highest economic benefit, meaning that an OWC equipped with a simpler (and cheaper) Wells turbine may lower the LCoE. Since Wells turbine damping is a function of Ω, neglecting the impact of turbine speed on the hydrodynamic subsystem is not a realistic assumption [56]. In other words, Wells turbine rotational speed control affects the OWC hydrodynamic performance and, therefore, rotational speed can, and should, be modulated to improve the overall W2W efficiency of the OWC system (as opposed to maximise only turbine efficiency). Finally, alongside hydrodynamic and turbine performance, the characteristics of the electric generator should also be considered in the complete W2W system (Figure 3.1).

In this chapter, a steady-state W2W control strategy for a Mutriku-like [76] OWC system, through Wells turbine rotational speed modulation, is devised. The W2W control problem for WECs can be generally tackled in two different ways. The first approach is to solve an online nonlinear constrained optimisation problem. A number of solutions to such optimal control problems for OWCs [62, 63], and other WEC types [334, 335], have emerged, but the resulting real-time numerical optimisation problems are complex and, in many cases, convexity is not guaranteed. In contrast to global optimisation methods, the steady-state W2W control strategy considered in this chapter follows a somewhat more traditional [49] and simpler method based on static efficiencies. More specifically, the effect of turbine rotational speed on the OWC W2W system performance is analysed, and a possible generator power curve for W2W efficiency maximisation is obtained by solving a static optimisation problem. Furthermore, the proposed steady-state W2W control approach also allows a direct comparison (Figure 6.5(a)) with traditional TEM control.

The structure of this chapter is organised as follows. In Section 6.1, some modelling aspects of the Mutriku-like OWC considered for the study case are presented, while the control system design approach is described in Section 6.2. Finally, the discussion of the results and main conclusions are provided in Sections 6.3 and 6.4, respectively.

6.1 Study case definition

To asses the performance of the proposed W2W control approach, a Mutriku-like OWC is selected as a relevant study case, especially since the Mutriku facility is a well-known, currently operative, grid-connected power plant, which also serves as a test site for air turbine rotational speed control. For this study, the considered manipulated inputs are the generator control torque, T_{ctrl}, and the safety valve position, u_{safety}, which are the essential inputs required to apply W2W control through turbine rotational speed modulation.

The OWC system dynamics are modelled using the set of equations introduced in Chapter 3, namely the modelling equations for the OWC hydrodynamic subsystem (3.2) and radiation force (3.3),

$$\begin{aligned}(m_{\text{p}} + A_p^{\infty})\dot{v} &= -\rho_{\text{w}} g S_{\text{owc}} z - S_{\text{owc}} \Delta p + f_{\text{ex}} - \int_{-\infty}^{t} k_{\text{r}}(t-\tau)\, v(\tau)\, \mathrm{d}\tau, \\ \dot{z} &= v,\end{aligned} \tag{6.1}$$

air chamber (from Equation(3.8), with $w_{\text{bypass}} = 0$),

$$\frac{\dot{p}_{\text{c}}}{p_{\text{c}}} = -\gamma \left(\frac{\dot{V}_{\text{c}}}{V_{\text{c}}} + \frac{w_{\text{turb}}}{m_{\text{c}}} \right), \tag{6.2}$$

and PTO (from Equation (3.12), with $P_{\text{fr}} = 0$),

$$\frac{\mathrm{d}}{\mathrm{d}t}\left(\frac{1}{2} I \Omega^2\right) = P_{\text{turb}} - T_{\text{ctrl}}\, \Omega. \tag{6.3}$$

The frequency dependent hydrodynamic parameters, $A_{\text{p}}(\omega)$, $B_{\text{p}}(\omega)$, $|\hat{F}_{\text{ex}}(\omega)|$, and $\angle \hat{F}_{\text{ex}}(\omega)$, for one of the Mutriku OWC units are shown in Figure 3.3. To obtain the frequency dependant hydrodynamic functions, the BEP [158], described in Section 2.2, is solved using the WAMIT software [164].

As already mentioned in Section 2.2.3.1, a suitable (and less computationally expensive) linear state space model needs to be adopted to approximate the radiation convolution integral in Equation (6.1). To this end, the FOAMM toolbox [336], which carries out a MM-based identification approach [178] (using frequency-domain data), is utilised to identify the matrices A_{r}, B_{r}, and C_{r} of the radiation LTI subsystem in Equation (2.54), for the heave mode of the considered OWC. A significant advantage of the FOAMM toolbox, over other possible model reduction techniques, is the fact that the user can select the frequencies between which the radiation model interpolates the frequency-domain data, noting that exact matching is obtained at the chosen frequency points. The order of the identified radiation model, n_{r}, is then twice the number of interpolation points, shown in Figure 6.1(a). For completeness,

Table 6.1: OWC system parameters.

Parameter	Value	Unit	Parameter	Value	Unit
m_{p}	27748	kg	I	3.06	kg m^2
A_{p}^{∞}	71618	kg	κ_{W}	0.775	-
ι	4.5	m	V_0	144	m^3
d_{r}	0.75	m	S_{owc}	19.35	m^2

Figure 6.1(b) compares the radiation kernel from WAMIT, $k_{\mathrm{r}}(t)$, and its corresponding approximation obtained using FOAMM toolbox, with $n_{\mathrm{r}} = 18$.

The dimensionless model for the Wells turbines installed at Mutriku is shown in Figure 3.4(a), while the Wells turbine damping is given in Equation (3.18). To compute the electric power, the dimensionless generator efficiency map in Figure 6.2 [110] is used, and electric power is computed as $P_{\mathrm{elec}} = P_{\mathrm{turb}}\eta_{\mathrm{gen}}$, where η_{gen} is the electric generator efficiency. Finally, the system parameters in Table 6.1 complete the W2W model of the Mutriku-like OWC considered in this chapter for control design.

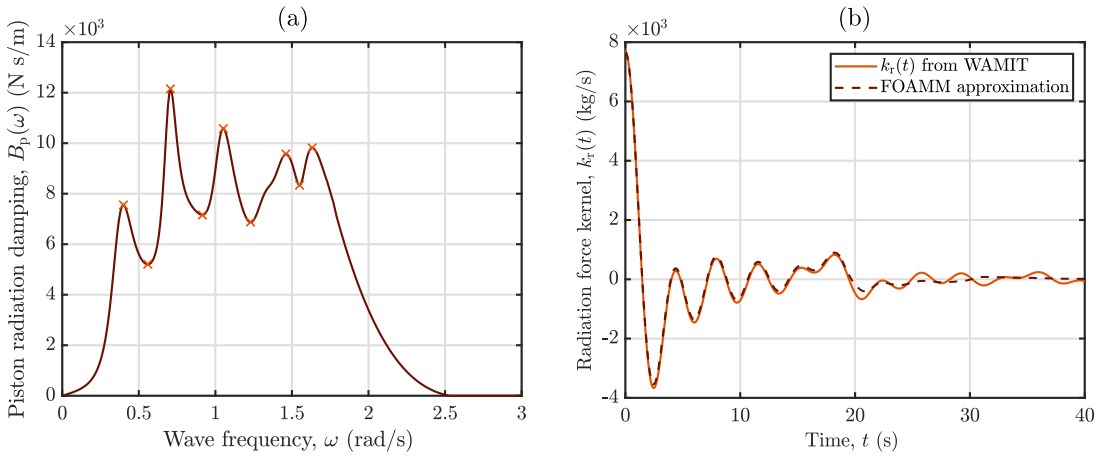

Figure 6.1: Radiation convolution approximation with FOAMM. (a) Radiation damping with the interpolation points selected in FOAMM, indicated by the orange crosses; (b) radiation kernel from WAMIT and FOAMM approximation.

To characterise the typical wave climate at the Mutriku power plant, eight different irregular sea states (SS1 - SS8) [76], generated from JONSWAP spectral density functions [180] (Equation (2.57)) with peak shape parameter $\gamma_{\mathrm{J}} = 3.3$, are considered. The significant wave height, H_{s}, and peak period, T_{p}, of the considered sea states at Mutriku [76] are listed in Table 6.2. It should be noted that the stochastic parameters characterising the eight SSs, SS1 - SS8 in Figure 6.3(a), result from wave measurements gathered at an undisturbed location, which is

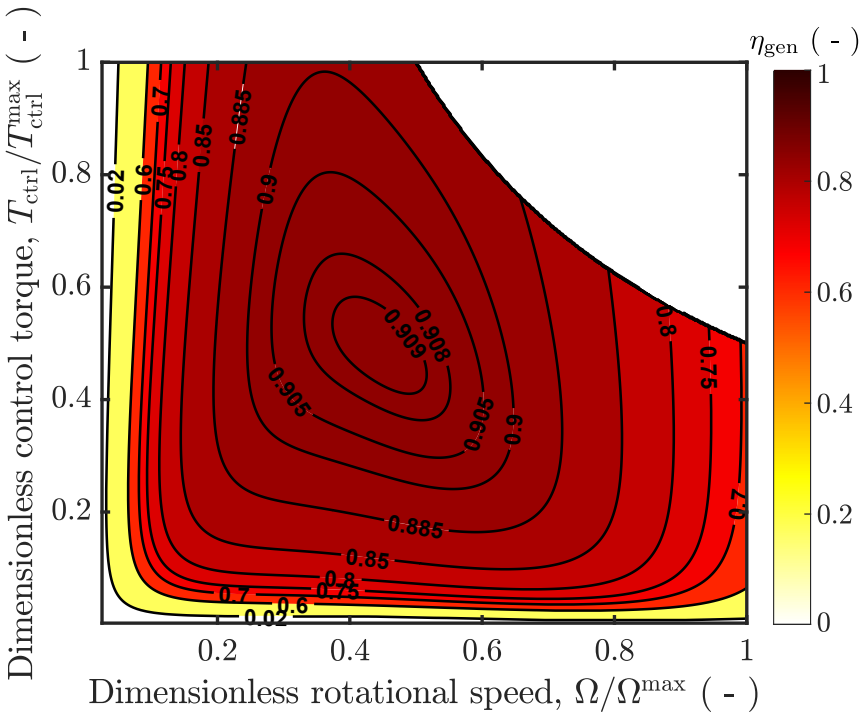

Figure 6.2: Electric generator efficiency, η_{gen}, as a function of the dimensionless rotational speed, $\Omega/\Omega^{\max}$, and the dimensionless control torque, $T_{\text{ctrl}}/T_{\text{ctrl}}^{\max}$. $\Omega^{\max}$ and $T_{\text{ctrl}}^{\max}$ are, respectively, the maximum allowable rotational speed and the maximum control torque. Adapted from [110].

relatively far from the actual location of the Mutriku facility. To take into account the wave shoaling effect[1] characterising the ocean waves at Mutriku power plant [337], the JONSWAP spectra, $S_{\text{J}}(\omega)$, are modified using an attenuation function [183], $\varphi_{\text{mtrk}}(\omega)$. Using the $\varphi_{\text{mtrk}}(\omega)$, shown in Figure 6.3(b), the JONSWAP spectra at Mutriku, S_{mtrk}, are obtained as

$$S_{\text{mtrk}} = S_{\text{J}}(\omega)\varphi_{\text{mtrk}}(\omega). \tag{6.4}$$

To generate an irregular wave time series, with the statistical properties of the target S_{mtrk}, a linear superposition of harmonic waves of different random frequencies, amplitudes, and phases is used, as detailed in [182].

6.2 Control system design

This section details the design procedure for the OWC W2W control approach proposed in this chapter.

[1]Wave shoaling is the change in behaviour and shape of the oceans waves, as they propagate into water of decreasing depth.

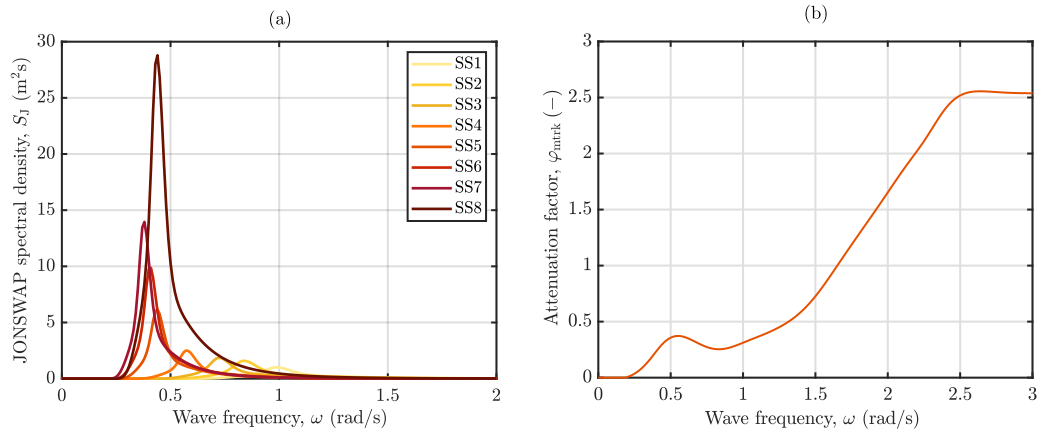

Figure 6.3: Mutriku wave climate modelling: (a) JONSWAP spectral density functions for the SSs in Table 6.2 and (b) attenuation function, $\varphi_{\text{mtrk}}(\omega)$.

6.2.1 Effect of turbine rotational speed

To better understand the impact of turbine rotational speed on each subsystem of the Mutriku-like OWC device presented in Section 6.1, a numerical investigation is carried out considering fifteen evenly spaced constant values of Ω, ranging from 50 to 400 rad/s. Subsequently, for each value of Ω, numerical simulations are run for the eight irregular sea states (SS1 - SS8) in Figure 6.3(a) and, ultimately, 120 different conditions are tested (i.e., 15 values of Ω and 8 SSs). In order to obtain statistically sound results [182], for each tested condition, 20 distinct realizations are run, for 1200 s each, using a time step of 0.01 s, for different random phase initialisations

For each realization, the time-averaged turbine efficiency, $\bar{\eta}_{\text{turb}}$, pneumatic power, $\bar{P}_{\text{pneu}}$, turbine power, $\bar{P}_{\text{turb}}$, and electric power, $\bar{P}_{\text{elec}}$, are calculated. Additionally, the hydrodynamic capture width ratio (CWR), ξ_{hydro}, aerodynamic CWR, ξ_{aero}, and

Table 6.2: Parameters of the sea states.

Sea state	H_s (m)	T_p (s)
SS1	0.88	6.40
SS2	1.03	7.55
SS3	1.04	8.75
SS4	1.08	11.05
SS5	1.48	14.55
SS6	1.81	15.70
SS7	2.07	16.90
SS8	3.20	14.55

electric CWR, ξ_{elec}, expressed as

$$\xi_{\text{hydro}} = \frac{\bar{P}_{\text{pneu}}}{\bar{P}_{\text{wave}}\,\iota}, \tag{6.5a}$$

$$\xi_{\text{aero}} = \frac{\bar{P}_{\text{turb}}}{\bar{P}_{\text{wave}}\,\iota} = \xi_{\text{hydro}}\bar{\eta}_{\text{turb}}, \tag{6.5b}$$

$$\xi_{\text{elec}} = \frac{\bar{P}_{\text{elec}}}{\bar{P}_{\text{wave}}\,\iota} = \xi_{\text{aero}}\bar{\eta}_{\text{gen}} = \xi_{\text{hydro}}\bar{\eta}_{\text{turb}}\bar{\eta}_{\text{gen}}, \tag{6.5c}$$

are also computed. In Equation (6.5), $\bar{P}_{\text{wave}}$ is the time-averaged wave power per metre of wave crest, $\bar{\eta}_{\text{gen}}$ is the time-averaged generator efficiency, and ι is the OWC capture width. In essence, ξ_{hydro} is the hydrodynamic efficiency, ξ_{aero} the wave-to-mechanical efficiency, and ξ_{elec} is the OWC W2W efficiency. Figure 6.4 shows the mean value of the quantities of interest, computed from 20 realizations, for three different sea states, namely (a) SS1, (b) SS4, and (c) SS8.

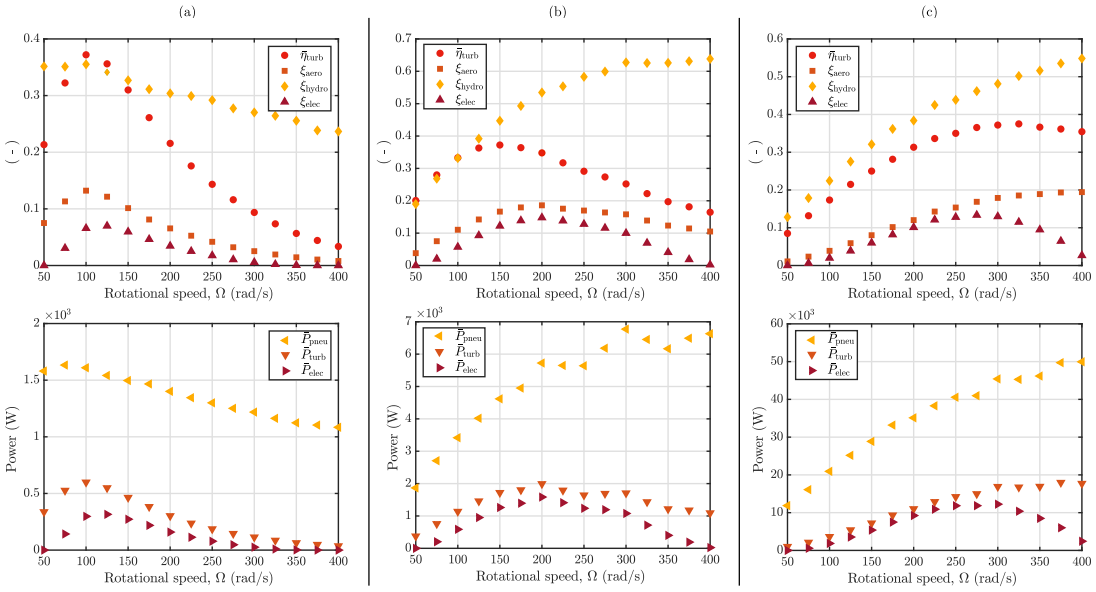

Figure 6.4: Effect of Ω on the OWC system performance, for three sea states: (a) SS1, (b) SS4, and (c) SS8.

6.2.2 Control system design

Figure 6.5(a) shows, for each sea state (SS1 - SS8), the value of $\bar{P}_{\text{elec}}$ (i.e., the eight blue curves) as a function of Ω and, moreover, two different generator control curves. The yellow dashed curve represents a traditional TEM control approach, while the orange curve is the proposed control approach for W2W efficiency maximisation. As shown in Figure 6.5(a), it is clear that the TEM control approach does not necessarily

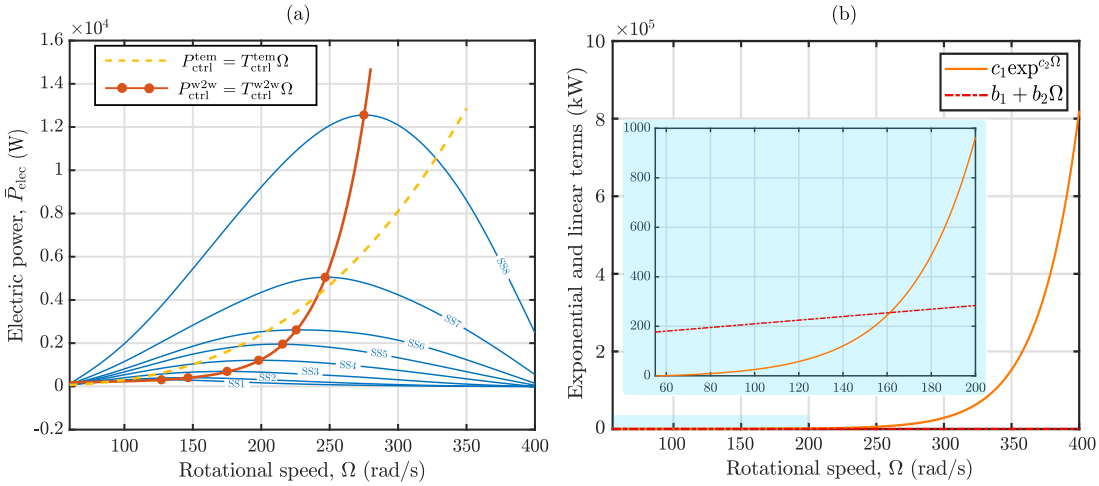

Figure 6.5: (a) The blue curves represent $\bar{P}_{\text{elec}}$, as a function of Ω, for different sea states (SS1 - SS8). Furthermore, the power curves, $P^{\text{w2w}}_{\text{ctrl}}$ from Equation (6.8), and $P^{\text{tem}}_{\text{ctrl}}$ from Equation (6.6), are also shown. (b) Contribution of the linear and exponential terms (6.8) to $P^{\text{w2w}}_{\text{ctrl}}$, with a focus (i.e., the blue shaded area) on the low speed region.

maximise electric power production, since the yellow curve often departs significantly from the maximum power points (i.e., the peaks of the eight blue curves).

As already mentioned in Section 5.2.2.1, a TEM control law has the following general form

$$T^{\text{tem}}_{\text{ctrl}} = P^{\text{tem}}_{\text{ctrl}}/\Omega = a_1\,\Omega^{a_2}, \tag{6.6}$$

where the control parameters a_1 and a_2 are selected in order to operate the turbine at its maximum efficiency point, i.e., Ψ_{mep}. Therefore, the control parameters in Equation (6.6) are set as $a_1 = \rho_{\text{air}}\, d_{\text{r}}^5\, f_{\Pi}(\Psi_{\text{mep}})$ and $a_2 = 2$, where a_1 is approximately constant, since $\rho_{\text{air}} \approx \rho_0$ (see, for instance, Figure 6.12(b)). To maximise the efficiency of the Wells turbine in Figure 3.4(a), $a_1 = 3 \times 10^{-4}$. To avoid exceeding the maximum allowable control torque and the PTO rated power, the control law in Equation (6.6) is augmented to:

$$T^{\text{tem}}_{\text{ctrl}} = \min\left(a_1\,\Omega^{a_2}, T^{\text{max}}_{\text{ctrl}}, \frac{P^{\text{rated}}}{\Omega}\right). \tag{6.7}$$

A possible W2W efficiency maximising control approach for the generator is found by fitting a suitable curve, $P^{\text{w2w}}_{\text{ctrl}}$, to the peak values of the set of $\bar{P}_{\text{elec}}$ curves in Figure 6.5. For the OWC system considered in this chapter, $P^{\text{w2w}}_{\text{ctrl}}$ is of the type

$$P^{\text{w2w}}_{\text{ctrl}} = \underbrace{b_1 + b_2\,\Omega}_{\text{linear term}} + \underbrace{c_1\,\exp^{c_2\,\Omega}}_{\text{exponential term}}, \tag{6.8}$$

where $b_1 = 136.088$, $b_2 = 0.739$, $c_1 = 1.151$, and $c_2 = 0.0337$. As shown in Figure 6.5(b), the linear term determines the value of $P^{\text{w2w}}_{\text{ctrl}}$ when Ω is relatively low

($< 100 - 120$ rad/s), while the exponential term becomes the dominant component of $P_{\text{ctrl}}^{\text{w2w}}$ when the value of Ω is relatively high (> 200 rad/s). Subsequently, a W2W efficiency maximising (unconstrained) control law is found as

$$T_{\text{ctrl}}^{\text{w2w}} = P_{\text{ctrl}}^{\text{w2w}}/\Omega = (b_1 + b_2\,\Omega + c_1\,\exp^{c_2\,\Omega})/\Omega, \tag{6.9}$$

and, similarly to TEM control, Equation (6.9) is extended as

$$T_{\text{ctrl}}^{\text{w2w}} = \min\left(\frac{b_1 + b_2\,\Omega + c_1\,\exp^{c_2\,\Omega}}{\Omega}, T_{\text{ctrl}}^{\max}, \frac{P^{\text{rated}}}{\Omega}\right). \tag{6.10}$$

It is important to note that, in contrast to the TEM control law in Equation (6.6), which is derived *analytically* [263], the W2W efficiency maximising approach in Equation (6.9) is obtained purely from data, therefore is specific for the considered Mutriku-like OWC detailed in Section 6.1.

For both control approaches (i.e., Equations (6.7) and (6.10)), the safety valve position is controlled as follows:

$$u_{\text{safety}} = \begin{cases} 1\,\text{(normal mode)} & \text{if } \Omega \le \Omega^{\max}, \\ 0\,\text{(safety mode)} & \text{else.} \end{cases} \tag{6.11}$$

If $\Omega \le \Omega^{\max}$, that is under normal operating conditions, the safety valve is fully open, i.e., $u_{\text{safety}} = 1$. When $\Omega > \Omega^{\max}$, the safety valve is closed, namely $u_{\text{safety}} = 0$, and the OWC device enters a safety mode until rotational speed decreases below a user-defined threshold value, $\Omega < \Omega^{\text{thr}} = 0.7\,\Omega^{\max}$, at which point the safety valve is reopened. In the numerical simulation, the control constraints for the considered OWC system are set [183], as $T_{\text{ctrl}}^{\max} = 216.5$ Nm, $P^{\text{rated}} = 18.5$ kW, and $\Omega^{\max} = 400$ rad/s.

Table 6.3: Results of the simulations.

Sea state	TEM control (6.7)			W2W control (6.10)			
	$\bar{\eta}_{\text{turb}}$ (%)	ξ_{hydro} (%)	ξ_{elec} (%)	$\bar{\eta}_{\text{turb}}$ (%)	ξ_{hydro} (%)	ξ_{elec} (%)	$\Delta\bar{P}_{\text{elec}}$ (%)
SS1	36.3	33.5	2.3	29.5	32.5	2.3	~ 0
SS2	36.4	34.6	4.2	30.0	35.1	4.2	~ 0
SS3	37.2	39.1	7.7	31.6	43.7	8.0	3.7
SS4	38.3	49.3	13.0	34.8	53.1	13.6	4.4
SS5	37.8	38.9	10.3	37.3	43.3	11.0	6.4
SS6	38.5	37.4	10.5	38.1	40.6	12.1	13.2
SS7	38.8	34.5	10.9	38.5	36.6	11.5	5.2
SS8	36.0	36.1	6.3	33.4	44.6	12.0	47.5

6.3 Result and discussion

Table 6.3 reports the percentage values of ξ_{hydro}, $\bar{\eta}_{\text{turb}}$, ξ_{elec}, and relative increase in electrical power, $\Delta\bar{P}_{\text{elec}}$, computed using TEM (6.7) and W2W (6.10) control. For each control strategy, numerical simulations are run for 1200 s with a time step of 0.01 s, and the results in Table 6.3 are the mean values obtained from 20 sea state realizations.

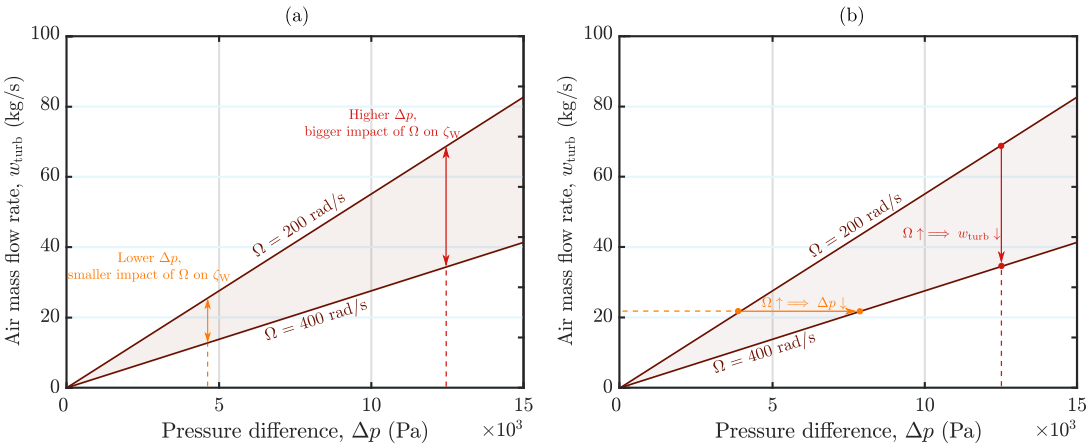

Figure 6.6: (a) Impact of Ω on w_{turb} (therefore on ζ_W), for two different values of Δp, and (b) effect of Ω on w_{turb} and Δp.

6.3.1 Discussion of the results

In Figure 6.4, it is possible to note that the turbine MEP does not coincide with the optimum operating points for the hydrodynamic subsystem and electric generator. To solely maximise turbine efficiency, since η_{turb} is only a function of Ψ, and since $\Psi \propto \Delta p\, \Omega^{-2}$, Ω should increase in relatively high-energy SSs (Figure 6.4(c)), where large pressure levels are available in the chamber. In low-energy SSs, Ω should decrease (Figure 6.4(a)) to keep Ψ around Ψ_{mep}.

Since Wells turbine damping is a function of Ω, as $\zeta_W \propto \Omega^{-1}$, hydrodynamic performance (namely, P_{pneu} and ξ_{hydro}) is influenced by rotational speed control. In particular, the effect of Ω on the hydrodynamic part increases when medium-to-high wave energy levels are available (Figure 6.4(b) and (c)), and vice-versa (Figure 6.4(a)). In fact, with high pressure levels in the pneumatic chamber, turbine damping is more significantly affected by variations in Ω, as shown in Figure 6.6(a). In general, an increase in Ω yields a stronger blockage effect on the turbine air flow and, consequently, w_{turb} decreases, while Δp tends to increase (Figure 6.6(b)). Ultimately, to maximise $\bar{P}_{\text{pneu}}$ (or ξ_{hydro}), a trade-off between Δp and w_{turb} has to be made.

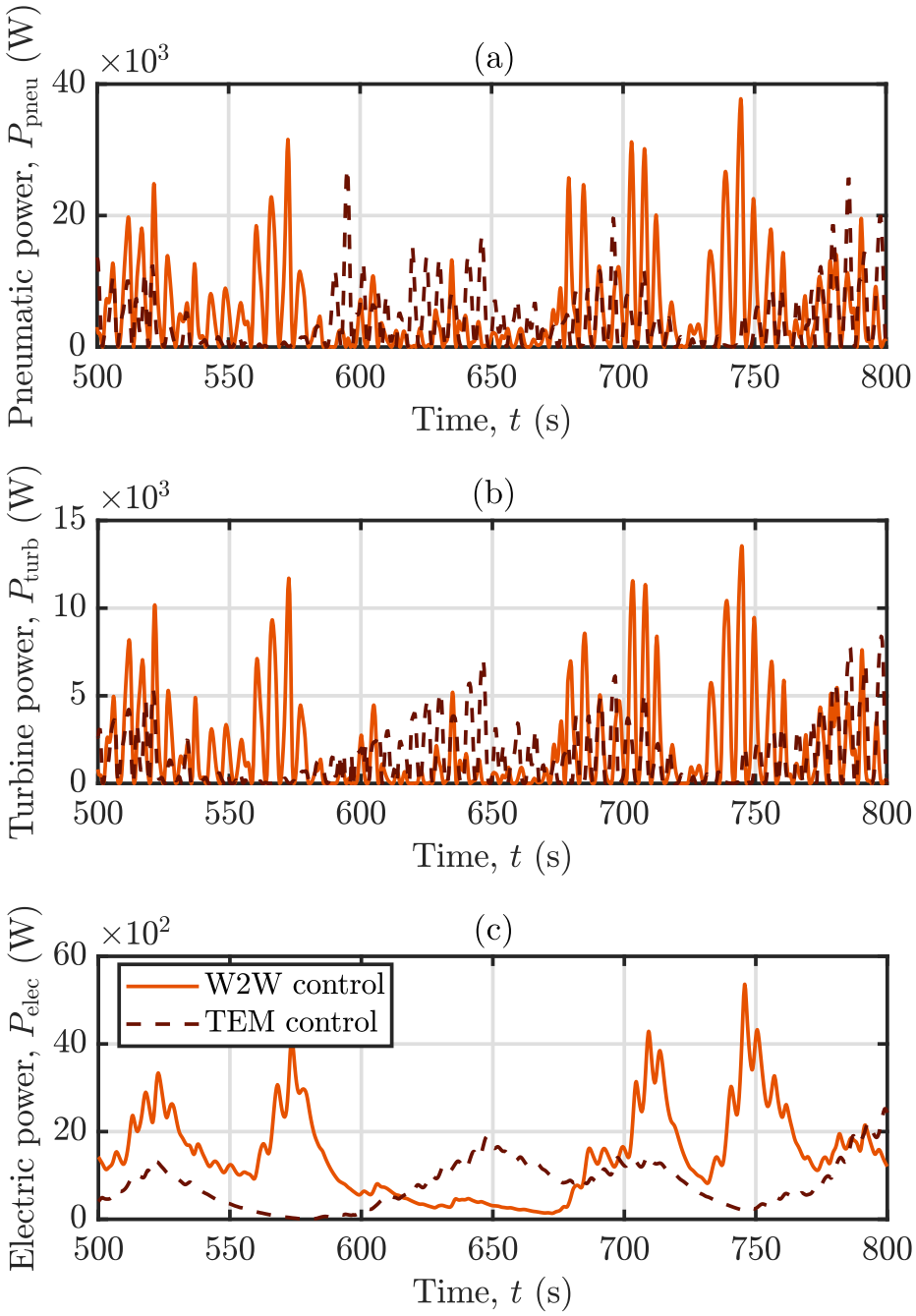

Figure 6.7: Time series of the (a) pneumatic power, P_{pneu}, (b) turbine power, P_{turb}, and (c) electric power, P_{elec}, obtained using TEM and W2W control, for one realisation of SS4.

From Table 6.3, in comparison to the TEM control, W2W control improves the values of ξ_{elec}, albeit moderately penalising $\bar{\eta}_{\text{turb}}$. When Ω is modulated, taking into account the whole (W2W) OWC system, $\bar{P}_{\text{elec}}$ significantly increases ($\bar{P}^{\%}_{\text{elec}}$ in Table 6.3), particularly for medium-to-high energy sea states (i.e., SS3 - SS8), where the impact of Ω on each OWC subsystem is more noteworthy. For instance, Figures 6.7, 6.8, and 6.9 show the time series of some quantities of interests, in SS4,

for both TEM and W2W control. As expected, electric power production is superior with W2W control (Figure 6.7(c)), at the cost of a lower turbine efficiency (Figure 6.8). For the sake of completeness, some variables of interests, for a realization of SS4, with W2W control, are shown in Figure 6.12.

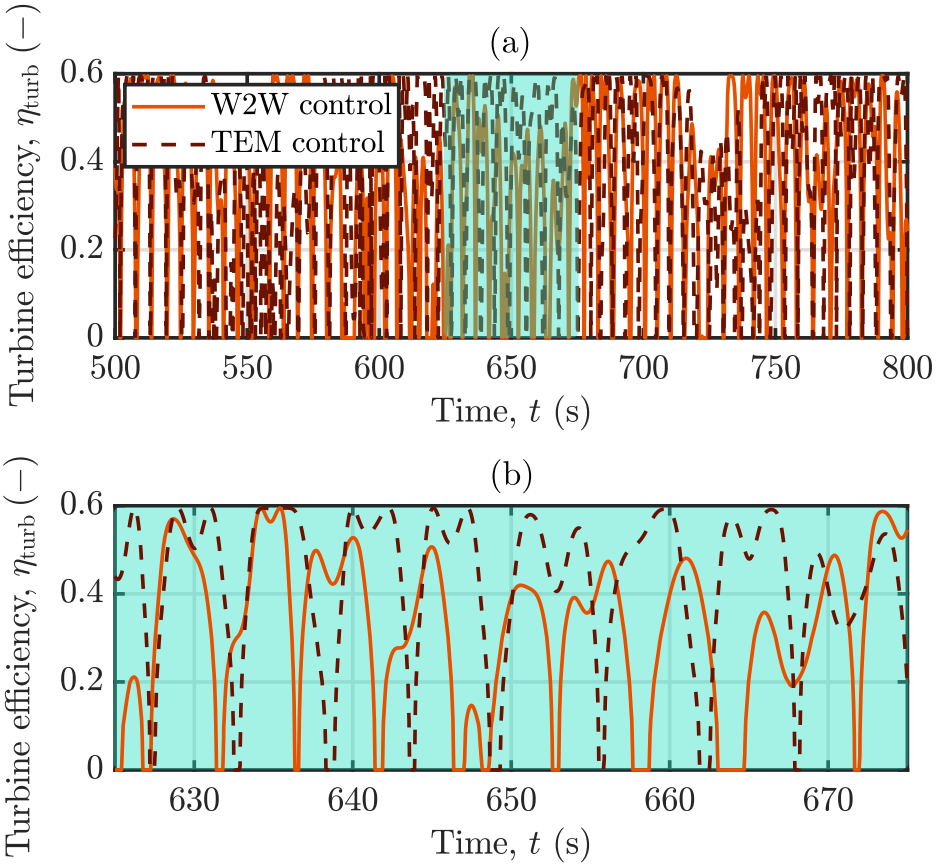

Figure 6.8: Time series of the (a) turbine efficiency, η_{turb}, and (b) a focus on η_{turb} (from $t = 620$ s to $t = 680$ s), obtained using TEM and W2W control, for one realisation of SS4.

In SS4, since T_{p} of SS4 is close to the heave mode resonance period of the Mutriku plant [183], ξ_{hydro} is relatively high, both with TEM control ($\xi_{\text{hydro}} = 49.3\%$) and W2W control ($\xi_{\text{hydro}} = 53.1\%$). In other words, for SS4, the hydrodynamic part of the OWC naturally works close to its optimum operating point (i.e., the resonance condition), meaning that the benefit of using W2W, as opposed to TEM, control on ξ_{hydro} is more marginal. Finally, since the orange curve almost intersects the yellow dashed curve at SS7 (Figure 6.5(a)), meaning that the two control approaches are similar to each other, the performance obtained with TEM and W2W control is similar in SS7, as shown in Table 6.3.

In Figure 6.7, in the time interval $t = 610\tilde{}680$ s, P_{elec} with TEM control is greater than P_{elec} with W2W control. This inversion is arguably due to the time constant of the OWC system and how the inherent system inertia affects the OWC control

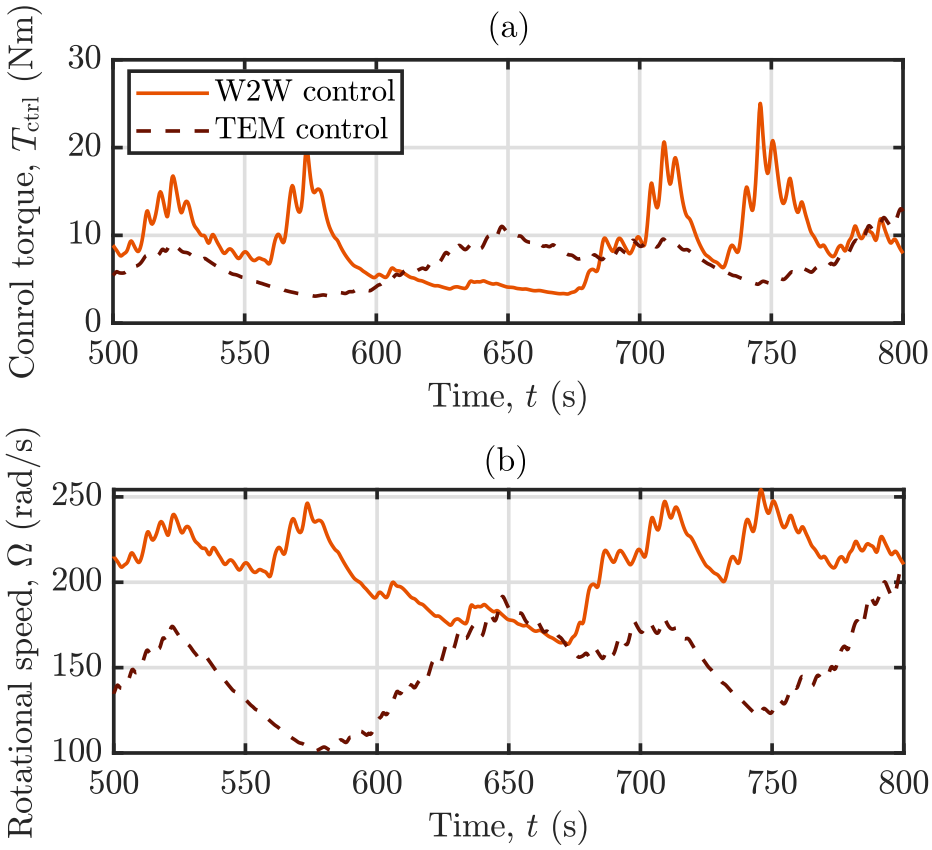

Figure 6.9: Time series of the (a) generator control torque, T_{ctrl}, and (b) turbine rotational speed, Ω, obtained using TEM and W2W control, for one realisation of SS4.

history. Investigating such aspect in detail is beyond the scope of this thesis but may be the objective of future works.

6.3.2 Main control co-design aspects

As already mentioned in Section 5.1.4, CCD techniques can significantly help to achieve the optimum *control-informed* WEC design [228] and are essential to minimise the LCoE. As such, it is worth highlighting some key co-design aspects related to W2W control.

As already stated, W2W efficiency maximisation, through turbine rotational speed modulation, is particularly suitable for a specific type of turbine, namely a Wells turbine. For instance, Figure 6.10 shows the values of ξ_{hydro} and $\bar{\eta}_{\text{turb}}$ obtained in SS4, using two different turbines, for different constant values of Ω. For each turbine type, the shaded area represents the range of possible values of ξ_{hydro}, as Ω varies from 50 rad/s to 400 rad/s. In contrast to the Wells turbine case, the variation of ξ_{hydro} with Ω is only marginal for the biradial turbine (the model for which is shown in Figure 3.4(b)), meaning that hydrodynamic performance is only

moderately affected by Ω and, therefore, W2W efficiency maximisation through the modulation of Ω is expected to be less effective. For the Wells turbine, ξ_{hydro} varies from 0.19 (for $\Omega = 50$ rad/s) to 0.63 (for $\Omega = 400$ rad/s), meaning that a somewhat more careful modulation of Ω is required to consider the effect of the hydrodynamic/aerodynamic interaction. Furthermore, the two green circles highlight the condition in which ξ_{turb} is maximised, highlighting the case in which the best trade-off between turbine and hydrodynamic performance is achieved, while the two blue dotted circles indicate the condition in which ξ_{elec} is maximised. It should be noted that, for the Wells turbine, the maximum values of ξ_{hydro}, $\bar{\eta}_{\text{turb}}$, ξ_{aero}, and ξ_{elec} are found at four different operating points. For the biradial turbine, when $\bar{\eta}_{\text{turb}}$ is maximum, ξ_{elec} and ξ_{aero} are also maximised, meaning that rotational speed control is, to some extent, more straightforward.

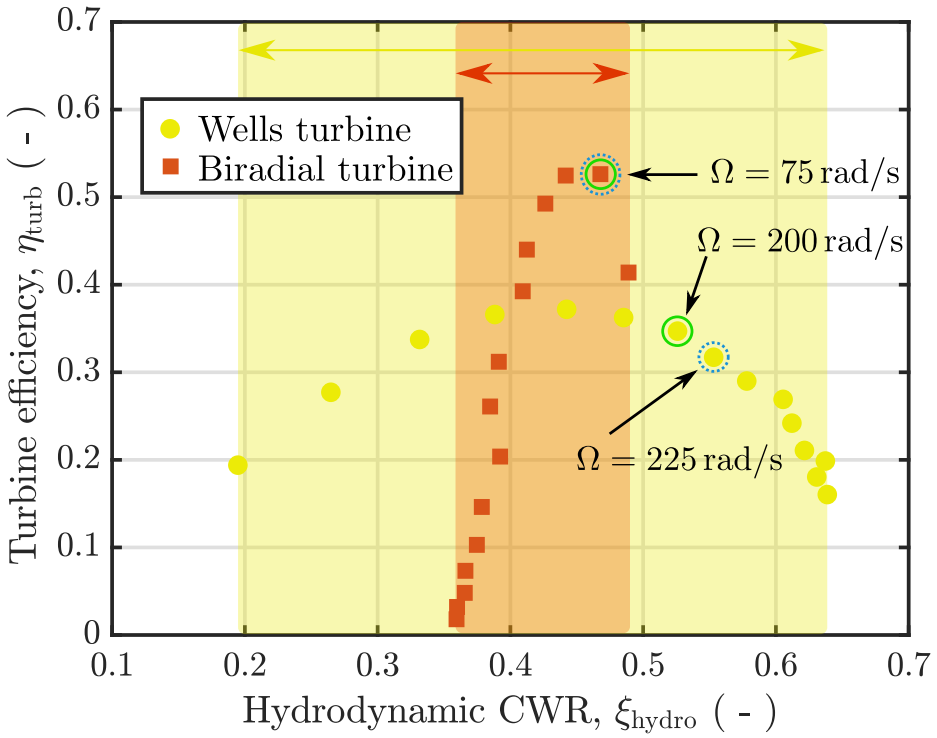

Figure 6.10: ξ_{hydro} and $\bar{\eta}_{\text{turb}}$ for fifteen constant values of Ω, in SS4. For each turbine type, the corresponding shaded area represents the range of possible values of ξ_{hydro}.

To use W2W control for OWC WECs to its full potential, a turbine with a relatively flat efficiency curve should be designed/installed. Indeed, with a flat and high-valued turbine efficiency characteristic, Ω could be more freely modulated to improve hydrodynamic, and electric, performance, without excessively penalising η_{turb}. In other words, the control envelope (possibility) for Ω increases. However, if the turbine efficiency curve is relatively peaky, rotational speed control should prioritize turbine performance; otherwise, unsatisfactory levels of electric energy are produced.

6.4 Conclusions

In light of the discussion in Section 6.3.1, Wells turbine rotational speed control affects all the energy conversion processes of an OWC system. As such, electric energy production significantly improves (e.g., Figure 6.11) if rotational speed is controlled while considering the complete W2W OWC system, especially for the most interesting operating conditions (i.e., the medium-to-high energy SSs). Additionally, to take full advantage of W2W control, it is vital to consider CCD aspects.

It should be noted that, in comparison with TEM control, the proposed W2W control strategy not only improves electric energy production, but also reduces the LCoE. Indeed, since the number of actuators does not vary, CapEx remains unchanged. Furthermore, since the main difference between TEM and the proposed W2W control is a slightly different modulation of Ω, as shown in Figure 6.9, the impact of the control action on OpEx [316] is expected to be similar, meaning that OpEx is also unlikely to change significantly.

Finally, it is important to note that, in this work, the impact of model uncertainties on the results of the simulation is not considered, and such aspect needs further investigation. In any case, given the crucial role of the air turbine on the overall OWC WEC performance, one can expect that turbine model uncertainties will impact W2W control much more significantly than hydrodynamic model uncertainties. Furthermore, some of the mean values of ξ_{elec} in Table 6.3 are close to each other. In future works, to better assess the improvement in electricity production when using W2W control, the standard deviations of ξ_{elec} should be considered.

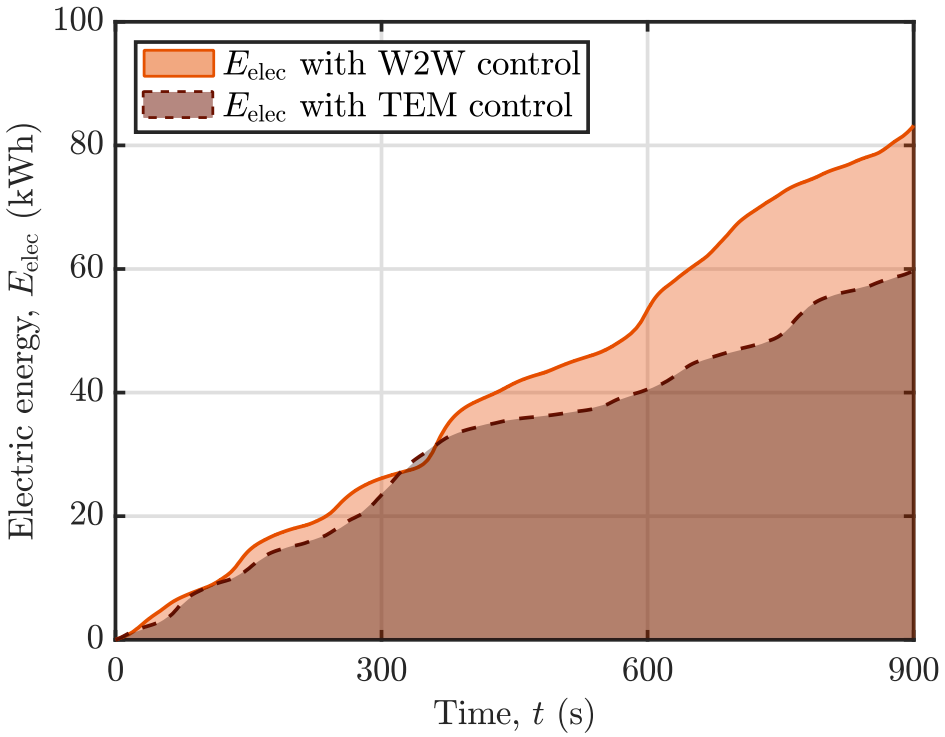

Figure 6.11: Electric energy production over 900 s using TEM and W2W control, for a realization of SS4.

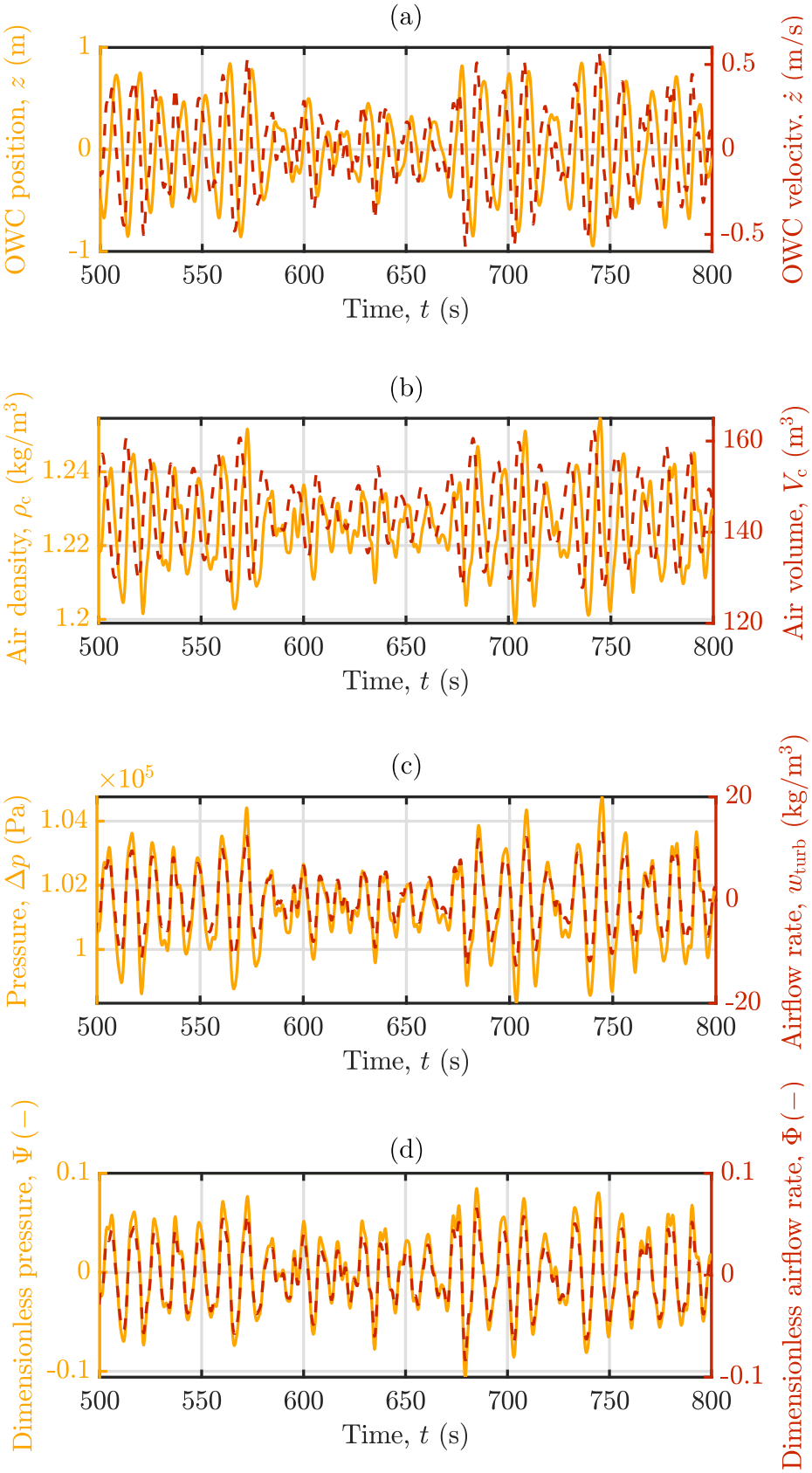

Figure 6.12: Time series obtained using W2W control, for one realisation of SS4.(a) OWC position, z, and velocity, $\dot{z}$; (b) air chamber density, ρ_c, and air chamber volume, V_c; (c) pressure difference, Δp, and turbine mass flow rate, w_{turb}; (d) dimensionless pressure head, Ψ, and dimensionless turbine mass flow rate Φ.

7

Optimal control for oscillating water columns

Contents

7.1 Pseudospectral control 149
7.1.1 Pseudospectral representation 149
7.1.2 Minimisation of residuals 150
7.2 RHPS control for OWCs 151
7.2.1 OWC OCP formulation 151
7.2.2 Fourier PS approximation 153
7.2.3 OWC OCP simplification 154
7.3 Result and discussion 154
7.3.1 Discussion of the results 155
7.3.2 Main control co-design aspects 158
7.4 Conclusions 161

In traditional WEC hydrodynamic control, the energy maximising control problem can be written, in the frequency-domain, as an impedance-matching problem (5.6). However, as already mentioned in Section 5.2.1.1, such a control formulation suffers from certain limitations (e.g., it is only specified at a single excitation frequency and does not consider constraints), which have significant implications in terms of actual control implementation [146]. As an alternative to control approaches based on the impedance-matching principle, optimal control strategies for energy (usually mechanical energy) maximisation have been developed for different types of WECs, especially to address the problem of WEC control in irregular waves and to make

use of optimal constraint handling. Since the ocean wave FSE is relatively easy to predict [338], MPC and MPC-like (i.e., spectral and moment-based) non-causal control strategies have been extensively considered in WEC control. For a review on WEC optimal control, see, for example, [50].

In OWCs, the two main issues associated with traditional TEM control (Section 5.2.2) are: (i) the *oversimplification* of the control objective (as discussed in Section 5.1) and (ii) nonoptimal constraint handling. Although the steady-state W2W control strategy presented in Chapter 6 offers a relatively simple solution to the first issue, the corresponding control law (Equation (6.9)) is derived, similarly to TEM control, without explicitly considering constraints, and is only subsequently augmented to avoid constraint violations (Equation 6.10), resulting in constrained optimal control, rather than optimal constrained control. In this chapter, to tackle aforementioned issues (i) and (ii), a *receding-horizon pseudospectral* (RHPS) optimal control approach for electric energy maximization of OWC systems is developed, and numerically tested on the Mutriku-like OWC model introduced in Section 6.1. Once again, given the interesting possibility of affecting hydrodynamic performance through speed modulation, a Wells turbine is considered in the study case. Despite the fact that the impact of biradial turbine rotational speed on OWC hydrodynamic efficiency is (almost) negligible [60], some energy maximising control solutions, using nonlinear MPC [293, 296], and IFM [297], have been proposed, as reported in Table 5.3.

Pseudospectral (PS), or *collocation*, methods belong to a family of techniques, known as *mean weighted residual* (MWR) methods [339], used to discretize partial differential equations and integrals. In PS methods, which are a branch of so-called spectral methods, state, and control, variables are approximated by a basis function expansion. Early applications of PS optimal control emerged in the late 80s [340], and in the 90s [341], although PS control has been more systematically used only in relatively recent years, mostly in aerospace [342]. Over the last decade, PS control has been also considered to tackle the energy maximising WEC OCP on, for instance, a nonlinear flap-type WEC (2014) [335] , a HPA WEC (2016) [343] , and an oscillating surge WEC (2017) [344]. In comparison to MPC [289], PS optimal control is an attractive solution to address the WEC OCP, especially due to the relatively fast convergence rate [335] provided by the PS discretization method, resulting in a more computationally efficient nonlinear program. Additionally, the PS representation allows an *analytic* simplification of the radiation convolution integral (Section 7.2.2), which appears in the WEC hydrodynamic model (e.g., Equation (6.1)), as opposed to the traditional approach of using a model reduction technique to approximate the convolution term with a suitable finite-order state space model [345].

The reminder of the chapter is organised as follows. Section 7.1 illustrates the PS formulation, and solution outline, for a generic control problem. In Section 7.2, the proposed RHPS control method for OWCs is detailed. Finally, discussion of the results and conclusions are given in Sections 7.3 and 7.4, respectively.

7.1 Pseudospectral control

In PS control, the original infinite-dimensional OCP is *directly transcribed* (e.g., [346]), meaning that the associated input, and state, variables are suitably discretized, into a *finite-dimensional* nonlinear program. This section serves as an illustrative example of PS control, for a generic control problem. For clarity, a bold text is used to indicate vectors and matrices.

7.1.1 Pseudospectral representation

Consider a generic dynamical system, written as

$$\dot{\mathbf{x}} = \mathbf{f}(\mathbf{x}(t), \mathbf{u}(t), t) \; t \in [0, \; T], \tag{7.1}$$

where $\mathbf{x}(t) \in \mathbb{R}^n$ is the state vector, $\mathbf{u}(t) \in \mathbb{R}^m$ is the control input vector, and $\mathbf{f} : \mathbb{R}^n \times \mathbb{R}^m \times \mathbb{R} \to \mathbb{R}^n$. Furthermore, suppose that the OCP is to find $\mathbf{u}^{\mathrm{opt}}$, namely the optimal control input, which minimises (or maximises) the following cost functional:

$$J = \int_0^T h(\mathbf{x}(t), \mathbf{u}(t), t)dt, \;\; h : \mathbb{R}^n \times \mathbb{R}^m \times \mathbb{R} \to \mathbb{R}^n, \tag{7.2}$$

subject to the dynamic of the system (7.1) and any state/input constraint.

The i-th component of $\mathbf{x}(t)$ ($i = 1, \dots n$), and the j-th component of $\mathbf{u}(t)$ ($j = 1, \dots m$), can be approximated using a basis function expansion, as

$$x_{\mathrm{i}}(t) \approx x_{\mathrm{i}}^{\mathrm{M}}(t) := \sum_{\mathrm{q}=1}^{\mathrm{M}} \tilde{x}_{\mathrm{iq}} \theta_{\mathrm{q}}(t) = \Theta(t) \hat{\mathbf{x}}_{\mathrm{i}}, \tag{7.3}$$

and

$$u_{\mathrm{j}}(t) \approx u_{\mathrm{j}}^{\mathrm{M}}(t) := \sum_{\mathrm{q}=1}^{\mathrm{M}} \tilde{u}_{\mathrm{jq}} \theta_{\mathrm{q}}(t) = \Theta(t) \hat{\mathbf{u}}_{\mathrm{j}}, \tag{7.4}$$

respectively. The term $\theta_{\mathrm{q}}(t)$ in Equations (7.3) and (7.4) indicates the q-th basis function. On the right-hand side of Equations (7.3) and (7.4), the vectors of the unknown coefficients, $\hat{\mathbf{x}}_{\mathrm{i}}$ and $\hat{\mathbf{u}}_{\mathrm{j}}$, can be expressed, as

$$\hat{\mathbf{x}}_{\mathrm{i}} = [\tilde{x}_{\mathrm{i1}}, \dots \tilde{x}_{\mathrm{iq}}, \dots \tilde{x}_{\mathrm{iM}}]^{\intercal}, \;\; \hat{\mathbf{u}}_{\mathrm{j}} = [\tilde{u}_{\mathrm{j1}}, \dots \tilde{u}_{\mathrm{jq}}, \dots \tilde{u}_{\mathrm{jM}}]^{\intercal}, \tag{7.5}$$

while $\Theta(t)$ is written as

$$\Theta(t) = [\theta_1(t), \dots \theta_{\mathrm{q}}(t), \dots \theta_{\mathrm{M}}(t)]. \tag{7.6}$$

For brevity of notation, it is convenient to introduce the matrices $\mathbf{X} \in \mathbb{R}^{M \times n}$ and $\mathbf{U} \in \mathbb{R}^{M \times m}$, as

$$\mathbf{X} = [\hat{\mathbf{x}}_1, \dots \hat{\mathbf{x}}_{\mathrm{i}}, \dots \hat{\mathbf{x}}_{\mathrm{n}}], \tag{7.7}$$

and

$$\mathbf{U} = [\hat{\mathbf{u}}_1, \dots \hat{\mathbf{u}}_{\mathrm{j}}, \dots \hat{\mathbf{u}}_{\mathrm{m}}], \tag{7.8}$$

respectively. Due to approximations (7.3) and (7.4), the cost functional (7.2) exclusively depends on the $M(n + m)$ parameters of $\mathbf{X}$ and $\mathbf{U}$. Therefore, the OCP is now finite-dimensional.

If the state approximation in (7.3), control input approximation in (7.4), and

$$\dot{x}_{\mathrm{i}}(t) \approx \dot{x}_{\mathrm{i}}^{\mathrm{M}}(t) := \sum_{\mathrm{q}=1}^{\mathrm{M}} \tilde{x}_{\mathrm{iq}} \dot{\theta}_{\mathrm{q}}(t) = \dot{\Theta}(t) \hat{\mathbf{x}}_{\mathrm{i}}, \tag{7.9}$$

are substituted into the generic system in (7.1), the i-th dynamic equation can be written, in residual form, as

$$r_{\mathrm{i}}(t) = \dot{x}_{\mathrm{i}}^{\mathrm{M}}(t) - f_{\mathrm{i}}(\mathbf{x}^{\mathrm{M}}(t), \mathbf{u}^{\mathrm{M}}(t), t), \tag{7.10}$$

where $\mathbf{x}^{\mathrm{M}}$ and $\mathbf{u}^{\mathrm{M}}$ are, respectively, the vectors of the approximated n state variables (in Equation (7.3)) and m control inputs (in Equation (7.4)).

7.1.2 Minimisation of residuals

The $M(n+m)$ optimal parameters, namely $\hat{\mathbf{x}}_{\mathrm{i}}$ and $\hat{\mathbf{u}}_{\mathrm{j}}$ in Equation (7.5), which minimise the n residuals, $r_{\mathrm{i}}(t)$, in Equation (7.10), can be obtained using a collocation, or PS, method. In essence, the system dynamic is 'collocated' upon N_{c} nodes (or collocation points), t_{k}, or, equivalently, the system dynamic equation is satisfied at the collocation points, meaning that

$$r_{\mathrm{i}}(t_{\mathrm{k}}) = \dot{\Theta}(t_{\mathrm{k}}) \hat{\mathbf{x}}_{\mathrm{i}} - f_{\mathrm{i}}(\mathbf{X}, \mathbf{U}, t_{\mathrm{k}}) = 0. \tag{7.11}$$

Finally, a suitable quadrature formula is utilised to approximate the functional in Equation (7.2), as

$$J = \int_0^T h(\mathbf{X}, \mathbf{U}, t) dt \approx \sum_{\mathrm{k}=0}^{\mathrm{N_c}} h(\mathbf{X}, \mathbf{U}, t_{\mathrm{k}}). \tag{7.12}$$

Ultimately, the original OCP, namely to find $\mathbf{u}^{\text{opt}}$ that maximises (or minimises) the functional in (7.2), subject to the system dynamic (7.1) and constraints on $\mathbf{x}(t)$ and $\mathbf{u}(t)$, is now simplified to the following finite dimensional optimisation problem: Find **X** and **U** to maximise (or minimise) the functional in (7.12) subject to state/input constraints and to the equality constraints due to the system dynamics (7.11). The simplified finite-dimensional problem is essentially a system of $n \times N_{\text{c}}$ equations (i.e., n state variables and N_{c} nodes).

7.2 RHPS control for OWCs

In this section, the proposed RHPS control method is applied to the Mutriku-like OWC detailed in Section 6.1, with the system parameters specified in Table 6.1. However, for computational simplicity of the optimisation problem, only linear constraints, namely the constraints on the maximum allowable speed, $\Omega \leq \Omega^{\max}$, and maximum generator torque, $T_{\text{ctrl}} \leq T_{\text{ctrl}}^{\max}$, are considered in the optimisation at this stage. Since, in contrast to TEM and steady-state W2W control (Chapter 6.2), RHPS control may require reactive (negative active) power at some point of the wave energy conversion cycle, and negative values of T_{ctrl} may occur. For most WECs, reactive power is required when WEC velocity and PTO force have opposite signs [347] but, due to the turbine rectifying property, the rotational speed of *self-rectifying* turbines is always positive (Figure 7.1). Therefore, the electric power is calculated as $P_{\text{elec}} = \text{sgn}(T_{\text{ctrl}})P_{\text{turb}}\eta_{\text{gen}}$. For completeness, a typical time trace of the absorbed wave power for a generic WEC, under optimal control conditions, is shown in Figure 7.2.

It is important to note that OWC RHPS control requires wave excitation force prediction, although, in this work, full knowledge of the excitation force is assumed. To the best of the author's knowledge, the impact of prediction errors on OWC optimal control has never been investigated and may be the objective of future works. However, some studies on the degradation of optimal control performance due to wave excitation force prediction errors can be found, for instance, in [348, 349].

7.2.1 OWC OCP formulation

For the considered Mutriku-like OWC, the state vector and control input are expressed, as

$$\mathbf{x}(t) = [z(t)\ v(t)\ \Delta p(t)\ \Omega(t)]^{\intercal}, \tag{7.13}$$

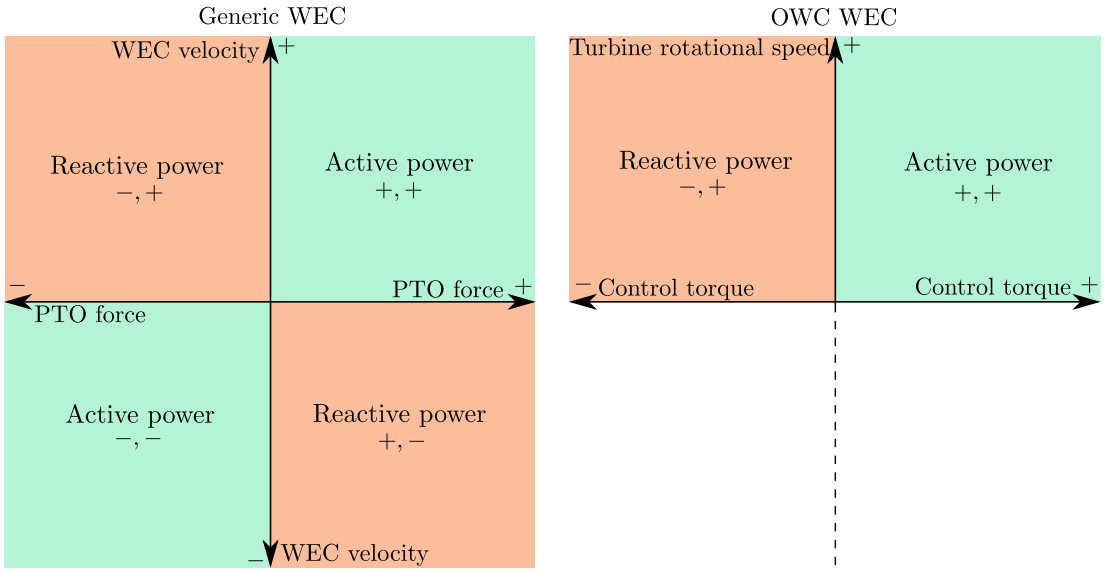

Figure 7.1: Active, and reactive, power region for a generic WEC and an OWC WEC with a self-rectifying air turbine, under optimal control. Figure adapted from: [347].

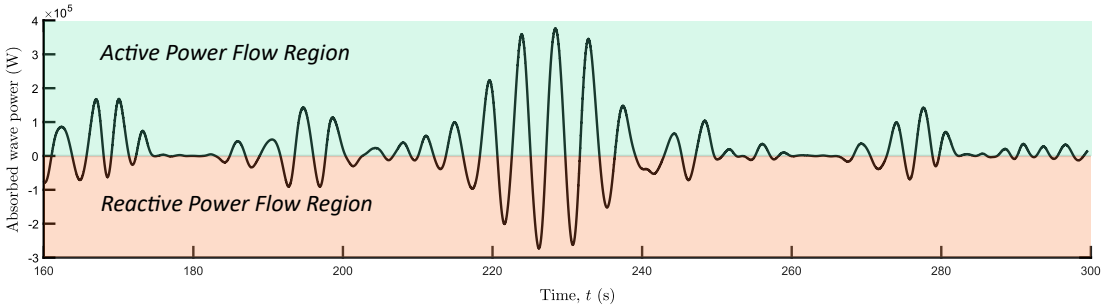

Figure 7.2: Typical time series of the absorbed power for a generic WEC under optimal control. Figure adapted from: [347].

and

$$u(t) = T_{\text{ctrl}}(t), \tag{7.14}$$

respectively. The electric energy maximising OWC OCP is therefore: Find $T_{\text{ctrl}}(t)$ to maximise electric energy production, written as

$$J = \int_0^T T_{\text{ctrl}}(t)\,\Omega(t)\,\eta_{\text{gen}}(T_{\text{ctrl}}, \Omega)dt, \;\; t \in [0\;\; T], \tag{7.15}$$

subject to the OWC system dynamics, defined in Equations (6.1) (hydrodynamic model), (6.2) (air chamber model), and (6.3) (PTO model), and the following state and input linear constraints:

$$\begin{aligned} T_{\text{ctrl}}(t) &\leq T_{\text{ctrl}}^{\max}, \\ \Omega(t) &\leq \Omega^{\max}. \end{aligned} \tag{7.16}$$

7.2.2 Fourier PS approximation

Among different possible choices of basis functions [343], a simple and computationally efficient truncated Fourier series (zero-mean trigonometric polynomial) is attractive, especially in light of the oscillatory nature of ocean waves. Using a Fourier PS approximation, the states and input are approximated as

$$\begin{aligned} x_{\mathrm{i}}(t) &\approx \sum_{\mathrm{q}=1}^{\mathrm{M}} x_{\mathrm{iq}}^{\mathrm{c}} \cos(q\omega_0 t) + x_{\mathrm{iq}}^{\mathrm{s}} \sin(q\omega_0 t) = \Theta(t)\hat{\mathbf{x}}_{\mathrm{i}} \\ u(t) &\approx \sum_{\mathrm{q}=1}^{\mathrm{M}} u_{\mathrm{q}}^{\mathrm{c}} \cos(q\omega_0 t) + u_{\mathrm{q}}^{\mathrm{s}} \sin(q\omega_0 t) = \Theta(t)\hat{\mathbf{u}}, \end{aligned} \tag{7.17}$$

and, furthermore, the derivative of the i-th approximated state variable is expressed as

$$\dot{x}_{\mathrm{i}}^{\mathrm{M}} = \dot{\Theta}(t)\hat{\mathbf{x}}_{\mathrm{i}} = \Theta(t) D_\theta \hat{\mathbf{x}}_{\mathrm{i}}, \tag{7.18}$$

where $\omega_0 = 2\pi/T$ is the fundamental frequency and $D_\theta \in \mathbb{R}^{2M\times 2M}$ is the block diagonal derivative matrix. The q-th block of $D_\theta \in \mathbb{R}^{2M\times 2M}$ is written as

$$D_\theta^{\mathrm{q}} = \begin{bmatrix} 0 & q\omega_0 \\ -q\omega_0 & 0 \end{bmatrix}. \tag{7.19}$$

The residual forms of the system dynamic equations (namely, Equations (6.1), (6.2), and (6.3)) collocated, using Equations (7.17) and (7.19), at N_{c} evenly spaced collocation points t_k, with N_{c} sufficiently large (N_{c}generally depends on the behaviour of the approximated state/control functions, type of basis functions, and length of the prediction horizon), are expressed as:

$$\begin{aligned} r_1 &= D_\theta \hat{\mathbf{x}}_1 - \hat{\mathbf{x}}_2, \\ r_2(t_k) &= m_{\mathrm{p}} \Theta(t_k) D_\theta \hat{\mathbf{x}}_2 + \rho_{\mathrm{w}} g S_{\mathrm{w}} \Theta(t_k)\hat{\mathbf{x}}_1 + S_{\mathrm{w}} \Theta(t_k)\hat{\mathbf{x}}_3 + \Theta(t_k) G_\theta \hat{\mathbf{x}}_2 - f_{\mathrm{ex}}(t_k), \\ r_3(t_k) &= \Theta(t_k) D_\theta \hat{\mathbf{x}}_3 + \left(\Theta(t_k)\hat{\mathbf{x}}_3 + p_0\right) \frac{\gamma}{V_0 - S_{\mathrm{w}}\Theta(t_k)\hat{\mathbf{x}}_1} \left(-S_{\mathrm{w}}\Theta(t_k)\hat{\mathbf{x}}_2 + \frac{d_{\mathrm{r}}}{\rho_c \kappa} \frac{\Theta(t_k)\hat{\mathbf{x}}_3}{\Theta(t_k)\hat{\mathbf{x}}_4} \right), \\ r_4(t_k) &= \Theta(t_k) D_\theta \hat{\mathbf{x}}_4 - (\rho_{\mathrm{air}} d_{\mathrm{r}}^5 f_\Pi \Theta(t_k)\hat{\mathbf{x}}_4 \Theta(t_k)\hat{\mathbf{x}}_4 - \Theta(t_k)\hat{\mathbf{u}})/I. \end{aligned} \tag{7.20}$$

The block diagonal matrix $G_\theta \in \mathbb{R}^{2M\times 2M}$ in (7.20) results from the approximation, obtained with the PS formulation (see, e.g., [335]), of the radiation convolution integral, written as

$$\int_{-\infty}^{t} k_{\mathrm{r}}(t_k - \tau) x_2^{\mathrm{M}}(\tau) \mathrm{d}\tau = \Theta(t_k)(G_\theta - A(\infty) D_\theta)\hat{\mathbf{x}}_2, \tag{7.21}$$

and the q-th block of G_θ is

$$G_\theta^{\mathrm{q}} = \begin{bmatrix} B(q\omega_0) & q\omega_0 A(q\omega_0) \\ -q\omega_0 A(q\omega_0) & B(q\omega_0) \end{bmatrix}. \tag{7.22}$$

7.2.3 OWC OCP simplification

By substituting the approximations in Equation (7.17) into (7.15) and (7.16), the cost functional and the state/input constraints become, respectively,

$$J = \int_0^T \Theta(t)\hat{\mathbf{u}}\,\Theta(t)\hat{\mathbf{x}}_4\,\eta_{\text{gen}}(\Theta(t)\hat{\mathbf{u}}, \Theta(t)\hat{\mathbf{x}}_4)\,dt, \tag{7.23}$$

and

$$\begin{aligned} \Theta(t)\hat{\mathbf{u}} &\leq T_{\text{ctrl}}^{\max}, \\ \Theta(t)\hat{\mathbf{x}}_4 &\leq \Omega^{\max}. \end{aligned} \tag{7.24}$$

Since this paper adopts a receding-horizon (RH) approach to tackle the OWC OCP, T in (7.23) is replaced with the length of the prediction horizon, T_{h}. Ultimately, the simplified OWC OCP is to find $\hat{\mathbf{x}}_{\text{i}}$ and $\hat{\mathbf{u}}$ to maximise the approximated cost functional, in Equation (7.23), subject to the state/input constraints, in Equation (7.24), and to the system dynamic (i.e., the residuals in Equation (7.20) are zero at the N_{c} nodes).

7.3 Result and discussion

To asses the performance of RHPS control, with respect to that obtained using TEM (Equation (6.7)), and steady-state W2W (Equation (6.10)) control, 20 realisations are run for 1200 s, with a time step of 0.01 s, for each SS in Table 6.2. Additionally, for RHPS control, the RH time step is 0.5 s, $M = 20$, and $T_{\text{h}} = 10$ s, which is a reasonable RH time window for wave prediction [338, 252]. Due to its capability of handling large sparse matrices, an interior-point method [350] is utilised to solve the optimisation problem, detailed in Section 7.2. The numerical method is implemented by the fmincon function in Matlab® [351], with default options for barrier parameter updates and Hessian calculations. Finally, to obtain a fair comparison among the considered control strategies, the control torque of the proposed RHPS control is set as follows:

$$T_{\text{ctrl}}^{\text{rhps}} = \min\left(T_{\text{ctrl}}^{\text{opt}}, \frac{P^{\text{rated}}}{\Omega}\right), \tag{7.25}$$

where $T_{\text{ctrl}}^{\text{opt}}$ is the optimal control solution.

It should be noted that the use of Fourier series to approximate non-periodic functions, in a RH framework, generates a discontinuity problem at the time window boundaries, known as the Gibbs phenomenon [352]. To solve this issue, alternative basis functions, such as half-range Chebyshev-Fourier (HRCF) basis functions [343], can be utilised, although the control synthesis process becomes more laborious, due

to the more complex description of the HRCF functions. Alternatively, to avoid the discontinuity problem, this work adopts the pragmatic option of keeping the Fourier basis functions by employing the solution detailed in [352], which proposes the construction of a buffer zone using an interpolating smoothing polynomial function. Apart from the solution offered by [352], another suitable option for retaining a Fourier PS approach, within a RH framework, is that of applying a windowing function to the (finite-time) wave excitation [353].

7.3.1 Discussion of the results

Tables 7.1 and 7.2, as well as Figures 7.3 and 7.6, compare RHPS control performance to, respectively, TEM and W2W control performance. Furthermore, Figures 7.4 and 7.5, and Figures 7.7 and 7.8, show, for each control strategy, the time traces of some variables of interest in, respectively, SS6 and SS7.

7.3.1.1 RHPS and TEM control

Table 7.1: Results of the simulations: RHPS and TEM control.

Sea state	TEM control				RHPS control				
	$\bar{\eta}_{\text{turb}}$ (%)	ξ_{hydro} (%)	ξ_{aero} (%)	ξ_{elec} (%)	$\bar{\eta}_{\text{turb}}$ (%)	ξ_{hydro} (%)	ξ_{aero} (%)	ξ_{elec} (%)	$\Delta\bar{P}_{\text{elec}}$ (%)
SS1	36.3	33.5	12.2	2.3	35.5	35.1	12.5	2.3	~ 0
SS2	36.4	34.6	12.6	4.2	32.9	36.5	12.0	4.2	~ 0
SS3	37.2	39.1	14.5	7.7	36.9	44.0	16.2	8.2	6.1
SS4	38.3	49.3	18.9	13.0	38.0	52.8	20.1	14.0	7.1
SS5	37.8	38.9	14.7	10.3	36.0	47.3	17.0	11.2	8.0
SS6	38.5	37.4	14.4	10.5	37.2	52.2	19.3	12.4	15.3
SS7	38.8	34.5	13.4	10.9	31.0	45.5	14.2	12.2	10.6
SS8	36.0	36.1	13.0	6.3	30.5	50.1	15.3	13.1	51.9

In Table 6.3, $\bar{\eta}_{\text{turb}}$, ξ_{hydro}, ξ_{aero}, ξ_{elec}, and $\Delta\bar{P}_{\text{elec}}$, for RHPS and TEM control, are reported. Similarly to steady-state W2W control (see Section 6.3.1), when the available wave power is significant (i.e., SS3 - SS8), RHPS control increases ξ_{elec} compared to TEM control, while lightly penalising $\bar{\eta}_{\text{turb}}$. In terms of OWC W2W behaviour, the eight tested SSs (SS1 - SS8) can be divided into four groups, namely (i) low-energy (SS1-SS3), (ii) medium-energy (SS5-SS6), (iii) medium-to-high-energy (SS7-SS8), and (iv) near-resonance (SS4) SSs. To this end, Figure 7.3

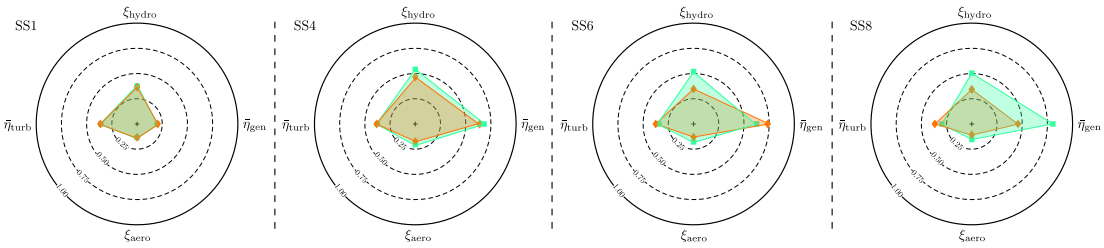

Figure 7.3: Graphical representation of efficiencies (and CWRs) obtained with RHPS control (■) and TEM control (♦), for four different sea states (namely SS1, SS4, SS6, and SS8). For each sea state, the values of ξ_{hydro} (top), $\bar{\eta}_{\text{turb}}$ (left), ξ_{aero} (bottom), and $\bar{\eta}_{\text{gen}}$ (right) are reported. The external black circles represent an ideal (i.e., unitary) efficiency/CWR value, while the three dashed circles indicate the isolines for efficiency values equal to 0.25, 0.50, and 0.75.

shows $\bar{\eta}_{\text{turb}}$, ξ_{hydro}, ξ_{aero}, and $\bar{\eta}_{\text{gen}}$, for RHPS and TEM control, in four different SSs (one from each group).

Regardless of the control approach, ξ_{elec} is always relatively small in low-energy SSs (SS1-SS3), especially since the generator operates inefficiently at low rotational speeds. For instance, as shown in Figure 7.3, for SS1, $\bar{\eta}_{\text{gen}} < 0.25$.

The W2W efficiency notably increases for medium-energy SSs (SS5-SS6), where the superior ξ_{elec} achieved by RHPS control is primarily due to the high value of ξ_{aero}, meaning that the wave-to-turbine energy conversion process is more efficient. Indeed, with RHPS control, ξ_{hydro} is significantly improved without excessively penalizing $\bar{\eta}_{\text{turb}}$, as shown in Table 7.1 and Figure 7.3, for SS6. The higher ξ_{hydro} obtained with RHPS control is arguably a result of the larger pressure peaks (see, for example, Figure 7.4), which consequently lead to an increase in the available pneumatic power (as shown in Figure 7.5).

For high-energy SSs (SS7-SS8), the larger ξ_{elec}, obtained with RHPS control, is mainly due to the significantly high value of $\bar{\eta}_{\text{gen}}$ (Figure 7.3, SS8), meaning that the generator is consistently operating in its high efficiency region. Furthermore, in comparison to TEM control, RHPS control also increases ξ_{hydro} in SS7-SS8. However, since $\bar{\eta}_{\text{turb}}$ drops dramatically, ξ_{aero} only marginally contributes to the improvement in ξ_{elec}, especially if compared to the leading role played by $\bar{\eta}_{\text{gen}}$.

Finally, the highest values of ξ_{hydro} and ξ_{elec} are unsurprisingly achieved in SS4 (for both TEM, and RHPS, control). Indeed, the T_{p} of SS4 is close to the heave mode resonant period of the considered OWC WEC (i.e., close to the design operating condition) and, therefore, the OWC system naturally operates in near-optimal conditions, with only a moderate control effort needed. In this peculiar operating condition, the efficiencies/CWRs obtained with RHPS, and TEM, control are rather evenly balanced, as indicated by the fact that the green/orange shaded areas in Figure 7.3, for SS4, are alike.

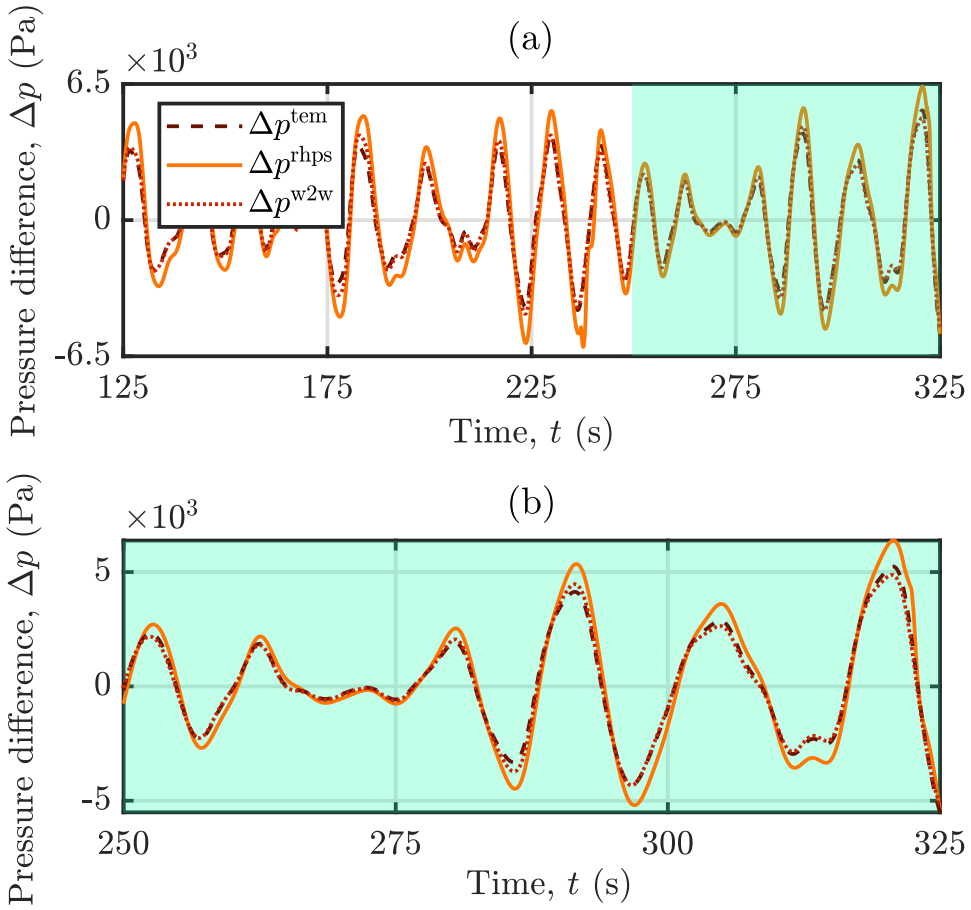

Figure 7.4: Time traces, from a realization of SS6, of the chamber pressure difference, Δp, using TEM (Δp^{tem}), RHPS (Δp^{rhps}), and steady-state W2W (Δp^{w2w}) control.

7.3.1.2 RHPS and steady-state W2W control

On the one hand, in low-to-medium energy SSs (SS1-SS6), the W2W efficiency provided by RHPS and steady-state W2W control are comparable to each other, meaning that RHPS control only marginally improves ξ_{elec}. Furthermore, as already mentioned in Section 7.3.1.1, the considered OWC effortlessly (i.e., without excessive control action) operates in near-optimal conditions in SS4, since T_{p} is close to the heave mode resonance period. As such, all the OWC subsystems work at relatively high efficiency values in SS4, with only minor differences between RHPS and static-efficiency-based W2W control (Table 7.2 and Figure 7.6, SS4).

On the other hand, RHPS control improves electricity production more significantly in SS7 and SS8, where optimal constraint handling plays a key role in determining the control performance. Indeed, optimal constraint handling optimally exploits the full rotational speed dynamic range, therefore operating the OWC system closer to its limits. For instance, Figure 7.7(b) shows the time traces of Ω, for each control strategy, in SS7, where RHPS control drives Ω close to $\Omega^{\max} = 400$ rad/s.

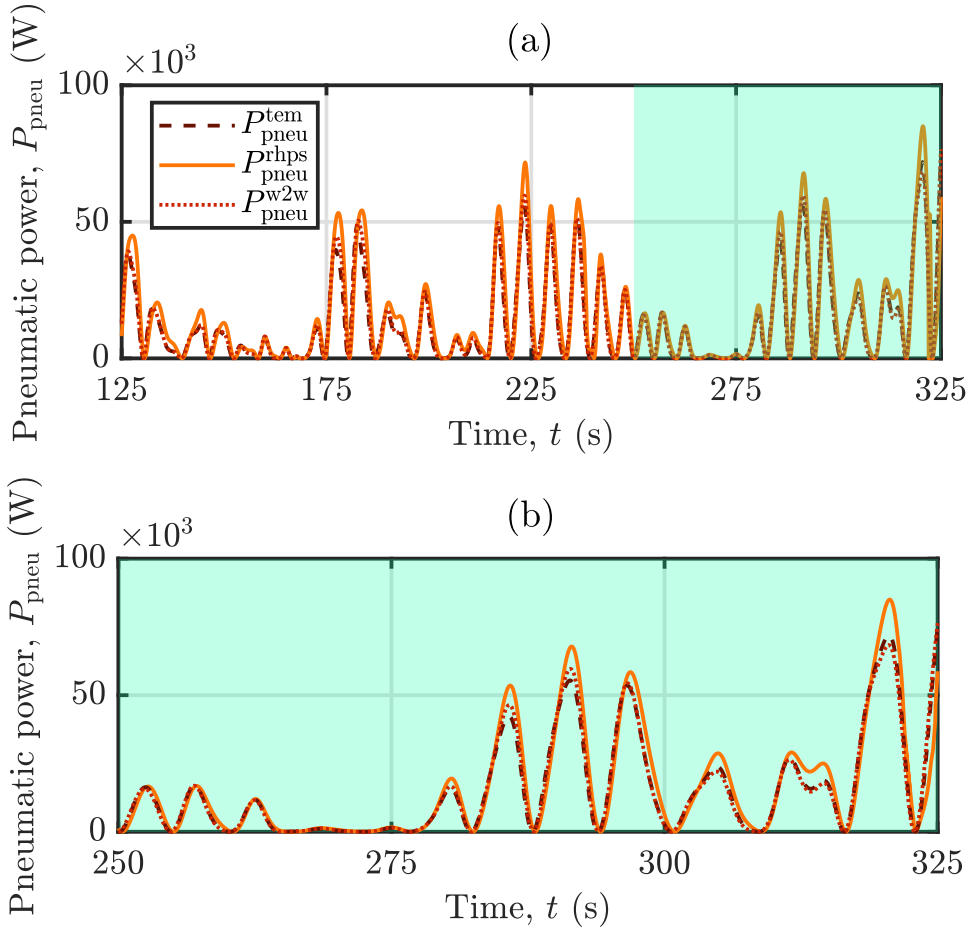

Figure 7.5: Time traces, from a realization of SS6, of the pneumatic power, P_{pneu}, using TEM ($P^{\text{tem}}_{\text{pneu}}$), RHPS ($P^{\text{rhps}}_{\text{pneu}}$), and steady-state W2W ($P^{\text{w2w}}_{\text{pneu}}$) control.

In relation to wave-to-turbine performance (i.e., ξ_{aero}), RHPS control consistently achieves a higher ξ_{aero} than that of W2W control, as shown in Table 7.2 and Figure 7.6. More specifically, for SS1-SS4, RHPS control takes more advantage of the air turbine, hence $\bar{\eta}_{\text{turb}}$ is higher. However, in SS5-SS8, where the effect of Ω on the hydrodynamic subsystem is more significant, RHPS control prioritises ξ_{hydro} (Figure 7.5), at the expense of a lower $\bar{\eta}_{\text{turb}}$ (Figure 7.8). In any case, as already mentioned in Section 7.3.1.1, the high ξ_{elec} obtained with RHPS control in SS7 and SS8 primarily depends on $\bar{\eta}_{\text{gen}}$ ($\sim 80 - 85\%$).

7.3.2 Main control co-design aspects

As already discussed in Section 6.3.2, a flat and high-valued turbine efficiency curve is ideal to maximise rotational speed control flexibility and improve overall OWC system performance. On the other hand, in comparison to η_{turb}, since the η_{gen} profile is already relatively flat and high, the sensitivity of RHPS control performance to an improvement in η_{gen} is expected to be marginal.

Table 7.2: Results of the simulations: RHPS and steady-state W2W control.

Sea state	W2W control				RHPS control				
	$\bar{\eta}_{\text{turb}}$ (%)	ξ_{hydro} (%)	ξ_{aero} (%)	ξ_{elec} (%)	$\bar{\eta}_{\text{turb}}$ (%)	ξ_{hydro} (%)	ξ_{aero} (%)	ξ_{elec} (%)	$\Delta\bar{P}_{\text{elec}}$ (%)
SS1	29.5	32.5	9.6	2.3	35.5	35.1	12.4	2.3	~ 0
SS2	30.0	35.1	10.5	4.2	32.9	36.5	12.0	4.2	~ 0
SS3	31.6	43.7	13.8	8.0	36.9	44.0	16.2	8.2	2.4
SS4	34.8	53.1	18.5	13.6	38.0	52.8	20.1	14.0	2.9
SS5	37.3	43.3	16.2	11.0	36.0	47.3	17.0	11.2	1.8
SS6	38.1	40.6	15.5	12.1	37.2	52.2	19.3	12.4	2.4
SS7	38.5	36.6	14.1	11.5	31.0	45.5	14.2	12.2	5.7
SS8	33.4	44.6	14.9	12.0	30.5	50.1	15.3	13.1	8.4

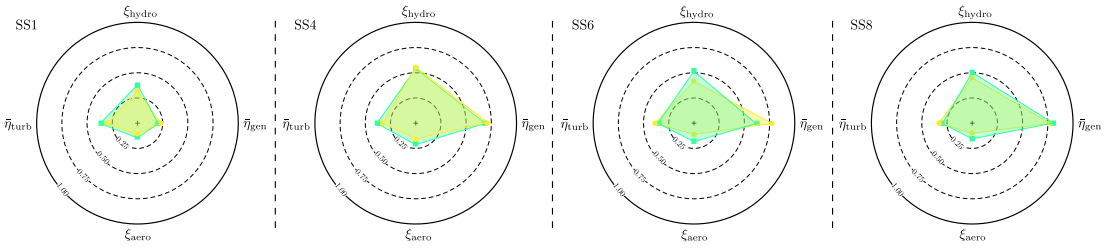

Figure 7.6: Graphical representation of efficiencies (and CWRs) obtained with RHPS control (■) and W2W control (●), for four different sea states (namely SS1, SS4, SS6, and SS8). For each sea state, the values of ξ_{hydro} (top), $\bar{\eta}_{\text{turb}}$ (left), ξ_{aero} (bottom), and $\bar{\eta}_{\text{gen}}$ (right) are reported. The external black circles represent an ideal (i.e., unitary) efficiency/CWR value, while the three dashed circles indicate the isolines for efficiency values equal to 0.25, 0.50, and 0.75.

The larger torque variations (Figure 7.7(a)) required by RHPS and W2W control, indicating increased control aggressiveness, may result in higher maintenance costs, consequently increasing OpEx [316]. However, besides turbine disintegration due to overspeeding or to water ingestion, the most detrimental event on OWCs is Wells turbine stall (i.e., $\Psi > \Psi_{\text{stall}}$), which generates high frequency vibrations [264]. To this end, it should be noted that RHPS and W2W control tends to keep Ω relatively high (Figures 6.9(b) and 7.7(b)), consequently lowering the risk of turbine stall.

Finally, in contrast to TEM and steady-state W2W control, RHPS control may require reactive power (i.e., $T_{\text{ctrl}} < 0$) to maximise energy production (see, for instance, Figure 7.9). The need for reactive power to maximise wave energy extraction is not unusual in traditional WEC (hydrodynamic) control [146], as shown, for instance, in Figure 7.2. However, due to the presence of the soft connection (i.e., the air chamber) between the PTO and hydrodynamic part, the

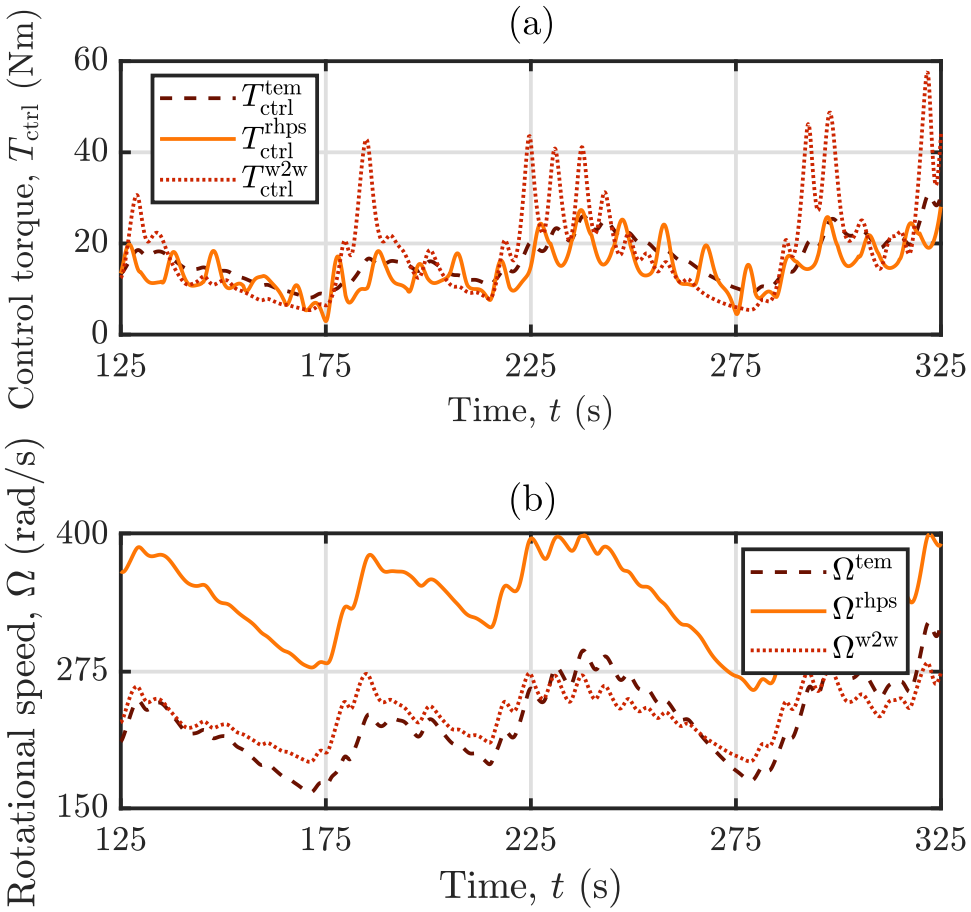

Figure 7.7: Time traces, from a realization of SS7, of the (a) rotational speed, Ω, and (b) control torque, T_{ctrl}, using TEM (Ω^{tem}, $T_{\text{ctrl}}^{\text{tem}}$), RHPS ($\Omega^{\text{rhps}}$, $T_{\text{ctrl}}^{\text{rhps}}$), and steady-state W2W (Ω^{w2w}, $T_{\text{ctrl}}^{\text{w2w}}$) control.

control action on OWCs has only a modest effect on ξ_{hydro}, especially if compared to what hydrodynamic control can do on some other WEC types [146]. Therefore, it should not come as a surprise that OWC optimal control requires considerably less reactive power (Figure 7.9) than optimal control for other WEC types (Figure 7.2). Figure 7.10 shows the mean time during which reactive power is required, for each SS, as a fraction of the total simulation time. It can be noted that reactive power is particularly needed in low-to-medium energy SSs (SS1-SS4), where ξ_{aero} plays an important role in maximising ξ_{elec}, while the electric generator cannot operate at high efficiency, due to the low rotational speed. On the other hand, in medium-to-high energy SSs (SS5-SS8), RHPS control takes advantage of turbine inertia to keep Ω high without utilising much reactive power, therefore effectively prioritizing $\bar{\eta}_{\text{gen}}$ over ξ_{aero} (see, for instance, Figure 7.3, SS8).

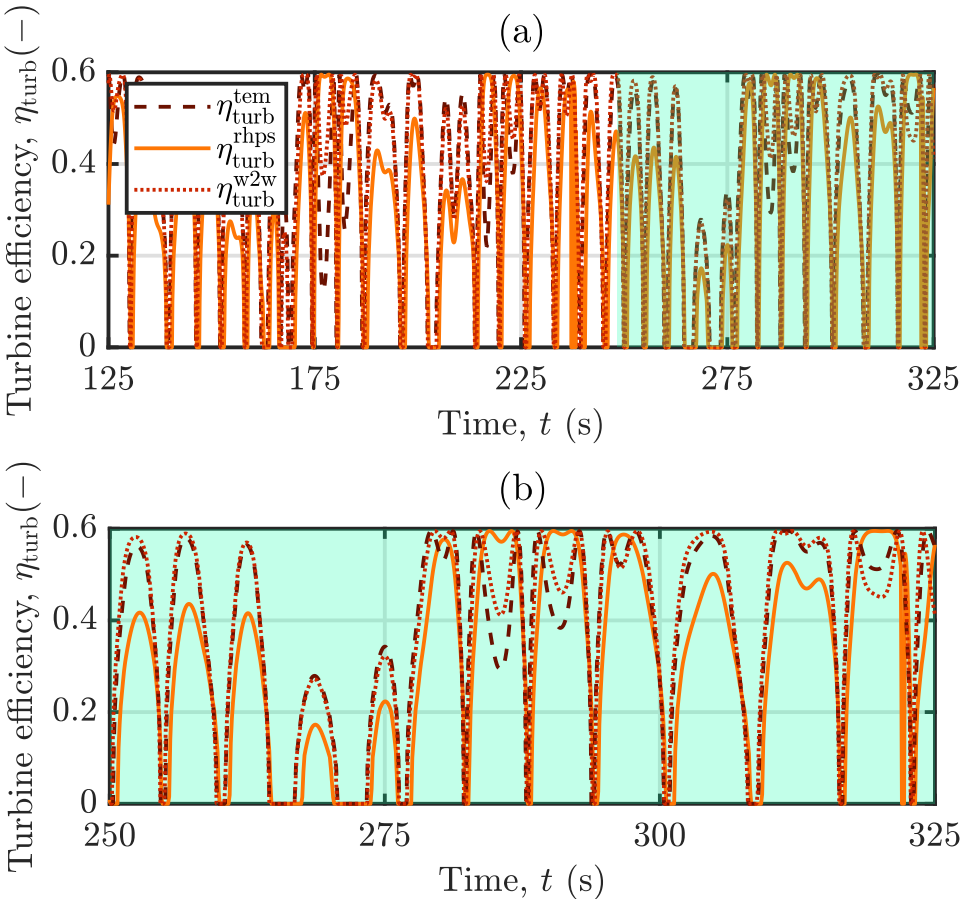

Figure 7.8: Time traces, from a realization of SS7, of the turbine efficiency, η_{turb}, using TEM ($\eta_{\text{turb}}^{\text{tem}}$), RHPS ($\eta_{\text{turb}}^{\text{rhps}}$), and steady-state W2W ($\eta_{\text{turb}}^{\text{w2w}}$) control.

7.4 Conclusions

The proposed RHPS control approach increases ξ_{elec} compared to TEM and, to some extent, steady-state W2W control, and also provides a relatively computationally efficient solution to the OWC OCP. Ultimately, the main advantage of the RHPS approach, over a simpler steady-state W2W strategy, is arguably that the control solution is optimally constrained, which is particularly important in high-energy SSs to exploit the entire rotational speed dynamic range. For instance, Figure 7.11 shows the dynamic range of Ω, in three different SSs (SS4, SS7, and SS8), for each control strategy. It can be noted that, in SS7 and SS8, RHPS control drives Ω closer to Ω^{max}, while steady-state W2W control is more conservative and keeps Ω around a mean optimal value. In high-energy SSs (i.e., SS7 and SS8), the dynamic range of Ω is broad with TEM control, since the large pressure peaks in the air chamber make Ψ vary significantly, therefore Ω has correspondingly large oscillations to follow Ψ_{mep}. On the other hand, in SS4 (i.e., in near-resonance conditions), where

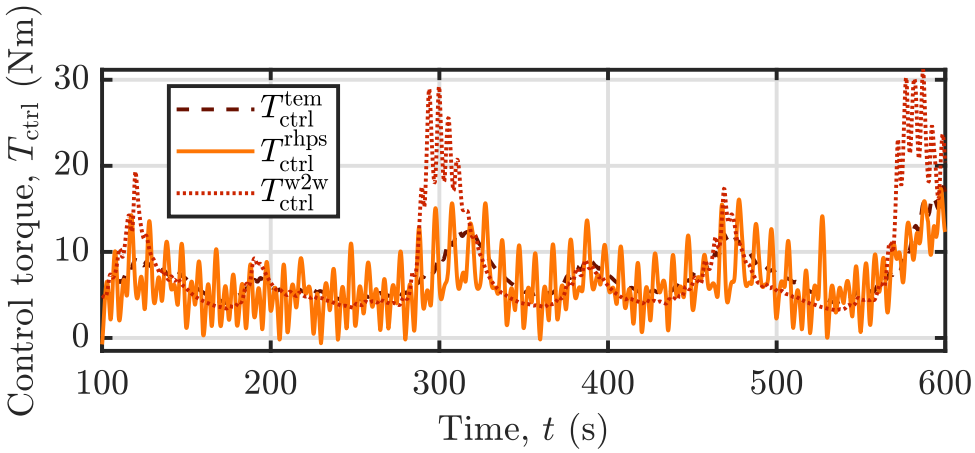

Figure 7.9: Time traces of the control torque, T_{ctrl}, for a realisation of SS4, for each considered control approach.

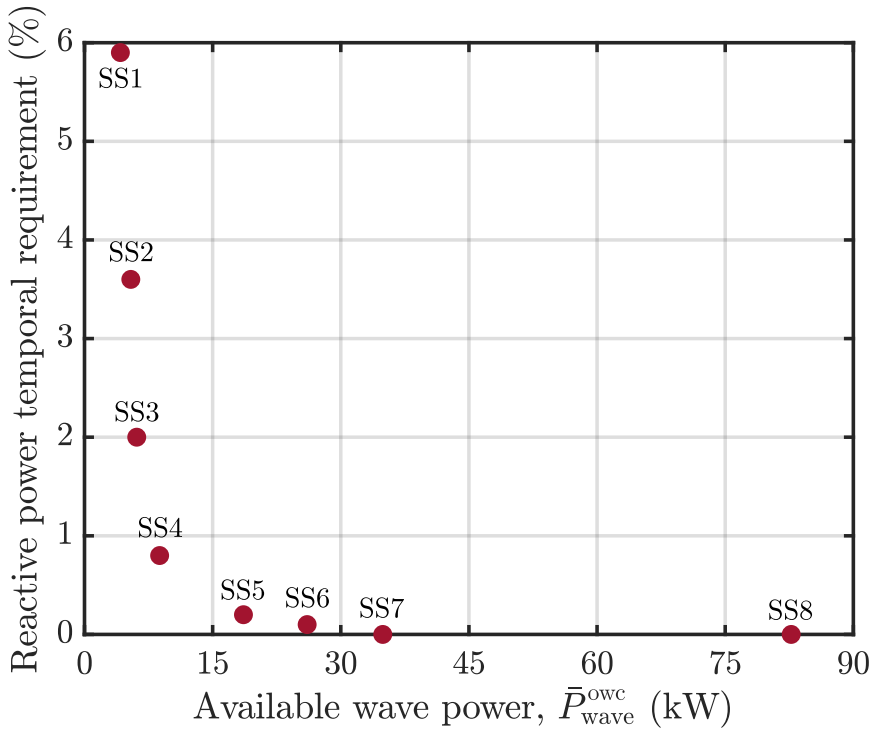

Figure 7.10: Percentage of time, compared to the total simulation time, during which reactive power is required, in each SS. Source: [63].

the control effort required to operate the OWC is more marginal, the dynamic range of Ω covered by each strategy is unsurprisingly similar.

In future works, a systematic study to investigate the stability of the proposed OWC RHPS control strategy should be developed. In any case, for the study case considered in this chapter, the solver always converges to a stable solution, although different choices of the optimisation starting point (or initial guess) affect the convergence time.

Finally, to reduce the computational burden of the optimisation problem, it is worth mentioning that the sine and cosine functions appearing in the Fourier PS representation can be approximated by a truncated Taylor series expansion. Furthermore, polynomial basis functions may be also considered, as a simpler alternative to trigonometric functions. To assess how much the computational burden varies using different basis functions, a systematic study should be carried out considering, for instance, different degrees of the polynomial basis functions and computing the computational burden, and accuracy, for each choice of basis functions.

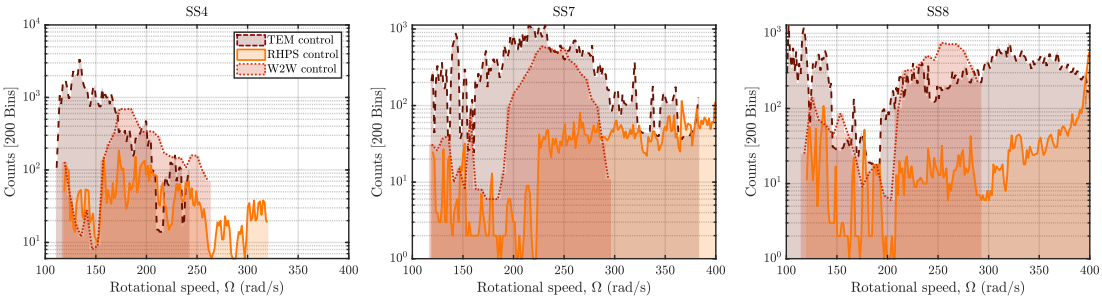

Figure 7.11: Rotational speed dynamic range analysis for each control strategy, namely TEM, steady-state W2W, and RHPS control. The figure shows a histogram in the range $\Omega = [100, 400]$ rad/s, with 200 bins. A logarithmic scale is used for the vertical axis.

8

Control co-design of power take-off and bypass valve for oscillating water columns

Contents

8.1 OWC control co-design 167
8.1.1 Performance function selection 167
8.1.2 PTO and bypass valve specifications 168
8.1.3 Design of the control system 170
8.1.4 Methodology 174
8.2 Results and discussion 174
8.2.1 Results 176
8.2.2 Discussion 176
8.3 Conclusions 181

Due to the coupling between the WEC control problem and the WEC geometry optimisation problem [227, 228], CCD [229, 230] techniques are vital to achieve optimum control-informed WEC designs [228, 231, 232, 233] (Figure 5.3). The benefit of CCD over a traditional design approach, as well as the main OWC CCD aspects, are discussed in Section 5.1.4.

In contrast with the work presented in Chapters 6 and 7, where the focus is on energy maximising control strategies for OWCs, this chapter addresses the OWC control problem from a more holistic perspective. To this end, a parametric CCD approach is conceived to optimise the bypass valve, and Wells turbine rotor diameter,

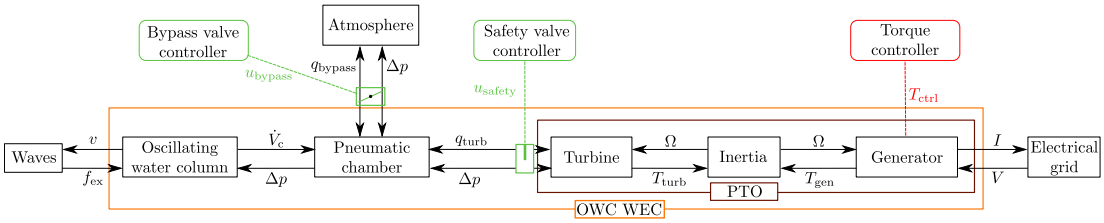

Figure 8.1: Wave-to-wire power flow of the OWC system considered in this chapter.

for a Mutriku-like OWC system, where the optimum system parameters minimise a 'surrogate' of the LCoE, which is chosen as a suitable high-level performance function. For each considered combination in the parametric space of bypass valve size and rotor diameter, suitable control strategies for the turbine rotational speed (Section 8.1.3.1), bypass valve position (Section 8.1.3.2), and safety valve position (Section 8.1.3.3), are designed. In this chapter, the the parametric space of bypass valve size and rotor diameter will be addressed as valve/turbine (VT) parametric space.

A complete OWC control strategy [51, 56], in the spirit of Section 5.1, should include: (i) Turbine rotational speed control, for maximising the OWC W2W performance in CR_2 [60, 61, 63, 297]; (ii) peak-shaving control [56], for improving the *capacity factor*, expressed as

$$\text{Capacity factor} = \frac{\text{Produced time-averged power}}{\text{Rated power}}, \tag{8.1}$$

when the device operates in CR_3. Peak-shaving control is essential to extend the OWC operational range in CR_3 by limiting, using any of the methods presented in Section 5.2.5, the available/converted pneumatic power. To date, only very little attention has been given to OWC rated power control, particularly for Wells turbines, where peak-shaving can be implemented by dissipating excessive pneumatic power via a bypass valve [226, 298]. With a biradial turbine, thanks to the fast response of its small in-series valve, real-time wave-by-wave peak-shaving control is feasible [256, 300]. However, even utilising wave forecasting techniques [252, 354], wave-by-wave bypass valve control is challenging to implement in real-time, due to the low actuation speed of the valve with respect to the wave celerity [103]. In light of such issues, a SS-based control approach to regulate the bypass valve position is proposed in this chapter, where the position of the bypass valve is essentially a function the SS or, equivalently, of the available wave power.

The reminder of the chapter is structured as follows. In Section 8.1, the proposed CCD approach is detailed. Results are discussed in Section 8.2 and conclusions are drawn in Section 8.3.

8.1 OWC control co-design

Figure 8.1 shows the W2W power flow for the OWC considered in this chapter. The system modelling equations are similar to those presented in Section 6.1 (i.e., Equations (6.1), (6.2), and (6.3)), with the only difference being the presence of the bypass valve in the air chamber model. An OWC chamber, equipped with a bypass valve, is modelled using Equation (3.8), where the bypass valve flow rate is computed from Equation (3.5).

8.1.1 Performance function selection

Due to the difficult problem of OpEx estimation, the 'complete' LCoE in Equation (1.1) cannot be easily used as a performance objective. As such, a 'surrogate' of the LCoE, denoted LCoE*, is adopted as a suitable performance function for the CCD approach.

Since design variations in the bypass valve, and PTO, primarily affect CapEx and electric energy production, OpEx is simplified as a proportion of CapEx, namely $\mathrm{OpEx} = b\,\mathrm{CapEx}$, with $0 \leq b \leq 1$. Additionally, although OpEx is a function, to some extent, of the control action [316], the impact of control on OpEx is not expected to change significantly, for different points in the VT parametric space, for the considered control approach (Section 8.1.3).

The capital cost is computed as $\mathrm{CapEx} = C_{\mathrm{str}} + C_{\mathrm{mov}}$, where C_{str} is the OWC structure cost and C_{mov} (see Figure 8.2), written as

$$C_{\mathrm{mov}}(d_{\mathrm{r}}, d_{\mathrm{bypass}}) = C_{\mathrm{pto}}(d_{\mathrm{r}}) + \mu(C_{\mathrm{safety}}(d_{\mathrm{r}}) + C_{\mathrm{bypass}}(d_{\mathrm{bypass}})), \tag{8.2}$$

is the cost of the moving parts, where

$$C_{\mathrm{pto}}(d_{\mathrm{r}}) = C_{\mathrm{mech}}(d_{\mathrm{r}}) + C_{\mathrm{elec}}(d_{\mathrm{r}}). \tag{8.3}$$

In Equations (8.2) and (8.3), C_{pto} is the PTO material and manufacturing cost, C_{bypass} and C_{safety} are the material costs of the bypass and safety valves, respectively, μ is the manufacturing cost factor of the valves, C_{mech} is the cost of the mechanical components (i.e., turbine, shaft, and bearings), and C_{elec} is the cost of the electric generator and ancillary components. By assuming geometric similarity for all the mechanical components, the mass of the material scales as d_{r}^3, while C_{mech} (in k$) is estimated [74], as

$$C_{\mathrm{mech}}(d_{\mathrm{r}}) = C_{\mathrm{mech}}^{\mathrm{pico}} \left(\frac{d_{\mathrm{r}}}{d_{\mathrm{r}}^{\mathrm{pico}}} \right)^{\beta}, \tag{8.4}$$

where the empirical coefficients, $C_{\text{mech}}^{\text{pico}}$ and β, are established from experience with the OWC power plant at Pico Island [103], while $d_{\text{r}}^{\text{pico}}$ is the Pico turbine rotor diameter. Moreover, C_{elec} (in k$) is calculated [74], as

$$C_{\text{elec}}(d_{\text{r}}) = 3.026\,(P^{\text{rated}}(d_{\text{r}}))^{0.7}, \tag{8.5}$$

where P^{rated} is the generator rated power in kilowatts. Since the diameter of the safety valve is approximately equal to d_{r}, C_{safety} can be computed as

$$C_{\text{safety}}(d_{\text{r}}) = \rho_{\text{steel}} \frac{\pi\, d_{\text{r}}^2}{4} t_{\text{h}} C_{\text{steel}}, \tag{8.6}$$

where C_{steel} is the cost per unit mass of steel, t_{h} is the safety valve thickness, and ρ_{steel} is the steel density. To calculate C_{bypass}, d_{r} is simply replaced by d_{bypass} in Equation (8.6). Figure 8.2 shows, for each point of the VT parametric space, the value of C_{mov}. Since d_{bypass} should somewhat depend on d_{r}, meaning that the required power dissipation is a function of the PTO size, d_{bypass} is specified as a ratio between the diameters, $d_{\text{bypass}}/d_{\text{r}}$.

For the considered CCD approach, since the air chamber volume is fixed, C_{str} is constant. To this end, it is assumed that C_{str} is a proportion of C_{mov} for the Mutriku OWC (i.e., $d_{\text{r}} = 0.75$ m and $d_{\text{bypass}}/d_{\text{r}} = 0$), indicated as $C_{\text{mov}}^{\text{mtrk}}$ in Figure 8.2, as

$$C_{\text{str}} = \varepsilon\, C_{\text{mov}}^{\text{mtrk}}, \tag{8.7}$$

where $\varepsilon > 1$.

Finally, if the simplifications introduced so far in the current section are applied, LCoE^* can be written as

$$\text{LCoE}^* = (1+b)\,\frac{\varepsilon\, C_{\text{mov}}^{\text{mtrk}} + C_{\text{mov}}}{E_{\text{elec}}^{\text{life}}} = (1+b)\,\overline{\text{LCoE}}^*, \tag{8.8}$$

where $E_{\text{elec}}^{\text{life}}$ is the produced electrical energy over the OWC WEC lifetime. Ultimately, since $(1 + b)$ is just a multiplicative coefficient, the CCD performance objective is to minimise $\overline{\text{LCoE}}^* = \overline{\text{LCoE}}^*(d_{\text{r}}, d_{\text{bypass}}, E_{\text{elec}}^{\text{life}})$.

8.1.2 PTO and bypass valve specifications

The PTO characteristics and control constraints are solely functions of d_{r}, as shown in Figure 8.3. Firstly, assuming the same turbine rotor material (of the Wells turbine at Mutriku), from geometric similarity, $I \propto d_{\text{r}}^5$, [183] as

$$\frac{I}{I^{\text{mtrk}}} = \left(\frac{d_{\text{r}}}{d_{\text{r}}^{\text{mtrk}}}\right)^5, \tag{8.9}$$

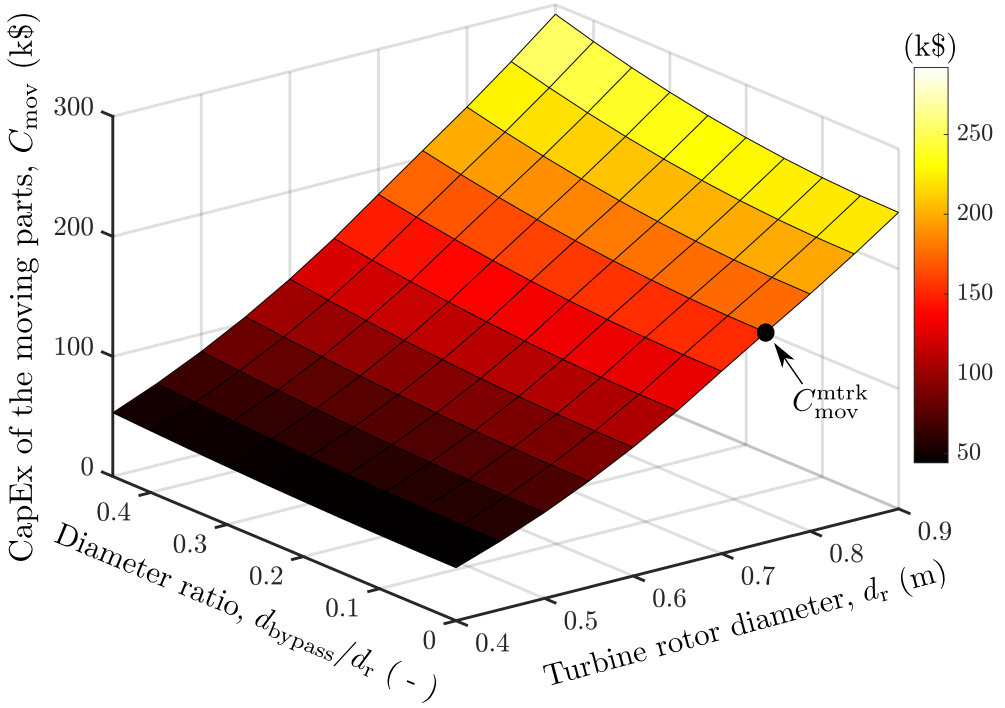

Figure 8.2: Cost of the moving parts, C_{mov}, as a function of the turbine rotor diameter, d_{r}, and the ratio between bypass valve diameter and turbine rotor diameter, $d_{\mathrm{bypass}}/d_{\mathrm{r}}$. $C_{\mathrm{mov}}^{\mathrm{mtrk}}$ is the cost of the moving parts of Mutriku OWC ($d_{\mathrm{r}} = 0.75$ m, $d_{\mathrm{bypass}}/d_{\mathrm{r}} = 0$).

where $d_{\mathrm{r}}^{\mathrm{mtrk}}$ and I^{mtrk} are the turbine rotor diameter and PTO inertia moment at Mutriku, respectively. Secondly, Ω^{max} [56] is specified as

$$\Omega^{\mathrm{max}} = \min(\Omega_{\mathrm{gen}}^{\mathrm{max}}, \Omega_{\mathrm{turb}}^{\mathrm{max}}), \tag{8.10}$$

where $\Omega_{\mathrm{gen}}^{\mathrm{max}}$ is set at 400 rad/s [68, 183] and, if a maximum blade tip speed of 160 m/s is assumed [183] (to avoid large air compressibility effects in the turbine), $\Omega_{\mathrm{turb}}^{\mathrm{max}}(d_{\mathrm{r}}) = 160(2/d_{\mathrm{r}})$. In general, Ω may also be curtailed to limit turbine noise emission [143, 224]. Without loss of generality, the PTO rated power, P^{rated}, can be calculated as the turbine power output when $\Omega = \Omega^{\mathrm{max}}$ and $\Psi = \Psi_{\mathrm{mep}}$. Finally, $T_{\mathrm{ctrl}}^{\mathrm{max}}$ is inferred from Ω^{max} and P^{rated} [183], as

$$T_{\mathrm{ctrl}}^{\mathrm{max}} = 2.266\frac{P^{\mathrm{rated}}}{\Omega^{\mathrm{max}}}. \tag{8.11}$$

The range of values for d_{r} is established considering the Wells turbine rotor diameter at Mutriku ($d_{\mathrm{r}}^{\mathrm{mtrk}} = 0.75$ m) as an initial guess, and pragmatic PTO limits. The upper bound choice (i.e., $d_{\mathrm{r}} = 0.90$ m) is driven by the fact that, if $d_{\mathrm{r}} > 0.90$ m, P^{rated} is sufficiently large to allow wave energy extraction in all high-energy SSs at Mutriku deployment site, even without a bypass valve (therefore, peak-shaving

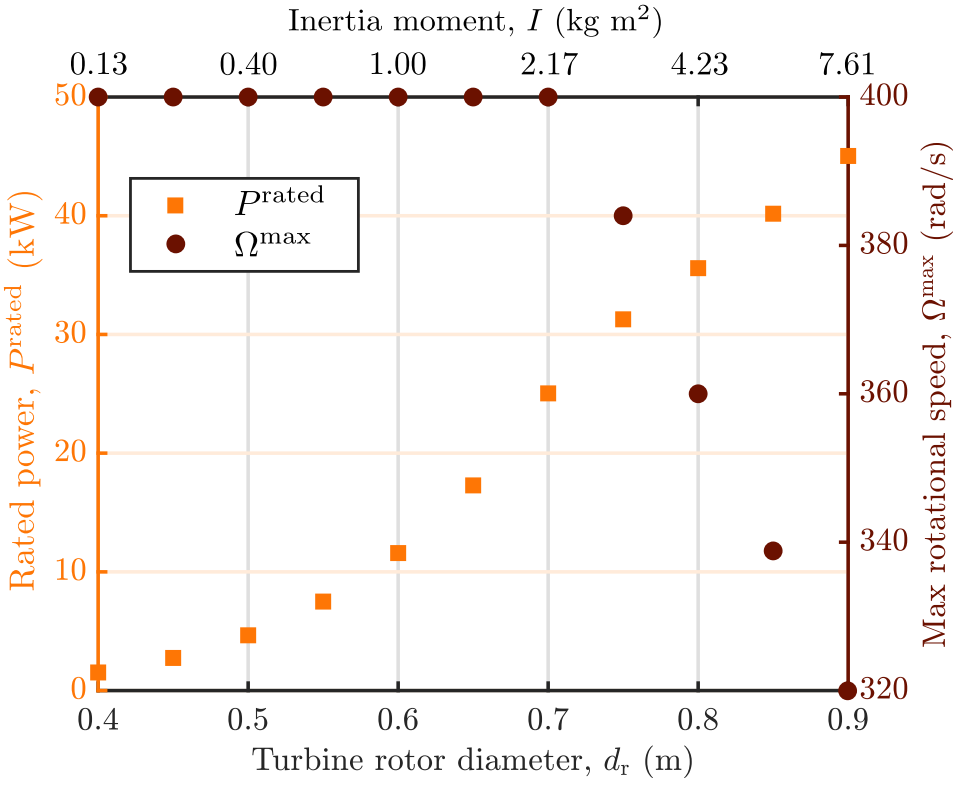

Figure 8.3: Maximum rotational speed, Ω^{max}, PTO rated power, P^{rated}, and turbine inertia (top x-axis label), I, as functions of the turbine rotor diameter, d_{r}. If $d_{\text{r}} > 0.7$ m, $\Omega^{\text{max}} = \Omega^{\text{max}}_{\text{turb}}$, whereas if $d_{\text{r}} \leq 0.7$ m, $\Omega^{\text{max}} = \Omega^{\text{max}}_{\text{gen}}$.

control is no longer required). Moreover, to operate close to the turbine MEP, $\Psi = \Psi_{\text{mep}}$, Ω should increase as d_{r} decreases. However, for $d_{\text{r}} < 0.40$ m, since Ω cannot exceed $\Omega^{\text{max}} (= \Omega^{\text{max}}_{\text{gen}})$, the turbine consistently operates at very low efficiency values and, consequently, the produced energy drops, inevitably increasing the LCoE.

The initial guess for $d_{\text{bypass}}/d_{\text{r}}$ takes inspiration from the Pico bypass valve (equivalent) diameter [103], $d^{\text{pico}}_{\text{bypass}}$. Since u_{bypass} is SS-based, as opposed to wave-by-wave controlled, the bypass valve (when open) yields continuous pneumatic power dissipation. To this end, it should be noted that the Pico bypass valve was not optimised for SS-based control and, therefore, the optimum $d_{\text{bypass}}/d_{\text{r}}$ for SS-based bypass valve control is arguably smaller than $d^{\text{pico}}_{\text{bypass}}/d^{\text{pico}}_{\text{r}} \approx 0.6$. Ultimately, $d_{\text{bypass}}/d_{\text{r}} = 0.3$ is set as the initial guess for $d_{\text{bypass}}/d_{\text{r}}$, while the lower and upper bounds are, respectively, 0 (i.e., no bypass valve) and 0.45.

8.1.3 Design of the control system

As shown in Figure 8.1, the considered OWC system has three manipulated inputs, namely u_{bypass}, u_{safety}, and T_{ctrl}. In this section, suitable high-level valve position

controllers, using u_{bypass} and u_{safety}, and a low-level rotational speed controller, using T_{ctrl}, are designed.

8.1.3.1 Rotational speed control

To consider the effect of Ω on the OWC W2W system, while keeping the computational cost of CCD reasonable, the W2W control strategy presented in Chapter 6 (as opposed to the RHPS control approach of Chapter 7) is adopted in the parametric CCD procedure. For the considered Mutriku-like OWC, a possible W2W efficiency maximising (steady-state) control law has the following (extended) form [60]:

$$T_{\text{ctrl}}^{\text{w2w}} = \min\left(\frac{b_1 + b_2\,\Omega + c_1\,\exp^{c_2\,\Omega}}{\Omega}, T_{\text{ctrl}}^{\max}, \frac{P^{\text{rated}}}{\Omega}\right), \tag{8.12}$$

where the free parameters, b_1, b_2, c_1, and c_2, are optimised, for each d_{r}, applying the optimisation procedure presented in Section 6.2.2. As already mentioned in Section 5.2.2.1, T_{ctrl} can be 'detuned', as $T_{\text{ctrl}} = P^{\text{rated}}/\Omega < T_{\text{ctrl}}^{\text{w2w}}$, to operate the OWC below the W2W peak efficiency and avoid exceeding P^{rated}. However, torque detuning yields an increase in Ω, which eventually attains $\Omega_{\max}$ and the OWC enters safety mode. To reduce safety valve actuation, but keep the OWC operational, a bypass valve can be used to dissipate excessive power. It should be noted that, for other types of WECs, torque detuning is typically the only available control solution to curtail the power to the electric generator (e.g., [355]), due to the lack of suitable peak-shaving actuators.

8.1.3.2 Bypass valve position control

Peak-shaving control can extend the range of SSs over which the OWC WEC retains power production operation. The bypass valve position, u_{bypass}, is controlled depending on the SS or, equally, on the mean wave power available to the OWC system, $\bar{P}_{\text{wave}}^{\text{owc}} = \iota \bar{P}_{\text{wave}}$. When $\bar{P}_{\text{wave}}^{\text{owc}}$ is lower than a certain threshold value, $\bar{P}_{\text{wave}}^{\text{thr}}$, power dissipation is not required and the bypass valve is closed ($u_{\text{bypass}} = 0$). When $\bar{P}_{\text{wave}}^{\text{owc}}$ exceeds the maximum wave power under which the OWC can operate, $\bar{P}_{\text{wave}}^{\max}$, the bypass valve is fully open ($u_{\text{bypass}} = 1$). Finally, when $\bar{P}_{\text{wave}}^{\text{thr}} < \bar{P}_{\text{wave}}^{\text{owc}} < \bar{P}_{\text{wave}}^{\max}$, $u_{\text{bypass}} = f_{\text{bypass}}(\bar{P}_{\text{wave}}^{*})$, where

$$\bar{P}_{\text{wave}}^{*} = \frac{\bar{P}_{\text{wave}}^{\text{owc}} - \bar{P}_{\text{wave}}^{\text{thr}}}{\bar{P}_{\text{wave}}^{\max} - \bar{P}_{\text{wave}}^{\text{thr}}} \tag{8.13}$$

is the relative wave power available to the OWC and $0 < f_{\text{bypass}}(\bar{P}_{\text{wave}}^{*}) < 1$. In essence, u_{bypass} is fully, and solely, determined by selecting: (i) $\bar{P}_{\text{wave}}^{\text{thr}}$, (ii) $\bar{P}_{\text{wave}}^{\max}$, and (iii) $f_{\text{bypass}}(\bar{P}_{\text{wave}}^{*})$.

As shown in Figure 8.4, the value of $\bar{P}^{\text{thr}}_{\text{wave}}$ is a function of d_{r}, and is chosen so that the bypass valve opens (i.e., $u_{\text{bypass}} \neq 0$) only if power dissipation is required. Therefore, $\bar{P}^{\text{thr}}_{\text{wave}}$ is the wave power at which torque detuning alone is no longer sufficient to avoid attaining $\Omega^{\max}$. Additionally, $\bar{P}^{\max}_{\text{wave}}$ is chosen considering the typical wave climate at Mutriku (Figure 8.7) and, in this work, $\bar{P}^{\max}_{\text{wave}} = 265\,\text{kW}$.

Arguably, the most straightforward choice for $f_{\text{bypass}}(\bar{P}^{*}_{\text{wave}})$ is a straight line, namely $f_{\text{bypass}} = f^{\text{line}}_{\text{bypass}} = \bar{P}^{*}_{\text{wave}}$, meaning that u_{bypass} is a linear function of $\bar{P}^{*}_{\text{wave}}$. However, $f_{\text{bypass}} = f^{\text{line}}_{\text{bypass}}$ may not necessarily be the optimal solution, since f_{bypass} should be designed taking into account: (i) How $\bar{P}_{\text{elec}}$ increases with $\bar{P}^{\text{owc}}_{\text{wave}}$ and (ii) how $\bar{P}_{\text{elec}}$ diminishes as the bypass valve opens (i.e., as u_{bypass} varies from 0 to 1). To this end, Figure 8.5(a) shows that, using unconstrained W2W steady-state control (6.9), $\bar{P}_{\text{elec}}$ increases linearly with $\bar{P}^{\text{owc}}_{\text{wave}}$, whereas Figure 8.5(b) shows that $\bar{P}_{\text{elec}}$ decreases as $u^{1.475}_{\text{bypass}}$. Therefore, for small values of u_{bypass}, $\bar{P}_{\text{elec}}$ decreases at a slower rate but, as u_{bypass} increases, $\mathrm{d}\bar{P}_{\text{elec}}/\mathrm{d}u_{\text{bypass}}$ becomes larger. This is arguably due to the fact that the pneumatic power in the air chamber strongly depends on Δp but, when u_{bypass} is small, the pressure levels in the chamber do not substantially decrease, resulting in relatively little pneumatic power dissipation. In the light of such considerations, to compensate for the varying sensitivity of the electrical power to u_{bypass}, f_{bypass} is designed by 'mirroring' the dashed-dotted brown curve in Figure 8.5(b) around the diagonal. In this way, for higher values of $\bar{P}^{*}_{\text{wave}}$ (> 0.45), f_{bypass} increases more slowly than $f^{\text{line}}_{\text{bypass}}$ while, for smaller values of $\bar{P}^{*}_{\text{wave}}$ (< 0.45), f_{bypass} increases faster than $f^{\text{line}}_{\text{bypass}}$. In other words, since $\bar{P}_{\text{elec}}$ linearly increases with $\bar{P}^{\text{owc}}_{\text{wave}}$ (Figure 8.5(a)), the electrical power decrease, defined as

$$\bar{P}^{\text{decr}}_{\text{elec}}(u_{\text{bypass}}) = \frac{\bar{P}_{\text{elec}}(u_{\text{bypass}} = 0) - \bar{P}_{\text{elec}}(u_{\text{bypass}})}{\bar{P}_{\text{elec}}(u_{\text{bypass}} = 0) - \bar{P}_{\text{elec}}(u_{\text{bypass}} = 1)}, \tag{8.14}$$

should ideally be a linear function of u_{bypass} (which, however, is not the case, as shown in Figure 8.5(b)). Therefore, f_{bypass} is essentially designed to compensate for the nonlinear sensitivity of $\bar{P}^{\text{decr}}_{\text{elec}}$ to u_{bypass}, and linearise the relationship between $\bar{P}^{\text{decr}}_{\text{elec}}$ and $\bar{P}^{\text{owc}}_{\text{wave}}$.

Figures 8.5(c) shows the full u_{bypass} computation, written as

$$u_{\text{bypass}} = \begin{cases} 0 & \text{if } \bar{P}^{\text{owc}}_{\text{wave}} \leq \bar{P}^{\text{thr}}_{\text{wave}}, \\ 1 & \text{if } \bar{P}^{\text{owc}}_{\text{wave}} \geq \bar{P}^{\max}_{\text{wave}}, \\ f_{\text{bypass}} & \text{else}, \end{cases} \tag{8.15}$$

where,

$$f_{\text{bypass}} = 2\bar{P}^{*}_{\text{wave}} - (\bar{P}^{*}_{\text{wave}})^{1.475}. \tag{8.16}$$

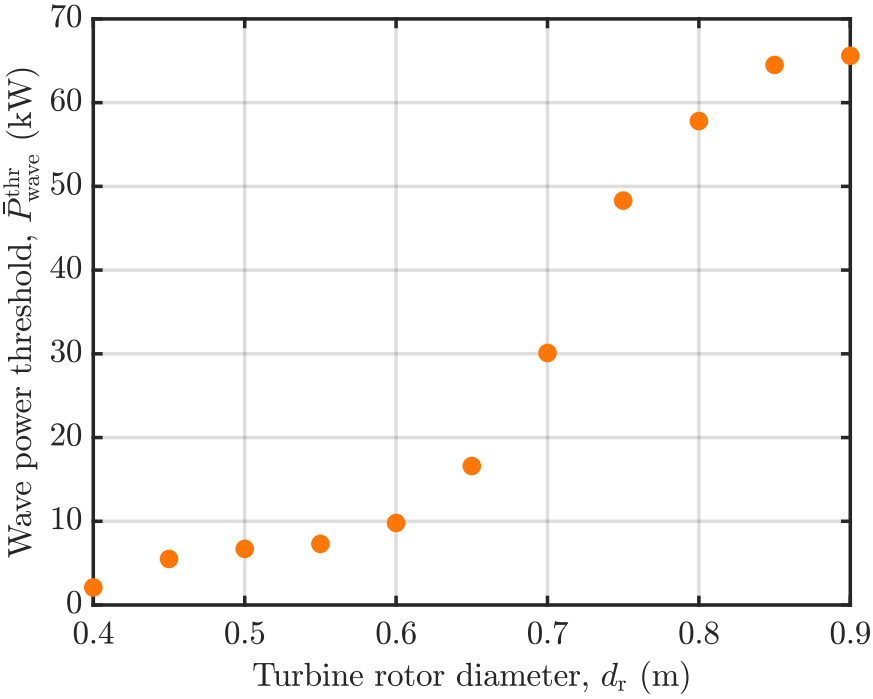

Figure 8.4: Wave power threshold, $\bar{P}^{\mathrm{thr}}_{\mathrm{wave}}$, for each considered turbine rotor diameter, d_{r}.

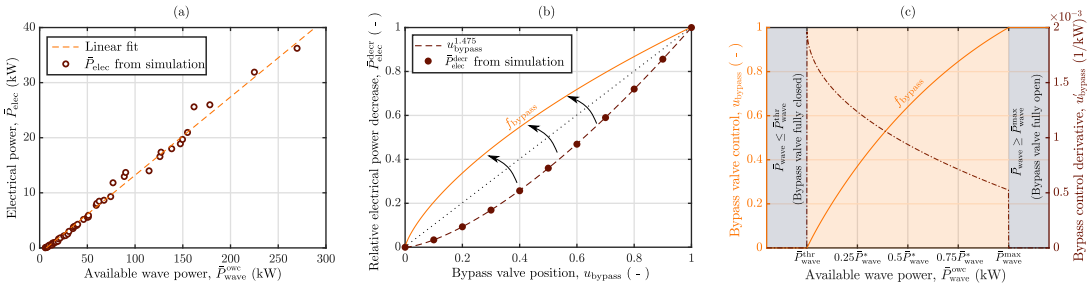

Figure 8.5: Bypass valve control design. (a) Time-averaged electrical power, $\bar{P}_{\mathrm{elec}}$, as a function of the available wave power, $\bar{P}^{\mathrm{owc}}_{\mathrm{wave}}$. (b) Relative electrical power decrease, $\bar{P}^{\mathrm{decr}}_{\mathrm{elec}}(u_{\mathrm{bypass}})$, as a function of the bypass valve position, u_{bypass}. (c) Bypass valve position controller, u_{bypass}, and its derivative $u'_{\mathrm{bypass}} = \mathrm{d}u_{\mathrm{bypass}}/\mathrm{d}\bar{P}^{\mathrm{owc}}_{\mathrm{wave}}$.

8.1.3.3 Safety valve position control

To avoid turbine overspeeding, and consequent risk of turbine rotor disintegration, the safety valve position is controlled as

$$u_{\mathrm{safety}} = \begin{cases} 1\,(\text{normal mode}) & \text{if } \Omega < \Omega^{\mathrm{max}}, \\ 0\,(\text{safety mode}) & \text{else.} \end{cases} \tag{8.17}$$

After entering safety mode, the normal operating mode is subsequently restored when $\Omega < \Omega^{\mathrm{thr}} = 0.7\Omega^{\mathrm{max}}$.

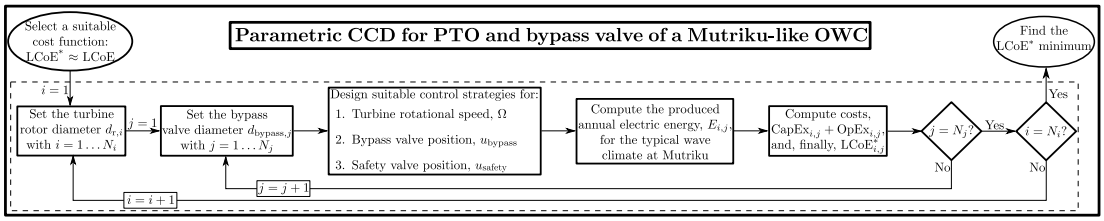

Figure 8.6: Flow chart of the proposed CCD approach.

8.1.4 Methodology

Figure 8.6 shows a schematic of the proposed CCD approach. For each combination of turbine rotor diameter, d_{r}, and bypass valve diameter (or diameter ratio), $d_{\mathrm{bypass}}/d_{\mathrm{r}}$, in the VT parametric space (110 possible cases), the control system is designed, as discussed in Section 8.1.3, and numerical simulations are run to calculate $E_{\mathrm{elec}}^{\mathrm{life}}$ and, finally, LCoE^{*}. Tables 8.1 and 8.2 report, respectively, the OWC modelling and cost-related parameters, considered in the simulation. To obtain $E_{\mathrm{elec}}^{\mathrm{life}}$, the produced annual electric energy at Mutriku is calculated, and a device lifetime of 25 years is assumed [103]. To this end, 15 realisations of 20 minutes each are run for 58 distinct irregular SSs, shown in Figure 8.7. The irregular SSs are generated from JONSWAP SDFs [180], with peak shape parameter $\gamma_{\mathrm{J}} = 3.3$. The significant wave height, H_{s}, and peak period, T_{p}, are selected considering the annual wave climate measured at the Mutriku site [310]. Furthermore, to take into account the shoaling effect at Mutriku, the attenuation function in Figure 6.3(b) is used, as detailed in Section 6.1 of this thesis. Finally, in addition to LCoE^{*}, another performance indicator, namely ζ_{cf} (Equation 8.1), is also calculated for each point in the VT parametric space.

Some simplifications are adopted in the numerical simulation. Firstly, full knowledge of the SS is assumed, although, in practice, online SS estimation techniques [356] can be used. Furthermore, relatively recent advances in meteorological modelling also allows wave SDF forecasting [357]. Since the typical timescale over which the SS changes (from 30 min to 3 h) [338] is much longer than the typical bypass valve actuation time (~ 10 seconds) [103], the dynamic of the bypass valve actuation system is ignored. Finally, no interruption to energy production (which may be due to a system failure or scheduled maintenance) over the OWC WEC lifetime is currently considered.

8.2 Results and discussion

In contrast with the potential use of a numerical optimisation method, the parametric approach taken in this study provides knowledge of the objective function across

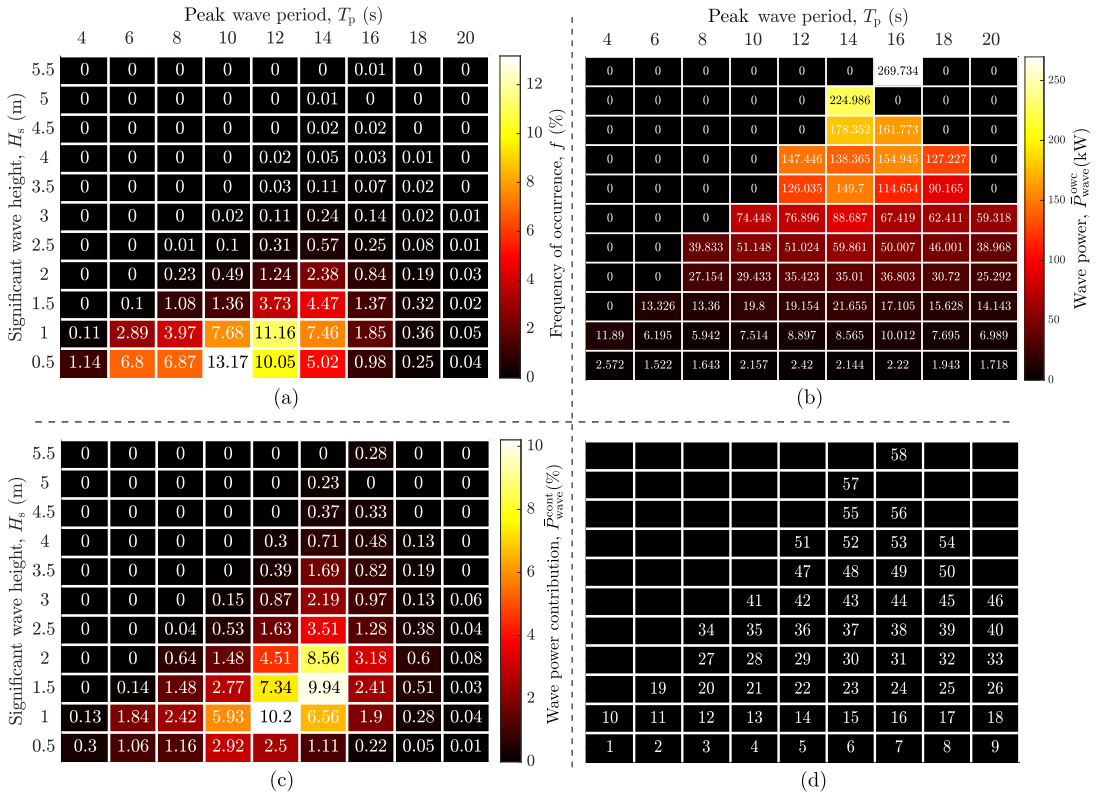

Figure 8.7: Annual wave climate at Mutriku. The four scatter plots show, for each combination of H_s and T_p, (a) the frequency of occurrence (over a year) of a specific sea state at Mutriku, (b) the mean available wave power, $\bar{P}^{owc}_{wave}$, (c) the contribution (specified as a percentage) of each irregular sea state to the total annual wave power available at Mutriku, and (d) the number (from 1 to 58) assigned at each irregular sea state considered in this work.

Table 8.1: OWC model parameters [183, 76, 103].

MP	Value	Unit	MP	Value	Unit
m_p	27748	(kg)	A_p^∞	71618	(kg)
I^{mtrk}	3.06	(kg m^2)	S_w	19.35	(m^2)
d_r^{mtrk}	0.75	(m)	ι	4.5	(m)
κ_W	0.775	(-)	V_0	144	(m^3)
d_r^{pico}	2.3	(m)	t_h	0.005	(m)

the full parametric space, therefore allowing a more exhaustive analysis into the impact of rated power control on the LCoE. For illustration, a specific case in the parametric space is addressed as Γ_i^j, where $i = d_r \times 100$ and $j = (d_{bypass}/d_r) \times 100$. For example, Γ_{55}^{15} indicates the case in which $d_{bypass}/d_r = 0.15$ and $d_r = 0.55$ m.

Table 8.2: Cost-related parameters [233, 74, 75].

CP	Value	Unit	CP	Value	Unit
b	0.45	(-)	β	2/3	(-)
μ	2.5	(-)	$C^{\text{pico}}_{\text{mech}}$	302.6	(k$)
C_{steel}	2.1	($/kg)	ρ_{steel}	7750	(kg/m^3)

8.2.1 Results

Figures 8.8 and 8.9 show $\text{LCoE}^*(\Gamma^{\text{j}}_{\text{i}})$ and $\zeta_{\text{cf}}(\Gamma^{\text{j}}_{\text{i}})$, respectively. For the sake of clarity, the vertical axis (i.e., the z-axis) of Figure 8.8 is reversed, meaning that LCoE^* decreases moving upwards. Additionally, Figure 8.10 shows LCoE^*, and/or ζ_{cf}, for some relevant combinations of d_{r} and $d_{\text{bypass}}/d_{\text{r}}$.

Finally, for the case in which LCoE^* is minimal (i.e., Γ^{15}_{55}), Figure 8.11 provides an insight into the effect of peak-shaving control, for all the 58 SSs. More specifically, Figures 8.11(c) and (d) clarify, respectively, how ζ_{cf} and LCoE^* vary for Γ^{15}_{55} compared with Γ^{0}_{55} (i.e., same d_{r}, but without bypass valve). To study the change in LCoE^* for each SS, the LCoE enhancement index (LEI), is defined as

$$\text{LEI} = 1 - \frac{\text{LCoE}^*(\Gamma^{15}_{55})}{\text{LCoE}^*(\Gamma^{0}_{55})}, \text{ with } \text{LEI} \leq 1. \tag{8.18}$$

Figure 8.11(d) shows the LEI for each SS. In essence:

$$\text{if} \begin{cases} \text{LEI} = 1, & \text{LCoE}^*(\Gamma^{0}_{55}) = \infty; \\ 0 < \text{LEI} < 1, & \text{LCoE}^*(\Gamma^{15}_{55}) < \text{LCoE}^*(\Gamma^{0}_{55}); \\ \text{LEI} = 0, & \text{LCoE}^*(\Gamma^{15}_{55}) = \text{LCoE}^*(\Gamma^{0}_{55}); \\ \text{LEI} < 0, & \text{LCoE}^*(\Gamma^{15}_{55}) > \text{LCoE}^*(\Gamma^{0}_{55}). \end{cases} \tag{8.19}$$

In general, since peak-shaving control plays a more important role as $\bar{P}^{\text{owc}}_{\text{wave}}$ increases, LEI is expected to be relatively higher (see Equation 8.19) in relatively high-energy SSs,

8.2.2 Discussion

From Figure 8.8, LCoE^* is, as expected, less sensitive to $d_{\text{bypass}}/d_{\text{r}}$, rather than to d_{r}. In fact, since the bypass valve is solely utilised for rated power control, and since C_{bypass} is only a marginal fraction of CapEx, $E^{\text{life}}_{\text{elec}}$ and CapEx are primarily affected by the turbine size and performance. Nevertheless, when $d_{\text{r}} \leq 0.45$ m, the sensitivity of LCoE^* to $d_{\text{bypass}}/d_{\text{r}}$ notably increases. This is due to the fact that, if $d_{\text{r}} \leq 0.45$ m, the impact of rated power control on $E^{\text{life}}_{\text{elec}}$ is more remarkable, as it significantly extends the operating range of small-sized turbines (which have lower P^{rated}). If $d_{\text{r}} = 0.90$ m,

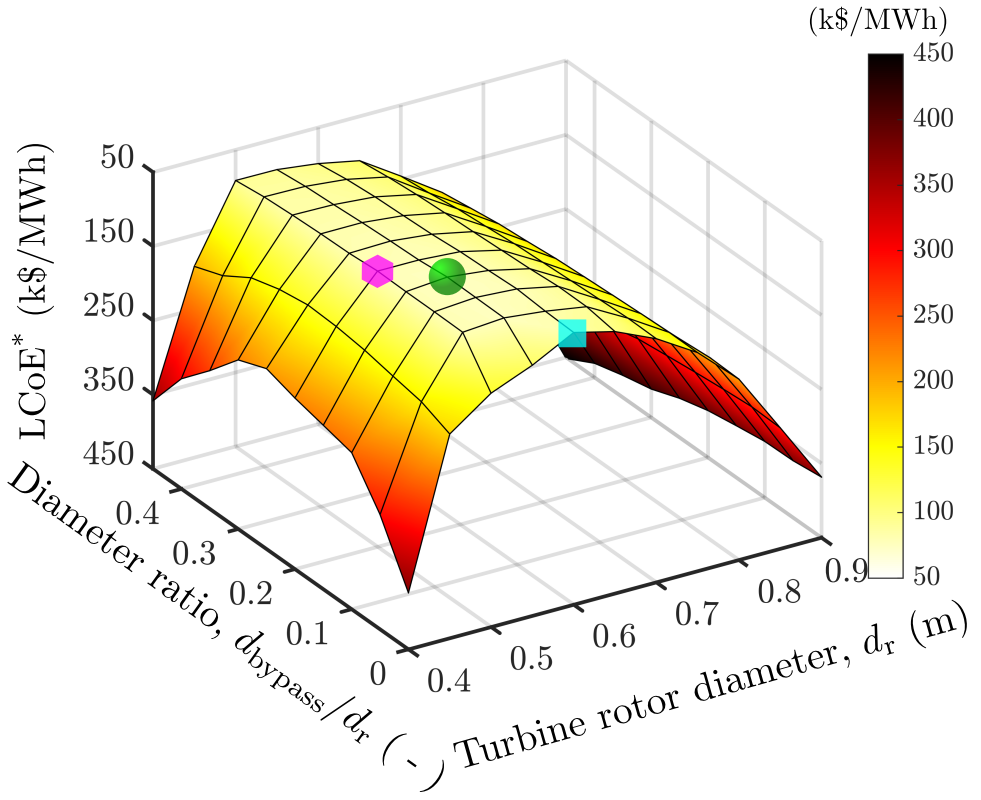

Figure 8.8: LCoE^* obtained from all the considered combinations of d_r and $d_\mathrm{bypass}/d_\mathrm{r}$. The green circle (● at Γ^{15}_{55}) highlights the condition for which LCoE^* is minimised, the blue square (■ at Γ^{0}_{60}) indicates the point at which the minimum LCoE^* is achieved without using a bypass valve, and the magenta hexagon (⬢ at Γ^{20}_{50}) shows the condition for which the maximum capacity factor, $\zeta^\mathrm{max}_\mathrm{cf}$, is found.

P^rated is relatively large and, consequently, LCoE^* increases with $d_\mathrm{bypass}/d_\mathrm{r}$, since the small enhancement in $E^\mathrm{life}_\mathrm{elec}$ obtained with peak-shaving is not worth the bypass valve additional cost. It is also important to note that, when $d_\mathrm{bypass}/d_\mathrm{r} = 0$, LCoE^* is minimum for $d_\mathrm{r} = 0.60\,\mathrm{m}$ while, using peak-shaving control, LCoE^* is minimised by a smaller (and cheaper) turbine, with $d_\mathrm{r} = 0.55\,\mathrm{m}$. Hypothetically, if $\Omega^\mathrm{max}_\mathrm{gen}$ is lower than 400 rad/s, since small-sized turbines operate efficiently only at relatively high speed, LCoE^* minimisation may suggest a larger d_r.

The selection of a suitable d_r is key for minimising LCoE^*, particularly if $d_\mathrm{bypass}/d_\mathrm{r} = 0$. However, as shown in Figures 8.9, 8.10(a), and 8.10(c), when $0.05 \leq d_\mathrm{bypass}/d_\mathrm{r} \leq 0.45$, a relatively flat low-valued region of LCoE^* appears for $0.50 \leq d_\mathrm{r} \leq 0.65\,\mathrm{m}$. As such, if a bypass valve is installed, it becomes easier to achieve a 'near-minimum' LCoE^* condition, as the choice of d_r is somewhat less critical.

Even though LCoE^* is the main performance function adopted in this CCD approach, since rated power control aims to maximise ζ_cf, it is also worth analysing ζ_cf (Figures 8.9 and 8.10(b)). Although a high capacity factor is typically desirable, the minimum LCoE^* (at Γ^{15}_{55}) does not coincide with the maximum ζ_cf (at Γ^{20}_{50}),

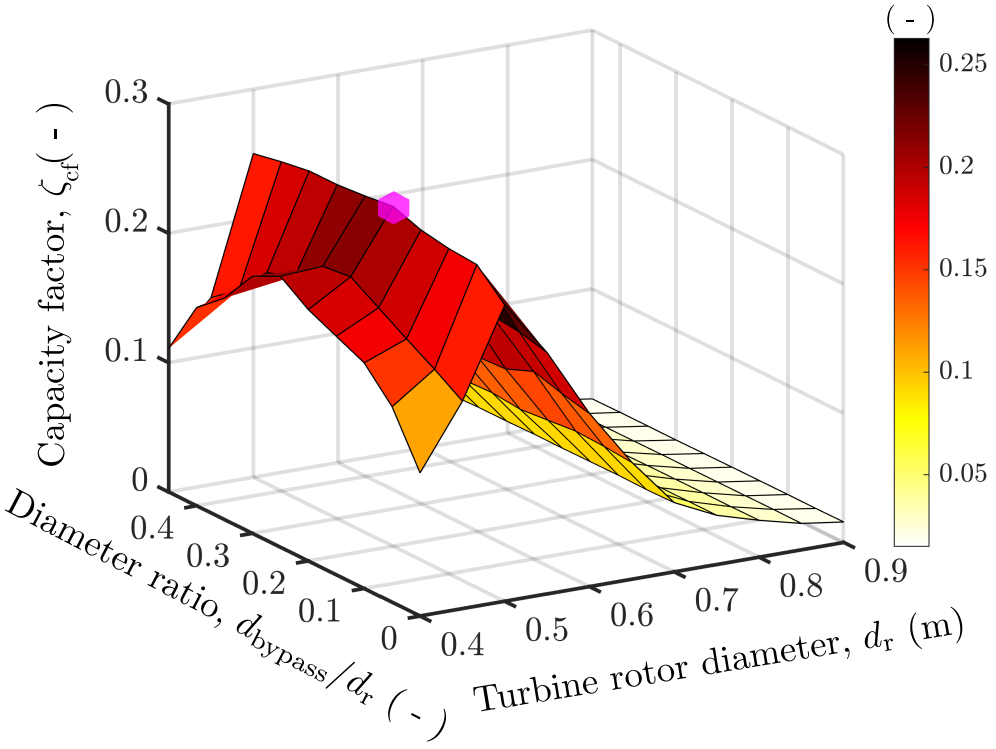

Figure 8.9: Average annual value of the capacity factor, ζ_{cf}, for each combination of turbine rotor diameter, d_r, and diameter ratio, d_{bypass}/d_r. The magenta hexagon (⬢ at Γ_{50}^{20}) shows the condition for which the peak value of ζ_{cf}, $\zeta_{cf}^{max} = 0.263$, is achieved.

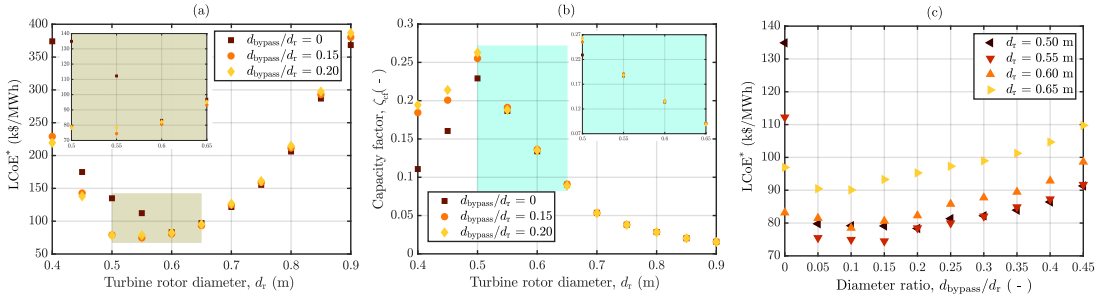

Figure 8.10: LCoE* and/or capacity factor, ζ_{cf}, for some significant combinations of d_r and/or d_{bypass}/d_r.

meaning that having $\zeta_{cf} = \zeta_{cf}^{max} = 0.263$ does not necessarily guarantee the best return on investment. Like LCoE*, ζ_{cf} is less sensitive to d_{bypass}/d_r than to d_r and, moreover, the sensitivity of ζ_{cf} to d_{bypass}/d_r increases for $d_r \leq 0.45$ m.

Figure 8.11 provides insight into the effect of peak-shaving, for each SS, considering Γ_{55}^{0} and Γ_{55}^{15}. First of all, Figures 8.11(a) and (b) show, respectively, the percentage value of bypassed pneumatic power, written as

$$P_{bypass}^{*} = \frac{P_{bypass}}{P_{bypass} + P_{pneu}} \times 100, \tag{8.20}$$

and ζ_{cf}, for Γ_{55}^{15}. Clearly, when $u_{bypass} = 0$, $P_{bypass}^{*} = 0$, meaning that there is no power

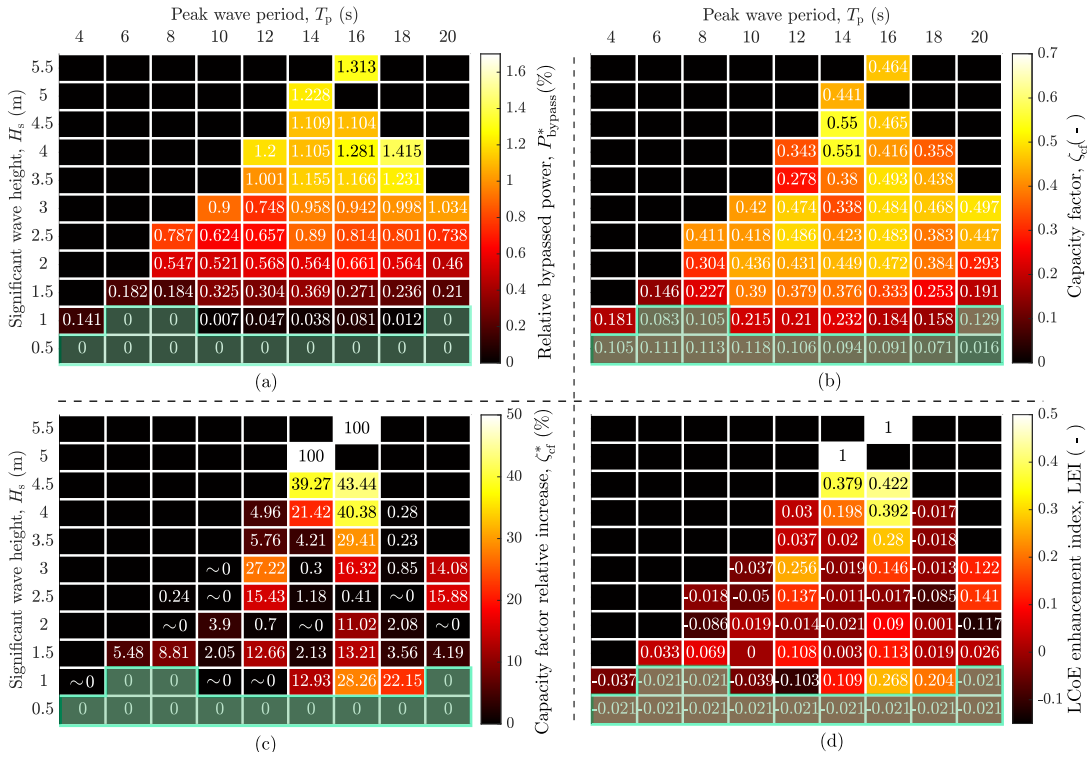

Figure 8.11: Insight into the effect of the bypass valve for Γ^{15}_{55} (and Γ^{0}_{55}). The green shaded areas highlight the sea states for which the bypass valve is closed ($u_{\text{bypass}} = 0$), since $\bar{P}_{\text{wave}} \leq \bar{P}^{\text{thr}}_{\text{wave}}$, meaning that pneumatic power is not dissipated. For each combination of H_{s} and T_{p}, the four scatter plots show: (a) the relative bypassed pneumatic power, P^*_{bypass}, for Γ^{15}_{55}; (b) the capacity factor, ζ_{cf}, for Γ^{15}_{55}; (c) the relative percentage increase in ζ_{cf}, ζ^*_{cf}, obtained for Γ^{15}_{55} in comparison with Γ^{0}_{55}; (d) the LCoE enhancement index, LEI, as defined in Eqs. (8.18) and (8.19).

dissipation. Secondly, Figure 8.11(c) shows the relative increase in ζ_{cf}, computed as

$$\zeta^*_{\text{cf}} = \frac{\zeta_{\text{cf}}(\Gamma^{15}_{55}) - \zeta_{\text{cf}}(\Gamma^{0}_{55})}{\zeta_{\text{cf}}(\Gamma^{15}_{55})} \times 100. \tag{8.21}$$

Similarly to P^*_{bypass}, when $u_{\text{bypass}} = 0$, $\zeta^*_{\text{cf}} = 0$. For SSs 57 and 58, $\zeta^*_{\text{cf}} = 100$, meaning that, unless a bypass valve is utilised, an OWC with $d_{\text{r}} = 0.55$ m remains (almost) permanently in safety mode, i.e., $\zeta_{\text{cf}}(\Gamma^{0}_{55}) \sim 0$. For some SSs, $\zeta^*_{\text{cf}} \sim 0$, therefore rated power control is neither deteriorating nor improving the capacity factor. This is arguably due to the fact that u_{bypass} is SS-based and that wave energy is typically characterised by a high peak-to-average power ratio. As such, there are time periods over which pneumatic power dissipation is not needed, since P_{pneu} is small, yet the bypass valve is dissipating power. Wave-by-wave u_{bypass} control may potentially provide a more effective control solution but, with currently available actuators, wave-by-wave real-time control of u_{bypass} is challenging [56, 103]. Finally, Figure 8.11(d) shows the LEI, defined in Equations (8.18) and (8.19). Since the ratio

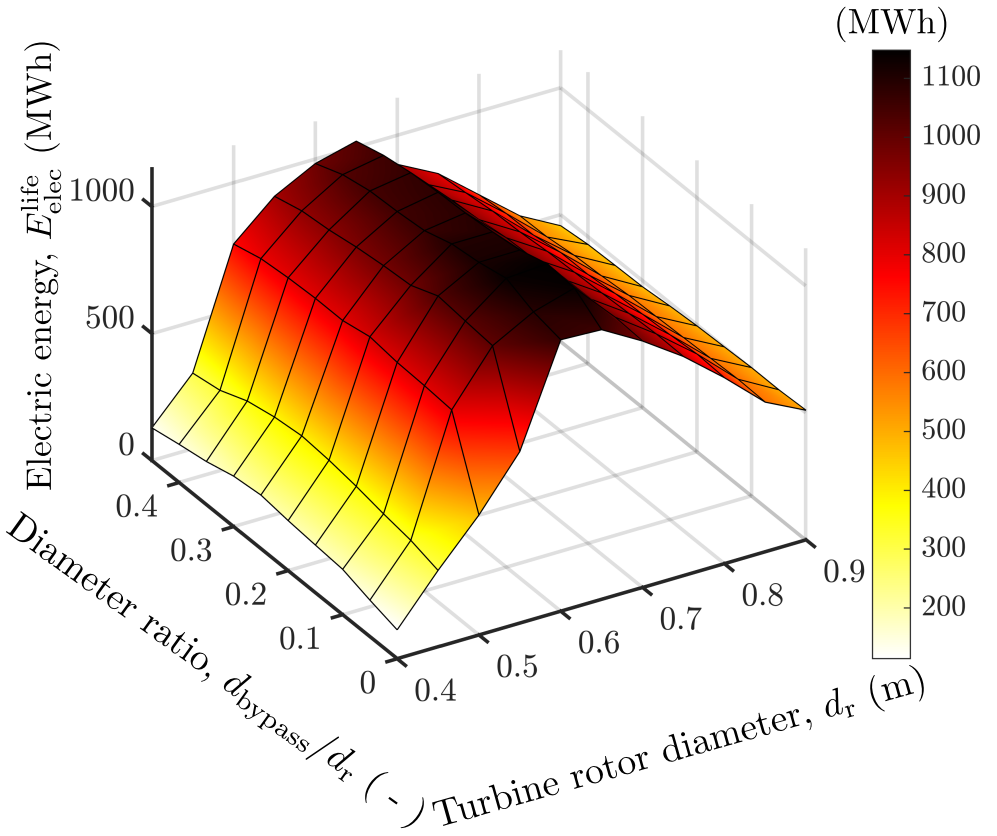

Figure 8.12: $E_{\text{elec}}^{\text{life}}$ obtained from all the considered combinations of d_{r} and $d_{\text{bypass}}/d_{\text{r}}$.

of $C_{\text{mov}}(\Gamma_{55}^{0})$ to $C_{\text{mov}}(\Gamma_{55}^{15})$ is 0.979, for the bypass valve at Γ_{55}^{15} to be economically worthwhile (i.e., LEI > 0), rated power control should improve the produced electric energy by, *at least*, a factor of 1.021. In essence, the additional wave energy converted thanks to peak-shaving control should (at the very least) counterbalance the bypass valve cost. Clearly, the 'profitability' factor, 1.021, is not a general result, so the economic advantages of the bypass valve need to be examined (with CCD) on a site-specific basis.

For the sake of completeness, Figure 8.12 shows the electric energy produced over the OWC WEC lifetime, for each possible design solution. Unsurprisingly, the maximum of $E_{\text{elec}}^{\text{life}}$ (i.e., Γ_{65}^{10}) does not coincide with the LCoE^{*} minimum (Γ_{55}^{15}), shown in Figure 8.8. In general, electric energy is higher if $d_{\text{r}} = 0.65$ m since, for the specific wave climate at Mutriku (Figure 8.7), the turbine with $d_{\text{r}} = 0.65$ m can operate at a high-efficiency speed range. For a more energetic wave climate, a larger (and more expensive) turbine would arguably be a better design solution for maximising electric energy, although that does not necessarily implies a reduction of the LCoE.

8.3 Conclusions

In view of the results discussed in Section 8.2.2, CCD techniques are vital to minimise the LCoE, especially since the control possibilities, such as rated power control, impact both $E_{\text{elec}}^{\text{life}}$ and costs. Additionally, although ζ_{cf} maximisation is not the ultimate objective, it is important to improve ζ_{cf} in WECs, particularly if wave energy is to compete against wind energy. By way of example, the annual mean ζ_{cf} of the Mutriku OWC is ~ 0.11 [358], while European wind turbines have an annual mean ζ_{cf} around 0.21 - 0.29 [359, 360]. With the use of suitable actuators (i.e., a bypass valve) and CCD (to determine the optimal control-informed system parameters), there is a remarkable margin for improvement in ζ_{cf} for OWC systems, as indicated by Figure 8.9.

A CCD approach may have two major issues: High computational burden and, potentially, complexity of automation. To this end, one of the key achievements of this work is that the CCD procedure in Figure 8.6 is relatively computationally efficient and simple to automate. Firstly, the design procedure of the control system (in Section 8.1.3) is straightforward (for example, u_{bypass} is fully defined by simply selecting $\bar{P}_{\text{wave}}^{\text{thr}}$, $\bar{P}_{\text{wave}}^{\text{max}}$, and f_{bypasss}). In fact, having a sufficiently simple control design loop is essential to easily automate the CCD procedure. More sophisticated control strategies can always be subsequently designed for the parametric points in the neighborhood of the LCoE^* minimum (which provides an informed initial guess obtained with the simple controllers). Moreover, since u_{bypass} is SS-based, not all the SSs need to be simulated, for all the $\Gamma_{\text{i}}^{\text{j}}$. Indeed, the produced electric energy, for a SS in which $\bar{P}_{\text{wave}} \leq \bar{P}_{\text{wave}}^{\text{thr}}$, remains unchanged with, or without, a bypass valve. Therefore, only the sea states for which $u_{\text{bypass}} \neq 0$ have to be re-simulated. Finally, it should be noted that, in the proposed CCD approach, the computation of LCoE^* for each point of the VT parametric space case is independent of the other points, meaning that numerical simulations for distinct points can run in parallel [361].

The LCoE^*, in Figure 8.8, provides a quantitative estimate of the potential reduction in the LCoE, obtained if the OWC parameters are optimised considering control. However, LCoE^* likely underestimates LCoE since: (i) Power production may be interrupted for maintenance or a system failure, (ii) even with maintenance, the OWC performance will deteriorate with age [264], (iii) losses in the power train, such as hydrodynamic viscous losses due to vortex shedding [236], are not considered [187], and (iv) C_{pto} does not include cost of development and design [74]. Concerning (i), if FTC is used to improve maintenance operation flexibility, and if maintenance is scheduled at a convenient time (i.e., in low-energy SSs), the increase in LCoE due to operation interruption may be limited. In any case, the

primary focus of this chapter is not to accurately compute LCoE, rather to develop an automatable CCD approach, with a reasonable computational burden, for an OWC WEC with power dissipation and rotational speed control possibilities.

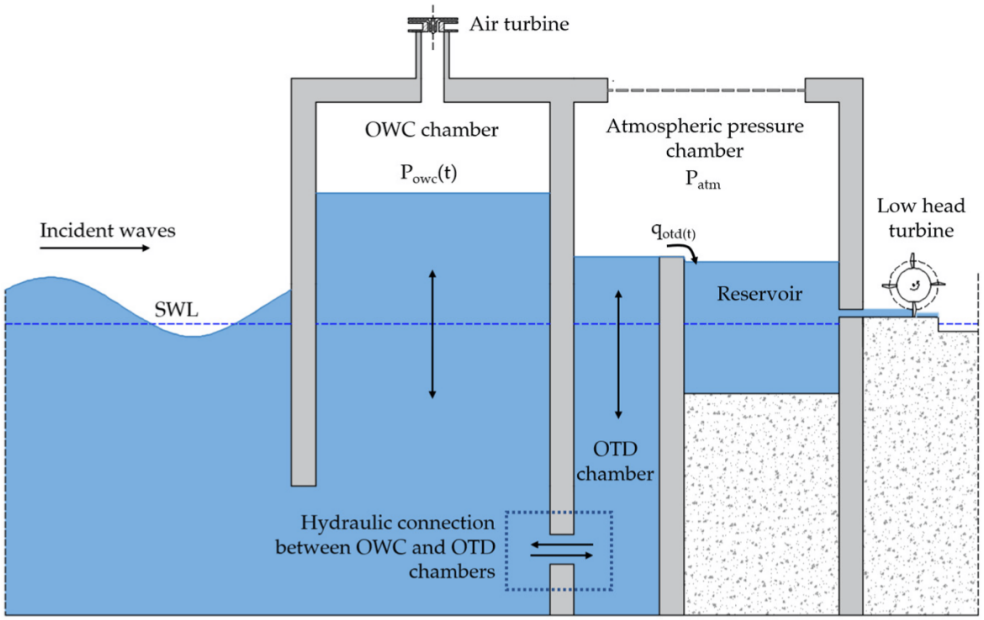

Figure 8.13: Schematic of a hybrid WEC combining OWC and overtopping wave energy conversion technologies. Source: [362].

Finally, it is important to bear in mind that, although LCoE serves as a suitable high-level performance function, LCoE is only a statistical metric characterising the average cost of energy production, and hence does not fully encompass the 'true value' of wave energy, related to the potential provision of electrical energy when other renewables (e.g., wind) are relatively dormant. For instance, the LCoE does not take into account the complementarity between wave energy and other renewable resources, real-time energy market factors (such as real-time energy market price/demand with respect to the availability of wave energy and/or other sources of renewable energy), energy storage possibilities (ability to store energy and use it when required), and the creation of job opportunities. In relation to energy storage, some early studies on a hybrid WEC combining OWC, and overtopping [363], based wave energy conversion technologies can be found [364, 362]. The idea behind this hybrid WEC concept, schematically shown in Figure 8.13, is to feed the overtopping device (OTD) with excessive wave power. In high-energy SSs, excessive wave power is essentially redirected, through the 'hydraulic connection' (Figure 8.13), to the OTD, which is not only used for OWC peak-shaving control, but may also serve as an energy storage mechanism. Ultimately, although the LCoE of the hybrid OWC/overtopping WEC is

likely higher than a simpler (and cheaper) conventional OWC device, the inherent energy storage system simplifies real-time energy supply, while reducing the need for potentially expensive electric energy storage units (such as batteries and capacitors). Therefore, though LCoE may be higher on average, the *value* of the energy produced may be significantly greater.

Part IV

Final remarks

In research, it is of fundamental importance not to miss the forest for the trees.

— John V. Ringwood

9 Conclusions and future perspectives

Contents

9.1 Main conclusions **187**
9.2 Future perspectives **189**

9.1 Main conclusions

To achieve carbon-neutrality and minimise the need for energy storage, it is imperative to diversify renewable energy resources [16] and, to this end, wave energy is attractive, especially due to its huge untapped potential [34] and relatively poor correlation, at least in some cases, with other renewables, such as wind energy [17, 20]. Since the main hindrance to OWC, and other WEC, commercialisation is the high LCoE, it is key to develop high-performance energy maximising control strategies to minimise the cost of producing electricity using ocean waves [48]. Therefore, this thesis work tackles the problem of LCoE minimisation from a control angle and, in particular, by (i) developing more complete, static-efficiency-based (Chapter 6) and dynamic (Chapter 7), control strategies for OWC WECs, (ii) devising a CCD approach (Chapter 8), primarily to asses the value of peak-shaving control with a bypass valve, and (iii) investigating possible control-oriented modelling techniques (Chapter 4).

Although a more systematic study on OWC SI modelling is needed, the results obtained for data-based OWC hydrodynamic modelling in Chapter 4 are quite

promising, especially in relation to nonlinear hydrodynamic modelling. More specifically, the main advantages of a global nonlinear KGP model, over a multi-linear ARX modelling solution, are:

- The real-time implementation of a global nonlinear SI model is arguably computationally more efficient, due to the capability of the nonlinear model to implicitly interpolate the predicted output, therefore eliminating the need for explicit switching/interpolating and sea state estimation mechanisms.
- The KGP model order, N_{kgp}, is expected to be smaller than the ARX multi-linear model order, N_{lm}.
- The nonlinear KGP model has a relatively simple parametric structure, but also captures the essential nonlinearities in the OWC hydrodynamic subsystem.

Finally, depending on the data space on which the model is identified, nonlinear SI hydrodynamic models can be more accurate and have broader validity then their physics-based counterparts, which are typically derived under a certain set of potentially limiting (in terms of model accuracy and validity) assumptions, especially under controlled conditions.

In terms of control strategies, since the critical review of the literature (Chapter 5) highlighted a rather exclusive attention on TEM control, the work presented in Chapters 6 and 7 aims to develop electric energy maximising control strategies for OWCs, in which the entire W2W power train is taken into account. Due to the interesting, and often disregarded, possibility of affecting hydrodynamic performance through Wells turbine rotational speed modulation, W2W control with a Wells turbine is investigated. In essence, the results presented in Chapters 6 and 7 show that, if rotational speed is modulated considering the overall W2W OWC system (rather than the turbine alone), electric energy production significantly improves, although turbine efficiency is slightly penalised. On the one hand, static-efficiency-based W2W control is attractive due to its simplicity, in comparison with RHPS control, and superior performance, with respect to TEM control. On the other hand, RHPS control provides higher electric energy production, especially in high-energy SSs, where the benefit of optimal constraint handling becomes particularly important. However, using RHPS control in real-time is more challenging, due to (i) the relatively high computational cost to solve, at each iteration, an (online constrained) optimisation problem, and (ii) the need for accurate prediction of the system behaviour. Furthermore, although turbine stall is the most detrimental effect on OWCs, the relative aggressiveness of static-efficiency-based W2W and RHPS control, as suggested by the larger torque variations in Figure 7.7(a), may increase

OpEx [316]. Ultimately, RHPS and static-efficiency-based W2W control are both worthwhile OWC control strategies, although the definitive 'winner' is yet to be determined. For a decisive comparison between the two control approaches, the LCoE should be adopted as a performance metric, ideally using CCD techniques and considering all control-related factors (such as the impact of the control action on OpEx, and peak-saving control possibilities).

In addition to rotational speed control, the literature review of Chapter 5 has also revealed a lack of attention to OWC peak-shaving control for increasing the capacity factor, especially for Wells turbines (Table 5.5). Since peak-shaving control typically requires an additional actuator (e.g., a bypass valve), and since the possibility of dissipating excessive pneumatic power plays a crucial role in the optimal PTO sizing problem, electric energy production cannot be adopted as an appropriate objective function. Therefore, to asses the value of (SS-based) peak-shaving control, an *easily automatable* parametric CCD approach (for the PTO and bypass valve) is developed to minimise a surrogate of the LCoE, selected as a suitable high-level performance metric. With peak-shaving control, the LCoE minimum is achieved for a smaller-sized (and therefore cheaper) PTO mechanism. Indeed, pneumatic power dissipation extends the PTO operational range, which is particularly *economically rewarding* for PTOs with a relatively small rated power, and to avoid the OWC from prematurely entering into a safety mode (with a consequent interruption of power production). Furthermore, the possibility of dissipating excessive power also simplifies the PTO optimal sizing problem, since the sensitivity of the LCoE to the PTO size is relatively low, at least in the region around the LCoE minimum (Figure 8.8), if a bypass valve is used. Finally, apart from the benefit of using peak-shaving, the study presented in Chapter 8 also sheds light on the vital role of CCD techniques in LCoE minimisation. Without a CCD approach, it is virtually impossible (unless a very lucky guess is made by the design engineer) to achieve the optimum control-informed OWC WEC design that minimises the LCoE.

9.2 Future perspectives

In relation to data-based modelling for OWCs, the work presented in this thesis has barely scratched the surface. Possible future directions in OWC SI modelling may include, but are not limited to, the following:

- More sophisticated nonlinear SI model structures, such as simple ANNs, may be considered for OWC hydrodynamic modelling, where an ideal SI model structure should be able to capture the essential (i.e., relevant from a control

perspective) linear and nonlinear system dynamics, yet be computationally simple for real-time control.

- Data-based OWC hydrodynamic models can be improved to include the influence of control on the water column motion, such as the effects of the Wells turbine rotational speed and/or bypass/safety valve positions.

- SI techniques may be also considered for modelling other OWC subsystems, such as the air chamber and PTO, as well as the entire W2W system. However, SI hydrodynamic modelling arguably remains a priority, especially due to the potentially limiting set of assumptions under which physics-based OWC hydrodynamic models are typically derived.

- Finally, the value of data-based, as opposed to physics-based, OWC hydrodynamic models still needs to be fully assessed, ideally on a controlled OWC WEC in real operating environment.

Concerning OWC control, there are different research topics which merit further investigation. It is possible to identify two broad areas of interest for future work on OWC control, depending on the 'level' of the considered control objective, namely (i) research focusing on *low-level* control objectives (i.e., efficiency/energy maximisation) and (ii) research focusing on *high-level* control objectives (i.e., LCoE minimisation and real-time energy demand/supply). A future agenda for the lower-level control objectives should include:

- A thorough investigation into data-based and data-driven control possibilities for OWCs, to take advantage of static and dynamic datasets, respectively [206].

- Computationally efficient optimal control for OWCs to achieve real-time control performance. To this end, some aspects worth considering are:

  - *Control-oriented modelling* for optimal control of OWC WECs. For instance, inspired by the relatively recent advances in nonlinear moment-based WEC control [365, 366], if the system nonlinearities (such as the generator efficiency [367]) are conveniently parameterised, it may be possible to prove convexity of the OWC OCP using a moment-based framework [368].
  - Optimised coding efficiency [369, 370] by, for example, replacing Fourier basis functions used in Chapter 7 (OWC RHPS control) by polynomials [371].

- Balanced-complexity (and balanced-fidelity) OWC wave-to-grid model-based control for energy maximisation. To date, grid-side aspects are rarely considered when designing OWC control strategies. Furthermore, in the few studies concerning OWC grid-side control (Section 5.2.6), the device-side model and control are typically oversimplified.

- Consider a robust implementation for the RHPS control of Chapter 7 by using, for instance, a robust OCP formulation [372], or a SMC-based feedback loop to track the optimal speed value (see, e.g., [373, 374]) rather than directly using the optimal torque value from the optimisation.

Furthermore, the following items may be part of a future agenda focusing on higher-level performance functions:

- The parametric CCD approach proposed in this thesis may be improved by considering, for instance:

  - Additional optimisation parameters (e.g., the OWC capture width), different types of turbines, and/or alternative control strategies (although, as mentioned in Chapter 8, simplicity in the control design loop is key to have a moderate CCD computational cost). If the OWC capture width is a free parameter of the optimisation, the computational cost of CCD increases exponentially, due to need for computing the frequency-dependant hydrodynamic parameters for each considered geometry. To reduce the computational burden, a solution may be to precompute (with, for example, WAMIT) the frequency-dependant hydrodynamic parameters for a discrete set of values of OWC capture width. Subsequently, data-based interpolation techniques can be used to determine the hydrodynamic parameters for any variation of the capture width within the training data space [375].
  - In relation to control possibilities, the bypass valve position may be not only controlled for increasing the capacity factor (i.e., peak-shaving control in CR_3), but also to avoid producing excessive energy (in any operating region, even in CR_2). To this end, it should be noted that, typically, energy suppliers bid in electricity markets and commit themselves to supply a certain amount of energy at an agreed price [376]. If suppliers fail to fulfil their commitment, meaning that they supply too much or too little electricity [377], they incur financial penalties.

- Since turbine speed control is essential to efficiently and safely operate the OWC system, OWC turbine rotational speed FTC must be addressed.
- To accurately compute the LCoE, more reliable OpEx estimation is needed and, from a control perspective, it is important to assess the impact of the control action on the lifetime of each OWC subsystem/component.

Finally, although this thesis does not focus on conceiving new design solutions for components and actuators of OWC-based WECs, it is worth mentioning some design possibilities that can help to increase energy production, and/or target high-level control objectives:

- Since the air turbine is the most critical element in the OWC W2W power flow, turbine design should be improved. For example, it is important to increase the operational range of Wells turbines and peak efficiency of impulse turbines.
- New/improved actuators may open up new opportunities for OWC hydrodynamic control and real-time wave-by-wave bypass valve control.
- More exotic design solutions for the PTO, such as twin unidirectional turbines (Figure 5.5), and hybrid WEC devices (e.g., the OWC/OTC device in Figure 8.13) can offer natural system redundancy and inherent energy storage mechanisms.

Appendices

A

Alternative OWC modelling

Contents

A.1 Uniform pressure model 195
A.1.1 Hydrodynamic and air chamber modelling 195
A.1.2 Relation between piston and uniform pressure models . . 196
A.2 Maeda's turbine model 197

A.1 Uniform pressure model

A.1.1 Hydrodynamic and air chamber modelling

The uniform pressure approach, introduced in [378], assumes a uniformly distributed pressure on the OWC surface, but allows water surface deformation, as shown in Figure 3.2 b). In the uniform pressure model, $\dot{V}_{\mathrm{c}}$ is decomposed into an excitation flow rate, q_{e}, and radiated flow rate, q_{r}, as

$$-\dot{V}_{\mathrm{c}} = q_{\mathrm{e}}(t) + q_{\mathrm{r}}(t). \tag{A.1}$$

The excitation flow rate is solely due to incident waves, when $\Delta p = 0$, while the radiated flow rate results from oscillations in air pressure inside the pneumatic chamber, in the absence of incident waves.

If the excitation waves are regular waves of frequency ω, Equation (A.1) can be expressed, in the frequency domain, [72] as

$$\hat{q}_{\mathrm{e}} + \hat{q}_{\mathrm{r}} = \left(J\frac{V_0}{\gamma p_0} + \frac{1}{\rho_0 \zeta} \right) \Delta\hat{p}, \tag{A.2}$$

where $\hat{q}_\mathrm{e}$ and $\hat{q}_\mathrm{r}$ are, respectively, the complex amplitudes of the excitation and radiated flow rates, such that $q_\mathrm{e} = \Re(\hat{q}_\mathrm{e} e^{\jmath\omega t})$ and $q_\mathrm{r} = \Re(\hat{q}_\mathrm{r} e^{\jmath\omega t})$. Similarly to the radiation force in Equation (2.46), the radiated flow rate can be decomposed into real and imaginary parts [158], as

$$\hat{q}_\mathrm{r} = -(G_\mathrm{owc}(\omega) + \jmath H_\mathrm{owc}(\omega))\Delta\hat{p}, \tag{A.3}$$

where the real-valued frequency-dependant coefficients $G_\mathrm{owc}(\omega)$ and $H_\mathrm{owc}(\omega)$ are the radiation conductance, and radiation susceptance, respectively. The chamber pressure complex amplitude can be computed by substituting the definition of $\hat{q}_\mathrm{r}$ in Equation (A.2) as:

$$\Delta\hat{p} = \left(\frac{1}{\rho_0\zeta} + G_\mathrm{owc}(\omega) + \jmath\left(\frac{\omega V_0}{\gamma p_0} + H_\mathrm{owc}(\omega)\right)\right)^{-1} \hat{q}_\mathrm{e}. \tag{A.4}$$

The radiation volumetric flow rate q_r is computed via the convolution integral:

$$q_\mathrm{r}(t) = -\int_{-\infty}^{t} h_\mathrm{r}(t-\tau)\,\Delta p(\tau)\,\mathrm{d}\tau, \tag{A.5}$$

resulting from the memory function $h_\mathrm{r}(t)$ computed from $G_\mathrm{owc}(\omega)$ as

$$h_\mathrm{r}(t) = \frac{2}{\pi}\int_0^\infty G_\mathrm{owc}(\omega)\cos(\omega t)\,\mathrm{d}\omega. \tag{A.6}$$

A.1.2 Relation between piston and uniform pressure models

The hydrodynamic coefficients of the piston modelling approach, $A_\mathrm{p}(\omega)$ and $B_\mathrm{p}(\omega)$, are related to those of the admittance approach, $G_\mathrm{owc}(\omega)$ and $H_\mathrm{owc}(\omega)$ [66]. Assuming $F_\mathrm{ex} = 0$, Equation (3.1) can be rewritten as

$$\left[\jmath\left(\omega(m_\mathrm{p} + A_\mathrm{p}(\omega)) - \frac{C_\mathrm{h}}{\omega}\right) + B_\mathrm{p}(\omega)\right]\hat{v}_\mathrm{r} = -\Delta\hat{p}\,S_\mathrm{owc}, \tag{A.7}$$

where $\hat{v}_\mathrm{r}$ is the complex amplitude of the piston velocity due to radiation (i.e., due to the time-varying air pressure in the chamber). Furthermore, $\hat{q}_\mathrm{r} = \jmath\omega S_\mathrm{owc}\hat{v}_\mathrm{r}$ and, therefore,

$$\hat{v}_\mathrm{r} = -\frac{(G_\mathrm{p}(\omega) + \jmath H_\mathrm{p}(\omega))\Delta\hat{p}}{\jmath\omega S_\mathrm{owc}}, \tag{A.8}$$

where $G_\mathrm{p}(\omega)$ and $H_\mathrm{p}(\omega)$ are, respectively, $G_\mathrm{owc}(\omega)$ and $H_\mathrm{owc}(\omega)$ specified for the water piston model. By substituting Equation (A.8) into Equation (A.7), the following identities can be derived

$$\begin{aligned}
\frac{S_\mathrm{owc}^2 G_\mathrm{p}(\omega)}{G_\mathrm{p}^2(\omega) + H_\mathrm{p}^2(\omega)} &= B_\mathrm{p}(\omega),\\
\frac{\omega S_\mathrm{owc}^2 H_\mathrm{p}(\omega)}{G_\mathrm{p}^2(\omega) + H_\mathrm{p}^2(\omega)} &= -\omega^2(m_\mathrm{p} + A_\mathrm{p}(\omega)) + \rho_\mathrm{w} g S_\mathrm{owc}.
\end{aligned} \tag{A.9}$$

It should be noted that $G_\mathrm{p}(\omega)$ and $H_\mathrm{p}(\omega)$ are expected to be similar, but not exactly equal to $G_\mathrm{owc}(\omega)$ and $H_\mathrm{owc}(\omega)$ [66].

A.2 Maeda's turbine model

Maeda *et al.* [189] proposed the following power and torque coefficients defined, respectively, as

$$C_{\mathrm{A}}(\phi_{\mathrm{x}}) = \frac{\Delta p\, q_{\mathrm{turb}}}{\frac{1}{2}\rho_{\mathrm{air}}\left(v_{\mathrm{x}}^2 + U^2\right) b_{\mathrm{c}} b_{\mathrm{h}} N_{\mathrm{b}} v_{\mathrm{x}}}, \tag{A.10}$$

and

$$C_{\mathrm{T}}(\phi_{\mathrm{x}}) = \frac{T_{\mathrm{turb}}}{\frac{1}{2}\rho_{\mathrm{air}}\left(v_{\mathrm{x}}^2 + U^2\right) b_{\mathrm{c}} b_{\mathrm{h}} N_{\mathrm{b}} r_{\mathrm{r}}}, \tag{A.11}$$

derived experimentally as a function of the flow coefficient,

$$\phi_{\mathrm{x}} = \frac{v_{\mathrm{x}}}{U}, \tag{A.12}$$

where b_{h} is the blade height, b_{c} is the blade chord, N_{b} is the number of rotor blades, r_{r} the turbine mean radius, $T_{\mathrm{turb}} = P_{\mathrm{turb}}/\Omega$ is the turbine torque, and v_{x} is the mean axial airflow velocity. The circumferential velocity at the mean radius is defined by

$$U = \Omega r_{\mathrm{r}}. \tag{A.13}$$

The flow rate, q_{turb}, is related to the mean axial velocity, v_{x}, through $q_{\mathrm{turb}} = v_{\mathrm{x}} A_{\mathrm{turb}}$, where A_{turb} is the area of the turbine duct.

To solve the pneumatic chamber equation (3.8), the turbine air mass flow rate, $w_{\mathrm{turb}} = \rho_{\mathrm{air}}\, q_{\mathrm{turb}}$, has to be computed as a function of Δp. Such a computation is simple if the turbine is modelled with Equation (3.14), but it is not straightforward with Maeda's model. Using $q_{\mathrm{turb}} = v_{\mathrm{x}} A_{\mathrm{turb}}$, Equation (A.10) can be expressed in terms of v_{x} (and ϕ_{x}) and Δp:

$$C_A(\phi_{\mathrm{x}})\left(v_{\mathrm{x}}^2 + U^2\right) = \frac{\Delta p A_{\mathrm{turb}}}{\frac{1}{2}\rho_{\mathrm{air}} b_{\mathrm{c}} b_{\mathrm{h}} N_{\mathrm{b}}}. \tag{A.14}$$

However, even if Δp is known, it is impossible to find an explicit relationship to determine v_{x} as a function of Δp, since ϕ_{x} in Equation A.14 also depends on v_{x}.

Maeda's dimensionless numbers are related to the dimensionless variables defined in Equation (3.15). By expressing q_{turb} as a function of Φ in Equation (3.15) and using (A.12), (A.13), and $q_{\mathrm{turb}} = v_{\mathrm{x}} A_{\mathrm{turb}}$, Φ can be rewritten as

$$\Phi = A_{\mathrm{turb}} r_{\mathrm{r}} \phi_{\mathrm{x}} / d_{\mathrm{r}}^3. \tag{A.15}$$

Furthermore, by writing the pressure difference Δp as function of Ψ in Equation (3.15) and using (A.10), the following identity is derived:

$$\Psi \rho_{\mathrm{air}} \Omega^2 d^2 = \frac{1}{2}\rho_{\mathrm{air}}\left(v_{\mathrm{x}}^2 + U^2\right)\frac{b_{\mathrm{c}} b_{\mathrm{h}} N_{\mathrm{b}}}{A_{\mathrm{turb}}} C_A. \tag{A.16}$$

If the definitions (A.12) and (A.13) are substituted into (A.16), Ψ can be expressed as

$$\Psi = \frac{1}{2}\left(\phi_{\mathrm{x}}^2 + 1\right)\frac{b_{\mathrm{c}} b_{\mathrm{h}} N_{\mathrm{b}} r_{\mathrm{r}}^2}{A_{\mathrm{turb}} d_{\mathrm{r}}^2}\, C_A. \tag{A.17}$$

Similarly to Φ and Ψ, one can also write Π as a function of ϕ_{x} using Equations (3.15) and (A.11):

$$\Pi = \frac{1}{2}\left(\phi_{\mathrm{x}}^2 + 1\right) C_T\, \frac{b_{\mathrm{c}} b_{\mathrm{h}} N_{\mathrm{b}} r_{\mathrm{r}}^3}{d_{\mathrm{r}}^5}. \tag{A.18}$$

Bibliography

[1] N. Armaroli and V. Balzani, "The future of energy supply: challenges and opportunities," *Angewandte Chemie International Edition*, vol. 46, pp. 52–66, 2007.

[2] H. Ritchie and M. Roser, "Energy, our world in data." https://ourworldindata.org/energy, 2020. Last accessed: 15/12/2023.

[3] K. Northon, "Long-term warming trend continued in 2017: NASA, NOAA." https://www.nasa.gov/press-release/long-term-warming-trend-continued-in-2017-nasa-noaa, 2018. Last accessed: 07/01/2024.

[4] T. J. Crowley, "Causes of climate change over the past 1000 years," *Science*, vol. 289, pp. 270–277, 2000.

[5] R. A. Berner, "The long-term carbon cycle, fossil fuels and atmospheric composition," *Nature*, vol. 426, no. 6964, pp. 323–326, 2003.

[6] E. Commision, "Energy." https://commission.europa.eu/topics/energy_en. Last accessed: 01/03/2024.

[7] U. Nations, "Global Roadmap for Accelerated SDG7 Action." https://www.un.org/en/page/global-roadmap#:~:text=A%20global%20roadmap%20setting%20out,of%20the%20High%2Dlevel%20Dialogue., 2021. Last accessed: 20/03/2024.

[8] U. Nations, "Transforming our world: The 2030 Agenda for Sustainable Development." https://sdgs.un.org/2030agenda, 2015. Last accessed: 20/03/2024.

[9] U. Nations, "The Paris Agreement." https://www.un.org/en/climatechange/paris-agreement, 2015. Last accessed: 20/03/2024.

[10] P. E. Brockway, A. Owen, L. I. Brand-Correa, and L. Hardt, "Estimation of global final-stage energy-return-on-investment for fossil fuels with comparison to renewable energy sources," *Nature Energy*, vol. 4, pp. 612–621, 2019.

[11] IEA50, "Global Energy Crisis." https://www.iea.org/topics/global-energy-crisis. Last accessed: 20/03/2024.

[12] REN21, "Renewables 2023: Global Status Report. A Comprehensive Annual Overview of the State of Renewable Energy." https://www.ren21.net/gsr-2023/. Last accessed: 20/03/2024.

[13] I. Government, "Climate Action Plan 2024." https://www.gov.ie/en/publication/79659-climate-action-plan-2024/#:~:text=The%20Plan%20provides%20a%20roadmap,Development%20(Amendment)%20Act%202021. Last accessed: 21/03/2024.

[14] I. W. TPC, "Wind Energy in Ireland." https://iea-wind.org/about-iea-wind-tcp/members/ireland/#:~:text=Total%20wind%20power%20capacity%20is%204%2C309%20MW. Last accessed: 21/03/2024.

[15] SEAI, "Energy in Ireland." https://www.seai.ie/data-and-insights/seai-statistics/key-publications/energy-in-ireland/. Last accessed: 21/03/2024.

[16] X. Li, "Diversification and localization of energy systems for sustainable development and energy security," *Energy policy*, vol. 33, pp. 2237–2243, 2005.

[17] J. Widén, N. Carpman, V. Castellucci, D. Lingfors, J. Olauson, F. Remouit, M. Bergkvist, M. Grabbe, and R. Waters, "Variability assessment and forecasting of renewables: A review for solar, wind, wave and tidal resources," *Renewable and Sustainable Energy Reviews*, vol. 44, pp. 356–375, 2015.

[18] B. G. Reguero, I. J. Losada, and F. Méndez, "A global wave power resource and its seasonal, interannual and long-term variability," *Applied Energy*, vol. 148, pp. 366–380, 2015.

[19] H. A. Said, S. Costello, and J. V. Ringwood, "On the complementarity of wave, tidal, wind and solar resources in Ireland," in *Proceedings of the 15th European Wave and Tidal Energy Conference*, (Bilbao, Spain), 2023.

[20] F. Fusco, G. Nolan, and J. V. Ringwood, "Variability reduction through optimal combination of wind/wave resources – An Irish case study," *Energy*, vol. 35, no. 1, pp. 314–325, 2010.

[21] J. Hals, *Modelling and phase control of wave-energy converters*. PhD thesis, Norges teknisk-naturvitenskapelige universitet, 2010.

[22] J. Cruz, *Ocean wave energy: current status and future prespectives*. Springer Science & Business Media, 2007.

[23] O. Edenhofer, R. Pichs-Madruga, Y. Sokona, K. Seyboth, S. Kadner, T. Zwickel, P. Eickemeier, G. Hansen, S. Schlömer, and C. V. Stechow, *Renewable energy sources and climate change mitigation: Special report of the intergovernmental panel on climate change*. Cambridge University Press, 2011.

[24] G. Mork, S. Barstow, A. Kabuth, and M. T. Pontes, "Assessing the global wave energy potential," in *Proceedings of the 29th International Conference on Ocean, Offshore and Arctic Engineering*, (Sanghai, China), pp. 447–454, 2010.

[25] K. Gunn and C. Stock-Williams, "Quantifying the global wave power resource," *Renewable Energy*, vol. 44, pp. 296–304, 2012.

[26] J. Portilla, J. Sosa, and L. Cavaleri, "Wave energy resources: Wave climate and exploitation," *Renewable Energy*, vol. 57, pp. 594–605, 2013.

[27] C. Maisondieu, "WEC survivability threshold and extractable wave power," in *Proceedings of the 11th European Wave and Tidal Energy Conference, Nantes, France*, pp. 07D4–2–(1–8), 2015.

[28] A. Ulazia, M. Penalba, G. Ibarra-Berastegui, J. V. Ringwood, and J. Saénz, "Wave energy trends over the bay of Biscay and the consequences for wave energy converters," *Energy*, vol. 141, pp. 624–634, 2017.

[29] M. Penalba, A. Ulazia, G. Ibarra-Berastegui, J. V. Ringwood, and J. Sáenz, "Wave energy resource variation off the west coast of Ireland and its impact on realistic wave energy converters' power absorption," *Applied Energy*, vol. 224, pp. 205–219, 2018.

[30] E. Bouws, D. Jannink, and G. J. Komen, "The increasing wave height in the North Atlantic Ocean," *Bulletin of the American Meteorological Society*, vol. 77, no. 10, pp. 2275–2278, 1996.

[31] I. R. Young, S. Zieger, and A. V. Babanin, "Global trends in wind speed and wave height," *Science*, vol. 332, no. 6028, pp. 451–455, 2011.

[32] G. A. Meehl, F. Zwiers, J. Evans, T. Knutson, L. Mearns, and P. Whetton, "Trends in extreme weather and climate events: Issues related to modeling extremes in projections of future climate change," *Bulletin of the American Meteorological Society*, vol. 81, no. 3, pp. 427 – 436, 2000.

[33] A. Jentsch and C. Beierkuhnlein, "Research frontiers in climate change: Effects of extreme meteorological events on ecosystems," *Comptes Rendus Geoscience*, vol. 340, no. 9, pp. 621–628, 2008.

[34] S. Astariz and G. Iglesias, "The economics of wave energy: A review," *Renewable and Sustainable Energy Reviews*, vol. 45, pp. 397–408, 2015.

[35] K. Nielsen, H. Bingham, and J. B. Thomsen, "On the absorption of wave power using ship like structures," in *Proceedings of the 28th International Offshore and Polar Engineering Conference (ISOPE), Sapporo, Japan*, pp. 719–727, International Society of Offshore and Polar Engineers, 2018.

[36] A. F. O. Falcão, "Wave energy utilization: A review of the technologies," *Renewable and Sustainable Energy Reviews*, vol. 14, no. 3, pp. 899–918, 2010.

[37] I. López, J. Andreu, S. Ceballos, I. Martínez de Alegría, and I. Kortabarria, "Review of wave energy technologies and the necessary power-equipment," *Renewable and Sustainable Energy Reviews*, vol. 27, pp. 413–434, 2013.

[38] B. Drew, A. R. Plummer, and M. N. Sahinkaya, "A review of wave energy converter technology," *Institution of Mechanical Engineers*, vol. 223, pp. 887–902, 2009.

[39] G. Bracco, E. Giorcelli, and G. Mattiazzo, "ISWEC: A gyroscopic mechanism for wave power exploitation," *Mechanism and Machine Theory*, vol. 46, no. 10, pp. 1411–1424, 2011.

[40] Q. Gao, Y. Xu, X. Yu, Z. Jing, T. Cheng, and Z. L. Wang, "Gyroscope-structured triboelectric nanogenerator for harvesting multidirectional ocean wave energy," *ACS Nano*, vol. 16, no. 4, pp. 6781–6788, 2022.

[41] A. Ermakov and J. V. Ringwood, "Rotors for wave energy conversion–Practice and possibilities," *IET Renewable Power Generation*, vol. 15, no. 14, pp. 3091–3108, 2021.

[42] J. Falnes, "A review of wave-energy extraction," *Marine Structures*, vol. 20, pp. 185–201, 2007.

[43] I. McLeod and J. V. Ringwood, "Powering data buoys using wave energy: A review of possibilities," *Journal of Ocean Engineering and Marine Energy*, vol. 8, 2022.

[44] Á. Serna and F. Tadeo, "Offshore hydrogen production from wave energy," *International Journal of Hydrogen Energy*, vol. 39, no. 3, pp. 1549–1557, 2014.

[45] P. Aboutalebi, A. J. Garrido, I. Garrido, D. T. Nguyen, and Z. Gao, "Hydrostatic stability and hydrodynamics of a floating wind turbine platform integrated with oscillating water columns: A design study," *Renewable Energy*, vol. 221, p. 119824, 2024.

[46] Y. Peña-Sanchez, *Hydrodynamic Excitation Force Estimation and Forecasting for Wave Energy Applications*. PhD thesis, National University of Ireland Maynooth, 2020.

[47] S. Astariz, A. Vazquez, and G. Iglesias, "Evaluation and comparison of the levelized cost of tidal, wave, and offshore wind energy," *Journal of Renewable and Sustainable Energy*, vol. 7, 2015.

[48] G. Chang, C. A. Jones, J. D. Roberts, and V. S. Neary, "A comprehensive evaluation of factors affecting the levelized cost of wave energy conversion projects," *Renewable Energy*, vol. 127, pp. 344–354, 2018.

[49] D. García-Violini, N. Faedo, F. Jaramillo-Lopez, and J. V. Ringwood, "Simple controllers for wave energy devices compared," *Journal of Marine Science and Engineering*, vol. 8, p. 793, 2020.

[50] N. Faedo, S. Olaya, and J. V. Ringwood, "Optimal control, MPC and MPC-like algorithms for wave energy systems: An overview," *IFAC Journal of Systems and Control*, vol. 1, pp. 37–56, 2017.

[51] M. Rosati, J. C. C. Henriques, and J. V. Ringwood, "Oscillating-water-column wave energy converters: A critical review of numerical modelling and control," *Energy Conversion and Management: X*, vol. 16, 2022.

[52] N. Faedo, D. García-Violini, Y. Peña-Sanchez, and J. V. Ringwood, "Optimisation-vs. non-optimisation-based energy-maximising control for wave energy converters: A case study," in *Proceedings of the 21th European Control Conference*, (Saint Petersburg, Russia), pp. 843–848, 2020.

[53] E. Commision, "Ocean Energy: Technology Market Report." https://publications.jrc.ec.europa.eu/repository/handle/JRC118311. Last accessed: 27/03/2024.

[54] IRENA, "Innovation Outlook: Ocean Energy Technologies." https://www.irena.org/Publications/2020/Dec/Innovation-Outlook-Ocean-Energy-Technologies. Last accessed: 27/03/2024.

[55] J. Weber, "WEC technology readiness and performance matrix–finding the best research technology development trajectory," in *Proceedings of the 4th International Conference on Ocean Energy*, (Dublin, Ireland), 2012.

[56] M. Rosati, J. V. Ringwood, and J. C. C. Henriques, "A comprehensive wave-to-wire control formulation for oscillating water column wave energy converters," *Trends in Renewable Energy Offshore*, pp. 329–337, 2022.

[57] M. Rosati and J. V. Ringwood, "Towards hydrodynamic control of an oscillating water column wave energy converter," in *Trends in Renewable Energies Offshore*, pp. 411–418, CRC Press, 2022.

[58] M. Rosati, T. Kelly, G. D. Violini, and J. V. Ringwood, "Data-based hydrodynamic modelling of a fixed OWC wave energy converter," in *Proceedings of the 14th European Wave and Tidal Energy Conference*, (Plymouth, UK), 2021.

[59] M. Rosati, T. Kelly, and J. V. Ringwood, "Nonlinear data-based hydrodynamic modeling of a fixed oscillating water column wave energy device," *IEEE Access*, vol. 9, 2021.

[60] M. Rosati and J. V. Ringwood, "Wave-to-wire efficiency maximisation for oscillating water column systems," in *Proceedings of the 22nd IFAC World Congress*, (Yokohama, Japan), International Federation of Automatic Control, 2023.

[61] M. Rosati, A. H. Said, and J. V. Ringwood, "Wave-to-wire control of an oscillating water column wave energy system equipped with a wells turbine," in *Proceedings of the 15th European Wave and Tidal Energy Conference*, (Bilbao, Spain), 2023.

[62] M. Rosati and J. V. Ringwood, "Receding-horizon pseudospectral control for energy maximization of oscillating-water-column wave energy systems," in *Proceedings of the 22nd European Control Conference*, (Stockholm, Sweeden), 2024.

[63] M. Rosati and J. V. Ringwood, "Electric energy maximization for oscillating water column wave energy systems using a receding-horizon pseudospectral control approach," *IEEE Transaction on Sustainable Energy*, 2024.

[64] M. Rosati and J. V. Ringwood, "Control co-design of power take-off and bypass valve for OWC-based wave energy conversion systems," *Renewable Energy*, vol. 219, 2023.

[65] B. Drew, A. R. Plummer, and M. N. Sahinkaya, "A review of wave energy converter technology," *Proceedings of the Institution of Mechanical Engineers, Part A: Journal of Power and Energy*, vol. 223, p. 887 – 902, 2009.

[66] A. F. O. Falcão and J. C. C. Henriques, "Oscillating-water-column wave energy converters and air turbines: A review," *Renewable Energy*, vol. 85, pp. 1391–1424, 2016.

[67] A. F. O. Falcão, J. C. C. Henriques, and L. M. C. Gato, "Self-rectifying air turbines for wave energy conversion: A comparative analysis," *Renewable and Sustainable Energy Reviews*, vol. 91, pp. 1231–1241, 2018.

[68] D. L. O'Sullivan and A. W. Lewis, "Generator selection and comparative performance in offshore oscillating water column ocean wave energy converters," *IEEE Transactions on Energy Conversion*, vol. 26, pp. 603–614, 2011.

[69] T. K. Das, P. Halder, and A. Samad, "Optimal design of air turbines for oscillating water column wave energy systems: A review," *The International Journal of Ocean and Climate Systems*, vol. 8, pp. 37–49, 2017.

[70] M. Tsili and S. Papathanassiou, "A review of grid code technical requirements for wind farms," *IET Renewable Power Generation*, vol. 3, pp. 308–332, 2009.

[71] H. A. Said and J. V. Ringwood, "Grid integration aspects of wave energy–Overview and perspectives," *IET Renewable Power Generation*, vol. 15, pp. 3045–3064, 2021.

[72] A. F. O. Falcão and J. C. C. Henriques, "The spring-like air compressibility effect in OWC wave energy converters: Hydro-, thermo-and aerodynamic analyses," in *International Conference on Offshore Mechanics and Arctic Engineering*, (Madrid, Spain), 2018.

[73] K. Rhinefrank, T. Brekken, B. Paasch, A. Yokochi, and A. Von Jouanne, "Comparison of linear generators for wave energy applications," in *Proceedings of the 46th AIAA Aerospace Sciences Meeting and Exhibit*, p. 1335, 2008.

[74] A. F. O. Falcão, "Stochastic modelling in wave power-equipment optimization: Maximum energy production versus maximum profit," *Ocean Engineering*, vol. 31, 2004.

[75] G. Laface, "Productivity analysis of different design for OWC nearshore in breakwater in pantelleria," Master's thesis, Politecnico di Torino, Turin, Italy, 2021.

[76] Y. Torre-Enciso, I. Ortubia, L. L. De Aguileta, and J. Marqués, "Mutriku wave power plant: From the thinking out to the reality," in *Proceedings of the 8th European Wave and Tidal Energy Conference*, (Uppsala, Sweden), pp. 319–329, 2009.

[77] F. Arena, V. Fiamma, V. Laface, G. Malara, A. Romolo, A. Viviano, G. Sannino, and A. Carillo, "Installing U-OWC devices along italian coasts," in *Proceedings of the 32nd International Conference on Ocean, Offshore and Arctic Engineering*, (Nantes, France), 2013.

[78] A. Fleming, G. MacFarlane, S. Hunter, and T. Denniss, "Power performance prediction for a vented oscillating water column wave energy converter with a unidirectional air turbine power take-off," in *Proceedings of the 12th European Wave and Tidal Energy Conference*, (Cork, Ireland), 2017.

[79] A. F. O. Falcão, J. C. C. Henriques, and J. J. Cândido, "Dynamics and optimization of the OWC spar buoy wave energy converter," *Renewable Energy*, vol. 48, pp. 369–381, 2012.

[80] Y. Masuda and M. E. McCormick, "Experiences in pneumatic wave energy conversion in japan," in *Costal Engineering*, (Taipei, Taiwan), pp. 1–33, ASCE, 1986.

[81] D. V. Evans, "The oscillating water column wave-energy device," *IMA Journal of Applied Mathematics*, vol. 22, pp. 423–433, 1978.

[82] D. Ross, *Power from the Waves*. Oxford University Press, USA, 1995.

[83] A. A. Hopkins, *Scientific American Reference Book; a Manual for the Office, Household and Shop*. New York: Scientific American Publishing Co., 1921.

[84] A. Palme, "Wave motion turbine," *Power*, vol. 52, pp. 200–201, 1920.

[85] Y. Masuda, "Wave-activated generator," in *Proceedings of the International Colloquium on the Exploitation of the Oceans*, (Bordeaux, France), 1971.

[86] Y. Masuda, "An experience of wave power generator through tests and improvement," in *Hydrodynamics of Ocean Wave-Energy Utilization*, (Berlin, Heidelberg), pp. 445–452, Springer Berlin Heidelberg, 1986.

[87] J. C. C. Henriques, J. C. C. Portillo, L. M. C. Gato, R. P. F. Gomes, D. N. Ferreira, and A. F. O. Falcão, "Design of oscillating-water-column wave energy converters with an application to self-powered sensor buoys," *Energy*, vol. 112, pp. 852–867, 2016.

[88] A. A. Wells, "Fluid driven rotary transducer." British patent spec No. 1595700, 1976.

[89] A. A. Babinstev, "Apparatus for converting sea wave energy into electrical energy." U.S. patent No. 3922739, 1978.

[90] T. V. Heath, "A review of oscillating water columns," *Philosophical Transactions of the Royal Society A: Mathematical, Physical and Engineering Sciences*, vol. 370, pp. 235–245, 2012.

[91] J. Butterworth, "The kaimei project," in *Proceedings of the Wave Energy Conference*, (Heathrow, UK), pp. 45–48, 1978.

[92] M. E. McCormick, *Ocean Wave Energy Conversion*. New York: Wiley, 1981.

[93] D. Richards and F. B. Weiskopf, "Studies with, and testing of the mccormick pneumatic wave energy turbine with some comments on PWECS systems," in *Coastal Engineering*, pp. 80–102, ASCE, 1986.

[94] G. F. Retief, F. P. J. Muller, G. K. Prestedge, L. C. Geustyn, and D. H. Swart, "Detailed design of a wave energy conversion plant," in *Proceedings of the 19th Conference on Coastal Engineering*, p. 171, 1984.

[95] R. D. Bolding, "Wave power pneumatic system for power generation." U.S. patent No. 4013379, 1974.

[96] Department of Energy Wave Energy Steering Committee, "1981 asses wave energy programme," tech. rep., United Kingdom Wave Consultants, 1981.

[97] J. Conroy, T. Dooley, and J. F. McNamara, "Stochastic modeling and data analysis of a prototype wave energy convertor," *Journal of Energy Resources Technology*, vol. 107, pp. 87–92, 1985.

[98] J. Butterworth, "A review of the islay shoreline wave power station," in *Proceedings of the 1st European Wave Energy Symposium*, (Edimburgh, UK), pp. 283–286, 1993.

[99] H. Ohneda, S. Igarashi, O. Shinbo, S. Sekihara, K. Suzuki, H. Kubota, and H. Morita, "Construction procedure of a wave power extracting caisson breakwater," in *Proceedings of 3rd Symposium on Ocean Energy Utilization*, pp. 171–179, 1991.

[100] M. Suzuki, C. Arakawa, and S. Takahashi, "Performance of wave power generating system installed in breakwater at sakata port in japan," in *International Ocean and Polar Engineering Conference*, ISOPE, 2004.

[101] M. Ravindran and P. M. Koola, "Energy from sea waves—the indian wave energy programme," *Current Science*, vol. 60, pp. 676–680, 1991.

[102] European Commission, "JOULE II - Economy/Energy/Environment Models." `https://cordis.europa.eu/article/id/5622-joule-ii-economyenergyenvironment-models`, 1996. Last accessed: 21/12/2023.

[103] A. F. O. Falcão, A. J. N. A. Sarmento, L. M. C. Gato, and A. Brito-Melo, "The pico OWC wave power plant: Its lifetime from conception to closure 1986–2018," *Applied Ocean Research*, vol. 98, p. 102104, 2020.

[104] The Queen's University Belfast, "Islay LIMPET wave power plant," tech. rep., European Commission, 2002.

[105] T. Kelly, *Experimental and Numerical Modelling of a Multiple Oscillating Water Column Structure*. PhD thesis, National University of Ireland Maynooth, 2018.

[106] Entec UK Ltd., "Cost estimation methodology - the marine energy challenge approach to estimating the cost of energy produced by marine energy systems," tech. rep., The Carbon Trust, 2006.

[107] T. Thorpe, "Chapter 15 - wave energy," in *2004 Survey of Energy Resources (20th Edition)*, pp. 401–417, Oxford: Elsevier Science, twentieth edition ed., 2004.

[108] D. Zhang, W. Li, and Y. Lin, "Wave energy in China: Current status and perspectives," *Renewable Energy*, vol. 34, pp. 2089–2092, 2009.

[109] J. C. C. Henriques, W. Sheng, A. F. O. Falcão, and L. M. C. Gato, "A comparison of biradial and wells air turbines on the mutriku breakwater OWC wave power plant," in *International Conference on Offshore Mechanics and Arctic Engineering*, pp. 19–22, ASME, 2017.

[110] L. M. C. Gato, A. A. D. Carrelhas, and J. C. C. Henriques, "Turbine-generator set laboratory tests in variable unidirectional flow," tech. rep., OPERA - Open Sea Operating Experience to Reduce Wave Energy Costs, Deliverable D3.2, 2017.

[111] F. Arena, A. Romolo, G. Malara, and A. Ascanelli, "On design and building of a U-OWC wave energy converter in the mediterranean sea: A case study," in *International Conference on Offshore Mechanics and Arctic Engineering*, ASME, 2013.

[112] F. Arena, A. Romolo, G. Malara, V. Fiamma, and V. Laface, "The first full operative U-OWC plants in the port of civitavecchia," in *International Conference on Offshore Mechanics and Arctic Engineering*, ASME, 2017.

[113] M. A. Mustapa, O. B. Yaakob, Y. M. Ahmed, C.-K. Rheem, K. K. Koh, and F. A. Adnan, "Wave energy device and breakwater integration: A review," *Renewable and Sustainable Energy Reviews*, vol. 77, pp. 43–58, 2017.

[114] H. Hotta, Y. Washio, H. Yokozawa, and T. Miyazaki, "R&D on wave power device "Mighty Whale"," *Renewable Energy*, vol. 9, pp. 1223–1226, 1996.

[115] L. Martinelli, P. Pezzutto, and P. Ruol, "Experimentally based model to size the geometry of a new OWC device, with reference to the mediterranean sea wave environment," *Energies*, vol. 6, pp. 4696–4720, 2013.

[116] J. P. Kofoed and P. Frigaard, "Chydraulic evaluation of the LEANCON wave energy converter," tech. rep., Department of Civil Engineering, Aalborg University, Denmark, 2008.

[117] R. P. F. Gomes, J. C. C. Henriques, L. M. C. Gato, and A. F. O. Falcão, "Hydrodynamic optimization of an axisymmetric floating oscillating water column for wave energy conversion," *Renewable Energy*, vol. 44, pp. 328–339, 2012.

[118] R. P. F. Gomes, J. C. C. Henriques, L. M. C. Gato, and A. F. O. Falcao, "Testing of a small-scale floating OWC model in a wave flume," in *Proceedings of the 4th International Conference on Ocean Energy*, (Dublin, Ireland), pp. 1–7, 2012.

[119] J. C. C. Henriques, R. P. F. Gomes, L. M. C. Gato, A. F. O. Falcão, E. Robles, and S. Ceballos, "Testing and control of a power take-off system for an oscillating-water-column wave energy converter," *Renewable Energy*, vol. 85, pp. 714–724, 2016.

[120] L. Blain, "Giant, megawatt-scale wave energy generator to be tested in scotland." `https://newatlas.com/energy/oceanenergy-oe35-wave-power/`, 2022. Last accessed: 21/12/2023.

[121] C. M. Wang, Z. Y. Tay, K. Takagi, and T. Utsunomiya, "Literature review of methods for mitigating hydroelastic response of VLFS under wave action," *Applied Mechanics Reviews*, 2010.

[122] A. Aubault, M. Alves, A. Sarmento, D. Roddier, and A. Peiffer, "Modeling of an oscillating water column on the floating foundation windfloat," in *Proceedings of the 30th International Conference on Offshore Mechanics and Arctic Engineering*, (Rotterdam, Netherlands), pp. 235–246, 2011.

[123] M. Boland, T. Kelly, R. Carolan, B. Walsh, and T. Dooley, "Scale model testing of the WASP - a novel wave measuting buoy," in *Proceedings of the 13th European Wave and Tidal Energy Conference*, (Naples, Italy), pp. 1–9, 2019.

[124] E. Lemos, N. Haraczy, and A. Shah, "Estimating the generating efficiency of the aquabuoy 2.0," *Mathematical Methods in Engineering Penn State Harrisburg, Middletown, PA*, 2018.

[125] R. Vertechy, M. Fontana, G. P. Papini Rosati, and M. Bergamasco, "Oscillating-water-column wave-energy-converter based on dielectric elastomer generator," in *Electroactive Polymer Actuators and Devices (EAPAD) 2013*, pp. 130–142, SPIE, 2013.

[126] M. Burdekin and B. Crossland, "Alan arthur wells. 1 may 1924 — 8 november 2005," *Biographical Memoirs of Fellows of the Royal Society*, vol. 53, pp. 365–384, 2007.

[127] S. Raghunathan and C. P. Tan, "Performance of biplane wells turbine," *Journal of Energy*, vol. 7, pp. 741–742, 1983.

[128] R. Arlitt, H. U. Banzhaf, R. Starzmann, and B. F., "Air turbine for wave power station." Patent No. WO 2009/089902, 2009.

[129] J. A. C. Kentfield, "Bi-flow directional air-turbine for wave energy extraction," in *Proceedings of Condensed Papers - 6th Miami International Conference on Alternative Energy Sources*, (Miami, Florida, USA), p. 59 – 60, 1983.

[130] C. Moisel and R. Starzmann, "Aerodynamic design and numerical investigation of a new radial bi-directional turbine for wave energy conversion," in *Proceedings of 10th European Wave Tidal Energy Conference*, (Aalborg, Denmark), 2013.

[131] C. Moisel and T. H. Carolus, "Experimental loss analysis on a model-scale radial bidirectional air-turbine for wave energy conversion," in *Proceedings of the 1st International Conference on Renewable Energies Offshore*, (Lisbon, Portugal), p. 343, CRC Press, 2015.

[132] H. Maeda, T. Setoguchi, K. Kaneko, T. Kim, M. Inoue, *et al.*, "The effect of turbine geometry on the performance of impulse turbine with self-pitch-controlled guide vanes for wave power conversion," in *The Fourth International Offshore and Polar Engineering Conference*, (Osaka, Japan), International Society of Offshore and Polar Engineers, 1994.

[133] M. Takao, Y. Kinoue, T. Setoguchi, T. Obayashi, and K. Kaneko, "Impulse turbine with self-pitch-controlled guide vanes for wave power conversion (effect of guide vane geometry on the performance)," *International Journal of Rotating Machinery*, vol. 6, pp. 355–362, 2000.

[134] M. E. McCormick, J. G. Rehak, and B. D. Williams, "An experimental study of a bidirectional radial turbine for pneumatic wave energy conversion," in *Proceedings of the Mastering the Oceans Through Technology*, vol. 2, (Newport, Rhode Island, USA), pp. 866–870, 1992.

[135] M. Takao, Y. Fujioka, and T. Setoguchi, "Effect of pitch-controlled guide vanes on the performance of a radial turbine for wave energy conversion," *Ocean Engineering*, vol. 32, pp. 2079–2087, 2005.

[136] T. Konno, Y. Nagata, M. Takao, and T. Setoguchi, "Experimental study of a radial turbine using floating nozzle for wave energy conversion," in *Proceedings of the 28th International Conference on Offshore Mechanics and Arctic Engineering*, (Honolulu, Hawaii, USA), pp. 1085–1091, 2009.

[137] R. Starzmann, *Aero-Acoustic Analysis of Wells Turbines for Ocean Wave Energy Conversion*. PhD thesis, Universität Siegen, Siegen, Germany, 2012.

[138] A. F. O. F. ao, L. M. C. Gato, and E. P. A. S. Nunes, "A novel radial self-rectifying air turbine for use in wave energy converters," *Renewable Energy*, vol. 50, pp. 289–298, 2013.

[139] L. M. C. Gato and A. F. O. Falcão, "Turbine with radial inlet and outlet flow rotor for use in bi-directional flows." Patent No. WO2011102746 A4, 2012.

[140] A. F. O. Falcão, L. M. C. Gato, and E. P. A. S. Nunes, "A novel radial self-rectifying air turbine for use in wave energy converters. Part 2. Results from model testing," *Renewable Energy*, vol. 53, pp. 159–164, 2013.

[141] A. S. Shehata, Q. Xiao, M. M. Selim, A. Elbatran, and D. Alexander, "Enhancement of performance of wave turbine during stall using passive flow control: First and second law analysis," *Renewable Energy*, vol. 113, pp. 369–392, 2017.

[142] A. S. Shehata, Q. Xiao, M. A. Kotb, M. M. Selim, A. Elbatran, and D. Alexander, "Effect of passive flow control on the aerodynamic performance, entropy generation and aeroacoustic noise of axial turbines for wave energy extractor," *Ocean Engineering*, vol. 157, pp. 262–300, 2018.

[143] J. C. C. Henriques, L. M. C. Gato, V. La Sala, and A. A. D. Carrelhas, "Acoustic noise emission of air turbines for wave energy conversion: Assessment and analysis," *Renewable Energy*, vol. 212, pp. 897–907, 2023.

[144] Dresser-Rand, "Hydroair variable radius turbine." `http://www.dresser-rand.com/literature/general/2210_HydroAir.pdf`, 2011. Last accessed: 23/12/2023.

[145] R. Curran and M. Folley, "Air Turbine Design for OWCs," in *Ocean Wave Energy-Current Status and Future Prospects*, pp. 189–219, Springer, 2008.

[146] J. V. Ringwood, "Wave energy control: Status and perspectives 2020," *IFAC-PapersOnLine*, vol. 53, pp. 12271–12282, 2020.

[147] C. Windt, N. Faedo, M. Penalba, F. Dias, and J. V. Ringwood, "Reactive control of wave energy devices–the modelling paradox," *Applied Ocean Research*, vol. 109, p. 102574, 2021.

[148] G. B. Airy, "Tides and waves," *Encyclopaedia Metropolitana , Mixed Sciences*, vol. 3, 1841.

[149] M. K. Ochi, *Ocean Waves: The Stochastic Approach*, vol. 6. Cambridge University Press, 2005.

[150] D. J. Tritton, *Physical Fluid Dynamics*. Springer Science & Business Media, 2012.

[151] M. Rosati, "Tecnica di molecular tagging per la misura di gradienti di temperatura in acetone gassoso rarefatto," Master's thesis, Politecnico di Milano, 2018.

[152] O. Faltinsen, *Sea Loads on Ships and Offshore Structures*, vol. 1. Cambridge University Press, 1993.

[153] C. Windt, J. Davidson, and J. V. Ringwood, "High-fidelity numerical modelling of ocean wave energy systems: A review of computational fluid dynamics-based numerical wave tanks," *Renewable and Sustainable Energy Reviews*, vol. 93, pp. 610–630, 2018.

[154] A. Zhang, P. Sun, F. Ming, and A. Colagrossi, "Smoothed particle hydrodynamics and its applications in fluid-structure interactions," *Journal of Hydrodynamics*, vol. 29, pp. 187–216, 2017.

[155] A. Calderer, X. Guo, L. Shen, and F. Sotiropoulos, "Coupled fluid-structure interaction simulation of floating offshore wind turbines and waves: A large eddy simulation approach," in *Journal of Physics: Conference Series*, IOP Publishing, 2014.

[156] M. Penalba, G. Giorgi, and J. V. Ringwood, "Mathematical modelling of wave energy converters: A review of nonlinear approaches," *Renewable and Sustainable Energy Reviews*, vol. 78, pp. 1188–1207, 2017.

[157] F. Opoku, M. N. Uddin, and M. Atkinson, "A review of computational methods for studying oscillating water columns – the Navier-Stokes based equation approach," *Renewable and Sustainable Energy Reviews*, vol. 174, 2023.

[158] J. Falnes and A. Kurniawan, *Ocean Waves and Oscillating Systems: Linear Interactions Including Wave-Energy Extraction*, vol. 8. Cambridge University Press, 2002.

[159] T. Sarpkaya, M. Isaacson, and J. V. Wehausen, "Mechanics of wave forces on offshore structures," *Journal of Applied Mechanics*, vol. 49, pp. 466–467, 1982.

[160] A. D. D. Craik, "The origins of water wave theory," *Annual Review of Fluid Mechanics*, vol. 36, pp. 1–28, 2004.

[161] G. Giorgi and J. V. Ringwood, "Computationally efficient nonlinear Froude–Krylov force calculations for heaving axisymmetric wave energy point absorbers," *Journal of Ocean Engineering and Marine Energy*, vol. 3, pp. 21–33, 2017.

[162] L. L. Erickson, "Panel methods - an introuction," tech. rep., Ames Research Center, Moffett Field, California, 1990.

[163] W. Kraus, "Panel methods in aerodynamics," *Numerical Methods in Fluid Dynamics*, pp. 237–297, 1978.

[164] J. N. Ewman and C. H. Lee, "WAMIT user manual." `http://www.wamit.com/manual.htm`, 2016. Last accessed: 18/03/2019.

[165] ANSYS Inc., "AQWA v14.5 user manual." `https://cybership.files.wordpress.com/2014/01/wb_aqwa.pdf`, 2012. Last accessed: 07/12/2023.

[166] A. Babarit and G. Delhommeau, "Theoretical and numerical aspects of the open source BEM solver NEMOH," in *Proceedings of the 11th European Wave and Tidal Energy Conference, Nantes, France*, pp. 08C1–1–(1–12), 2015.

[167] O. Masson, "Développements du programme ACHIL3D," tech. rep., Laboratoire de Mécanique des Fluides CNRS, Ecole Central de Nantes, 1998.

[168] W. E. Cummins, "The impulse response function and ship motion," tech. rep., Schiffstechnik, 1962.

[169] T. F. Ogilvie, "Recent progress toward the understanding and prediction of ship motions," tech. rep., Office of Naval Research, 1966.

[170] U. A. Korde and J. V. Ringwood, *Hydrodynamic Control of Wave Energy Devices*. Cambridge University Press, 2016.

[171] J. Falnes, "On non-causal impulse response functions related to propagating water waves," *Applied Ocean Research*, vol. 17, pp. 379–389, 1995.

[172] T. Pérez and T. I. Fossen, "Time vs. frequency-domain identification of parametric radiation force models for marine structures at zero speed," *Modeling, Identification and Control*, vol. 29, pp. 1–19, 2008.

[173] Y. Peña-Sanchez, N. Faedo, and J. V. Ringwood, "A critical comparison between parametric approximation methods for radiation forces in wave energy systems," in *Proceedings of the 29th International Ocean and Polar Engineering Conference*, (Honolulu, USA), 2019.

[174] T. Perez and T. I. Fossen, "A matlab toolbox for parametric identification of radiation-force models of ships and offshore structures," *Modeling, Identification and Control*, vol. 30, p. 1, 2009.

[175] Y.-H. Yu, M. Lawson, K. Ruehl, and C. Michelen, "Development and demonstration of the WEC-Sim wave energy converter simulation tool," in *Proceedings of the 2nd Marine Energy Technology Symposium*, (Seattle, USA), pp. 1–8, 2014.

[176] N. Tom, M. Lawson, and Y.-H. Yu, "Demonstration of the recent additions in modelling capabilities for the WEC-Sim wave energy converter design tool," in *Proceedings of the 34th International Conference on Ocean, Offshore and Arctic Engineering*, (Newfoundland, Canada), pp. 1–11, 2015.

[177] W. Sheng, R. Alcorn, and A. Lewis, "A new method for radiation forces for floating platforms in waves," *Ocean Engineering*, vol. 105, pp. 43–53, 2015.

[178] N. Faedo, Y. Peña-Sanchez, and J. V. Ringwood, "Finite-order hydrodynamic model determination for wave energy applications using moment-matching," *Ocean Engineering*, vol. 163, pp. 251–263, 2018.

[179] C. L. Bretschneider, "Wave variability and wave spectra for wind-generated gravity waves," tech. rep., Beach Erosion Board, US Army, Corps of Engineers, Washington D.C., 1959.

[180] K. Hasselmann, T. Barnett, E. Bouws, H. Carlson, D. Cartwright, K. Enke, J. Ewing, H. Gienapp, D. Hasselmann, P. Kruseman, A. Meerburg, P. Müller, D. Olbers, K. Richter, W. Sell, and H. Walden, "Measurements of wind-wave growth and swell decay during the Joint North Sea Wave Project (JONSWAP)," tech. rep., Ergänzungsheft zur Deutschen Hydrographischen Zeitschrift, 1973.

[181] W. J. Pierson Jr. and L. Moskowitz, "A proposed spectral form for fully developed wind seas based on the similarity theory of SA Kitaigorodskii," *Journal of Geophysical Research*, vol. 69, pp. 5181–5190, 1964.

[182] A. Mérigaud and J. V. Ringwood, "Free-surface time-series generation for wave energy applications," *IEEE Journal of Oceanic Engineering*, vol. 43, pp. 19–35, 2018.

[183] J. C. C. Henriques, J. C. C. Portillo, W. Sheng, L. M. C. Gato, and A. F. O. Falcão, "Dynamics and control of air turbines in oscillating-water-column wave energy converters: Analyses and case study," *Renewable and Sustainable Energy Reviews*, vol. 112, pp. 571–589, 2019.

[184] T. Kelly, T. Dooley, and J. V. Ringwood, "Experimental determination of the hydrodynamic parameters of an OWC," in *Proceedings of the 12th European Wave and Tidal Energy Conference*, (Cork, Ireland), 2017.

[185] C. Zhang, J. Dai, L. Cui, and D. Ning, "Experimental study of nonlinear states of oscillating water column in waves," *Physics of Fluids*, vol. 35, 2023.

[186] B. A. Kharkeshi, R. Shafaghat, K. Rezanejad, and R. Alamian, "Measuring and investigating the effect of sloshing on the performance of an OWC wave energy converter by means of a novel experimental approach," *Ocean Engineering*, vol. 275, 2023.

[187] A. F. O. Falcão, "Control of an oscillating-water-column wave power plant for maximum energy production," *Applied Ocean Research*, vol. 24, pp. 73–82, 2002.

[188] S. L. Dixon and C. Hall, *Fluid Mechanics and Thermodynamics of Turbomachinery*. Butterworth-Heinemann, 2013.

[189] H. Maeda, S. Santhakumar, T. Setoguchi, M. Takao, Y. Kinoue, and K. Kaneko, "Performance of an impulse turbine with fixed guide vanes fn2 for wave power conversion," *Renewable Energy*, vol. 17, pp. 533–547, 1999.

[190] N. Mohan, *Advanced Electric Drives: Analysis, Control, and Modeling Using MATLAB/Simulink*, ch. 10, pp. 143–156. Hoboken, USA: John Wiley & Sons, Ltd, 2014.

[191] P. C. Krause, O. Wasynczuk, S. D. Sudhoff, and S. D. Pekarek, *Analysis of Electric Machinery and Drive Systems*, ch. 6, pp. 215–270. Piscataway, USA: Wiley-IEEE Press, 3rd ed., 2013.

[192] H. B. Bingham, Y.-H. Yu, K. Nielsen, T. T. Tran, K.-H. Kim, S. Park, K. Hong, H. A. Said, T. Kelly, J. V. Ringwood, *et al.*, "Ocean energy systems wave energy modeling task 10.4: Numerical modeling of a fixed oscillating water column," *Energies*, vol. 14, 2021.

[193] W. K. Tease, J. Lees, and A. Hall, "Advances in oscillating water column air turbine," in *Proceedings of the 7th European Wave and Tidal Energy Conference*, (Porto, Portugal), 2007.

[194] A. A. D. Carrelhas, L. M. C. Gato, J. C. C. Henriques, A. F. O. F. ao, and J. Varandas, "Test results of a 30 kw self-rectifying biradial air turbine-generator prototype," *Renewable and Sustainable Energy Reviews*, vol. 109, pp. 187–198, 2019.

[195] Y. Zou and J. He, "Comprehensive modeling, simulation and experimental validation of permanent magnet synchronous generator wind power system," in *Proceedings of the 52nd Industrial and Commercial Power Systems Technical Conference*, (Detroit, USA), pp. 1–9, 2016.

[196] D.-Z. Ning, R.-Q. Wang, Q.-P. Zou, and B. Teng, "An experimental investigation of hydrodynamics of a fixed OWC wave energy converter," *Applied Energy*, vol. 168, pp. 636–648, 2016.

[197] S. Dai, S. Day, Z. Yuan, and H. Wang, "Investigation on the hydrodynamic scaling effect of an OWC type wave energy device using experiment and CFD simulation," *Renewable Energy*, vol. 142, pp. 184–194, 2019.

[198] M. Penalba, T. Kelly, and J. V. Ringwood, "Using NEMOH for modelling wave energy convertes: A comparative study with WAMIT," in *Proceedings of the 12th European Wave and Tidal Energy Conference*, (Cork, Ireland), 2017.

[199] N. Faedo, S. Olaya, and J. V. Ringwood, "Optimal control, MPC and MPC-like algorithms for wave energy systems: An overview," *IFAC Journal of Systems and Control*, vol. 1, pp. 37–56, 2017.

[200] L. Ljung, *System Identification: Theory for the User*. Prentice Hall, 1999.

[201] J. Davidson, S. Giorgi, and J. V. Ringwood, "Identification of wave energy device models from numerical wave tank data—part 1: Numerical wave tank identification tests," *IEEE Transactions on Sustainable Energy*, vol. 7, pp. 1012–1019, 2016.

[202] J. Davidson, S. Giorgi, and J. V. Ringwood, "Linear parametric hydrodynamic models for ocean wave energy converters identified from numerical wave tank experiments," *Ocean Engineering*, vol. 103, pp. 31–39, 2015.

[203] L. Zadeh, "On the identification problem," *IRE Transactions on Circuit Theory*, vol. 3, pp. 277–281, 1956.

[204] S. Giorgi, J. Davidson, and J. V. Ringwood, "Identification of wave energy device models from numerical wave tank data—part 2: Data-based model determination," *IEEE Transactions on Sustainable Energy*, vol. 7, pp. 1020–1027, 2016.

[205] L. Ljung, "Perspectives on system identification," *Annual Reviews in Control*, vol. 34, pp. 1–12, 2010.

[206] E. Pasta, N. Faedo, G. Mattiazzo, and J. V. Ringwood, "Towards data-driven and data-based control of wave energy systems: Classification, overview, and critical assessment," *Renewable and Sustainable Energy Reviews*, vol. 188, 2023.

[207] G. Bacelli, R. G. Coe, D. Patterson, and D. Wilson, "System identification of a heaving point absorber: Design of experiment and device modeling," *Energies*, vol. 10, p. 472, 2017.

[208] H. Cho, G. Bacelli, and R. G. Coe, "Linear and nonlinear system identification of a wave energy converter," tech. rep., Sandia National Laboratories, Albuquerque, New Mexico, USA, 2018.

[209] S. Giorgi, J. Davidson, M. Jakobsen, M. Kramer, and J. V. Ringwood, "Identification of dynamic models for a wave energy converter from experimental data," *Ocean Engineering*, vol. 183, pp. 426–436, 2019.

[210] F. Jaramillo-Lopez, B. Flannery, J. Murphy, and J. V. Ringwood, "Modelling of a three-body hinge-barge wave energy device using system identification techniques," *Energies*, vol. 13, p. 5129, 2020.

[211] R. G. Coe, G. Bacelli, and D. Forbush, "A practical approach to wave energy modeling and control," *Renewable and Sustainable Energy Reviews*, vol. 142, p. 110791, 2021.

[212] M. Rosati, J. V. Ringwood, H. B. Bingham, B. Joensen, and K. Nielsen, "A data-based modelling approach for a vented oscillating water column wave energy converter," in *Trends in Renewable Energies Offshore*, pp. 339–347, CRC Press, 2022.

[213] G. D. Gkikas and G. A. Athanassoulis, "Development of a novel nonlinear system identification scheme for the pressure fluctuation inside an oscillating water column-wave energy converter part i: Theoretical background and harmonic excitation case," *Ocean Engineering*, vol. 80, pp. 84–99, 2014.

[214] "National instruments: Test, measurement and embedded systems." `http://www.ni.com/`. Last accessed: 06/01/2024.

[215] S. Jacob, "Experimental and numerical modelling of an oscillating water column structure in irregular sea states," Master's thesis, Dundalk Institute of Technology, 2019.

[216] A. J. Jerri, "The shannon sampling theorem—its various extensions and applications: A tutorial review," *Proceedings of the IEEE*, vol. 65, pp. 1565–1596, 1977.

[217] J. Falnes, "Optimum control of oscillation of wave-energy converters," *International Journal of Offshore and Polar Engineering*, vol. 12, 2002.

[218] J. V. Ringwood, G. Bacelli, and F. Fusco, "Energy-maximizing control of wave-energy converters: The development of control system technology to optimize their operation," *IEEE Control Systems Magazine*, vol. 34, pp. 30–55, 2014.

[219] Mathworks, "Loss function and model quality metrics." `https://uk.mathworks.com/help/ident/ug/model-quality-metrics.html`. Last accessed: 22/07/2024.

[220] J. Rissanen, "Modeling by shortest data description," *Automatica*, vol. 14, pp. 465–471, 1978.

[221] O. Nelles, *Nonlinear System Identification: From Classical Approaches to Neural Networks and Fuzzy Models*. Springer, 2001.

[222] H. A. Said, D. García-Violini, and J. V. Ringwood, "Wave-to-grid (W2G) control of a wave energy converter," *Energy Conversion and Management: X*, vol. 14, p. 100190, 2022.

[223] J. C. C. Henriques, L. M. C. Gato, A. F. O. Falcão, E. Robles, and F.-X. Faÿ, "Latching control of a floating oscillating-water-column wave energy converter," *Renewable Energy*, vol. 90, pp. 229–241, 2016.

[224] M. Takao, K. Itakura, T. Setoguchi, T. H. Kim, K. Kaneko, and M. Inoue, "Noise characteristics of turbines for wave power conversion," in *Proceedings of the Eleventh International Ocean and Polar Engineering Conference*, (Stavanger, Norway), 2001.

[225] A. A. D. Carrelhas, L. M. C. Gato, and F. J. F. Morais, "Aerodynamic performance and noise emission of different geometries of Wells turbines under design and off-design conditions," *Renewable Energy*, vol. 220, 2024.

[226] K. Monk, V. Winands, and M. Lopes, "Chamber pressure skewness corrections using a passive relief valve system at the pico oscillating water column wave energy plant," *Renewable Energy*, vol. 128, pp. 230–240, 2018.

[227] B. Guo and J. V. Ringwood, "Geometric optimisation of wave energy conversion devices: A survey," *Applied Energy*, vol. 297, p. 117100, 2021.

[228] P. B. Garcia-Rosa, G. Bacelli, and J. V. Ringwood, "Control-informed geometric optimization of wave energy converters: The impact of device motion and force constraints," *Energies*, vol. 8, pp. 13672–13687, 2015.

[229] J. T. Allison and D. R. Herber, "Multidisciplinary design optimization of dynamic engineering systems," *AIAA Journal*, vol. 52, pp. 691–710, 2014.

[230] H. K. Fathy, J. A. Reyer, P. Y. Papalambros, and A. G. Ulsov, "On the coupling between the plant and controller optimization problems," in *Proceedings of the 2001 American Control Conference*, (Arlington, USA), pp. 1864–1869, 2001.

[231] C. A. M. Ströfer, D. T. Gaebele, R. G. Coe, and G. Bacelli, "Control co-design of power take-off systems for wave energy converters using wecopttool," *IEEE Transactions on Sustainable Energy*, vol. 14, pp. 1–11, 2023.

[232] G. Bacelli and R. G. Coe, "Comments on control of wave energy converters," *IEEE Transactions on Control Systems Technology*, vol. 29, pp. 478–481, 2021.

[233] Y. Peña-Sanchez, D. García-Violini, and J. V. Ringwood, "Control co-design of power take-off parameters for wave energy systems," in *Proceedings of the 9th IFAC Symposium on Mechatronic Systems*, (Los Angeles, USA), pp. 311–316, 2022.

[234] M. Garcia-Sanz, "Control co-design: An engineering game changer," *Advanced Control for Applications: Engineering and Industrial Systems*, vol. 1, 2019.

[235] B. Guo, D. Ning, R. Wang, and B. Ding, "Hydrodynamics of an oscillating water column WEC - breakwater integrated system with a pitching front-wall," *Renewable Energy*, vol. 176, pp. 67–80, 2021.

[236] A. Çelik, "An experimental investigation into the effects of front wall geometry on OWC performance for various levels of applied power take off dampings," *Ocean Engineering*, vol. 248, p. 110761, 2022.

[237] J. C. C. Henriques and L. M. C. Gato, "Use of a residual distribution Euler solver to study the occurrence of transonic flow in Wells turbine rotor blades," *Computational Mechanics*, vol. 29, pp. 243–253, 2002.

[238] S. Salter and J. Taylor, "The design of a high-speed stop valve for oscillating water columns," in *Proceedings of the 2nd European Wave Power Conference*, (Lisbon, Portugal), pp. 195–202, 1996.

[239] L. M. C. Gato, L. Eça, and A. F. O. Falcão, "Performance of the Wells turbine with cariable pitch rotor blades," *Journal of Energy Resources Technology, Transaction of the ASME*, vol. 113, pp. 141–146, 1991.

[240] B. Guo, D. Ning, R. Wang, and B. Ding, "Hydrodynamics of an oscillating water column WEC - breakwater integrated system with a pitching front-wall," *Renewable Energy*, vol. 176, pp. 67–80, 2021.

[241] D. D. Raj, V. Sundar, and S. A. Sannasiraj, "Enhancement of hydrodynamic performance of an oscillating water column with harbour walls," *Renewable Energy*, vol. 132, pp. 142–156, 2019.

[242] D. García-Violini, N. Faedo, F. Jaramillo-Lopez, and J. V. Ringwood, "Simple controllers for wave energy devices compared," *Journal of Marine Science and Engineering*, vol. 8, 2020.

[243] A. F. O. Falcão and J. C. C. Henriques, "Effect of non-ideal power take-off efficiency on performance of single-and two-body reactively controlled wave energy converters," *Journal of Ocean Engineering and Marine Energy*, vol. 1, pp. 273–286, 2015.

[244] A. J. N. A. Sarmento, L. M. C. Gato, and A. F. O. Falcão, "Turbine-controlled wave energy absorption by oscillating water column devices," *Ocean Engineering*, vol. 17, pp. 481–497, 1990.

[245] J. Perdigao and A. Sarmento, "Overall-efficiency optimisation in OWC devices," *Applied Ocean Research*, vol. 25, pp. 157–166, 2003.

[246] U. A. Korde, "Development of a reactive control apparatus for a fixed two-dimensional oscillating water column wave energy device," *Ocean Engineering*, vol. 18, pp. 465–483, 1991.

[247] K. Budal and J. Falnes, "Wave power conversion by point absorbers: A Norwegian project," *International Journal of Ambient Energy*, vol. 3, pp. 59–67, 1982.

[248] R. E. Hoskin, B. M. Count, N. K. Nichols, and D. A. C. Nicol, "Phase control for the oscillating water column," in *IUTAM Symposium on Hydrodynamics of Ocean-Wave Energy Utilisation*, (Lisbon, Portugal), pp. 257–268, 1985.

[249] R. Jefferys and T. Whittaker, "Latching control of an oscillating water column device with air compressibility," in *IUTAM Symposium on Hydrodynamics of Ocean-Wave Energy Utilisation*, (Lisbon, Portugal), pp. 281–291, 1985.

[250] J. C. C. Henriques, J. M. Lemos, L. Eça, L. M. C. Gato, and A. F. O. Falcão, "A high-order discontinuous Galerkin method with mesh refinement for optimal control," *Automatica*, vol. 85, pp. 70–82, 2017.

[251] A. Rahoor, "Comparison of control strategies for wave energy converters," tech. rep., Master Programme in Renewable Electricity Production, Upsalla Universitet, 2020.

[252] F. Paparella, K. Monk, V. Winands, M. F. P. Lopes, D. Conley, and J. V. V. Ringwood, "Up-wave and autoregressive methods for short-term wave forecasting for an oscillating water column," *IEEE Transactions on Sustainable Energy*, vol. 6, pp. 171–178, 2015.

[253] J. Marques Silva, S. M. Vieira, D. Valério, J. C. C. Henriques, and P. D. Sclavounos, "Air pressure forecasting for the mutriku oscillating-water-column wave power plant: Review and case study," *IET Renewable Power Generation*, vol. 15, pp. 3485–3503, 2021.

[254] J. C. C. Henriques, A. F. O. Falcão, R. P. F. Gomes, and L. M. C. Gato, "Latching control of an oscillating water column spar-buoy wave energy converter in regular waves," *Journal of Offshore Mechanics and Arctic Engineering*, vol. 135, 2013.

[255] J. C. C. Henriques, J. C. Chong, A. F. O. Falcão, and R. P. F. Gomes, "Latching control of a floating oscillating water column wave energy converter in irregular waves," in *Proceedings of 33rd the International Conference on Ocean, Offshore and Arctic Engineering*, (San Francisco, California, USA), 2014.

[256] J. C. C. Henriques, L. M. C. Gato, J. M. Lemos, R. P. F. Gomes, and A. F. O. Falcão, "Peak-power control of a grid-integrated oscillating water column wave energy converter," *Energy*, vol. 109, pp. 378–390, 2016.

[257] A. Babarit, M. Guglielmi, and A. H. Clément, "Declutching control of a wave energy converter," *Ocean Engineering*, vol. 36, pp. 1015–1024, 2009.

[258] S. H. Salter, J. R. M. Taylor, and N. J. Caldwell, “Power conversion mechanisms for wave energy,” *Proceedings of the Institution of Mechanical Engineers, Part M: Journal of Engineering for the Maritime Environment*, vol. 216, pp. 1–27, 2002.

[259] M. Amundarain, M. Alberdi, A. J. Garrido, and I. Garrido, “Modeling and simulation of wave energy generation plants: Output power control,” *IEEE Transactions on Industrial Electronics*, vol. 58, pp. 105–117, 2011.

[260] M. Alberdi, M. Amundarain, A. Garrido, I. Garrido, O. Casquero, and M. De la Sen, “Complementary control of oscillating water column-based wave energy conversion plants to improve the instantaneous power output,” *IEEE Transactions on Energy Conversion*, vol. 26, pp. 1021–1032, 2011.

[261] D. T. Gaebele, M. E. Magaña, T. K. A. Brekken, J. C. C. Henriques, A. A. D. Carrelhas, and L. M. C. Gato, “Second order sliding mode control of oscillating water column wave energy converters for power improvement,” *IEEE Transactions on Sustainable Energy*, vol. 12, pp. 1151–1160, 2021.

[262] S. Ceballos, J. Rea, I. Lopez, J. Pou, E. Robles, and D. L. O’Sullivan, “Efficiency optimization in low inertia Wells turbine-oscillating water column devices,” *IEEE Transactions on Energy Conversion*, vol. 28, pp. 553–564, 2013.

[263] P. A. P. Justino and A. F. de O. Falcão, “Rotational Speed Control of an OWC Wave Power Plant,” *Journal of Offshore Mechanics and Arctic Engineering*, vol. 121, pp. 65–70, 1999.

[264] D. L. Bruschi, J. C. S. Fernandes, A. F. O. Falcão, and C. P. Bergmann, “Analysis of the degradation in the Wells turbine blades of the Pico oscillating-water-column wave energy plant,” *Renewable and Sustainable Energy Reviews*, vol. 115, 2019.

[265] M. Stefanizzi, S. M. Camporeale, and M. Torresi, “Experimental investigation of a wells turbine under dynamic stall conditions for wave energy conversion,” *Renewable Energy*, vol. 214, p. 369 – 382, 2023.

[266] J. C. C. Henriques, R. P. F. Gomes, L. M. C. Gato, A. F. O. Falcão, E. Robles, and S. Ceballos, “Testing and control of a power take-off system for an oscillating-water-column wave energy converter,” *Renewable Energy*, vol. 85, pp. 714–724, 2016.

[267] F. M. Strati, G. Malara, and F. Arena, “Performance optimization of a U-oscillating-water-column wave energy harvester,” *Renewable Energy*, vol. 99, pp. 1019–1028, 2016.

[268] K. Ogata, *Modern Control Engineering*. Prentice Hall, 2010.

[269] A. J. Garrido, I. Garrido, M. Amundarain, M. Alberdi, and M. De la Sen, “Sliding-mode control of wave power generation plants,” *IEEE Transactions on Industry Applications*, vol. 48, pp. 2372–2381, 2012.

[270] F. Mʼzoughi, S. Bouallegue, A. J. Garrido, I. Garrido, and M. Ayadi, “Fuzzy gain scheduled PI-based airflow control of an oscillating water column in wave power

generation plants," *IEEE Journal of Oceanic Engineering*, vol. 44, pp. 1058–1076, 2018.

[271] K. Ezhilsabareesh, R. Suchithra, and A. Samad, "Performance enhancement of an impulse turbine for OWC using grouped grey wolf optimizer based controller," *Ocean Engineering*, 2019.

[272] A. O'dwyer, *Handbook of PI and PID Controller Tuning Rules*. World Scientific, 2009.

[273] M. Amundarain, M. Alberdi, A. Garrido, and I. Garrido, "Neural rotational speed control for wave energy converters," *International Journal of Control*, vol. 84, pp. 293–309, 2011.

[274] F. M'zoughi, I. Garrido, A. J. Garrido, and M. De La Sen, "Rotational speed control using ANN-based MPPT for OWC based on surface elevation measurements," *Applied Sciences*, vol. 10, 2020.

[275] F. M'zoughi, I. Garrido, A. J. Garrido, and M. De La Sen, "ANN-based airflow control for an oscillating water column using surface elevation measurements," *Sensors*, vol. 20, 2020.

[276] S. Ceballos, J. Rea, E. Robles, I. Lopez, J. Pou, and D. O'Sullivan, "Control strategies for combining local energy storage with wells turbine oscillating water column devices," *Renewable Energy*, vol. 83, pp. 1097–1109, 2015.

[277] F. M'zoughi, I. Garrido, S. Bouallègue, M. Ayadi, and A. J. Garrido, "Intelligent airflow controls for a stalling-free operation of an oscillating water column-based wave power generation plant," *Electronics*, vol. 8, p. 70, 2019.

[278] F. M'zoughi, I. Garrido, A. J. Garrido, and M. De La Sen, "Self-adaptive global-best harmony search algorithm-based airflow control of a wells-turbine-based oscillating-water column," *Applied Sciences*, vol. 10, 2020.

[279] F. M'zoughi, S. Bouallegue, A. J. Garrido, I. Garrido, and M. Ayadi, "Stalling-free control strategies for oscillating-water-column-based wave power generation plants," *IEEE Transactions on Energy Conversion*, vol. 33, pp. 209–222, 2017.

[280] C. Edwards and S. Spurgeon, *Sliding Mode Control: Theory and Applications*. Taylor and Francis Group, CRC Press, 1998.

[281] V. I. Utkin, "Sliding mode control design principles and applications to electric drives," *IEEE Transactions on Industrial Electronics*, vol. 40, pp. 23–36, 1993.

[282] F. D. Mosquera, C. A. Evangelista, P. F. Puleston, and J. V. Ringwood, "Optimal wave energy extraction for oscillating water columns using second-order sliding mode control," *IET Renewable Power Generation*, vol. 14, pp. 1512–1519, 2020.

[283] F. D. Mosquera, C. A. Evangelista, P. F. Puleston, and J. V. Ringwood, "Control para máxima extracción de energía undimotriz por modos deslizantes de segundo orden real con ganancias adaptivas," in *Proceeding of the 27th Congreso Argentino de Control Automático*, (Buenos Aires, Argentina), 2020.

[284] F. M'zoughi, A. J. Garrido, I. Garrido, S. Bouallègue, and M. Ayadi, "Sliding mode rotational speed control of an oscillating water column-based wave generation power plants," in *2018 International Symposium on Power Electronics, Electrical Drives, Automation and Motion (SPEEDAM)*, pp. 1263–1270, IEEE, 2018.

[285] M. E. Magaña and R. Danielle, "Sliding mode control of an array of three oscillating water column wave energy converters to optimize electrical power," in *Proceedings of the 13th European Wave and Tidal Energy Conference*, (Cork, Ireland), 2019.

[286] F. M'zoughi, I. Garrido, A. J. Garrido, and M. De la Sen, "Fuzzy gain scheduled-sliding mode rotational speed control of an oscillating water column," *IEEE Access*, vol. 8, pp. 45853–45873, 2020.

[287] G. Rajapakse, S. Jayasinghe, A. Fleming, and M. Negnevitsky, "A model predictive control-based power converter system for oscillating water column wave energy converters," *Energies*, vol. 10, pp. 1631–1648, 2017.

[288] M. Blanco, D. Ramirez, M. E. Zarei, and M. Gupta, "Dual multivector model predictive control for the power converters of a floating OWC WEC," *International Journal of Electrical Power & Energy Systems*, vol. 133, p. 107263, 2021.

[289] R. Genest and J. V. Ringwood, "A critical comparison of model-predictive and pseudospectral control for wave energy devices," *Journal of Ocean Engineering and Marine Energy*, vol. 2, pp. 485–499, 2016.

[290] S. K. Mishra, S. Purwar, and N. Kishor, "An optimal and non-linear speed control of oscillating water column wave energy plant with wells turbine and DFIG," *International Journal of Renewable Energy Resources*, vol. 6, pp. 995–1006, 2016.

[291] S. K. Mishra, B. Appasani, A. V. Jha, I. Garrido, and A. J. Garrido, "Centralized airflow control to reduce output power variation in a complex OWC ocean energy network," *Complexity*, vol. 2020, 2020.

[292] C. Napole, O. Barambones, M. Derbeli, J. A. Cortajarena, I. Calvo, P. Alkorta, and P. F. Bustamante, "Double fed induction generator control design based on a fuzzy logic controller for an oscillating water column system," *Energies*, vol. 14, 2021.

[293] M. E. Magaña, C. Parlapanis, D. T. Gaebele, and O. Sawodny, "Maximization of wave energy conversion into electricity using oscillating water columns and nonlinear model predictive control," *IEEE Transactions on Sustainable Energy*, vol. 13, pp. 1283–1292, 2022.

[294] A. F. O. Falcão, J. C. C. Henriques, and L. M. C. Gato, "Air turbine optimization for a bottom-standing oscillating-water-column wave energy converter," *Journal of Ocean Engineering and Marine Energy*, pp. 1–14, 2016.

[295] A. F. O. Falcão, J. C. C. Henriques, and L. M. C. Gato, "Rotational speed control and electrical rated power of an oscillating-water-column wave energy converter," *Energy*, vol. 120, pp. 253–261, 2017.

[296] J. Marques Silva, S. M. Vieira, D. Valério, and J. C. C. Henriques, "Model predictive control based on air pressure forecasting of OWC wave power plants," *Energy*, 2023.

[297] J. M. Silva, S. M. Vieira, D. Valério, and J. C. C. Henriques, "GA-optimized inverse fuzzy model control of OWC wave power plants," *Renewable Energy*, vol. 204, pp. 556–568, 2023.

[298] A. F. O. Falcão, L. C. Vieira, P. A. P. Justino, and J. M. C. S. André, "By-Pass Air-Valve Control of an OWC Wave Power Plant," *Journal of Offshore Mechanics and Arctic Engineering*, vol. 125, pp. 205–210, 2003.

[299] J. C. C. Henriques, A. A. D. Carrelhas, L. M. C. Gato, A. F. O. Falcão, J. C. C. Portillo, and J. Varandas, "Peak-shaving control - A new control paradigm for OWC wave energy converters," in *Proceedings of the 12th European Wave and Tidal Energy Conference*, (Cork, Ireland), 2017.

[300] A. A. D. Carrelhas, L. M. C. Gato, and J. C. C. Henriques, "Peak shaving control in OWC wave energy converters: From concept to implementation in the mutriku wave power plant," *Renewable and Sustainable Energy Reviews*, vol. 180, 2023.

[301] T. Senjyu, R. Sakamoto, N. Urasaki, T. Funabashi, H. Fujita, and H. Sekine, "Output power leveling of wind turbine generator for all operating regions by pitch angle control," *IEEE Transactions on Energy Conversion*, vol. 21, pp. 467–475, 2006.

[302] M. Alberdi, M. Amundarain, A. J. Garrido, I. Garrido, and F. J. Maseda, "Fault-ride-through capability of oscillating-water-column-based wave-power-generation plants equipped with doubly fed induction generator and airflow control," *IEEE Transactions on Industrial Electronics*, vol. 58, pp. 1501–1517, 2010.

[303] M. Alberdi, M. Amundarain, A. Garrido, and I. Garrido, "Neural control for voltage dips ride-through of oscillating water column-based wave energy converter equipped with doubly-fed induction generator," *Renewable Energy*, vol. 48, pp. 16–26, 2012.

[304] I. Villanueva, A. Rosales, P. Ponce, and A. Molina, "Grid-voltage-oriented sliding mode control for DFIG under balanced and unbalanced grid faults," *IEEE Transactions on Sustainable Energy*, vol. 9, pp. 1090–1098, 2018.

[305] D. Ramirez, M. Blanco, M. E. Zarei, and M. Gupta, "Robust control of a floating OWC WEC under open-switch fault condition in one or in both VSCs," *IET Renewable Power Generation*, vol. 14, pp. 2538–2549, 2020.

[306] M. E. Zarei, D. Ramírez, C. V. Nicolas, and J. R. Arribas, "Three-phase four-switch converter for SPMS generators based on model predictive current control for wave energy applications," *IEEE Transactions on Power Electronics*, vol. 35, pp. 289–302, 2019.

[307] M. E. Zarei, D. Ramirez, C. Veganzones, and J. Rodriguez, "Predictive direct control of SPMS generators applied to the machine side converter of an OWC power plant," *IEEE Transactions on Power Electronics*, vol. 35, pp. 6719–6731, 2020.

[308] D. B. Murray, J. G. Hayes, D. L. O'Sullivan, and M. G. Egan, "Supercapacitor testing for power smoothing in a variable speed offshore wave energy converter," *IEEE Journal of Oceanic Engineering*, vol. 37, pp. 301–308, 2012.

[309] G. Rajapakse, S. Jayasinghe, A. Fleming, and M. Negnevitsky, "Grid integration and power smoothing of an oscillating water column wave energy converter," *Energies*, vol. 11, 2018.

[310] A. A. D. Carrelhas and L. M. C. Gato, "Reliable control of turbine–generator set for oscillating-water-column wave energy converters: Numerical modelling and field data comparison," *Energy Conversion and Management*, vol. 282, 2023.

[311] M. Blanke, M. Kinnaert, J. Lunze, M. Staroswiecki, and J. Schröder, *Diagnosis and Fault-Tolerant Control*. Springer, 2006.

[312] Z.-S. Hou and Z. Wang, "From model-based control to data-driven control: Survey, classification and perspective," *Information Sciences*, vol. 235, pp. 3–35, 2013.

[313] V. Jayashankar, S. Anand, T. Geetha, S. Santhakumar, V. Jagadeesh Kumar, M. Ravindran, T. Setoguchi, M. Takao, K. Toyota, and S. Nagata, "A twin unidirectional impulse turbine topology for OWC based wave energy plants," *Renewable Energy*, vol. 34, pp. 692–698, 2009.

[314] K. Mala, J. Jayaraj, V. Jayashankar, T. Muruganandam, S. Santhakumar, M. Ravindran, M. Takao, T. Setoguchi, K. Toyota, and S. Nagata, "A twin unidirectional impulse turbine topology for OWC based wave energy plants – Experimental validation and scaling," *Renewable Energy*, vol. 36, pp. 307–314, 2011.

[315] L. Rodríguez, B. Pereiras, J. Fernández-Oro, and F. Castro, "Optimization and experimental tests of a centrifugal turbine for an OWC device equipped with a twin turbines configuration," *Energy*, vol. 171, pp. 710–720, 2019.

[316] K. M. Nielsen, T. S. Pedersen, P. Andersen, and S. Ambühl, "Optimizing control of wave energy converter with losses and fatigue in power take off," *IFAC-PapersOnLine*, vol. 50, pp. 14680–14685, 2017.

[317] U. A. Korde, "A power take-off mechanism for maximizing the performance of an oscillating water column wave energy device," *Applied Ocean Research*, vol. 13, pp. 75–81, 1991.

[318] P. Hardy, B. S. Cazzolato, B. Ding, and Z. Prime, "A maximum capture width tracking controller for ocean wave energy converters in irregular waves," *Ocean Engineering*, vol. 121, pp. 516–529, 2016.

[319] F.-X. Faÿ, M. Marcos, and E. Robles, "Novel predictive latching control for an oscillating water column buoy," in *Proceedings of the 12th European Wave and Tidal Energy Conference*, (Cork, Ireland), 2017.

[320] A. A. D. Carrelhas, L. M. C. Gato, A. F. O. Falcão, and J. C. C. Henriques, "Control law design for the air-turbine-generator set of a fully submerged 1.5 MW mwave prototype. part 2: Experimental validation," *Renewable Energy*, vol. 171, pp. 1002–1013, 2021.

[321] A. A. D. Carrelhas, L. M. C. Gato, A. F. O. Falcão, and J. C. C. Henriques, "Control law design for the air-turbine-generator set of a fully submerged 1.5 MW mwave prototype. part 1: Numerical modelling," *Renewable Energy*, vol. 181, pp. 1402–1418, 2022.

[322] C. Roh and K.-H. Kim, "Deep learning prediction for rotational speed of turbine in oscillating water column-type wave energy converter," *Energies*, vol. 15, 2022.

[323] I. Garrido, A. J. Garrido, M. Alberdi, M. Amundarain, and O. Barambones, "Performance of an ocean energy conversion system with DFIG sensorless control," *Mathematical Problems in Engineering*, vol. 2013, 2013.

[324] F. M'zoughi, I. Garrido, and A. J. Garrido, "Symmetry-breaking for airflow control optimization of an oscillating-water-column system," *Symmetry*, vol. 12, 2020.

[325] O. Barambones, J. M. Gonzalez de Durana, and I. Calvo, "Adaptive sliding mode control for a double fed induction generator used in an oscillating water column system," *Energies*, vol. 11, p. 2939, 2018.

[326] S. K. Mishra, S. Purwar, and N. Kishor, "Event-triggered nonlinear control of OWC ocean wave energy plant," *IEEE Transactions on Sustainable Energy*, vol. 9, pp. 1750–1760, 2018.

[327] R. Suchithra, K. Ezhilsabareesh, and A. Samad, "Optimization based higher order sliding mode controller for efficiency improvement of a wave energy converter," *Energy*, vol. 187, 2019.

[328] D. T. Gaebele, M. E. Magaña, T. K. A. Brekken, and J. C. C. Henriques, "Constrained sliding mode control for oscillating water column wave energy converters.," *IFAC-PapersOnLine*, vol. 53, pp. 12327–12333, 2020.

[329] A. F. O. Falcão and P. A. P. Justino, "OWC wave energy devices with air flow control," *Ocean Engineering*, vol. 26, pp. 1275–1295, 1999.

[330] S.-K. Song and J.-B. Park, "Modeling and control strategy of an oscillating water column-wave energy converter with an impulse turbine module," in *Proceedings of the 15th International Conference on Control, Automation and Systems*, (Busan, Korea), pp. 1983–1988, 2015.

[331] S. K. Song and J. B. Park, "Control strategy of an impulse turbine for an oscillating water column-wave energy converter in time-domain using lyapunov stability method," *Applied Sciences*, vol. 6, p. 281, 2016.

[332] I. Ahmad, F. M'zoughi, P. Aboutalebi, I. Garrido, and A. J. Garrido, "Fuzzy logic control of an artificial neural network-based floating offshore wind turbine model integrated with four oscillating water columns," *Ocean Engineering*, vol. 269, 2023.

[333] F. Shiravani, J. A. Cortajarena, P. Alkorta, and O. Barambones, "A nonlinear generalized predictive control scheme for the oscillating water column plants," *Ocean Engineering*, vol. 284, 2023.

[334] A. S. Haider, T. K. A. Brekken, and A. McCall, "Application of real-time nonlinear model predictive control for wave energy conversion," *IET Renewable Power Generation*, vol. 15, no. 14, pp. 3331–3340, 2021.

[335] G. Bacelli and J. V. Ringwood, "Nonlinear optimal wave energy converter control with application to a flap-type device," in *Proceedings of the 19th IFAC World Congress*, vol. 47, (Cape Town, South Africa), pp. 7696–7701, 2014.

[336] F. Toolbox, "`http://www.eeng.nuim.ie/coer/downloads/`." Last accessed: 15/12/2023.

[337] J. C. C. Henriques, J. J. Cândido, M. T. Pontes, and A. F. O. Falcão, "Wave energy resource assessment for a breakwater-integrated oscillating water column plant at Porto, Portugal," *Energy*, vol. 63, pp. 52–60, 2013.

[338] Y. Peña-Sanchez, A. Mérigaud, and J. V. Ringwood, "Short-term forecasting of sea surface elevation for wave energy applications: The autoregressive model revisited," *IEEE Journal of Oceanic Engineering*, vol. 45(2), pp. 462–471, 2018.

[339] B. Fornberg, *A Practical Guide to Pseudospectral Methods*. Cambridge University Press, 1996.

[340] J. Vlassenbroeck and R. Van Dooren, "A chebyshev technique for solving nonlinear optimal control problems," *IEEE Transaction on Automatic Control*, vol. 33, no. 4, pp. 333–340, 1988.

[341] G. Elnagar, M. Kazemi, and M. Razzaghi, "The pseudospectral legendre method for discretizing optimal control problems," *IEEE Transaction on Automatic Control*, vol. 40, no. 10, pp. 1793–1796, 1995.

[342] I. M. Ross and M. Karpenko, "A review of pseudospectral optimal control: From theory to flight," *Annual Reviews in Control*, vol. 36, no. 2, pp. 182–197, 2012.

[343] R. Genest and J. V. Ringwood, "Receding horizon pseudospectral control for energy maximization with application to wave energy devices," *IEEE Transaction on Control System Technology*, vol. 25, no. 1, pp. 29–38, 2016.

[344] N. M. Tom, Y.-H. Yu, A. D. Wright, and M. J. Lawson, "Pseudo-spectral control of a novel oscillating surge wave energy converter in regular waves for power optimization including load reduction," *Ocean Engineering*, vol. 137, pp. 352–366, 2017.

[345] Y. Peña-Sanchez, N. Faedo, and J. V. Ringwood, "A critical comparison between parametric approximation methods for radiation forces in wave energy systems," in *Proceedings of the 29th International Ocean and Polar Engineering Conference*, (Honolulu, USA), 2019.

[346] O. Von Stryk, *Numerical Solution of Optimal Control Problems by Direct Collocation*. Springer, 1993.

[347] H. A. Said, D. García-Violini, N. Faedo, and J. V. Ringwood, "On the ratio of reactive to active power in wave energy converter control," *IEEE Open Journal of Control Systems*, vol. 3, pp. 14–31, 2024.

[348] F. Fusco and J. V. Ringwood, "A model for the sensitivity of non-causal control of wave energy converters to wave excitation force prediction errors," in *Proceedings of the 9th European Wave and Tidal Energy Conference*, (Southampton, UK), 2011.

[349] Z. Liao, P. Stansby, and G. Li, "A generic linear non-causal optimal control framework integrated with wave excitation force prediction for multi-mode wave energy converters with application to M4," *Applied Ocean Research*, vol. 97, 2020.

[350] R. A. Waltz, J. L. Morales, J. Nocedal, and D. Orban, "An interior algorithm for nonlinear optimization that combines line search and trust region steps," *Mathematical Programming*, vol. 107, no. 3, pp. 391–408, 2006.

[351] Mathworks, "Fmincon function documentation." `https://uk.mathworks.com/help/optim/ug/fmincon.html#d126e98025`. Last accessed: 02/08/2024.

[352] H. Fu and C. Liu, "A buffered Fourier spectral method for non-periodic PDE," *International Journal of Numerical Analysis and Modelling*, vol. 9, no. 2, 2012.

[353] C. Auger, A. Mérigaud, and J. V. Ringwood, "Receding-horizon pseudo-spectral control of wave energy converters using periodic basis functions," *IEEE Transaction on Sustainable Energy*, vol. 10, no. 4, pp. 1644–1652, 2019.

[354] C. Roh, "Enhancing power generation stability in oscillating-water-column wave energy converters through deep-learning-based time delay compensation," *Processes*, vol. 11, no. 6, p. 1787, 2023.

[355] D. García-Violini, Y. Peña-Sanchez, N. Faedo, F. Ferri, and J. V. Ringwood, "A broadband time-varying energy maximising control for wave energy systems (LiTe-Con+): Framework and experimental assessment," *IEEE Transactions on Sustainable Energy*, vol. 14, no. 3, 2023.

[356] H. Majidian, L. Wang, and H. Enshaei, "Part A: A review of the real-time sea-state estimation, using wave buoy analogy," *Ocean Engineering*, vol. 266, 2022.

[357] P. A. E. M. Janssen, "Progress in ocean wave forecasting," *Journal of Computational Physics*, vol. 227, no. 7, pp. 3572–3594, 2008.

[358] G. Ibarra-Berastegi, J. Sáenz, A. Ulazia, P. Serras, G. Esnaola, and C. Garcia-Soto, "Electricity production, capacity factor, and plant efficiency index at the Mutriku wave farm (2014–2016)," *Ocean Engineering*, vol. 147, pp. 20–29, 2018.

[359] N. Boccard, "Capacity factor of wind power realized values vs. estimates," *Energy Policy*, vol. 37, no. 7, pp. 2679–2688, 2009.

[360] F. Monforti, M. Gaetani, and E. Vignati, "How synchronous is wind energy production among European countries?," *Renewable and Sustainable Energy Reviews*, vol. 59, pp. 1622–1638, 2016.

[361] R. Oberdieck and E. N. Pistikopoulos, "Parallel computing in multi-parametric programming," in *Computer Aided Chemical Engineering* (Z. Kravanja and M. Bogataj, eds.), Proceedings of the 26th European Symposium on Computer Aided Process Engineering, pp. 169–174, Elsevier, 2016.

[362] I. Simonetti, A. Esposito, and L. Cappietti, "Experimental proof-of-concept of a hybrid wave energy converter based on oscillating water column and overtopping mechanisms," *Energies*, vol. 15, no. 21, 2022.

[363] P. Contestabile, G. Crispino, E. Di Lauro, V. Ferrante, C. Gisonni, and D. Vicinanza, "Overtopping breakwater for wave energy conversion: Review of state of art, recent advancements and what lies ahead," *Renewable Energy*, vol. 147, pp. 705–718, 2020.

[364] L. Cappietti, I. Simonetti, V. Penchev, and P. Penchev, "Laboratory tests on an original wave energy converter combining oscillating water column and overtopping devices," in *Trends in Renewable Energies Offshore*, pp. 8–10, CRC Press, 2018.

[365] N. Faedo, G. Scarciotti, A. Astolfi, and J. V. Ringwood, "On the approximation of moments for nonlinear systems," *IEEE Transactions on Automatic Control*, vol. 66, no. 11, pp. 5538–5545, 2021.

[366] N. Faedo, G. Giorgi, J. Ringwood, and G. Mattiazzo, "Optimal control of wave energy systems considering nonlinear Froude–Krylov effects: Control-oriented modelling and moment-based control," *Nonlinear Dynamics*, vol. 109, no. 3, pp. 1777–1804, 2022.

[367] N. Faedo, G. Giorgi, J. V. Ringwood, and G. Mattiazzo, "Nonlinear moment-based optimal control of wave energy converters with non-ideal power take-off systems," in *Proceedings of the 41st International Conference on Offshore Mechanics and Arctic Engineering*, vol. Volume 8: Ocean Renewable Energy, (Hamburg, Germany), 2022.

[368] N. Faedo, *Optimal Control and Model Reduction for Wave Energy Systems: A Moment-Based Approach*. PhD thesis, National University of Ireland Maynooth, 2020.

[369] MathWorks, "Techniques to improve performance." `https://uk.mathworks.com/help/matlab/matlab_prog/techniques-for-improving-performance.html`, 2023. Last accessed: 29/02/2024.

[370] MathWorks, "Profile your code to improve performancee." `https://uk.mathworks.com/help/matlab/matlab_prog/profiling-for-improving-performance.html`, 2023. Last accessed: 29/02/2024.

[371] C. Moler, "The tetragramma function and numerical craftmanship," tech. rep., MathWorks, 2002.

[372] N. Faedo, D. García-Violini, G. Scarciotti, A. Astolfi, and J. V. Ringwood, "Robust moment-based energy-maximising optimal control of wave energy converters," in *2019 IEEE 58th Conference on Decision and Control (CDC)*, pp. 4286–4291, IEEE, 2019.

[373] N. Faedo, F. D. Mosquera, E. Pasta, G. Papini, Y. Peña-Sanchez, C. A. Evangelista, F. Ferri, J. V. Ringwood, and P. Puleston, "Experimental assessment of combined sliding mode and moment-based control (SM2C) for arrays of wave energy conversion systems," *Control Engineering Practice*, vol. 144, 2024.

[374] N. Faedo, F. D. Mosquera, C. A. Evangelista, J. V. Ringwood, and P. F. Puleston, "Preliminary experimental assessment of second-order sliding mode control for wave energy conversion systems," in *Proceedings of the 2022 Australian and New Zealand Control Conference*, (Gold Coast, Australia), pp. 63–68, 2022.

[375] D. García-Violini, Y. Peña-Sanchez, A. Zarketa, and M. Penalba, "Data-base hydrodynamic coefficients interpolator for control co-design of wave energy converters," in *Proceedings of the 15th European Wave and Tidal Energy Conference*, (Bilbao, Spain), 2023.

[376] Q. Wang, C. Zhang, Y. Ding, G. Xydis, J. Wang, and J. Østergaard, "Review of real-time electricity markets for integrating distributed energy resources and demand response," *Applied Energy*, vol. 138, pp. 695–706, 2015.

[377] P. Freaser, "More of a good thing – Is surplus renewable electricity an opportunity for early decarbonisation?." `https://www.iea.org/commentaries/more-of-a-good-thing-is-surplus-renewable-electricity-an-opportunity-for-early-decarbonisation`, 2019. Last accessed: 01/03/2024.

[378] D. V. Evans, "Wave-power absorption by systems of oscillating surface pressure distributions," *Journal of Fluid Mechanics*, vol. 114, pp. 481–499, 1982.